Sugimoto, Yohei (2014) *Hazardous asteroid mitigation: campaign planning and credibility analysis.* PhD thesis.

Hazardous asteroid mitigation:

Campaign planning and credibility analysis

Yohei Sugimoto

Submitted in fulfilment of the requirements for the

Degree of Doctor of Philosophy

Aerospace Sciences Research Division

School of Engineering

University of Glasgow

ADVISORS:
Dr. Gianmarco Radice
Dr. Matteo Ceriotti

EXAMINERS:
Prof. Alan Fitzsimmons, Queen's University
Prof. Martin Lee, University of Glasgow

LOCATION:
Glasgow, Scotland

DATE:
18 March 2014

Abstract

Of all the natural hazards that could befall on Earth, only an Earth impact of a large comet or asteroid has the potential to wipe out the entire civilisation in a single event while that of a small object could be mitigated by a space program. Over the last decade, Near Earth Objects (NEOs) have rapidly become of interest to scientists and engineers as these small celestial bodies offer tantalising clues to the origins of the solar system and one day they could be used as stepping-stones for further space exploration. The purpose of this dissertation is to present a comprehensive study of such asteroid impact hazards and their mitigation.

During the early stages of hazardous Near Earth Asteroid (NEA) mitigation campaign planning, the fundamental asteroid characteristics (e.g., mass, size, albedo, etc.) should be accurately determined to increase the chance of successful mitigation. However, given a limited warning time, an asteroid impact mitigation campaign would hinge upon uncertainty-based information consisting of remote observational data of the identified Earth-threatening object, general knowledge of NEAs, and engineering judgment. Due to this ambiguity, the campaign credibility could be profoundly compromised. It is therefore imperative to comprehensively evaluate the inherent uncertainty in deflection and properly plan the campaign in order to ensure successful mitigation.

In the thesis, three different (ground-based, space-based, and proximity) preliminary characterisation approaches to the identified threatening object are defined. Their corresponding uncertain information about the fundamental asteroid characteristics is quantified through Evidence Theory based on the existing literature about the NEO population as well as the capability of the three different characterisation approaches. The outcomes of four active hazard mitigation/asteroid deflection techniques (kinetic impactor, nuclear interceptor, gravity tractor, and solar collector) are then evaluated under the uncertainty-based information.

In addition, the thesis investigates the influence of internal density inhomogeneity of the target asteroid on the outcome of the instantaneous deflection approach: kinetic impactor whose deflection efficiency is subject to the actual position of the asteroid's centre of mass with respect to the actual kinetic impact site. Following this, perturbations of a gravity tractor spacecraft orbiting an irregularly-shaped asteroid due to the inhomogeneous asteroid gravitational field are analysed. The effects of asteroid shape and rotational state on a solar collector mission are also briefly evaluated, assuming a rotating ellipsoidal asteroid.

Finally, the thesis extends to the study of a multi-deflection mitigation approach that aims for a high confidence level on successful mitigation and, more specifically, explores a dual-deflection campaign consisting of an instantaneous/quasi-instantaneous deflection technique (kinetic impactor, nuclear interceptor, or solar collector) as a primary mission and a slow-push deflection technique (gravity tractor) as a secondary mission. Here, both deflection efficiency and campaign credibility are taken into consideration. The results of dual-deflection campaign planning show that there are trade-offs between the competing aspects: the total mitigation system mass, mission duration, deflection distance, and the confidence in successful mitigation. The design approach is found to be useful for multi-deflection campaign planning under the uncertainty-based information, allowing to select the best possible combination of deflection missions from a catalogue of various mitigation campaign options, without compromising the campaign credibility.

Table of contents

List of figures

List of tables

Preface

All numerical simulations were run using MathWorks' Matlab® R2010b, R2011a, and R2013a on Windows 7 and Windows 8 systems. Unless otherwise stated, values for physical constants are consistent with those published in 2010 by the Committee on Data for Science and Technology (CODATA), found on physics.nist.gov/cuu/Constants/index.html (link valid as of 23 December 2013) or in Mohr et al. (2012).

COLOPHON

This thesis is written on Windows 8.1 with Microsoft® Office Word 2013.

Acknowledgments

Journal and conference publications

Some ideas and figures in the dissertation may have appeared in the following publications:

[1] Y. Sugimoto, G. Radice, and J. P. Sanchez, "Effects of NEO composition on deflection methodologies," the 2nd IAA Planetary Defense Conference, Bucharest, Romania, 9-12 May, 2011.
[2] Y. Sugimoto, G. Radice, and J.P. Sanchez, "Effects of NEO composition on deflection methodologies," *Acta Astronautica,* vol. 90, pp. 14-21, 2013.
[3] Y. Sugimoto, M. Ceriotti, G. Radice, and J.P. Sanchez, "Hazardous near Earth asteroid mitigation campaign planning based on uncertain information on fundamental asteroid characteristics," the 3rd IAA Planetary Defense Conference, Flagstaff, USA, 15-19 April, 2013.
[4] L. Palacios, Y. Sugimoto, A. Lawal, and G. Radice, "A robust Near Earth Asteroid mitigation campaign of multiple formation flying gravity tractors," the 64th International Astronautical Congress, Beijing, China, 23-27 September, 2013.
[5] Y. Sugimoto, G. Radice, M. Ceriotti, and J.P. Sanchez, "Hazardous near Earth asteroid mitigation campaign planning based on uncertain information on fundamental asteroid characteristics," *Acta Astronautica*, DOI:10.1016/j.actaastro.2014.02.022, 2014.

The conference publications [1] and [3] were awarded the 3rd and 1st best student papers by the planetary defense conference in 2011 and 2013, respectively.

Declaration

I hereby declare that this submission is my own work and that, to the best of my knowledge and Belief, it contains no material previously published or written by another person nor material which to a substantial extent has been accepted for the qualification of any other degree or diploma of a university or other institute of higher learning, except where due acknowledgment is made in the text.

Tokyo, Japan, 18 April 2014

Yohei Sugimoto

Nomenclatures & Definitions

Acronyms

ARM	:	Asteroid Redirect Mission
AU	:	Astronomical Unit, 149,597,870 km
BPA	:	Basic Probability Assignment
CC	:	Carbonaceous Chondrite
COF	:	Centre of Figure
COM	:	Centre of Mass
CEP	:	Circular Error Probability/Circle of Equal Probability
CR	:	Concentration Ratio
DS1	:	Deep Space 1
EDS	:	Earth Departure Stage
ERO	:	Easily Retrievable Object
ESA	:	European Space Agency
ETS-VI	:	Engineering Test Satellite VI
GEODSS	:	Ground-based Electro-Optical Deep Space Surveillance
GT	:	Gravity Tractor
HLV	:	Heavy-Lift Launch Vehicle
IEO	:	Inner Earth Object
IRAS	:	Infrared Astronomical Satellite
JAXA	:	Japanese Aerospace Exploration Agency
KI	:	Kinetic Impactor
KI-GT	:	KI mission followed by GT mission
LINEAR	:	Lincoln Near-Earth Asteroid Research
LONEOS	:	Lowell Observatory Near-Earth-Object Search
MOI	:	Momentum of Inertia
MOID	:	Minimum Orbital Interception Distance
NASA	:	National Aeronautics and Space Administration
NEA	:	Near Earth Asteroid
NEAT	:	Nearby Earth Astrometric Telescope
NEC	:	Near Earth Comet
NEO	:	Near Earth Object
NEOWISE	:	Near Earth Object Wide-field Infrared Survey Explorer
NI	:	Nuclear Interceptor
NI-GT	:	NI mission followed by GT mission
OC	:	Ordinary Chondrite
OSIRIS-REx	:	Origins Spectral Interpretation Resource Identification Security Regolith Explorer
Pan-STARRS	:	Panoramic Survey Telescope And Rapid Response System
PHA	:	Potentially Hazardous Asteroid
PHO	:	Potentially Hazardous Object
SC	:	Solar Collector
SC-GT	:	SC mission followed by GT mission
SCARLET	:	Solar Concentrator Array with Refractive Linear Element Technology
SKE	:	Specific Kinetic Energy
SNE	:	Specific (Absorbed) Nuclear Energy

SRP	:	Solar Radiation Pressure
TNT	:	Trinitrotoluene
TRL	:	Technology Readiness Level
UN	:	United Nations
VI	:	Virtual Impactor
XIES	:	Xenon Ion Engine System
YTW	:	Yield to Weight

Nomenclatures

Chapter 1: Introduction

$\mathbf{v}_\infty$	:	unperturbed geocentric hyperbolic excess velocity vector
$\mathbf{b}$	:	impact parameter/b-plane deflection vector
$R_\oplus$	:	Earth's radius, 6,371 km
$b_\oplus$	:	b-plane deflection scaling actual deflection equal to $R_\oplus$
v_e	:	Earth's escape velocity, 11.2 km/s
v_∞	:	$\|\mathbf{v}_\infty\|$
G	:	gravity constant, 6.67259×10^{-11} m^3/kg/s^2
$M_\oplus$	:	mass of the Earth, 5.9742×10^{24} kg
$M_\odot$	:	mass of the Sun, 1.98855×10^{30} kg
$\mu_\odot$	:	GM product of the Sun, $GM_\odot$
a	:	semimajor axis, AU
e	:	eccentricity
i	:	inclination, deg
$\mathbf{v}_\oplus$	:	Earth's heliocentric velocity vector
$\mathbf{v}'_\oplus$	:	$\mathbf{v}_\oplus$ projected on b-plane
η	:	incoming asymptote direction
ζ	:	negative direction of $\mathbf{v}'_\oplus$
ξ	:	$\eta \times \zeta$
b	:	$\|\mathbf{b}\|$
Δv	:	instantaneous velocity change, cm/s
t_{int}	:	interception epoch/deflection start time
t_f	:	deflection termination time
Θ	:	Earth b-plane azimuth angle
$b_{\min}$	:	minimal required b-plane deflection ($b_\oplus$ for impact risk mitigation)
b_{safe}	:	safe b-plane deflection for impact risk mitigation
b_{key}	:	b-plane deflection for keyhole avoidance
$\mathbf{r}$	:	heliocentric position vector in rotating frame
δs_r	:	displacement in radial direction
δs_θ	:	displacement in transversal direction
δs_h	:	displacement in direction normal to orbit plane in rotating frame
r	:	$\|\mathbf{r}\|$
θ_{MOID}	:	true anomaly at MOID point, deg
M	:	mean anomaly, deg
ω	:	argument of pericentre, deg
Ω	:	argument of ascending node, deg
$\delta\mathbf{v}$	:	vector of instantaneous velocity change
δv_t	:	$\delta\mathbf{v}$ component in direction tangential to orbit
δv_h	:	$\delta\mathbf{v}$ component in direction normal to orbit plane in rotating frame

δv_n	:	$\delta \mathbf{v}$ component in direction parallel to $\delta v_t \times \delta v_h$
θ_{int}	:	true anomaly at t_{int}, deg
v	:	asteroid orbital velocity, km/s
t_{MOID}	:	time at MOID point
n	:	mean motion
n_f	:	mean motion at t_f
$\mathbf{x}$	:	position vector in Cartesian coordinate
$\mathbf{x}_{\text{MOID}}$	:	$\mathbf{x}$ at MOID point
VI_1	:	virtual impactor 1
VI_2	:	virtual impactor 2
VI_3	:	virtual impactor 3
VI_4	:	virtual impactor 4
VI_5	:	virtual impactor 5
VI_6	:	virtual impactor 6
Δv_{min}	:	required Δv for $b = b_{\text{min}}$, cm/s
Δv_{safe}	:	required Δv for $b = b_{\text{safe}}$, cm/s
Δv_{key}	:	required Δv for $b = b_{\text{key}}$, cm/s

Chapter 2: Preliminary characterisation

p_v	:	geometric albedo
M_a	:	asteroid mass, kg
$\mathbf{a}$	:	acceleration vector
$\mathbf{F}$	:	force vector
$\mathbf{v}$	:	velocity vector
ρ_{bulk}	:	bulk-density, g/cm^3
P_{bulk}	:	bulk-porosity
P_{mac}	:	macro-porosity
P_{mic}	:	micro-porosity
ρ_{mic}	:	micro-density, g/cm^3
d	:	equivalent diameter of asteroid, m
V	:	asteroid volume, m^3
κ	:	thermal conductivity, W/m/K
c	:	specific heat capacity, J/kg/K
$\mathbf{p}$	:	vector of mitigation system design parameters
$\mathbf{x}$	:	vector of mitigation system design variables
$\mathbf{y}$	:	vector of mitigation performance indicators
Bel	:	Belief
Pl	:	Plausibility
$\mathcal{A}$	:	event $\mathcal{A}$
$\mathcal{E}$	:	elementary proposition
$m(\mathcal{E})$	:	degree of confidence in elementary proposition $\mathcal{E}$
$\mathcal{U}$	:	universal set/frame of discernment
$\varnothing$	:	empty set
$\mathcal{B}$	:	event $\mathcal{B}$
$\mathcal{C}$	:	event $\mathcal{C}$
$m(\mathcal{A})$	:	degree of confidence in the truth of event $\mathcal{A}$
$m_1(\mathcal{B})$	:	degree of confidence in the truth of event $\mathcal{B}$
$m_2(\mathcal{C})$	:	degree of confidence in the truth of event $\mathcal{C}$
p_1	:	uncertain parameter
p_{11}-p_{14}	:	upper and lower bounds of intervals of p_1
m_{11}-m_{13}	:	BPAs associated with each interval

n	:	number of combination
i	:	combination index
C_i	:	combination/combined proposition
$m_c(C_i)$	:	degree of confidence in the truth of combined proposition C_i
μ_0	:	opacity of asteroid material, m²/kg
ΔH_{sub}	:	sublimation enthalpy, J/kg
T_{sub}	:	sublimation temperature, K

Chapter 3: Asteroid deflection techniques

β	:	momentum multiplication/momentum enhancement factor
β_0	:	base-line β coefficient
U	:	impact velocity, km/s
Y	:	asteroid tensile strength, N/m²
δ	:	impactor density, g/cm³
F_{esc}	:	ratio of the momentum of an escaping ejecta mass element to the momentum of a total ejecta mass
$\mathbf{v}_{imp}$	:	kinetic impact velocity vector with respect to asteroid body frame
m_{KI}	:	KI spacecraft mass
$\Delta\mathbf{v}$	:	vector of instantaneous velocity change by KI or NI, cm/s
δv	:	$\|\Delta\mathbf{v}\|$
δv_{debris}	:	contribution of scattering debris to δv
δv_x	:	contribution of X-ray to δv
δv_n	:	contribution of neutron to δv
δv_γ	:	contribution of gamma ray to δv
m_{debris}	:	mass of scattering debris
m_{dry}	:	dry mass
S	:	ratio between the total area of the nuclear blast and the part of that impinging on the asteroid
R_a	:	asteroid radius
H	:	stand-off distance of NI spacecraft from asteroid
v_{debris}	:	impacting velocity of scattering debris
E_t	:	total yield energy of the nuclear blast
f_{debris}	:	proportion of kinetic energy in E_t
S_{SC}	:	scattering factor
E_A	:	received energy per unit area
dm_A	:	mass per unit area
z	:	depth from asteroid surface
ρ_a	:	asteroid (bulk) density
v_e	:	vaporised material velocity
z_{max}	:	maximum depth at which evaporation takes place
P_A	:	total linear momentum per unit area
ε	:	angle between the direction of the radiation and the direction tangential to the asteroid surface
$m_{ablated}$	:	mass ablated from the asteroid's surface
S_{cap}	:	surface area of a spherical cap
P	:	total linear momentum
λ	:	asteroid central angle
$f_{radiation}$	:	proportion of radiation energy in E_t
λ_{max}	:	distance between the epicentre of the nuclear explosion and the horizon of the asteroid from the epicentre of the nuclear explosion
YTW	:	yield-to-weight ratio

m_{wh}	:	nuclear warhead mass onboard NI spacecraft
m_{NI}	:	NI spacecraft mass
f_{wh}	:	fraction of m_{NI} that accounts for m_{wh}
H_{opt}	:	optimal stand-off distance of NI spacecraft from asteroid
Q_D^*	:	threshold specific energy/catastrophic disruption threshold, J/kg
SKE	:	specific kinetic energy, J/kg
SNE	:	specific absorbed nuclear energy, J/kg
P_{solar}	:	received power density of the solar beam focused on the asteroid surface, W/m^2
η_{eff}	:	efficiency of the SC assembly/solar reflectivity, 90%
$\varphi_s|_{\mathrm{1AU}}$	:	solar flux at 1 AU, 1,367 W/m^2
$R_{\mathrm{SC}-\odot}$	:	SC's heliocentric distance, AU
A_{SC}	:	cross-section area of the reflective surface of the SC perpendicular to the direction of the sunlight
A_{spot}	:	area of the illuminated spot on the asteroid's surface
CR	:	concentration ratio, $A_{\mathrm{SC}}/A_{\mathrm{spot}}$
ΔQ	:	energy absorbed by asteroid surface material
Q_{rad}	:	radiation loss from P_{solar}
Q_{cond}	:	conduction loss from P_{solar}
T	:	asteroid surface temperature, K
T_0	:	initial surface temperature of asteroid material, K
σ	:	Stefan-Boltzmann constant, 5.670373×10^{-8} kg/s^3/K^4
ε_{bb}	:	blackbody emissivity, 1.0
E_v	:	enthalpy of sublimation, J/kg
$\dot{m}_{\mathrm{exp}}$	:	expelled mass flow rate per unit area, kg/s/m^2
$\left(\dot{m}_{\mathrm{exp}}\right)_{\mathrm{total}}$	:	total sublimated mass flow rate, kg/s
x	:	horizontal surface position
y	:	vertical surface position
x_{max}	:	maximum horizontal surface position
y_{max}	:	maximum vertical surface position
t	:	illumination time
V_{rot}	:	rotational velocity
t_{in}	:	time when asteroid surface moves inside illuminated spot
t_{out}	:	time when asteroid surface moves outside illuminated spot
$\bar{v}_{\mathrm{exp}}$	:	average velocity of expelled particles
M_m	:	mass of single molecule
k	:	Boltzmann constant, 1.3806488×10^{-23} J/K
$\mathbf{a}_{\mathrm{solar}}$	:	acceleration of asteroid due to sublimation of asteroid material
m_{SC}	:	SC spacecraft mass
d_{SC}	:	collector's diameter
Q_{spot}	:	energy absorbed by illuminated spot
φ	:	thruster canting angle, deg
ϕ	:	half-angle of exhaust cone of ion beam, deg
F	:	total force required for hovering
T_{GT}	:	thrust force provided by ion thrusters onboard GT spacecraft
m_{GT}	:	GT spacecraft mass
$\mathbf{a}_{\mathrm{GT}}$	:	acceleration of asteroid by GT
m_{prop}	:	propellant mass
m_i	:	initial GT spacecraft mass at asteroid arrival time
I_{sp}	:	specific impulse, s
g_0	:	gravity acceleration on Earth, m/s^2

Δt	:	GT mission duration
m_{ps}	:	power subsystem mass
ξ	:	specific thrust of ion thrusters, N/kW
α	:	specific mass of power subsystem, kg/kW
α_{min}	:	minimum required specific mass, kg/kW
P_{max}	:	maximum required output of power subsystem, kW

Chapter 4: On the effects of NEO inhomogeneity and dynamics

CEP	:	circular error probability or circle of equal probability, 0-1.0R$_{\mathrm{a}}$
ρ_{body}	:	main body's density, g/cm^3
ρ_{neck}	:	neck region's density, g/cm^3
$\mathbf{R}_{\mathrm{COM}}$	:	COM offset vector with respect to centre of the asteroid figure O_{COF}
$\mathbf{I}_a$	:	MOI, kg m^2
Δv_{X}	:	impulsive velocity change along X-axis, mm/s
Δv_{Y}	:	impulsive velocity change along Y-axis, mm/s
Δv_{Z}	:	impulsive velocity change along Z-axis, mm/s
$\hat{\mathbf{r}}_{\mathrm{imp}}$	:	normalised vector of impact point of KI with respect to COM
v_{KI}	:	KI spacecraft's terminal approach velocity parallel to X or Z-axis
U	:	asteroid's gravitational potential, kg^2/s^2
r	:	radius
φ	:	latitude
λ	:	longitude
$P(r, \varphi, \lambda)$	:	any point on and above asteroid surface
R	:	reference length or mean semi-major axis of asteroid
l	:	degree
m	:	order
$\bar{C}_{00}$	:	spherical harmonic coefficients of asteroid that scales value GM_a
$\bar{P}_{lm}$	:	fully normalised Legendre functions
$\bar{C}_{lm}$	:	fully normalised spherical harmonic coefficients of asteroid
$\bar{S}_{lm}$	:	fully normalised spherical harmonic coefficients of asteroid
C_{R}	:	SRP coefficient
$\mathbf{F}_{\mathrm{g}}$	:	gravity force vector
$\mathbf{F}_{\mathrm{SRP}}$	:	vector of force acting on GT spacecraft due to SRP
$\mathbf{r}$	:	position vector of GT spacecraft in asteroid body frame
P_{SRP}	:	solar radiation pressure, N/m^2
$\mathbf{R}_{\mathrm{GT}-\odot}$	:	heliocentric distance of GT spacecraft, AU
A_{R}	:	reference surface of GT spacecraft, m^2

Chapter 5: Towards designing a credible mitigation campaign

m_1	:	mass of primary mitigation system at NEA arrival, kg
m_2	:	mass of secondary mitigation system at NEA arrival, kg
t_1	:	Earth departure time of primary deflection mission
tof_1	:	flight time of primary deflection mission, day
t_2	:	Earth departure time of secondary deflection mission
tof_2	:	flight time of secondary deflection mission, day
t_{int1}	:	primary interception time /deflection start time
$\Delta \mathbf{v}_{\mathrm{imp}}$	:	impact velocity increment of KI in addition to $\mathbf{v}_{\mathrm{imp}}$, km/s
Δt_{GT}	:	GT mission duration, day
Δt_{SC}	:	SC mission duration, day
T_a	:	one asteroid orbital period, day

m_{EDS1}	:	mass of primary mitigation system at EDS, ton
m_{EDS2}	:	mass of secondary mitigation system at EDS, ton
m_0	:	sum of m_{EDS1} and m_{EDS2}, ton
t_{f1}	:	asteroid arrival time of primary mitigation system
t_{f2}	:	asteroid arrival time of secondary mitigation system
b_{nom}	:	nominal b-plane deflection
b_1	:	worst-possible deflection achieved by primary deflection mission
b_2	:	worst-possible deflection achieved by dual-deflection campaign
Bel_{nom}	:	Belief of b_{nom}
Pl_{nom}	:	Plausibility of b_{nom}
b_{trim}	:	post-primary deflection trim deflection through secondary mission

1

1. Introduction

"It is all a matter of time scale. An event that would be unthinkable in a hundred years may be inevitable in a hundred million."

— Carl Sagan, *Cosmos*, 1980

This chapter presents an overview of near-Earth objects (NEOs) and the NEO impact hazards to the Earth, followed by introduction to the present planetary defense efforts, asteroid deflection on b-plane, and virtual impactors. Finally, the research motivation, objectives, and the thesis structure are summarised at the end of the chapter.

1.1. Fundamentals of near-Earth asteroids

Near-Earth objects (NEOs) are small celestial bodies, such as asteroids and comets in the solar system that orbit the Sun, fly by and intersect the orbital path of the Earth. Some of them occasionally make close approaches to the Earth, and pose potentially catastrophic impact risks. The current statistics [1] show that approximately 99% of the identified NEOs are near-Earth asteroids (NEAs). In recent years, NEAs are increasingly becoming of interest to scientists and space engineers for multiple reasons; firstly because asteroids are believed to be the remnants of the solar dust cloud (i.e., nebula) from which the solar system formed approximately 4.6 billion years ago; and secondly because they are relatively easily-accessible celestial bodies from Earth due to small delta-v requirements for a flyby, rendezvous, or for an even more challenging sample return mission. Their easy accessibility is often compared with that of the Moon or Mars; the delta-v required for transferring from a low-Earth orbit to rendezvous with the Moon is about 6.0 km/s and with Mars is about 6.3 km/s whereas for a NEA rendezvous it can be as low as 3.8 km/s [1], or even lower if a

gravitational assist "swing-by" is used [2]. For the planet Earth and any ecological systems on it, however, NEOs pose a constant threat. Hence, understanding the nature of NEOs would help us better understand the mysteries of formation and evolution of the solar system, and ultimately the origin of life on Earth; while at the same time, it is an indispensable prerequisite to the very survival of human civilisation on the planet.

Looking back over the history of asteroid discoveries, the biggest asteroid, and the only dwarf planet in the inner solar system, namely (1) Ceres, between the orbits of Mars and Jupiter, was first discovered by an Italian astronomer, Giuseppe Piazzi on 1 January 1801. The discovery rate of asteroids remained low until about 1900 and increased only slightly, but steadily towards the end of the 20th century [3]. Shortly thereafter, the rate of asteroid discoveries has increased exponentially thanks to the recent extensive sky surveys (e.g., LINEAR, NEAT, Spacewatch, LONEOS, Catalina, Pan-STARRS, NEOWISE, etc.), detecting hundreds of new objects each year as chronologically shown in Figure 1. About 636,000 asteroids, mostly in the main belt (i.e., asteroid belt) between the orbits of Mars and Jupiter, and over 10,000 NEAs had been discovered as of 9 November 2013. Red dots in Figure 1 represent asteroids that cross the Earth's path, and thus they are all NEAs, while those shown by green dots are not. However, in the solar system, millions of asteroids including at least 100,000 NEAs larger than 100 m in diameter and 1,000 NEAs larger than 1 km are believed to be present.
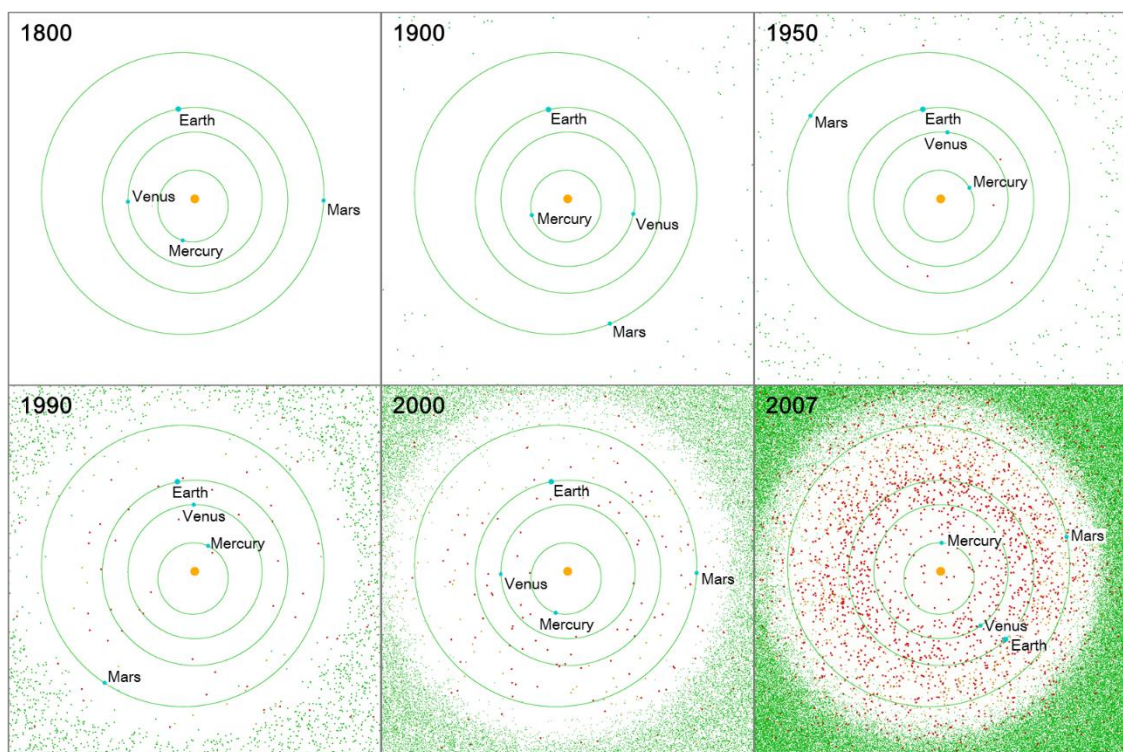
Figure 1 History of asteroid discovery from 1800 to 2007 [4]. Exponential increase in discovery rate can be seen due to the recent sky survey efforts.

Only recently, these minor celestial bodies in the solar system have been visited by spacecraft to perform close observations and reveal fundamental characteristics that cannot be appreciated or detected from Earth. Table 1 is the list of past, current, and future space missions that have visited asteroids or comets.

Table 1 Past, present, and future missions to asteroids, comets, and dwarf planets [5].

Object	Mission	Year	Type
Comet Giacobinni-Zinner	ICE	1985	flyby
Comet Halley	Vega 1, 2; Giotto; Suisei	1986	flyby
(951) Gaspra	Galileo	1991	flyby
Comet Grigg-Skjellerup	Giotto	1992	flyby
(243) Ida	Galileo	1993	flyby
(253) Mathilde	NEAR Shoemaker	1997	flyby
(9969) Braille	Deep Space 1	1999	flyby
(433) Eros	NEAR Shoemaker	2000-2001	orbiter, lander
Comet Borrelly	Deep Space 1	2001	flyby
Comet Wild 2	Stardust	2004-2006	sample return
Comet Tempel 1	Deep Impact, Stardust NExT	2005, 2011	flyby
(25143) Itokawa	Hayabusa	2005-2010	sample return
(2867) Steins	Rosetta	2008	flyby
(21) Lutetia	Rosetta	2010	flyby
Comet Hartley	Deep Impact/EPOXI	2010	flyby
(4) Vesta	Dawn	2011	orbiter
Comet churyumov-Gerasimenko	Rosetta	2014-2015	orbiter, lander
(134340) Pluto	New Horizons	2015	flyby
(1) Ceres	Dawn	2015	orbiter
(162173) 1999 JU$_3$	Hayabusa 2	2018-2020	sample return
(101955) Bennu	OSIRIS-REx	2019-2023	sample return
500-ton NEA (*TBD)	ARM	2017-2025	rendezvous, capture, redirection

As can be seen, missions to these small bodies have been increasing in number in recent years. Among them, sample return missions are invaluable for the insight into the solar system as well as for the planetary defense purposes. For example, the Hayabusa mission has revealed the direct connection between asteroidal mineral composition and spectral counterparts available on Earth (i.e., meteorites) for the first time by returning the surface grain samples of asteroid (25143) Itokawa back to Earth [6]. There are a couple of new sample return missions namely Hayabusa 2 and OSIRIS-REx (Origins Spectral Interpretation Resource Identification Security Regolith Explorer) to be launched in 2014 and 2016, respectively. A spacecraft will be sent to C-type asteroid (162173) 1999 JU$_3$ for

Hayabusa 2 and to B-type asteroid (101955) Bennu, also known as 1999 RQ_{36}, for OSIRIS-REx. These exploration missions are expected to reveal the nature of the "believed-to-be" most primitive small bodies in the solar system. In-situ characterisation of C-type asteroids by these missions is invaluable because relatively dark objects like C-type asteroids are the most difficult to characterise from the ground. Further information about the taxonomy of asteroids is presented in Subsection 1.1.1.

After the close Earth encounter of (367943) Duende, also known as 2012 DA_{14}, and the Chelyabinsk meteor event in early 2013, the technology demonstration of orbital manipulation and retrieval of asteroids, for both planetary defense and space resources utilisation purposes, have become an important topic amongst scientists, engineers, and politicians. The Asteroid Redirect Mission (ARM) concept as part of the Asteroid Initiative (see Figure 2) is a potential future deep space mission originally designed by Keck Institute for Space Studies [7] and proposed by NASA in 2013 on the White House's 2014 budget request. The ARM aims to bring a 7-m diameter, 500-ton NEA to a high lunar orbit or the second Earth-Moon Lagrange point by 2025 and to investigate it through unmanned robotic and manned missions. The ARM's initial goal is to develop the technology to manipulate an asteroid's orbit for multiple purposes; to assess the ability for astronauts to work in space far beyond the low Earth orbit of the International Space Station (e.g., in cislunar space); and to develop technologies for planetary defense, extraterrestrial resources utilisation, and human missions to Mars. The ARM is however currently lacking a suitable NEO for capturing (easily retrievable objects: EROs) and is facing NASA budget cut.
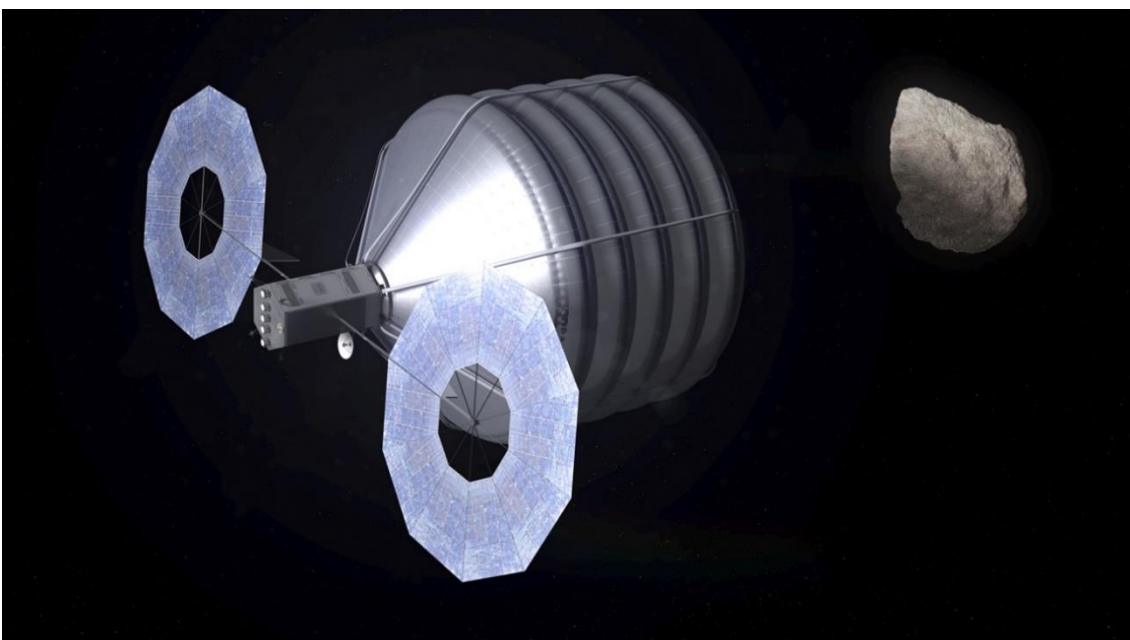
Figure 2 Conceptual image of Asteroid Redirect Mission (ARM) as an important part of NASA's Asteroid Initiative and Grand Challenge [8].

1.1.1. Taxonomic classification of asteroids

There are various types of asteroids that can be categorised in terms of geometric albedos of their surfaces. One of the most well-recognised asteroid classifications is Tholen's taxonomic classification [9] which is based on geometric albedo and spectral characteristics of asteroid surface mineralogy. Within the asteroid belt, C-type asteroids account for 75% of the entire discovered asteroid population followed by S-type asteroids accounting for 17%, and M-type asteroids representing the third most populous group [10]. C-type asteroids are extremely dark objects with geometric albedo lower than 0.04 whereas S-type and M-type asteroids with geometric albedo greater than 0.1 are relatively bright in space.

- C-group (dark carbonaceous objects, about 75% of the asteroid population)
  - ➢ B-type
  - ➢ F-type
  - ➢ G-type
  - ➢ C-type (standard C-group's asteroids, albedo: <0.04)

- S-type (silicaceous objects, about 17% of the asteroid population, albedo: 0.10-0.22)

- X-group
  - ➢ M-type (metallic objects, the third most populous group, albedo: 0.10-0.18)
  - ➢ E-type
  - ➢ P-type

- Other classes
  - ➢ A-type
  - ➢ D-type
  - ➢ T-type
  - ➢ Q-type
  - ➢ R-type
  - ➢ V-type

In the near-Earth region, the population of S-type asteroids outnumber that of C-type asteroids (see Figure 3). This predominance of S-type may be biased due to the difficulty in identifying darker NEAs (e.g., C-type asteroids) through ground-based optical observations, and thus, further efforts on NEAs discovery by means of infrared space telescopes are required. The new infrared space telescopes called Sentinel [11], dedicated to NEAs discovery, is expected reveal the true/unbiased asteroid taxonomical population. The Sentinel telescopic spacecraft will be put on Venus like orbit in order to have an ideal field of view for "NEO hunting." It will be, if the mission is successful, the first ever privately funded "deep space" mission. Further discussion on the origin of NEAs and asteroid-meteorite relationships is given in the following Subsection.
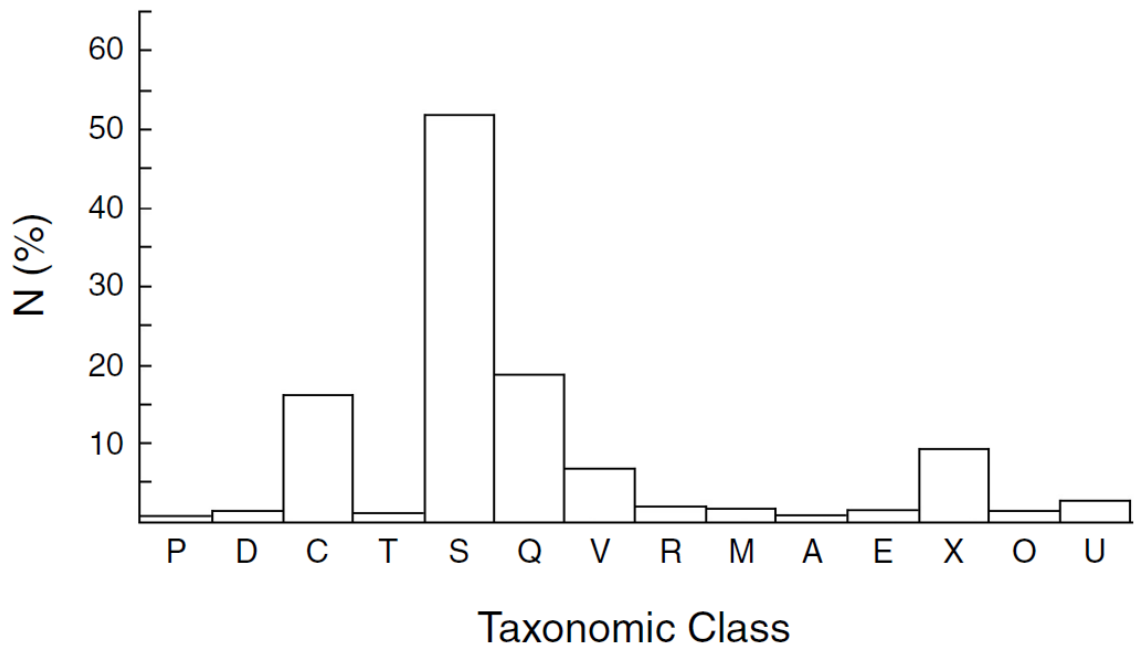
Figure 3 Taxonomic class of 300 NEAs [12]. S-type asteroids are dominant (<50%) in the near-Earth region although this statistical information is likely biased due to the difficulty of discovering darker NEAs such as C-type asteroids which are dominant in the asteroid belt.

Figure 4 is a breakdown of meteorites actually seen to fall on Earth, which clearly shows that the stony type of meteorites (i.e., ordinary chondrites) dominate the meteorite population available on Earth. This agrees well with the fact that the stony type of asteroids (i.e., S-type) dominates the NEA population as shown in Figure 3 but why are there so many S-type asteroids in near-Earth space and so many ordinary chondrites on Earth?

iron ◼ stony-iron ◼ achondrite ◼ carbonaceous ◼ enstatite ◼ ordinary ◼ others
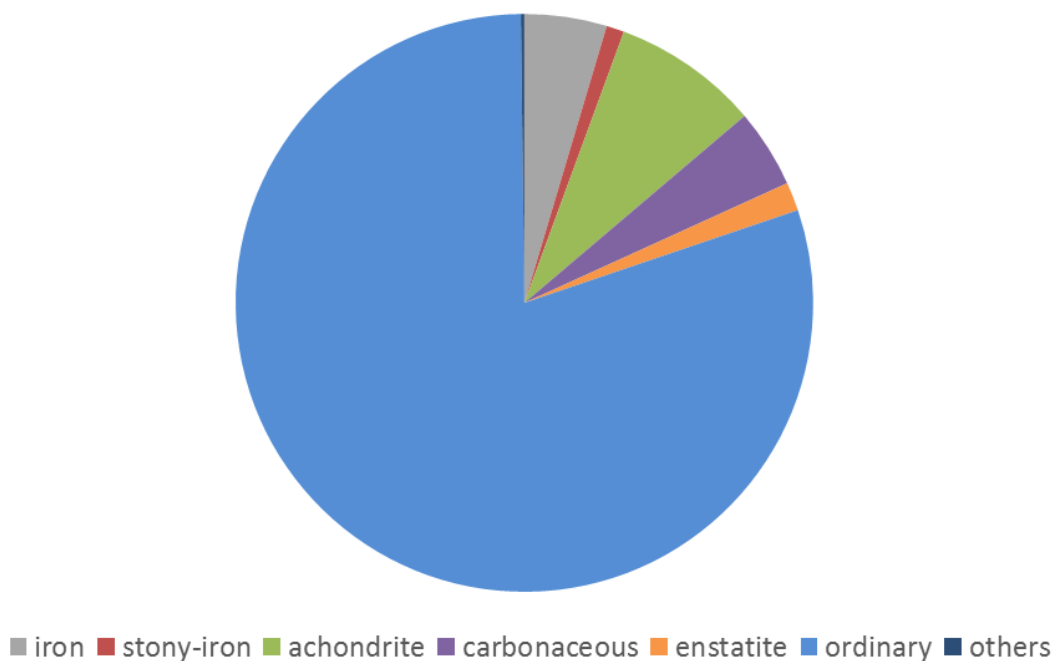
Figure 4 Relative abundance of meteorites actually seen to fall on Earth [13, 14].

1.1.2. Asteroid and meteorite relationships

Observational, dynamical, and spectroscopic arguments suggest that most meteorites originate from the asteroid belt [13]. Although 75% of the asteroid population in the asteroid belt is C-type (i.e., primitive asteroids), there are differences between the relative abundance of asteroid types in the asteroid belt, that of NEA types, and that of meteorite types collected on Earth. There are several factors that combine to bias the meteorite population available on Earth, resulting in our limited samples of the asteroid belt.

Dynamical processes that deliver meteorites from the asteroid belt to Earth are biased towards sampling relatively narrow zones in the asteroid belt. The previous studies by Wetherill [15] in 1985 and Wisdom [16] in 1987 suggest that the vast majority of meteorites and NEAs originate from the near the 3:1 Kirkwood gap and the v 6 resonance. These zones are in the inner asteroid belt, in which there are abundance of primarily differentiated and relatively less primitive asteroids: S-type for instance [17].

Another factor that contributes to the biased meteorite population on Earth is relative strength of meteorites [18]. Some asteroids and fragments of them (i.e., meteorites) begin to evolve into Earth-crossing objects by being ejected at high velocity from parent bodies through major impact events [19]. To survive the impact events without being shattered into tiny fragments that are too small to survive Earth's atmospheric entry, the meteorite must have sufficient cohesive strength [20]. This would strongly bias towards selecting more cohesive meteorites (e.g., ordinary chondrites, completely metallic iron meteorites, mostly metallic stony-irons, etc.) whereas less cohesive meteorites (e.g., carbonaceous chondrites) with relatively weaker strength would be eliminated through the impact processes.

Such cohesive strength of meteorites is also an important selection factor for the meteorites that survive collisional events in near-Earth space and for those that survive the deceleration and heating of atmospheric entry [18]. According to the previous study on cosmic-ray exposure ages of meteorites by Wetherill and Chapman [18, 21], collisional events in near-Earth space do make NEAs shattered into smaller fragments while they are in Earth-crossing orbits. Earth's atmospheric entry involves a series of thermal and dynamical stresses that typically break up most fragile, stony meteorites from one large individual body into smaller fragments [18].

Although the meteorite samples on Earth are limited and biased due to the multiple factors stated above, they provide us with valuable information about the fundamental physical properties of asteroids. This doctoral thesis will deal with three asteroid taxonomic classes: S-type, C-type, and M-type asteroids, and therefore, three different types of meteorite analogues: ordinary chondrites, carbonaceous chondrites, and iron meteorites. These meteorite types will be referred to as potential meteorite analogues of S-type, C-type, and M-type asteroids, respectively [22, 23]. Meteorite analogues are often assumed through spectrum analyses of asteroid surface composition. The meteorite type whose spectral/compositional characteristics (e.g., silicaceous, carbonaceous, metal-rich, etc.) are most similar to the measured reflectance spectra of an asteroid surface is assumed to be its meteorite analogue. Since internal composition of an asteroid has never been uncovered and studied thus far, the connections between taxonomic classes and meteorite analogues may be valid for asteroid surfaces but not necessarily for their interiors.

The other major problem of the meteorite analogues is that the space environment can affect the reflectance spectra of asteroid surface material. Asteroid mineral composition can be interpreted through observing remotely sensed reflectance spectra of asteroid surfaces. The previous study of the lunar surface have revealed that the spectra of the surface material, the regolith, can be strongly affected by its long-term exposure to the impact, thermal, and radiation environment in space [24]. These regolith processes can alter the spectra of asteroid material, making the identification of asteroid mineralogy more complicated [25]. Such selection and alteration affect our understanding of the connection between asteroids and meteorites, resulting in the limited use of the meteorite collection as representative samples of asteroids.

1.1.3. Orbital classification of near-Earth asteroids

NEAs can be not only categorised by the taxonomic classification but also sorted in four distinct orbital types: Apollo, Aten, Amor, and inner Earth objects (i.e., IEO or Atira) as illustrated in Figure 5. Among the four orbital types, Apollo and Aten groups are the only two types that intersect the Earth's path and occasionally make close Earth approaches or impacts with the Earth at the worst case scenarios.

Some of these NEOs including near-Earth comets (NECs) that are threatening to the Earth are sub-grouped as potentially hazardous objects (PHOs). PHOs are all the discovered NEAs and NECs with an orbit that takes them to the vicinity (>0.05 AU) of the Earth and

have a diameter of 140 m or larger which is thought to be large enough to provide a regional scale catastrophe. Amongst 10,414 NEOs (including only 94 NECs) discovered as of 9 November 2013 [1], 1,433 NEAs are identified as potentially hazardous asteroids (PHAs) and being tracked by NEA monitoring programs such as the Ground-based Electro-Optical Deep Space Surveillance (GEODSS), Spaceguard, etc. Through the extensive NEA observations in recent years, nearly 90% of NEAs larger than 1 km (above the global catastrophe threshold) have been detected, and yet, none of them present a significant impact risk to Earth, at least, for the next centuries to come [26]. The current discovery status on those smaller than 1 km in diameter is insufficient and thus they are yet to be found more in number.

Apollo
Semimajor Axis ≥ 1.0 AU
Perihelion ≤ 1.02 AU
Earth Crossing

Aten
Semimajor Axis < 1.0 AU
Aphelion ≤ 1.0167 AU
Earth Crossing

Amor
1.02 AU < Perihelion ≤ 1.3 AU

Inner Earth Objects (IEOs)
Aphelion < 0.983 AU
Always inside Earth's orbit
(aka Apohele)

Type	Near-Earth Population
Apollo	62% of known asteroids
Aten	6% of known asteroids
Amor	32% of known asteroids
IEO	6 known asteroids
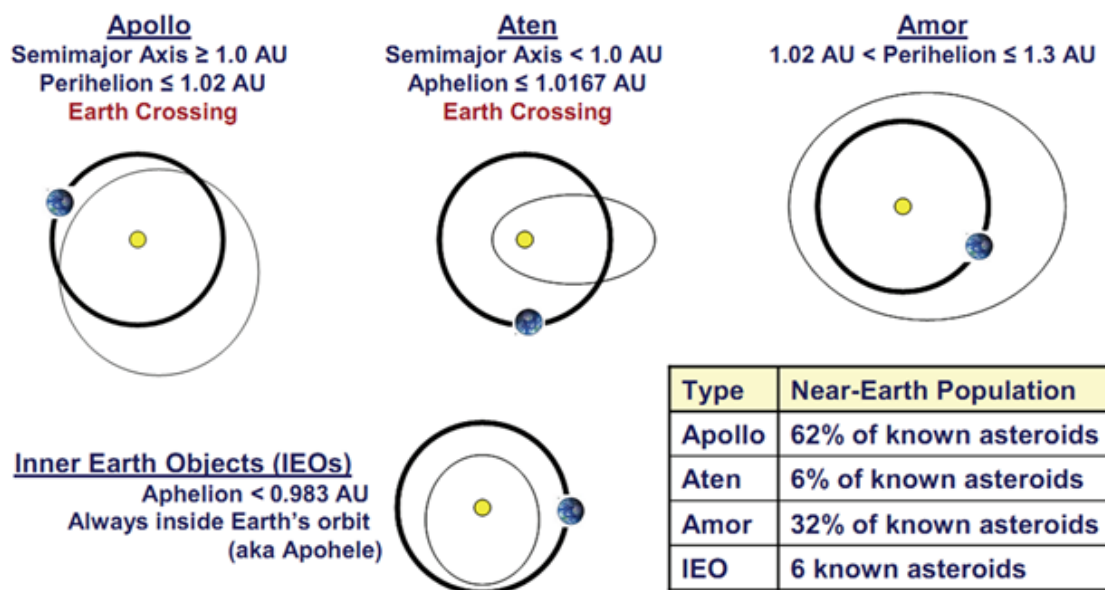
Figure 5 Four orbital types of NEAs [27]. Only NEAs of Apollo and Aten groups can pose a potential impact risk to the planet Earth.

1.1.4. Impact hazards

By looking back over the history of the Earth-Moon system and looking into their present-day landscapes, we can see that there is clear evidence of the incessant bombardments by asteroids and comets ever since the formation of the planetary system, 4.6 billion years ago. It is believed that the extinction of dinosaurs on Earth about 65 million years ago was triggered by a single very large, >10 km meteor impact, also known as the Cretaceous-Palaeogene (K-Pg) extinction event [28]. Although today's NEO impact hazards may not be as significant or frequent as those of millions of years ago any more, the solar system of today still contains abundant NEOs and thus Earth impact events are merely a matter of time scale. In the recent history of planet Earth, the most well-recognised impact event that

humanity has experienced would be the Tunguska event in Siberia, on 30 June 1908 shown in Figure 6 [29] or the Chelyabinsk event occurred on 15 February 2013. In the Tunguska event, the massive airburst of a meteoric object (most likely a cometary fragment) of ~30 m in diameter with an explosive yield equivalent to 2-15 megatons of TNT devastated over 2,000 km^2 of the Tunguska forest which is, for example, roughly the same size as the city of Tokyo. Such a local scale impact event is believed to occur once in a few centuries whereas a dinosaur-killer/multi-kilometre sized object that can trigger a mass extinction impact event roughly once in a hundred million years. Although the Tunguska's airburst occurred well above (5-10 km) an almost deserted forest in Russia, the consequences of an impact event similar to the Tunguska event above a densely populated area would be devastating.

Photo: Leonid Kulik Expedition, 1927
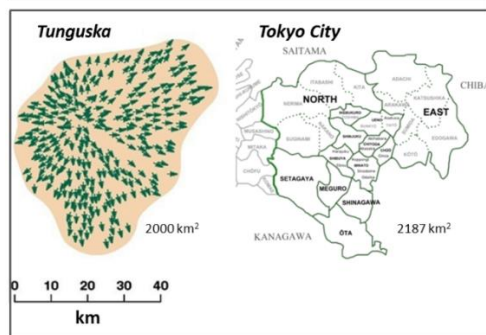
Figure 6 Tunguska event in Siberia, on 30 June 1908 [29]. An airburst explosive yield is estimated to be equivalent to 2-15 megatons of TNT devastated over 2,000 km^2 of the Tunguska forest. The size of the flattened forest is nearly equal to the size of Tokyo city.

Since NEO impact events are all a matter of time scale, the statistics on the frequencies of various scales of impact hazards elucidate which impact scenario is more or less likely and thus more or less hazardous to the Earth. Table 2 shows impact frequencies and typical consequences associated with various types of NEO impact events. According to this, the next destructive NEO impact event would be most likely brought by an object 10-50 m in diameter, which agrees well with the fact that NEAs of this size range make up the majority of the discovered PHAs larger than 10 m in diameter [26].

Table 2 Impact frequency and typical consequence [26]. Airburst events are rather frequent compared with more devastating scenarios such as those of global catastrophe.

Type of Event	Characteristic Diameter of Impacting Object	Approximate Impact Energy (MT)	Approximate Average Impact Interval (years)
Airburst	25 m	1	200
Local scale	50 m	10	2,000
Regional scale	140 m	300	30,000
Continental scale	300 m	2,000	100,000
Below global catastrophe threshold	600 m	20,000	200,000
Possible global catastrophe	1 km	100,000	700,000
Above global catastrophe threshold	5 km	10 million	30 million
Mass extinction	10 km	100 million	100 million

More importantly, such a smaller impactor sometimes remains unidentified until it is found just a few days before its close approach or, its Earth impact. For example, 2011 MD, a 5-20 m sized asteroid was discovered by the Lincoln Near-Earth Asteroid Research (LINEAR) on 22 June 2011 before it passed close to Earth's surface at a distance of about 12,000 kilometres on 27 June 2011, only five days after the detection of 2011 MD. A meteor impact of this scale (i.e., a few kilotons of TNT) would however not be as devastating as the Tunguska event but mostly ends up with the majority of the meteor evaporated as it passes through the Earth's atmosphere, lighting up in the sky as a shooting star, and being observed by people nearby or CCTV cameras by chance. Such a smaller meteoric event is actually beneficial as it allows to draw public attention to impact hazards as well as to collect the remnants: "meteorite falls" which provide us with information about the possible constituents of the meteorites' parent body.

It should be noted however that "when working with the statistics of small samples, and particularly when less likely scenarios have outcomes that are much more catastrophic than the most likely scenario, one should not assume that the next event will be the most likely one [26]." NASA's Sentry System, in fact, has identified a number of hundred-metre sized NEAs as potentially-hazardous although their threat levels are often downgraded and rarely upgraded as more precise orbital determination takes place. One of such hazardous bodies is asteroid (99942) Apophis whose equivalent diameter is approximately 325 ± 15 m. Its net energy at impact would be 510 megatons of TNT, if it were to hit the Earth in 2036. Apophis,

whose orbit is illustrated in Figure 7, is classified as an Apollo. The probability of the impact on 13 April 2036 was once believed to be 1 in 250,000; however, Apophis' appearance on 9 January 2013 provided scientists with enough information to rule out the possibility of an impact in 2036 [30]. What made this Apophis case remarkable was not just its impact threat but its close Earth approach seven years prior to 2036. Apophis will pass very close to the Earth (i.e., within the orbits of geosynchronous communication satellites) on 13 April 2029. This close Earth approach can put Apophis through a narrow strip, also known as keyhole [31], in the uncertain region on the 2029 b-plane (the b-plane will be defined in Section 1.3). If it does, Apophis is redirected to a resonant return and it will collide with the Earth on a subsequent encounter. One keyhole on the 2029 b-plane, namely the 2036 keyhole, results in Apophis' Earth impact on 13 April 2036. Thankfully, the chance of the 2036 keyhole passage at the 2029 encounter of the asteroid was ruled out in 2013, hence that of the Earth impact in 2036 [30]. Nevertheless, an Apophis-like object impacts Earth only about once every 100,000 years, hence the next NEO impact would be most likely brought by 140 m or smaller in diameter, only a fraction of which have been discovered as of today.
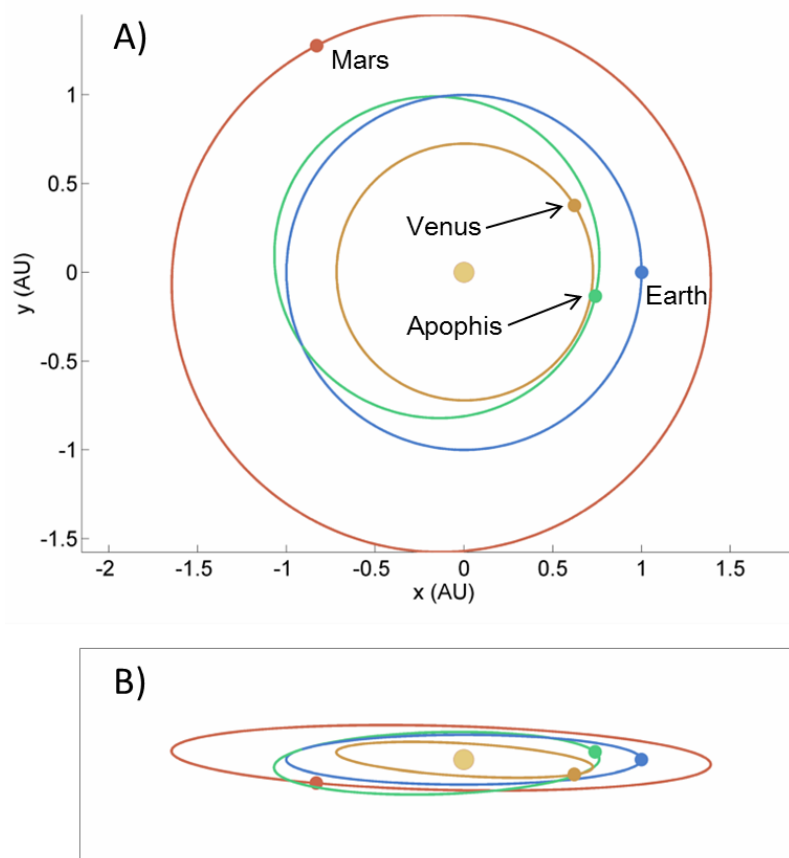
Figure 7 Orbits of (99942) Apophis, Mars, Earth and Venus. Apophis orbits between the orbits of Venus and Mars such that it comes across the orbit of the Earth and occasionally makes close approaches to Earth. A) Ecliptic plane view. B) Sideways view.

1.2. Planetary defense against hazardous objects

Given the fact that a small Tunguska-like NEO impact event is relatively frequent (i.e., once every two or three centuries) and a non-negligible number of sub-kilometre sized NEOs are posing substantial impact risks over the next few centuries, developing technologies for planetary defense against NEOs is becoming more and more of interest to the planetary defense community including national space agencies, governments, and private organisations [26]. Earth impacts by NEAs can have a much greater effect than more common natural disasters such as earthquakes or hurricanes, however, they are one of a few natural catastrophes that humanity would be technologically capable of averting in advance, if threats are identified with a sufficient amount of warning.

The warning time is one of the most important terms in the field of planetary defense. There are various definitions of the word "warning time" but, in this thesis, it basically means the period of time between the identification of a specific threat and the predicted Earth impact. Depending on the given warning time (e.g., months, a few years to decades, etc.), there are a variety of possible planetary defense efforts, where they can be basically divided into the following three categories:

● Preliminary characterisation (Tracking and characterisation of hazardous NEAs)

● Hazard mitigation (Deflection/Orbital change of identified threats by spacecraft)

● Civil defense (Evacuation, sheltering civilians in the predicted area of devastation)

There are different types of preliminary characterisation and hazard mitigation approaches depending on the specific threat characteristics and the hazard scenario, which will be detailed in the following main chapters of the thesis. Civil defense will not be studied as much in detail as preliminary characterisation and hazard mitigation in this dissertation, and thus, interested readers should refer to the literature about civil defense efforts [32].

1.2.1. Discovery, tracking, and characterisation efforts

Through the previous/on-going sky surveillance programs for NEO hunting conducted by the world-leading astronomical observatories and research institutions: LINEAR, NEAT, Spacewatch, LONEOS, Catalina, Pan-STARRS, NEOWISE, etc., over 10,000 NEOs of various sizes have been discovered as of 9 November, 2013 [1]. Following these successful

sky surveillance programs, the B612 Foundation is now driving a space-based surveillance mission called Sentinel: the first privately funded deep space mission fully dedicated to NEO detection for planetary defense purposes to be launched by December 2016 [11]. The Sentinel 20-inch infrared space telescope will be put in a Venus-like orbit as shown in Figure 8, and is expected to identify 90% of NEOs as small as 140 m in diameter during 5.5 years of its surveillance operations. The United Nations (UN) has recently announced their asteroid defense plan to the world's space agencies. The UN's plan is to create an International Asteroid Warning Network so nations can share what they know about asteroids and cooperate with scientists from several countries' space agencies to look for the smallest and most frequent Earth impactors, as well as make plans to divert them away from the Earth.
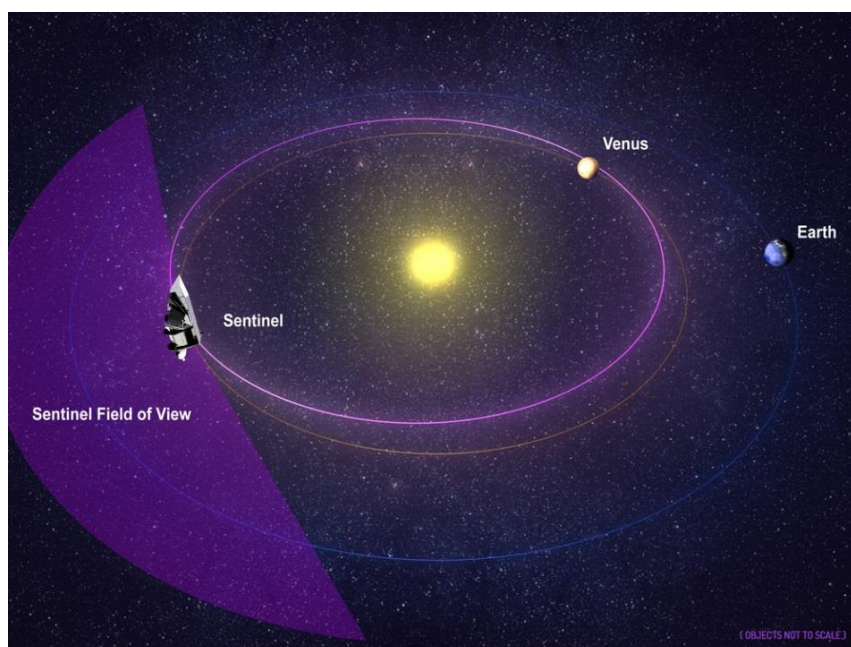
Figure 8 Sentinel mission's overview [11]. The Sentinel telescopic spacecraft will be put on Venus like orbit in order to have an ideal field of view for "NEAs hunting".

Among the discovered NEOs, PHOs are closely monitored by NEO tracking programs such as NASA's Sentry system so as to update their orbits and identify possible near future impact hazards with non-negligible risk [26]. Orbital determination of PHOs is one of the most important components of planetary defense efforts. The accuracy of orbital determination of small, ~140-m diameter bodies is not as good as that of greater sized objects such as the planets, their moons, and relatively large asteroids: impact risks of small, hundred-metre sized PHOs (e.g., Apophis, 2011 AG$_5$, 2007 VK$_{184}$, etc.) are subject to high levels of uncertainty in orbit determination, resulting in the difficulty in accurately predicting Earth impacts a few decades in advance.

NEO characterisation has two roles: acquisition of general knowledge of the entire NEO population (e.g., orbital determination, common physical aspects, accumulation of statistical data, etc.) and identification of the prerequisite physical properties of a specific threat during the early stages of mitigation campaign planning. We have only begun to understand the fundamentals of small celestial bodies thanks to the space exploration missions to asteroids and comets listed in Table 1. Our general knowledge of the NEO population is currently still limited; however, it will improve step by step through the next generation of missions such as JAXA's Hayabusa 2 mission (see Figure 9) currently under development and to be launched in 2014 [33], and NASA's OSIRIS-REx to be launched in 2016 [34]. In practice, precursor missions for proximity characterisation of Earth-menacing objects will make effective use of the flight-proven heritage of these asteroid explorers.

Figure 9 Hayabusa 2 mission to (162173) 1999 JU$_3$ [33]. Similarly to the former Hayabusa mission, Hayabusa 2 will attempt collection of asteroid material by its "sampler horn".

1.2.2. Mitigation campaigns

Given an identified threatening object on a collision course with Earth, global scale responses to the threat are required in order to mitigate the impact risk depending on the scale/scenario of the threat. Such a hazardous NEO mitigation campaign should consist of multiple planetary defense efforts including preliminary characterisation, orbital change, and civil defense. Preliminary characterisation will provide us with information about the specific threatening NEO. One or multiple asteroid deflection missions will then be set up based on the preliminary characterisation while civil defense should be ready in case the deflection attempts fail. However, in this thesis, the term "mitigation campaign" will simply represent risk mitigation efforts: orbit manipulation of the threat by one or multiple asteroid

deflection techniques. A mitigation campaign against a specific threatening object will vary widely depending on the asteroid taxonomic class, orbit, scale, available warning time, and selected deflection missions that are available in the list of mitigation campaign options shown in Figure 10.
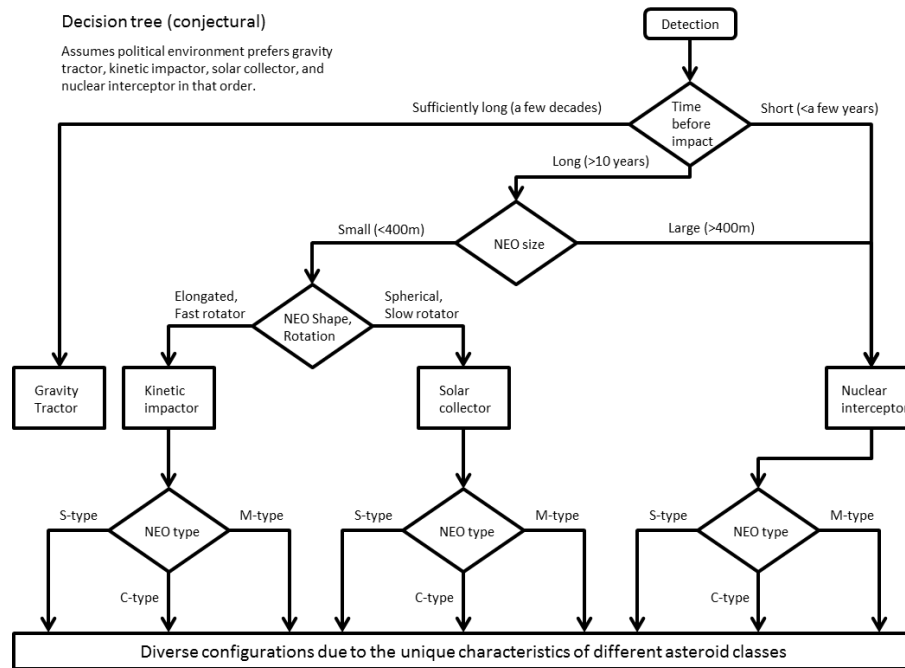
Figure 10 Variety of mitigation campaign components. The configuration of an asteroid mitigation system will be strongly subject to the hazard scenario.

1.2.3. Asteroid deflection techniques

Currently, several of asteroid deflection concepts: kinetic impactor, nuclear interceptor, asteroid tugboat, solar collector, laser ablation, mass driver, gravity tractor, ion beam shepherd, solar sail, electrostatic tractor, and enhancement of natural effects (most typically the use of photon pressure or solar energy) have been proposed [26, 35-44]; however, none of them have ever been practically demonstrated. Although most of them are technologically challenging, some are viable with current Technology Readiness Levels (TRLs). A kinetic impactor would be built on the heritage of the Deep Impact spacecraft that successfully demonstrated a high speed impact on Comet Tempel 1 in 2005 [45]. A gravity tractor could take inspiration from the Hayabusa or Deep Space 1 (DS1) that successfully demonstrated deep space maneuverer by its electric propulsion system [46, 47]. Sanchez *et al*. [48] recently performed multi-criteria comparison analysis of different asteroid deflection techniques and the results have shown that some of them (e.g., kinetic impactor, nuclear interceptor, solar collector, etc.) could be effective against Earth-threatening NEOs with a diameter under 150 m given 10 years of warning or longer.

This however may not always be valid if the preliminary NEO characterisation is insufficient since deflection techniques such as the kinetic impactor and nuclear interceptor physically interact with the target body; and the solar collector sublimates surface material. These techniques will be therefore, strongly dependent on not only the physical characteristics but also the mineral composition and properties of the object. Again, as no asteroid deflection concept has ever been demonstrated in space, their deflection efficiency is subject to the accuracy of mathematical modelling, and inherent assumptions. Further details about modelling of deflection techniques are presented later in Chapter 3.

1.3. Asteroid deflection on b-plane

In the literature about planetary encounters, the concept of a target plane called a b-plane, is often introduced when dealing with asteroid and comet encounters [31]. The b-plane is orientated normal to the incoming asymptote of the osculating geocentric hyperbola, in other words, it is orientated normal to the object's unperturbed geocentric/hyperbolic excess velocity vector $\mathbf{v}_\infty$ as shown in Figure 11. The b-plane analysis can not only determine whether an Earth collision is possible, but also determine how close to the Earth the encounter will be. Furthermore, understanding the position of an Earth encountering object on the b-plane (i.e., the uncertainty ellipsoid projected on the b-plane) is prerequisite to the keyhole analysis. With the b-plane we obtain the minimum distance of the unperturbed trajectory at the closest approach point, which is the impact parameter $\mathbf{b}$ denoted by a red arrow in Figure 11. The impact parameter itself does not reveal whether the perturbed trajectory will intersect the figure of Earth projected on the b-plane, but this information can be available by scaling Earth's radius $R_\oplus$ according to Equation (1)

$$b_\oplus = R_\oplus \sqrt{1 + \frac{v_e^2}{v_\infty^2}} \tag{1}$$

where v_e is Earth's escape velocity and v_∞ is the hyperbolic excess velocity of the incoming asteroid.

$$v_e^2 = \frac{2GM_\oplus}{R_\oplus} \tag{2}$$

$$v_\infty^2 = \mu_\odot \left(3 - 1/a - 2\sqrt{a(1-e^2)}\cos i \right) \tag{3}$$

With this we can determine that a given trajectory intersects the Earth figure projected on the b-plane if $b_\oplus < \|\mathbf{b}\|$, and not otherwise.

A convenient geocentric b-plane reference system (ξ, η, ζ) is set by aligning the negative ζ-axis with the projection of Earth's heliocentric velocity $\mathbf{v}_\oplus$, the positive η-axis with the hyperbolic excess velocity $\mathbf{v}_\infty$ (i.e., normal to the b-plane), and the positive ξ-axis in such a way that the reference system is positively orientated. On the b-plane, ξ-component of $\mathbf{b}$ represents the minimum Earth-asteroid distance by varying the timing of the encounter of the Earth and the asteroid such that ζ-component of $\mathbf{b}$ is zero. This distance, known as the minimum orbital intersection distance (MOID), is equivalent to the minimum separation between the osculating ellipses, without regard to the location of the objects on their orbits. Throughout the thesis, the MOID is basically set to zero and thus the incoming asteroid passes through the origin of the b-plane reference frame (i.e. the centre of Earth). The objective of an asteroid deflection mission is therefore, to change the timing of the asteroid encounter with the Earth or to modify the impact parameter $\mathbf{b}$ on the b-plane (mainly $\hat{\imath}_\zeta$ component of it) to a desired distance (e.g., at least $b_\oplus = 1.0$ and more if possible) through either an instantaneous velocity change Δv at the interception/deflection start time t_{int} or continuous acceleration on the target asteroid over the interval $(t_{\text{int}} - t_f)$, where t_f is the time when the deflection manoeuvre (i.e., orbital manipulation of the asteroid) terminates.

b: Impact parameter
η: Incoming asymptote direction
ζ: negative direction of Earth's heliocentric velocity projected on b-plane $\mathbf{v}'_\oplus$
ξ: $\eta \times \zeta$
Θ: Earth b-plane azimuth angle
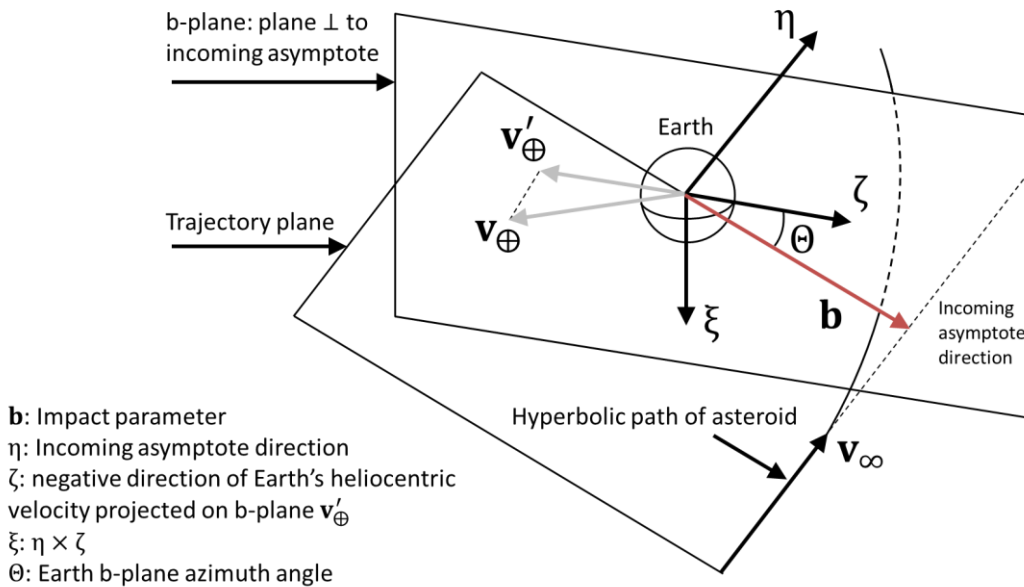
Figure 11 B-plane reference frame (ξ, η, ζ) on the Earth b-plane. The red arrow represents the impact parameter b which is to be manipulated through an asteroid deflection mission for planetary defense purposes. As can be seen, the asteroid trajectory is hyperbolic in this coordinate frame due to the influence of Earth's gravity, which in turn means that asteroid deflection should be better discussed on the b-plane for convenience.

1.3.1. Required deflection on b-plane

Depending on the NEO hazard scenario: Earth impact hazard, keyhole passage, etc., the required deflection on the b-plane varies considerably. In this thesis, three different required deflection distances – minimum deflection distance, safe deflection distance, and keyhole deflection distance – are defined in order to study a variety of hazard mitigation scenarios.

1.3.1.1. Minimum deflection distance: b_{min}

When a hazardous asteroid is identified to be on a collisional course with the Earth (even though such cases are rather rare due to ambiguous orbit determination), a hazardous asteroid mitigation attempt should be made and, at least, achieve the minimal required deflection on the b-plane to avoid the Earth impact, in other words, to make sure that $b > b_{min} = b_\oplus$ is true (see Figure 12). $b_\oplus$ is dependent on how fast the Earth encounter takes place or, more precisely, on the hyperbolic excess velocity v_∞ of the asteroid in Equation (1).
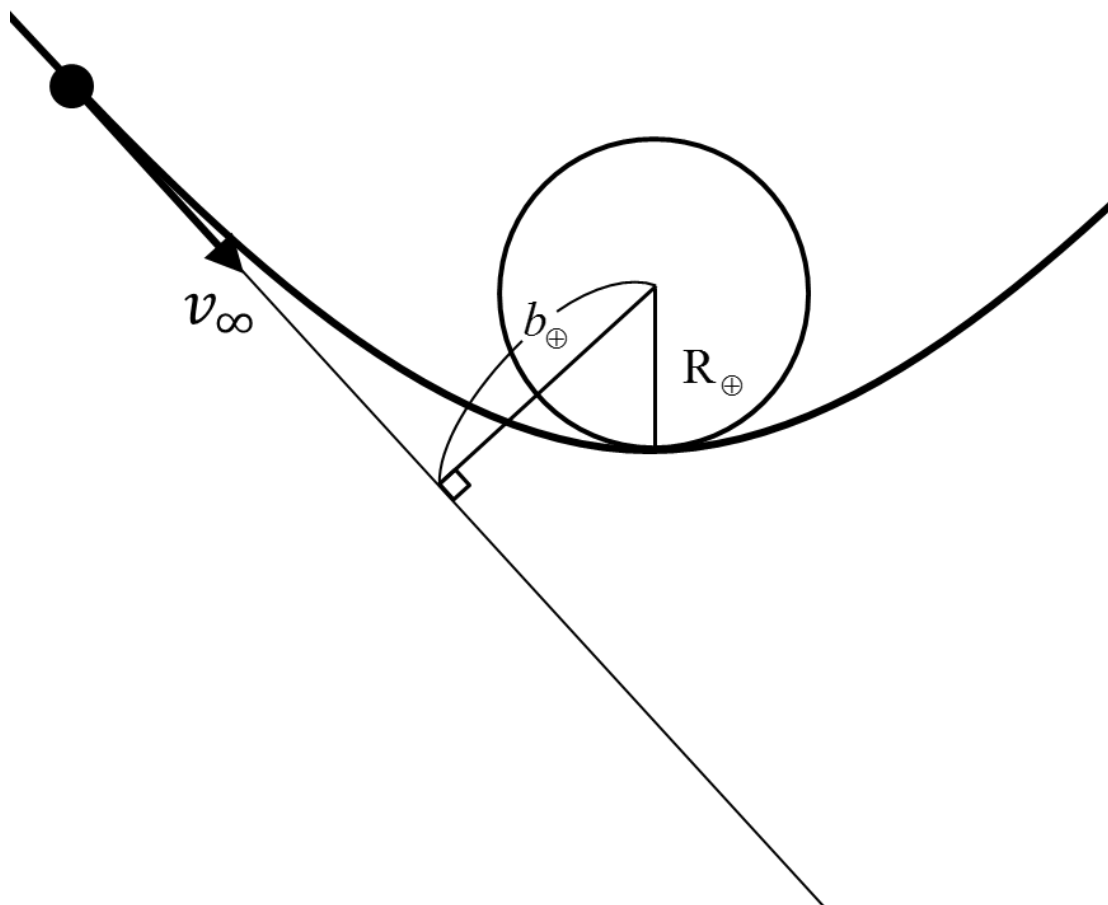
Figure 12 Theoretical minimum deflection distance required for impact avoidance: $b_\oplus$. In reality, asteroid orbit determination and deflection attempts involve a certain amount of uncertainty so that this minimum deflection distance does not necessarily guarantees a successful mitigation.

1.3.1.2. Safe deflection distance: b_{safe}

The safe deflection distance is assumed to be about $2\frac{1}{2}\ b_\oplus$ (i.e., approximately 16,000 km deflection in real scale) throughout this thesis, which is thought to be sufficient to provide a safe margin in missing Earth by the National Research Council [26]. The safe deflection distance varies according to the minimum deflection distance b_{min} (i.e., $b_\oplus$), hence the orbit or v_∞ of the target hazardous object.

1.3.1.3. Keyhole deflection distance: b_{key}

When an asteroid makes a close approach to Earth but with no impact risk, there is a small chance of it passing through a tiny narrow stripe called "keyhole" on the b-plane as shown in Figure 13 [31]. If the asteroid passes through a keyhole, it will be put on a resonant return and impact Earth on a subsequent close encounter. Keyholes are typically very small (a few tens of metres to about 10 km at most) whereas a b-plane uncertainty ellipse semi-major axis is often much greater than keyholes mainly due to the inevitable uncertainties in orbit determination of small bodies that propagate through the numerical integration of the asteroid's orbit over time until the b-plane passage. Given in-situ measurements by spacecraft [49], the uncertainty ellipse semi-major axis is still expected to be about a few hundred kilometres for one sigma. For this reason, the required deflection distance for keyhole avoidance should be, at least, greater than the semi-major axis of the b-plane uncertainty ellipse due to the ambiguous asteroid orbit determination of the small bodies.
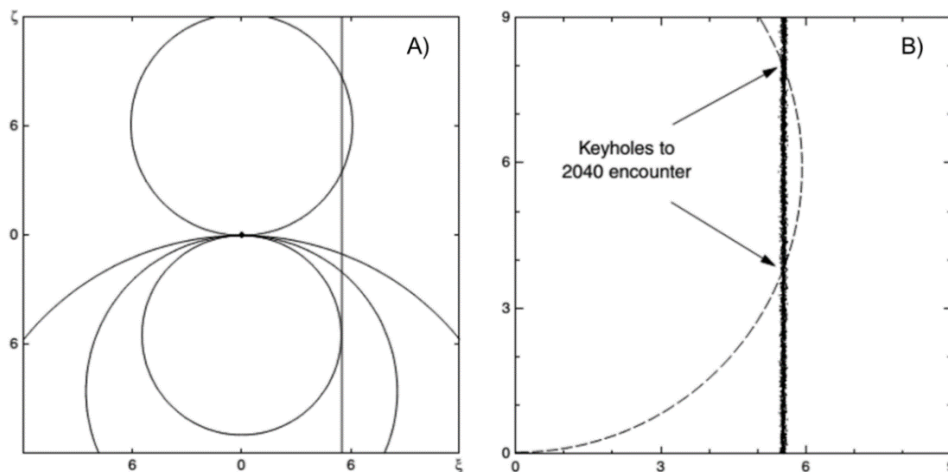
Figure 13 Circles corresponding to various mean-motion resonances on the b-plane of the 2027 encounter with Earth of asteroid 1999 AN$_{10}$. Distances are in Earth radii augmented for gravitational focusing (b$_\oplus$). A) Uppermost circle: 7:13 resonance; then, with the centres along the ζ-axis, from top to bottom: 3:5, 10:17, and 11:19 resonances. The vertical line at ξ=5.5× b$_\oplus$ represents fictitious asteroids, all with the same orbit as 1999 AN$_{10}$ and spaced in the time of encounter with Earth. B) Explicit depiction of keyholes for the 2040 returns on the 2027 b-plane of 1999 AN$_{10}$. The stream of Monte Carlo points corresponds to the vertical line in A). The dashes represent the best-fitting circle passing through the impacting zones [31].

1.3.2. Formulation of asteroid deflection on b-plane

A deflection on a b-plane can be derived by computing the perturbed orbit from the unperturbed orbit of the asteroid. Proximal motion equations [50], which are given as a function of the variation of the orbital elements are used to compute the deflection in this dissertation. The variation of the orbital elements can be computed with Gauss's planetary equations [51]. Assuming that the deflection manoeuvre is a perturbation on the orbit of the asteroid, the perturbed deflection orbit can be regarded to be proximal to the unperturbed orbit. The variation of the position of the asteroid with respect to the genuine position can be derived by using the proximal motion equations described as

$$\delta \mathbf{r} = [\delta s_r \quad \delta s_\theta \quad \delta s_h]^T \tag{4}$$

$$\delta s_r \approx \frac{r}{a} \delta a + \frac{ae\sin\theta_{\mathrm{MOID}}}{\eta} \delta M - a\cos\theta_{\mathrm{MOID}}\delta e \tag{5}$$

$$\delta s_\theta \approx \frac{r}{\eta^3}(1 + e\cos\theta_{\mathrm{MOID}})^2 \delta M + r\delta\omega$$

$$+ \frac{r\sin\theta_{\mathrm{MOID}}}{\eta^2}(2 + e\cos\theta_{\mathrm{MOID}})\delta e + r\cos i\delta\Omega \tag{6}$$

$$\delta s_h \approx r(\sin u_{\mathrm{MOID}}\delta i - \cos u_{\mathrm{MOID}}\sin i\delta\Omega) \tag{7}$$

where δs_r, δs_θ, and δs_h are the displacements in the radial and transversal directions, and the direction perpendicular to the orbit plane in a rotating frame $\{\hat{\imath}_r \quad \hat{\imath}_\theta \quad \hat{\imath}_h\}$, respectively. θ_{MOID} is the true anomaly of the asteroid at the MOID point along the unperturbed orbit. ω and e are the argument of pericentre and the eccentricity of the asteroid, respectively. The argument of latitude at the MOID point along the unperturbed orbit u_{MOID} and η can be described as below.

$$u_{\mathrm{MOID}} = \theta_{\mathrm{MOID}} + \omega \tag{8}$$

$$\eta = \sqrt{1 - e^2} \tag{9}$$

1.3.2.1. Instantaneous deflection

In this case, Gauss's planetary equations written for an instantaneous change in the asteroid velocity vector $\delta\mathbf{v}$ is used to compute the variation of the orbital parameters a, e, i, Ω, and ω between unperturbed and perturbed orbits with the total variation in the mean anomaly δM. The components of $\delta\mathbf{v}$ are expressed in the directions tangential and normal to the asteroid's orbit in rotating frame and the direction perpendicular to the orbit plane at $\theta = \theta_{\text{int}}$ where θ_{int} is the true anomaly of the asteroid at t_{int}.

$$\delta\mathbf{v} = [\delta v_t \quad \delta v_n \quad \delta v_h]^T \tag{10}$$

$$\delta a = \frac{2a^2 v}{\mu_\odot}\delta v_t \tag{11}$$

$$\delta e = \frac{1}{v}\left[2(e + \cos\theta_{\text{int}})\delta v_t - \frac{r}{a}\sin\theta_{\text{int}}\delta v_n\right] \tag{12}$$

$$\delta i = \frac{r\cos u_{\text{int}}}{h}\delta v_h \tag{13}$$

$$\delta\Omega = \frac{r\cos u_{\text{int}}}{h}\delta v_h \tag{14}$$

$$\delta\omega = \frac{1}{ev}\left[2\sin\theta_{\text{int}}\delta v_t + \left(2e + \frac{r}{a}\cos\theta_{\text{int}}\right)\delta v_n\right]$$
$$-\frac{r\sin u_{\text{int}}\cos i}{h\sin i}\delta v_h \tag{15}$$

$$\delta M = \frac{b}{eav}\left[2\left(1 + \frac{e^2 r}{p}\right)\sin\theta_{\text{int}}\delta v_t + \frac{r}{a}\cos\theta_{\text{int}}\delta v_n\right]$$
$$+\delta n(t_{\text{MOID}} - t_{\text{int}}) \tag{16}$$

t_{MOID} is the time at the MOID point along the orbit of the asteroid and $u_{\text{int}} = \theta_{\text{int}} + \omega$. Equation (16) takes the instantaneous change of the orbit geometry at time t_{int} and the change in the semimajor axis given by $\delta n(t_{\text{MOID}} - t_{\text{int}})$ into consideration, where δn is given as below.

$$\delta n = \sqrt{\frac{\mu_\odot}{a^3}} - \sqrt{\frac{\mu_\odot}{(a + \delta a)^3}} \tag{17}$$

1.3.2.2. Continuous slow-push deflection

In the case of a continuous low thrust deflection, Gauss's variational equations are numerically integrated over the interval $(t_{\text{int}}\text{-}\,t_f)$, applying the acceleration provided by the deflection strategy. δM is computed in a parallel manner to Equation (17)

$$\delta M = \left(n_f - n\right)t_{\text{MOID}} + nt_{\text{int}} - n_f t_f + \Delta M \tag{18}$$

where n is the mean motion, n_f is the mean motion at the deflection termination time t_f. ΔM is then calculated through the numerical integration of Gauss's equations.

Finally, once $\delta \mathbf{r}$ at t_{MOID} is computed, it is transformed to a deflection vector $\delta \mathbf{x}$ in a Cartesian coordinate frame $\{\hat{\imath}_x \quad \hat{\imath}_y \quad \hat{\imath}_z\}$ and then to a deviation vector of impact parameter $\delta \mathbf{b}$ (where $\delta \mathbf{b}$ is equal to $\mathbf{b}$ throughout this thesis) in the Earth's b-plane coordinate frame $\{\hat{\imath}_\xi \quad \hat{\imath}_\eta \quad \hat{\imath}_\zeta\}$ through Equations (19) and (20).

$$\delta \mathbf{x} = [\delta x \quad \delta y \quad \delta z]^T = \mathbf{A} \cdot \delta \mathbf{r} \tag{19}$$

$$\delta \mathbf{b} = [\delta \xi \quad \delta \eta \quad \delta \zeta]^T = \mathbf{B} \cdot \delta \mathbf{x} \tag{20}$$

Coordinate transformation matrices $\mathbf{A}$ and $\mathbf{B}$ are given by Equations (21) and (22) where $\mathbf{x}_{\text{MOID}}$ is a position vector of the asteroid at the MOID in the Cartesian reference frame.

$$\mathbf{A} = [\hat{\mathbf{x}} \quad \hat{\mathbf{y}} \quad \hat{\mathbf{z}}]^T = \left[\frac{\mathbf{x}_{\text{MOID}}}{\|\mathbf{x}_{\text{MOID}}\|} \quad \hat{\mathbf{z}} \times \hat{\mathbf{x}} \quad \frac{\mathbf{x}_{\text{MOID}} \times \dot{\mathbf{x}}_{\text{MOID}}}{\|\mathbf{x}_{\text{MOID}} \times \dot{\mathbf{x}}_{\text{MOID}}\|}\right]^T \tag{21}$$

$$\mathbf{B} = [\hat{\boldsymbol{\xi}} \quad \hat{\boldsymbol{\eta}} \quad \hat{\boldsymbol{\zeta}}]^T = \left[\frac{\mathbf{v}_\oplus \times \hat{\boldsymbol{\eta}}}{\|\mathbf{v}_\oplus \times \hat{\boldsymbol{\eta}}\|} \quad \frac{\mathbf{v}_\infty}{\|\mathbf{v}_\infty\|} \quad \hat{\boldsymbol{\xi}} \times \hat{\boldsymbol{\eta}}\right]^T \tag{22}$$

1.4. Virtual Earth-threatening impactors

Virtual Earth-threatening impactors are imaginary hazardous asteroids on a collision course with Earth that will be intercepted by mitigation campaigns in this study. In this thesis, six virtual impactors are randomly generated based on the realistic orbital distribution of the NEA populations (see Table 3) modelled by Bottke *et al*. [52] by taking into account the relative impact frequency of each possible trajectory [53]. Interested readers should refer to

further explanations on the NEA population model and the relative impact frequency of each possible trajectory of Earth impactors can be found in the respective papers. The orbital characteristics of the virtual impactors and impactors' scale and scenario are presented in the following subsections.

Table 3 Statistics of steady-state NEO and IEO populations [52]. The Apollo group is dominant in the NEO population, followed by the Amor group on second and Aten group on third.

	NEO	Amor	Apollo	Aten	IEO
Predicted pop. size w.r.t. NEO pop. (%)	100	32 ± 1	62 ± 1	6 ± 1	2 ± 0
No. of predicted NEOs with $H < 18$	960 ± 120	310 ± 38	590 ± 71	58 ± 9	20 ± 3
No. of known NEOs with $H < 18$	426	204	195	26	0
Obs. completeness for $H < 18$ NEOs (%)	44	66	33	45	0
$a < 2.0$ AU (%)	49 ± 4	27 ± 3	55 ± 4	100	100
$e < 0.4$ (%)	15 ± 1	25 ± 3	9 ± 1	27 ± 0	48 ± 1
$e < 0.6$ (%)	52 ± 2	87 ± 4	34 ± 2	52 ± 1	73 ± 1
$i < 10°$ (%)	26 ± 1	41 ± 2	20 ± 1	5 ± 0	9 ± 0
$i < 20°$ (%)	55 ± 2	74 ± 1	48 ± 2	19 ± 0	25 ± 0
$i < 30°$ (%)	72 ± 1	87 ± 1	67 ± 1	42 ± 0	49 ± 0

Note. The percentages refer to predicted values for $H < 18$ objects.

1.4.1. Orbits of virtual impactors

The orbits of these virtual Earth impactors are shown in Figure 14. The orbital types of VI_1-VI_6 are either Apollos (VI_1, VI_2, and VI_3) or Atens (VI_4, VI_5, and VI_6). Table 4 shows their orbital parameters where a, e, i, Ω, ω, and θ_{MOID} represent the semi-major axis, eccentricity, inclination, argument of the ascending node, argument of the pericentre, and the true anomaly at MOID point, respectively. The orbit of VI_1 is relatively circular and thus very Earth-like among them (however it is inclined by 7.5 degrees to the ecliptic plane) whereas VI_2 has a highly elliptical orbit with the second largest semi-major axis (1.78 AU). Note that VI_2 is the only Apollo whose perihelion is within 1 AU. VI_3 has the largest semi-major axis (2.66 AU) that makes its aphelion more than 4 AU away from the Sun. VI_4 is apparently the most Earth-like among all the three Aten asteroids (however it still passes by close to the Sun relative to the Apollos) while the other two VI_5 and VI_6 are highly inclined and their perihelia are <0.5 AU from the Sun. Mitigation missions to highly inclined objects will be expensive in general but those approaches close to the Sun are of interest to a specific deflection technique that makes use of sunlight such as the solar collector concept [38].
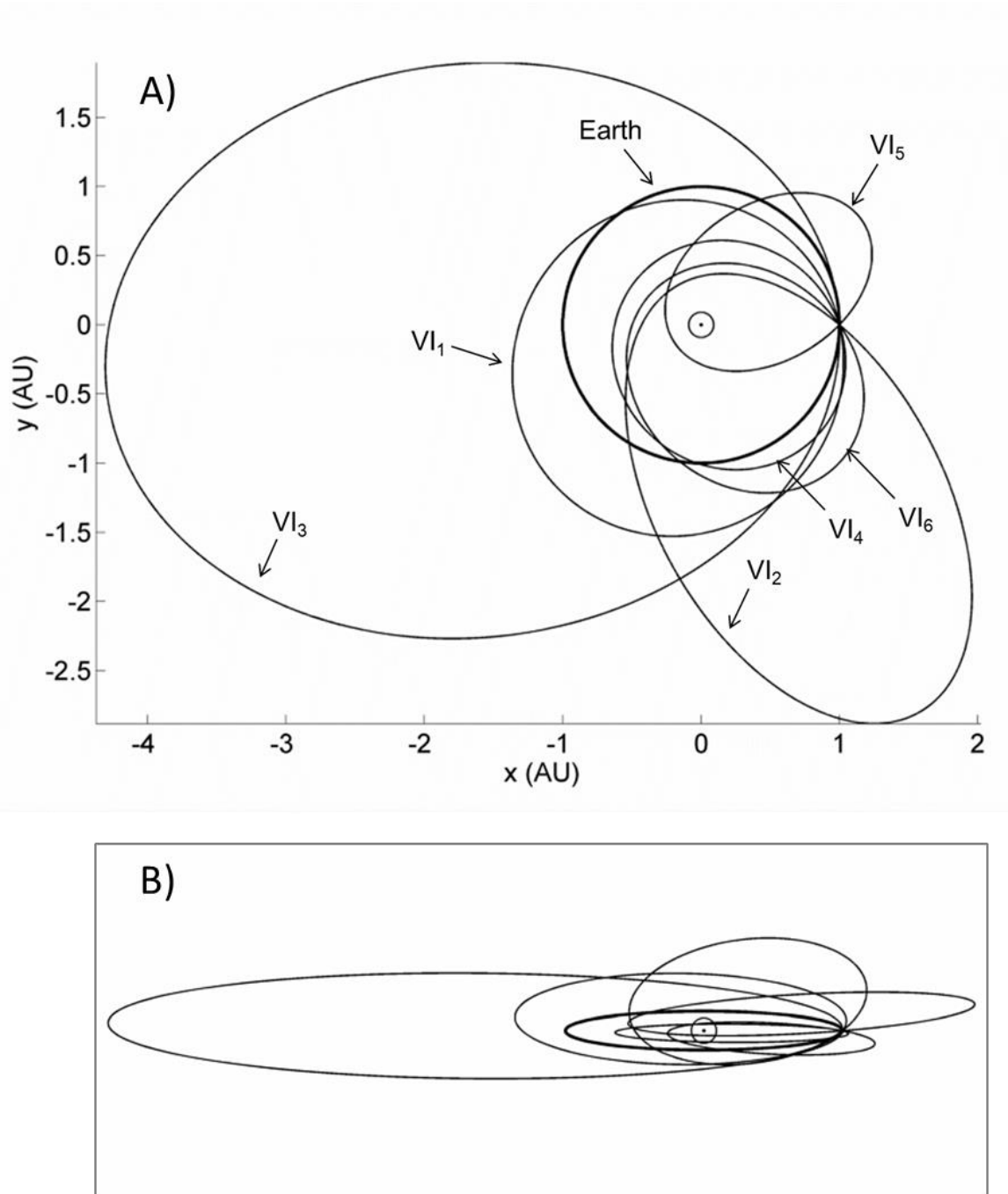
Figure 14 Orbits of virtual impactors VI$_1$-VI$_6$ and Earth. They can be categorised into two orbital groups: Apollo (VI$_1$, VI$_2$, and VI$_3$) and Aten (VI$_4$, VI$_5$, and VI$_6$) groups. A) Ecliptic plane view. B) Sideway view.

Table 4 Ephemeris of virtual impactors VI$_1$-VI$_6$.

Virtual impactor	a (AU)	e	i (deg)	Ω (deg)	ω (deg)	θ_{MOID} (deg)
VI$_1$	1.24	0.289	7.5	180	242	298
VI$_2$	1.78	0.813	2.5	0	119	241
VI$_3$	2.66	0.625	2.5	180	186	354
VI$_4$	0.81	0.731	2.5	180	32.4	148
VI$_5$	0.87	0.345	12.5	0	132	228
VI$_6$	0.95	0.550	22.5	180	307	233

Impact velocities with respect to the Earth, and resultant energy delivered to the Earth by impact of VI_1-VI_6 are summarised in Table 5. The mass of each impactor refers to the nominal value given in Table 10. The energy delivered to Earth is therefore subject to the taxonomic class of the virtual impactors, hence three different values of resultant impact energy for each virtual impactor can be seen here.

Table 5 Impact velocities with respect to the Earth and resultant delivered energy to the Earth by VI_1-VI_6. The equivalent diameters of VI_1-VI_6 are all equally 140 m and the masses are 3.17 × 10^9, 2.05 × 10^9, and 9.32 × 10^9 kg for S-type, C-type, and M-type, respectively.

	Impact velocity (km/s)	Energy delivered by impact (megatons of TNT) S-type / C-type / M-type
VI_1	8.40	26.75 / 17.30 / 78.65
VI_2	28.03	297.67 / 192.50 / 875.18
VI_3	8.42	26.92 / 17.41 / 79.15
VI_4	21.16	170.00 / 109.68 / 498.63
VI_5	11.22	47.67 / 30.83 / 140.14
VI_6	19.85	149.30 / 96.55 / 438.96

1.4.2. Hazard scenario and scale of virtual impactors

The Earth impact events of all the virtual impactors take place on 13 April 2036 while they are discovered and identified to be truly hazardous 10-20 years before the impact event. A mitigation campaign will be launched and executed sometime in this 10-20 year warning time although it is rather optimistic for hundred-metre sized threats, considering the limited capability of asteroidal orbit determination by today's telescopic surveillance [32].

Note that the warning time in this thesis is defined as the time period between the detection of a hazardous NEA and the Earth impact epoch of the hazardous NEA; however, it does not take the mission preparation time into consideration. It is assumed that mitigation systems will be developed and fabricated based on a spacecraft bus in a similar way to the interceptor stack concept proposed by Adams *et al*. [54] such that the preparation time does not require many years unlike conventional space exploration missions.

The equivalent diameter of the virtual impactors is 140 m unless otherwise stated. This is due to the fact that NEOs with 140 m in diameter will represent the worst case among the small NEA population that has not been sufficiently discovered through the previous NEO surveys (e.g. the George E. Brown, Jr. Near-Earth Object Survey section of the 2005 NASA Authorization Act, etc.). Although the B612 Foundation's Sentinel mission will be able to detect 90% of NEOs 140 m in diameter or greater by 2020 and a fraction of those smaller

than 140 m, NEO surveys on ~140-m sized NEOs will not reach a discovery rate as high as 90% any time soon [26]. The mass (i.e., bulk-density) and the other prerequisite physical properties for mitigation mission planning such as the rotation state and thermodynamic properties of the asteroid will be detailed later in Chapter 2.

Although a kilometre sized object could collide with the Earth in the near future, as those undiscovered may be on collisional trajectory, the size of an Earth-threatening object basically scales the cost of mitigation campaigns (of course, this is not always the case if the use of high yield-to-weight nuclear interception is allowed for instance) but is not significant to the main focuses of this study: the uncertain information and mitigation campaign credibility. While characterisation of larger NEAs may be carried out more accurately and affect mitigation mission design, this thesis does not intend to focus on kilometre sized objects but it will only deal with hazard mitigation of the modest, 140/280-m sized NEAs with warning time of 10-20 years.

The aim of an asteroid deflection is to make the impact parameter b on the 2036 b-plane larger than, at least the minimal required deflection distance $b_{\min} = b_{\oplus}$, or the desired safe distance $b_{\text{safe}} = 2\frac{1}{2} b_{\oplus}$. Two different deflection distances $b_{\min}$ and b_{safe}, the required minimum impulsive velocity change $\Delta v_{\min}$ for $b_{\min}$, and Δv_{safe} for b_{safe} are shown in Table 6 for each virtual impactor, where these required velocity changes are tangential to the asteroid orbits. They are computed for a kinetic impact at the optimal interception epochs (i.e., perihelia of VI_{1-6}) when a required velocity change is minimal while satisfying $\Delta b = b_{\oplus}$, given the 10-year warning time. Finally, Figures 15-20 summarise the variation of the achievable deflection distance by $\Delta v_{\min}$ applied to VI_1-VI_6 at any timing of instantaneous velocity change between 13 April 2026 and 13 April 2036.

Table 6 Minimum deflection distance $b_{\min}$, safe deflection distance b_{safe}, required velocity change $\Delta v_{\min}$ for $b_{\min}$, and Δv_{safe} for b_{safe}, given Δv at the first perihelion epoch t_{int} of each impactor within the 10-year mitigation window before the impact epoch on 13 April 2036.

Virtual impactor	$b_{\min}$ (Earth-radius)	$\Delta v_{\min}$ (cm/s)	b_{safe} (Earth-radius)	Δv_{safe} (cm/s)	t_{int} (date)
VI_1	1.66	0.79	4.16	1.98	2026/10/9
VI_2	1.08	0.19	2.70	0.48	2026/12/10
VI_3	1.66	1.38	4.16	3.44	2027/8/14
VI_4	1.13	0.43	2.83	1.07	2026/8/31
VI_5	1.41	0.79	3.53	1.98	2026/9/17
VI_6	1.15	0.49	2.87	1.24	2027/2/17
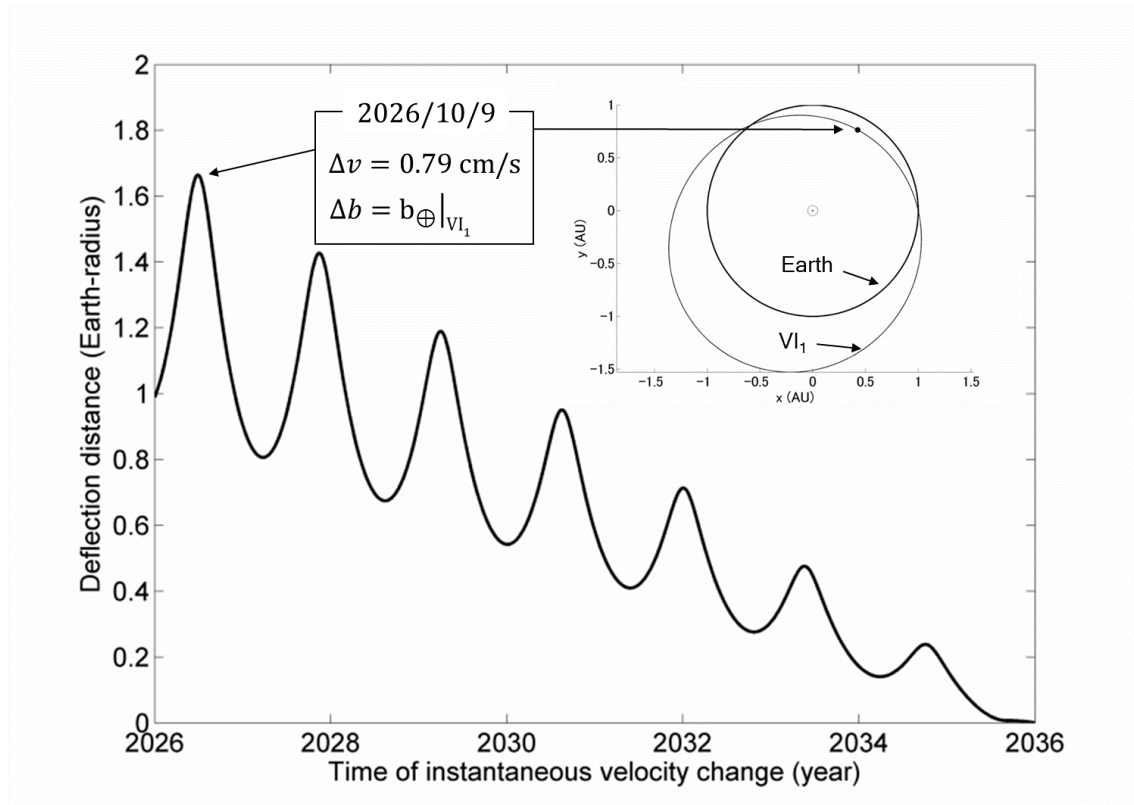
Figure 15 Variation of deflection distance of VI$_1$ on the 2036 b-plane, given $\Delta v = 0.79$ cm/s.
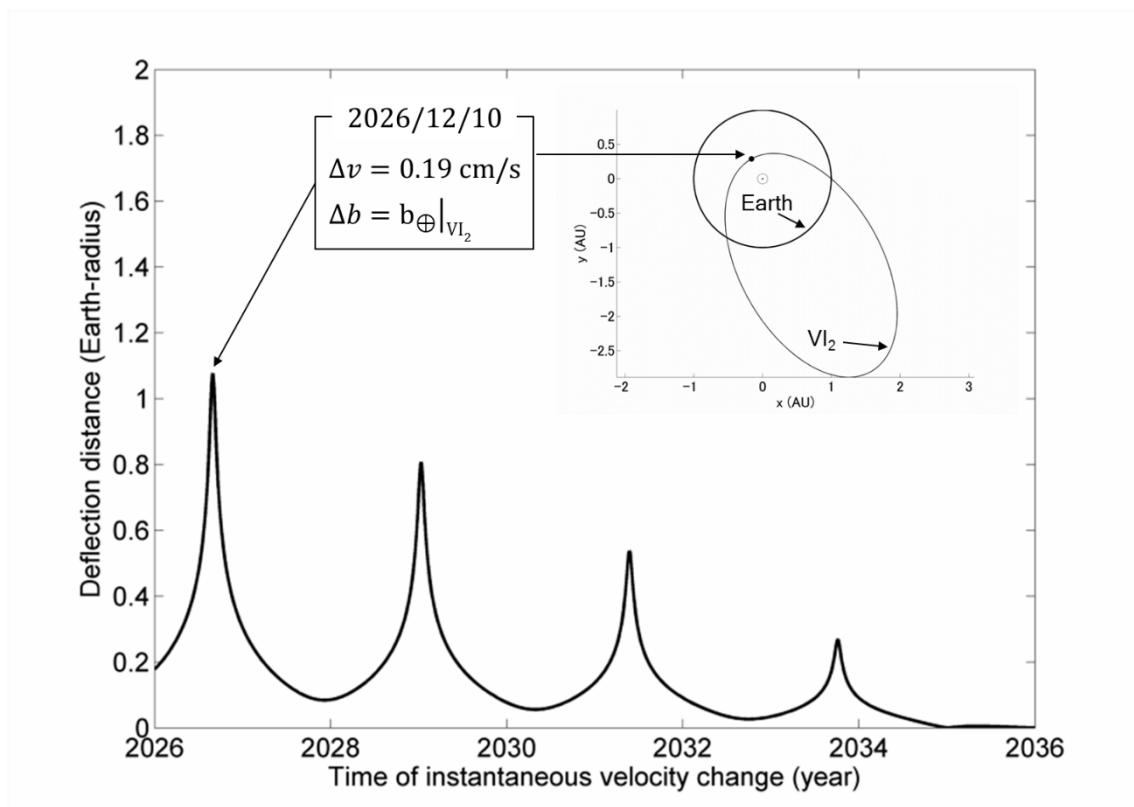
Figure 16 Variation of deflection distance of VI$_2$ on the 2036 b-plane, given $\Delta v = 0.19$ cm/s.
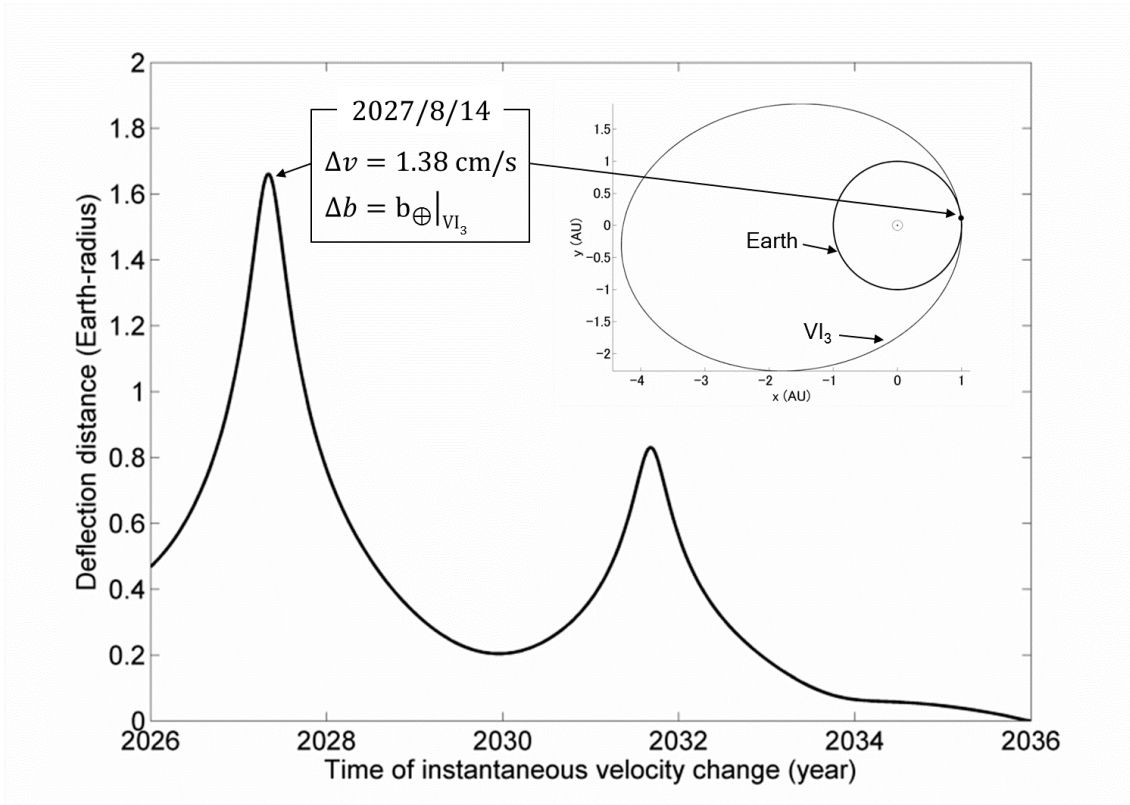
Figure 17 Variation of deflection distance of VI$_3$ on the 2036 b-plane, given $\Delta v = 1.38$ cm/s.
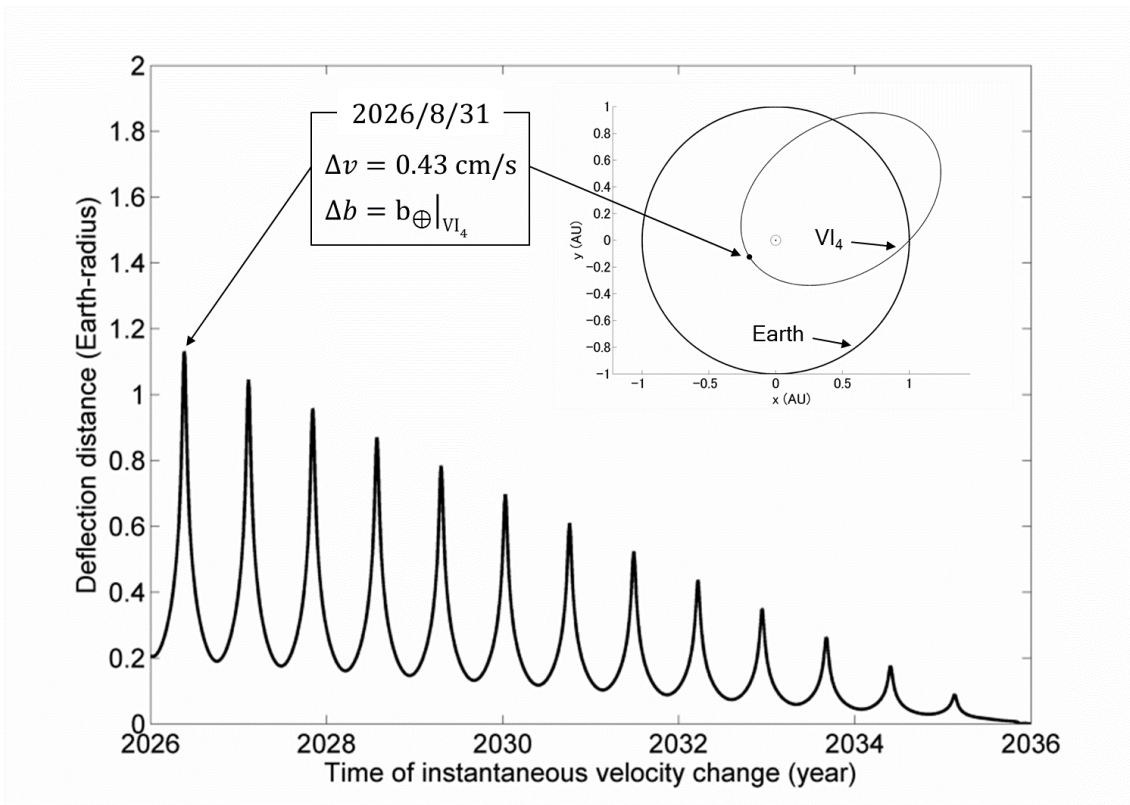
Figure 18 Variation of deflection distance of VI$_4$ on the 2036 b-plane, given $\Delta v = 0.43$ cm/s.
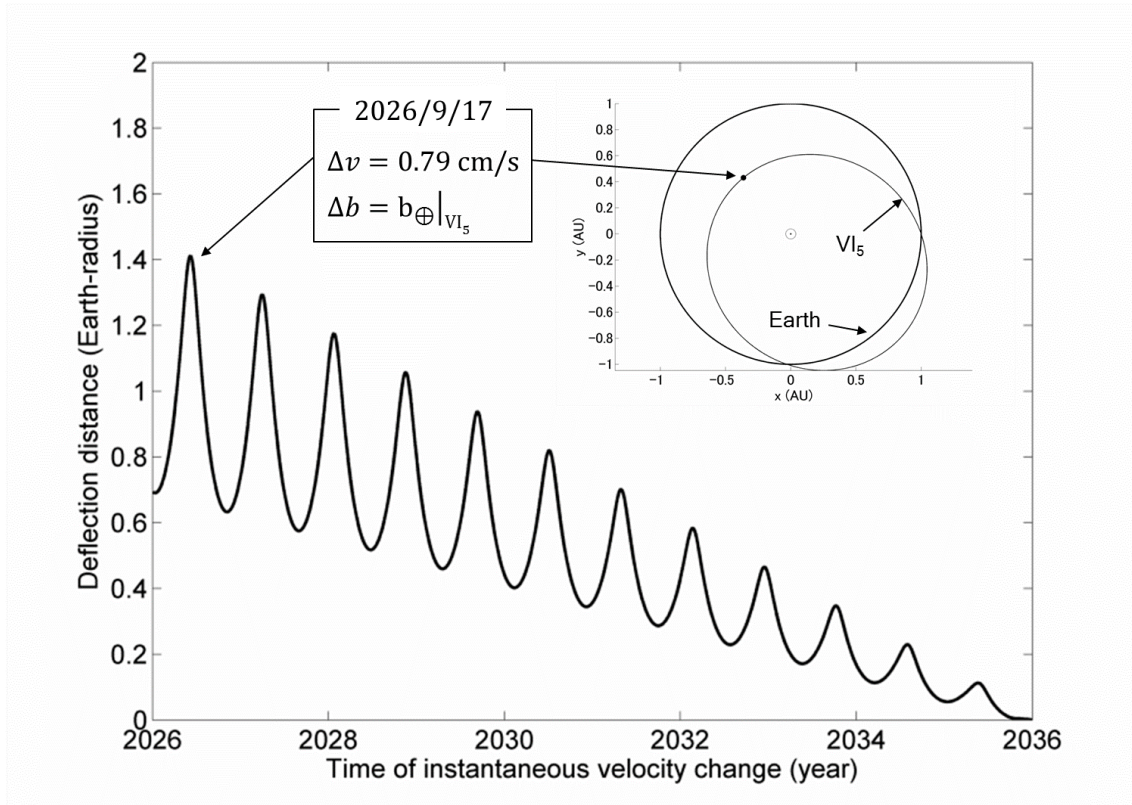
Figure 19 Variation of deflection distance of VI$_5$ on the 2036 b-plane, given $\Delta v = 0.79$ cm/s.
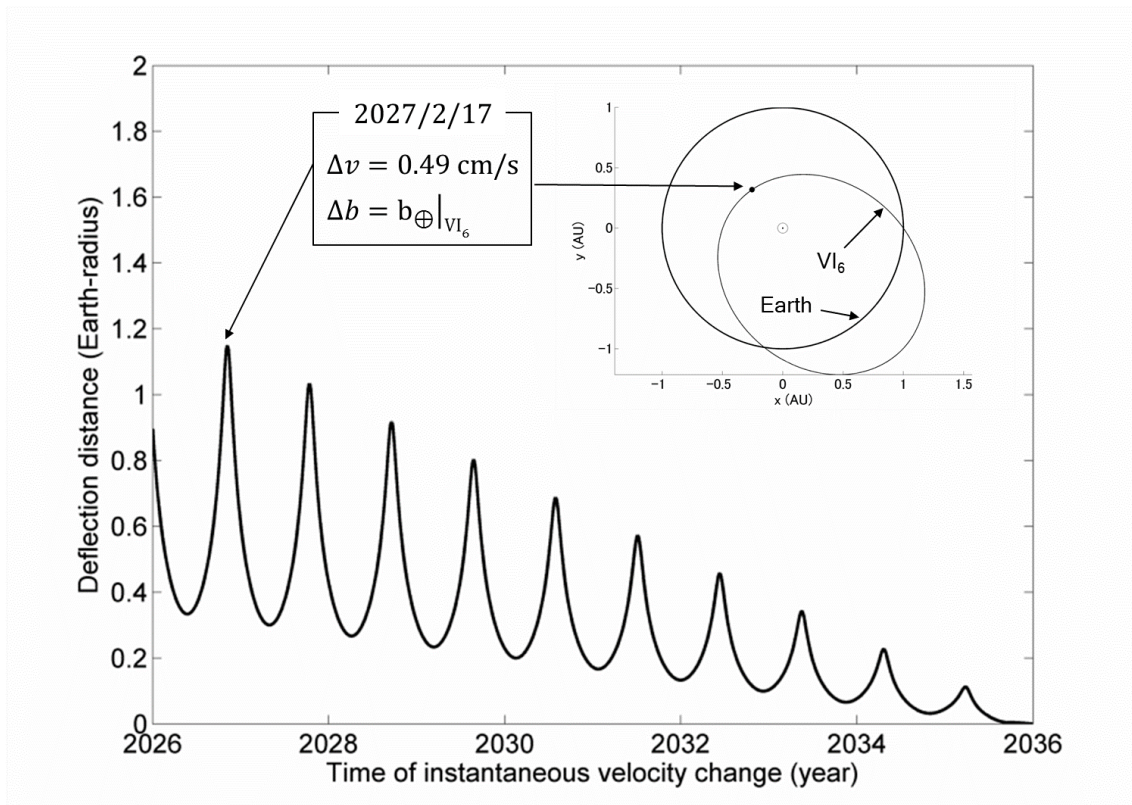
Figure 20 Variation of deflection distance of VI$_6$ on the 2036 b-plane, given $\Delta v = 0.49$ cm/s.

1.5. Research motivation and objectives

Beginning with NEAR Shoemaker in 2000-2001, a number of proximity exploration missions to small celestial bodies by space probes (e.g., Stardust in 2004, Hayabusa in 2005-2010, Dawn in 2011~ and Rosetta in 2004~) have been sent over the last decade [5]. Hayabusa 2 [33] now in its final development stage and OSIRIS-REx [34] in its design stage, and they are envisaged to return samples back from C-type asteroids (162173) 1999 JU$_3$ and (101955) Bennu in 2014 and 2016, respectively. As an example of space missions related to planetary defense, Deep Impact in 2005 demonstrated a hypervelocity impact by a man-made object on the comet, namely Tempel 1, which greatly contributed to our understanding of impacting and crater-forming phenomena, as well as the development of planetary defense technology. Thanks to these former missions, development of the planetary defense technology for potentially hazardous NEOs is of increasing interest to national space agencies. Tracking, orbital manipulation, and retrieval of asteroids have also become a very popular topic amongst scientists, engineers, and politicians particularly after the close Earth flyby of asteroid (367943) Duende and the Chelyabinsk meteor event occurred early in 2013. NASA is now planning to send a robotic mission to a 500-ton, <10-m-wide near-Earth asteroid (NEA), safely redirect it to a high lunar orbit or to the Earth-Moon Lagrange point: L2, and perform in-situ robotic and human exploration for both planetary defense and resource utilisation purposes [7]. However, asteroid deflection and retrieval initiatives are both still in their infancy and abound with scientific, engineering, political, and educational challenges to be addressed and overcome at the international level.

A variety of asteroid mitigation concepts (kinetic impactor, nuclear interceptor, low-thrust propulsion, solar collector, laser ablation, mass driver, gravity tractor, ion beam shepherd, etc.) have been proposed. Some of these concepts appear to be feasible with the current technology developed through deep space exploration missions, whereas others require certain levels of technological advancement before they can be considered as feasible deflection alternatives. Meanwhile, a deflection technique which makes use of nuclear devices (the most powerful and yet feasible technique so far) for example, involves political issues to be tackled with by corresponding nations. In 2009, Sanchez *et al.* [48] performed a multicriteria comparison analysis of hazard mitigation and the results have demonstrated that several deflection methodologies could be effective against modest-sized NEAs under 150 m in diameter whose accumulative impact probability is 0.3% in the next two decades. These results however may not always be valid if the characterisation of the target asteroid is insufficient since some deflection methodologies are strongly subject to the preliminary

characterisation. For example, a kinetic impactor or a nuclear interceptor physically interacts with an asteroid and a solar collector sublimates the asteroid's surface material and thus is highly dependent not only on the physical properties but also on the mineral composition of the asteroid. In order to properly deflect an asteroid, the target asteroid must be first well understood through the preliminary characterisation missions.

Hawkins and Bellerose [55] recently presented a preliminary study on future concept of operation developments at NEAs aiming to obtain more credible information on their characteristics (orbits, spin states, masses, sizes, densities, porosities, albedos, etc.) as a prerequisite to planetary defense campaign planning. There are seven different possible scenarios from remote sensing to surface interaction – telescope, radar-based, space-based, short flyby, year-long proximity, surface, robot/human-based in-situ sample return operations – depending on not only the available warning time but also navigation, instrument and spacecraft features, Sun-Earth relative position as well as telecommunication windows. These characterisation scenarios are compared with each other in terms of their inherent uncertainty in available information. The results revealed that each characterisation concept is unique for the different type of encounter. This means in turn that an asteroid deflection mission will be also unique for the different type of orbit. Furthermore, effects of the uncertainty-based information from different levels of characterisation approaches on asteroid deflection attempts are yet to be estimated so as the outcome of a mitigation campaign can be more predictable during the early stages of campaign planning.

It is therefore crucial to reasonably quantify the uncertainty-based information about the fundamental physical properties of the target body according to the available information in the first place. This allows us not only to deliberately plan the primary deflection campaign but also to prepare for complementary alternatives in case of primary mission failure. Recent work by Sugimoto *et al*. [56, 57] has shown that, particularly for impact hazard scenarios with 10 years of warning time, only limited information about the hazardous NEA would be available and that this will most likely come only from ground-based or space-based characterisation approaches. In such cases, the majority of deflection techniques will be subject to the epistemic uncertainties and the measurement errors in the fundamental NEA characteristics, which could lead to the confidence level on the outcome of deflection attempt to be substantially jeopardised. It is therefore desirable to investigate mitigation campaign planning that involves the design of a reliable and robust hazardous NEA mitigation system in order to guarantee high confidence in successful mitigation campaign even if the preliminary NEA characterisation is incomplete.

In summary, the main objectives of this doctoral thesis are to:

- Develop a level-headed uncertainty quantification approach for epistemic uncertainties in fundamental asteroid characteristics prerequisite to mitigation system design.

- Investigate effects of uncertain asteroid characterisation on asteroid deflection missions: kinetic impactor, nuclear interceptor, solar collector, and gravity tractor.

- Evaluate effects of the inhomogeneity of the asteroid on the kinetic impactor and dynamics of spacecraft orbiting/hovering about an irregularly-shaped asteroid.

- Demonstrate a NEA mitigation campaign planning approach that results in efficient, reliable, and robust mitigation, given uncertainty-based information about the asteroid.
    - ➢ High efficiency means large deflection in short campaign period with small mass.
    - ➢ Reliability is equal to the confidence level on the successful nominal deflection.
    - ➢ Robustness represents keyhole avoidance capability of a mitigation campaign.

1.6. Thesis structure

This doctoral thesis is divided into six main chapters, which cover different topics of the study on hazardous asteroid mitigation. The ultimate goal of the thesis is, however, NEO hazard mitigation campaign planning and its credibility analysis. Each chapter is basically a complete piece of work by itself while some detailed information and mathematical formulations that are referred to but omitted in the main chapters are available in Appendices.

Chapter 2 details preliminary characterisation efforts of NEAs, including the uncertainty quantification of the NEA characteristics. Physical properties of NEAs that are essential to mitigation campaign planning and their determination efforts are first introduced. Ground-based, space-based, and proximity characterisation approaches and their respective levels of associated uncertainty are defined. The uncertainty quantification technique: Evidence Theory is then introduced, which can quantify epistemic uncertainty without assuming any distribution functions on the fundamental asteroid characteristics. Finally, some constant design parameters that are also prerequisite to mitigation system design are defined in order to make the research reproducible for interested readers.

Chapter 3 presents the concepts and mathematical modelling of the four deflection techniques – kinetic impactor, nuclear interceptor, solar collector, and gravity tractor – which are divided into two sections: instantaneous deflection techniques and slow-push deflection techniques. For the instantaneous deflection techniques, modelling of the momentum multiplication is crucial such that one sub-session is allocated for it. In the last section, the

effects of the uncertain NEA characterisation on the outcome of each deflection technique are evaluated in terms of reliability as individual mitigation system for different preliminary characterisation approaches to the identified hazardous NEA.

Chapter 4 put an emphasis on understanding of the effects of the inhomogeneous internal structure of the target uncooperative body on kinetic impactor missions. Here, a novel asteroid modelling approach is presented, which takes inhomogeneous asteroid density distribution, COM offset, and MOI into account. This asteroid model is then applied to a kinetic impactor asteroid deflection simulation and the deflection efficiency (i.e., instantaneous velocity change of the asteroid) is computed through Monte Carlo approach. Also, the influences of inhomogeneous gravity of the asteroid on a spacecraft hovering in proximity to it are investigated by modelling an irregularly-shaped NEA whose shape model is analogue to that of asteroid Eros apart from its size. Finally, the effects of rotation and shape of the ellipsoidal asteroid on a solar collector mission are briefly evaluated.

Chapter 5 covers the main topic of this doctoral thesis: the comprehensive analysis of dual-deflection mitigation campaigns consisting of primary instantaneous and secondary slow-push deflection missions, where both mitigation efficiency and campaign credibility are taken into consideration. Here, three different combinations of primary and secondary deflection missions are studied. A multi-objective optimisation algorithm is applied to dual-deflection mitigation campaign planning such that a series of competing aspects are comprehensively evaluated.

Finally, Chapter 6 summarises the research findings that have been identified in each chapter and states the conclusions of the doctoral thesis. In addition, some recommendations for extension projects of this research are presented in this chapter. In addition to the main thesis chapters, Appendices complement important information, mathematical formulations, and additional results of numerical simulations which are omitted in the main chapters. This allows interested readers to refer to the further detailed information in order to reproduce the research findings and outcomes for comparison purposes, etc.

2

2. Preliminary characterisation

"Knowledge is prerequisite to survival. I believe our future depends on how well we know this Cosmos in which we float like a mote of dust in the morning sky."

— Carl Sagan, *Cosmos*, 1980

Characterising an asteroid is certainly not an easy job but often involves a significant amount of uncertainty as well as various assumptions in the asteroid properties. In reality, the orbits and physical properties of many PHOs and the known NEOs are not very accurately determined. For example, the current characterisation of the well-known PHO, asteroid (99942) Apophis (in terms of mass, size, internal porosity, shape, etc.) would not suffice to plan any reliable mitigation mission to it although the odds of an Earth impact at the 2036 close approach was ruled out through the series of ground-based observations attempted in 2013[1] [30]. Thankfully, it is confirmed that the asteroid will not impact the Earth in the foreseeable future; however, before the 2013 observations, the effects of the 2029 pre-encounter involving potential keyhole passage made it difficult to predict Apophis' trajectory at the 2036 Earth encounter as accurate as today's and left the impact odds of one in 250,000 [58] around that time.

During the early stages of mitigation campaign planning, the fundamental physical characteristics of the asteroid such as size, mass, density, porosity, albedo, and its orbit must be accurately determined in order to plan an effective mitigation mission as well as to

---

[1] Apophis passed within 0.0966 AU of Earth in 2013, allowing astronomers to refine the trajectory for future close approaches. The observations redefined the size of Apophis as 325 ± 15 m (previously defined as 270 ± 60 m) and the odds of an impact in 2036 as less than one in a million.

maximise the chance of mission success. Traditionally, this fundamental and yet inevitable issue of determining the asteroid physical properties has been often ignored when designing an asteroid deflection system and evaluating its deflection performance [48]. In reality, a deflection attempt will be inevitably subject to the uncertain asteroidal characteristics, and therefore, it is crucial to reasonably represent the epistemic uncertainties in the physical properties of the target asteroid, which will ultimately allow us to take the campaign credibility into account and to plan a secondary deflection mission accordingly.

In this chapter, the aforementioned NEA characteristics essential to mitigation campaign planning are detailed respectively in Section 2.1 and then, three different levels of preliminary NEA characterisation approaches considered in this thesis are defined in Section 2.2. Subsequently, the uncertainty quantification technique: Evidence Theory [59] is introduced and applied to the uncertainty-based information about the NEA characteristics in order to quantify the epistemic uncertainties in Section 2.3. Finally, a series of constant physical properties that are also prerequisite to mitigation system design, are presented in Section 2.4.

2.1. Physical properties essential to campaign planning

Fundamental physical properties of the hazardous asteroid – mineral composition, size, mass, density, porosity, shape, rotational state, thermodynamic properties, etc. – must be determined as precisely as possible in order to design a more effective and reliable asteroid mitigation system during the early stages of campaign planning.

In the following subsection, determination efforts and problems associated with NEA characterisation of the fundamental physical properties subject to epistemic uncertainties and measurement errors are briefly detailed.

2.1.1. Determination of asteroid taxonomic class and composition

Optical observations are combined with mid-infrared or (rarely) radar observations, to determine the geometric albedo p_v (i.e., the fraction of light that is reflected by the asteroid surface) of an asteroid. Its taxonomic class (e.g., S-, C-, M-type, etc.) can be measured through optical and near-infrared spectroscopy. More detailed information such as mineral components – olivine, troilite, plagioclase, feldspar, orthopyroxene, etc. – and their proportion can then be estimated from meteorite analogues corresponding to the asteroid surface material through near-infrared reflectance spectrum analysis (see Figure 21).

However, the meteorite analogues corresponding to the surface material do not always provide reliable information on the actual mineral composition. For example, the latest analysis of the in-situ fine-grain samples of asteroid (25143) Itokawa collected by the Hayabusa spacecraft (see Figure 22) indicated that there was a lower amount of Fe-Ni metal than typical LL ordinary chondrites: OCs have (0.5-7.2%) [60].
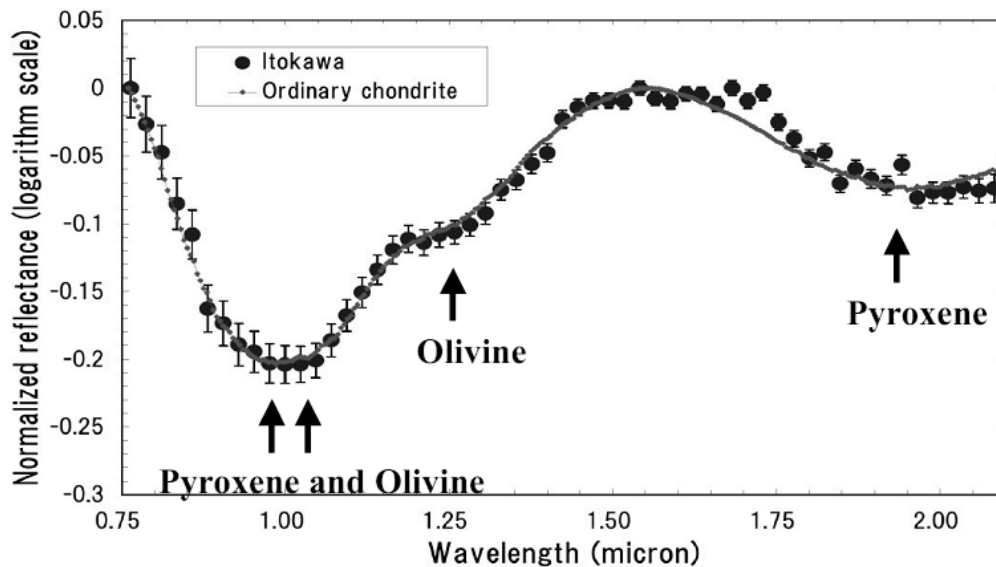
Figure 21 Near infrared reflectance spectrum. Dots show the observed data of Itokawa and the line is a spectrum of ordinary chondrites [46].
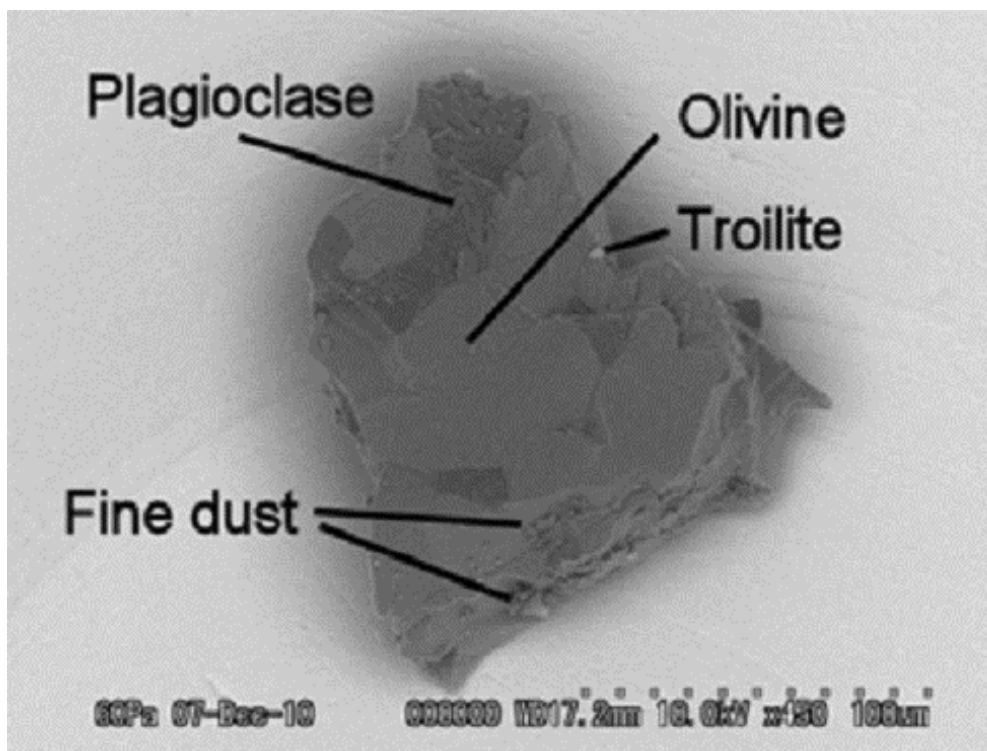
Figure 22 A relatively large Itokawa particle captured during first touchdown onto the surface of Muses-C regio [60].

This implies that mineral and chemical constituents of asteroids and comets can only be accurately determined through in-situ observations by a spacecraft. The photometric surface characterisation of asteroid Itokawa by the Hayabusa spacecraft revealed a modestly homogeneous compositional feature all around Itokawa's surface [61] while the near-infrared spectrometer onboard the Hayabusa found a variation of more than 10% in albedo and absorption band depth in the surface reflectance of Itokawa. This contradiction could be interpreted as effects of space weathering and the variation in surface roughness due to occasional brief impact events on asteroid Itokawa [62]. However, most importantly, these results may not hold true for the general subsurface composition of an asteroid. In reality, we should not rule out the possibility of an asteroid having inhomogeneous composition due to collisions between disparate bodies since subsequent brief impacts and regolith gardening can result in a subtle spectral variation in surface regolith and hence bias the compositional information [63]. Nevertheless, throughout the thesis, mineral composition will be considered to be homogeneous over the entire target asteroid unless otherwise stated. However, the surface albedo remains uncertain since the degree of space weathering and the variation in surface roughness cannot be well characterised by distant ground-based and/or space-based observations (i.e. mostly available characterisation options). The inhomogeneity of the asteroidal mineral composition will be discussed in Chapter 4 where a more rigorous, novel asteroid model is introduced in order to evaluate the effects of the compositional non-uniformity on the outcome of a specific type of deflection technique such as a kinetic impactor.

In general the majority of existing literature on planetary defense has regarded the mineral composition of the target asteroid as silicaceous, rock-forming silicates (i.e., typical S-type mineral composition); this study will however deal with, not only silicaceous, but also carbonaceous and iron metallic compositions (i.e., typical C-type and M-type mineral compositions) as a possible composition of the target asteroid. Although it is true that the majority of discovered NEAs are identified to be S-type asteroids, the distribution of NEA taxonomic classes based on optical observations is affected by selection bias of small, low albedo objects [64], and thus, further NEO discoveries through mid-infrared observations (e.g., NEOWISE [65]) should reveal the unbiased NEA class distribution. Throughout the thesis, S-type asteroids will be considered to be composed of silicaceous meteoric material: ordinary chondrites, while C-type asteroids will be considered to be composed of carbonaceous meteoric material – CM chondrites. Although a handful of M-types asteroids – 16 Psyche, 216 Kleopatra, 758 Mancunia, 785 Zwetana, 1986 DA, etc. – are identified as

being highly metallic [12, 63], M-type asteroids will be treated as pure iron-nickel bodies in this study, consisting of iron meteoric material.

2.1.2. Size determination

The equivalent diameter of a NEA is first estimated by referring to the correlation between its absolute magnitude (i.e., optical brightness) observed by telescope and a "taxonomic and albedo model with the absolute magnitude" dependent size/diameter distribution [10]. However, this size determination technique cannot provide much detail as what radar observations can offer. Since sub-kilometre sized NEAs (e.g., Itokawa) can have irregular shapes and rotate over periods of a few hours or less (see Figure 23), their optical brightness is usually not constant with time throughout optical observations [66]. While this could be exploited for rotation state analysis, size determination of these small objects are often very doubtful unless radar observations are available, resulting in uncertainty in diameter by a factor of two or more [26]. Throughout the thesis, NEAs are basically treated as a spherical body with an equivalent diameter for model simplification while Chapter 4 about the effects of the asteroid inhomogeneity on the outcomes of asteroid deflection missions will deal with problems associated with the geometry, rotation state and obliquity (i.e., axis tilt) of the target asteroid.
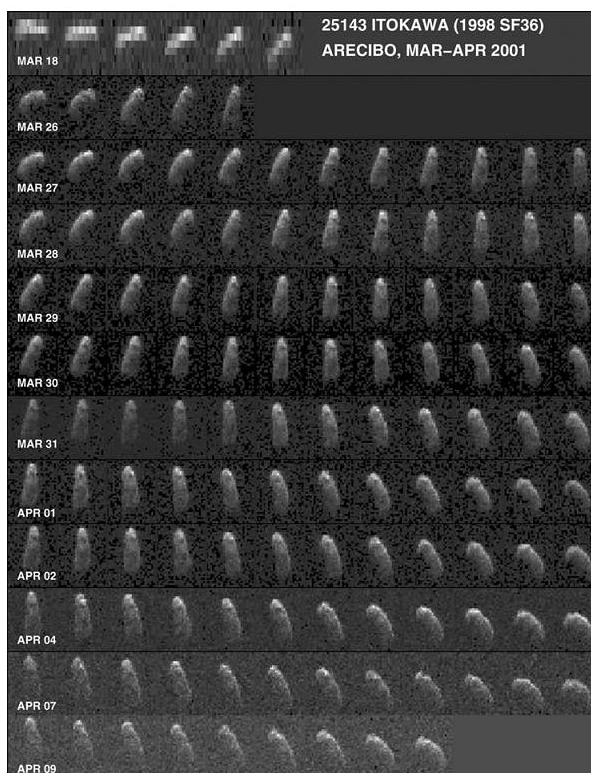
Figure 23 Arecibo delay-Doppler images of asteroid (25143) Itokawa. Range (time delay) increases from top to bottom and Doppler frequency increases from left to right, so rotation is counter-clockwise [67].

2.1.3. Mass determination

Amongst the fundamental asteroidal properties, mass determination will be one of the most crucial issues because the efficiency (i.e., achieved deflection distance or velocity change) of asteroid deflection techniques is basically inversely proportional to the mass of the target body according to Newton's equation of motion given by Equation (23) where M_a is the mass of the asteroid, $\mathbf{a} = \mathrm{d}\mathbf{v}/\mathrm{d}t$ is the acceleration of the asteroid achieved through the asteroid deflection mission and $\mathbf{F}$ is the force applied to the asteroid by a given deflection technique.

$$\mathbf{a} = \frac{\mathrm{d}\mathbf{v}}{\mathrm{d}t} = \mathbf{F}/M_a \qquad (23)$$

Figure 24 shows the number of NEOs that have been characterised in a variety of aspects − mass, size, shape, mineralogy, composition, spin properties, albedo, apparent visible magnitude, taxonomic class, etc. As can be seen, only a handful of NEOs have been characterised accurately such that their masses are determined within an accuracy of a few percent. For mass determination of small bodies, ground-based measurements which take advantage of perturbations in asteroid-asteroid or asteroid-planet interactions are contentious because of the extremely low levels of gravitational interactions between such small asteroids and other celestial bodies [68]. In-situ observations of asteroid-spacecraft gravitational interactions are therefore prerequisite to determine their masses more precisely. For example, asteroid (25143) Itokawa was the first sub-kilometre NEA visited by a spacecraft, whose mass was expected to be determined very precisely. Although Hayabusa was in very close proximity to asteroid Itokawa and hence the gravitational interaction was noticeable, the mass determination by Doppler lidar measurements still left 5% of relative uncertainty [69]. This means that, with current technological level, mass determination of hundred-metre sized small NEAs will likely be subject to a 5% or so uncertainty, even following detailed proximity observations.

In most cases, however, unless gravitational interactions with other close-by celestial objects are significant, masses of small NEAs are likely determined by their densities and porosities estimated from remote observations from Earth, and, thus involve a significant amount of measurement errors and epistemic uncertainties. For example, the estimated mass of (99942) Apophis with an effective diameter of 260 m is inevitably subject to a series of uncertainties − measurement errors, the possible mischaracterisation in its physical

properties, internal structure, inhomogeneity of the mineral composition, and ignorance of Apophis' geometry: the mass of asteroid (99942) Apophis is currently determined to be 0.7-6.1×10^{10} kg (i.e. average of 2.4×10^{10} kg with uncertainty of –71-154%) [70]. The main reason for such a large amount of uncertainty in the mass determination of Apophis is because the size of Apophis is very uncertain (325 ± 15 m [30]). This implies that, if a precursor characterisation mission to a hazardous NEA is not available, the mass determination will involve relative uncertainty in mass of a factor of two for radar observations; a factor of ~8 for most photometric observations; and a degree of magnitude given no physical characterisation attempt.
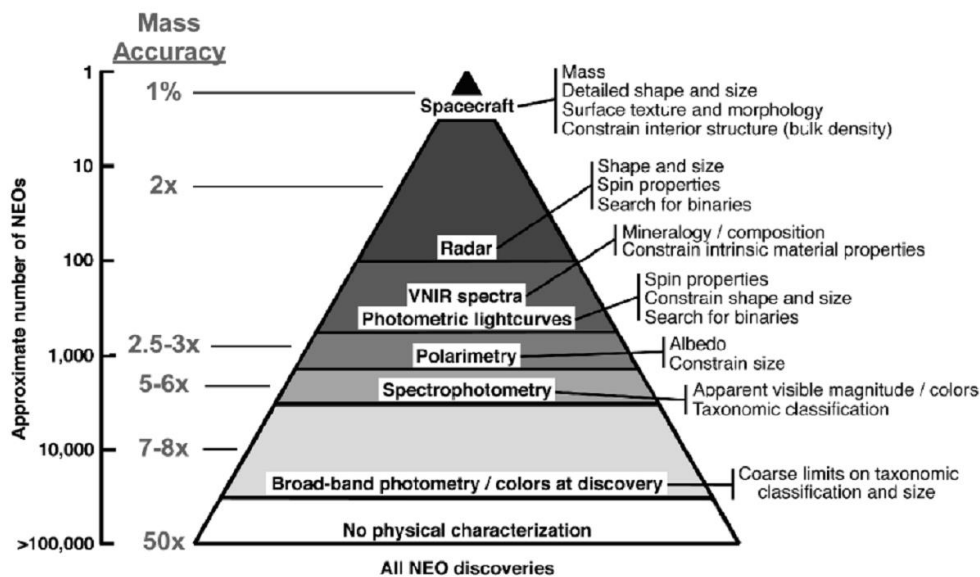
Figure 24 Approximate number of NEOs and corresponding appropriate characterisation approach [3]. Only a handful of discovered NEOs can be characterised well such that whose masses will be known within an accuracy of 1% or so.

2.1.4. Density and porosity of asteroid

As mentioned in Subsection 2.1.3, density and porosity determination is a prerequisite for mass determination of small NEAs particularly when only a ground-based or spaced-based characterisation approach is available. Density and porosity of an asteroid should be determined at both macroscopic and microscopic scales such that bulk density/porosity can be estimated. The word micro-density/micro-porosity means the density/porosity of rocks (i.e., gravels, cobbles, boulders, etc.) that are forming an asteroid whereas macro-porosity means empty spaces inside the asteroid due to internal gaps between the rocks.

Micro-density and micro-porosity of the rocks that comprise an asteroid are usually estimated from a spectral analysis of the asteroid surface material through telescope or radar

observations assuming the mineral composition is homogeneous not merely all over the asteroid surface but also its interior. This assumption contributes to the uncertainty in mass determination since the asteroid interior compositions and structures are, in reality, not likely to be as homogeneous as the observable asteroid surfaces that are mostly covered with regolith blankets or pebbles and boulders of similar or identical mineral composition. According to Britt [71], metal-rich, higher density particles tend to move towards the centre of the asteroid more easily than lower density silicate particles do, through the internal jostling process of rubble particles.

Macro-porosity of an asteroid accounts for the internal structural cracks and is often estimated simply by assuming the asteroid as either a monolithic, heavily-fractured but coherent body, or rubble-pile body. It can be indirectly determined by measuring the spin state of the asteroid. According to the original study by Pravec and Harris in 2000 [72] and the more recent one by Asphaug in 2004 [73], NEOs larger than about 140 m in diameter appear to be rubble piles whereas smaller ones appear to be more cohesive, however, not necessarily completely monolithic but, more likely, partially fractured. For this reason, 140-m sized objects could be either monolithic, heavily-fractured but coherent, or rubble piles. Since the internal structures of NEOs are mostly unknown, macro-porosity determination usually relies on literature data and thermal infrared observations from the ground [74].

Finally, bulk-density ρ_{bulk} and bulk-porosity P_{bulk} of an asteroid can be estimated from micro-density ρ_{mic}, micro-porosity P_{mic}, and macro-porosity P_{mac}, given by Equations (24) and (25), respectively. Asteroid mass M_a can then be determined from Equation (26) where d is the asteroid equivalent diameter. Bulk porosities of over fifty main-belt asteroids studied by Baer *et al.* range widely between 0-70% [74], depending on respective impact and cratering histories [22, 23]. Bulk-porosity determination is therefore, also one of the critical components for asteroid mass determination. For example, before the Hayabusa spacecraft visited asteroid (25143) Itokawa, Müller *et al.* assumed Itokawa's bulk porosity as 28% (i.e., the bulk porosity of S-type asteroid Ida) to estimate the mass of Itokawa [75]. This estimate resulted to be about 20% smaller than the in-situ measurement value of 47% obtained by Hayabusa [74].

$$P_{\text{bulk}} = P_{\text{mac}}(1 - P_{\text{mic}}) + P_{\text{mic}} \tag{24}$$

$$\rho_{\text{bulk}} = \rho_{\text{mic}}(1 - P_{\text{bulk}}) \tag{25}$$

$$M_a = \rho_{\text{bulk}} \times 4\pi(d/2)^3/3 \tag{26}$$

2.1.5. Rotational state of asteroid

The rotational state of an asteroid is often estimated from a periodic variation of light curves (i.e., light intensity of a celestial body as a function of time) available from ground-based telescopic observations. Figure 25 shows preliminary light curves of 2008 TT_{26} and 2008 UP_{100} whose diameters are ~50-100 m [66]. Rotation periods of asteroids under 200 m in diameter are mostly shorter than 2.2 hours, known as the "rubble pile spin barrier", although a few smaller asteroids, such as 2008 TT_{26} and 2008 UP_{100}, have spin rates longer than this threshold [66, 76]. The light curves data presents a considerable amount of uncertainty particularly when there are only a limited number of observations available [77].

Fast rotating asteroids could be a challenging problem for asteroid deflection techniques of any kind. Deflection approaches that make use of a direct momentum transfer by impact (e.g., kinetic impactor and nuclear interceptor) can possibly shatter fast rotating asteroids into pieces due to the effect of a large centrifugal acceleration. Meanwhile, for a solar collector, asteroids rotating too fast can potentially make the evaporation process of the surface material impossible due to short illumination time. Furthermore, a gravity tractor, even though it does not require any physical interaction with the asteroid, is not entirely immune to the rotational motion of the asteroid and can be subject to orbital instability due to the proximal gravity resonance. Such issues associated with asteroid dynamical/rotational states will be addressed in Chapter 4. Although asteroid internal structural features (e.g., macro porosities) may be estimated from the asteroid rotational states, correlation between the rotational states and the asteroid internal structures is out of the scope of this study.
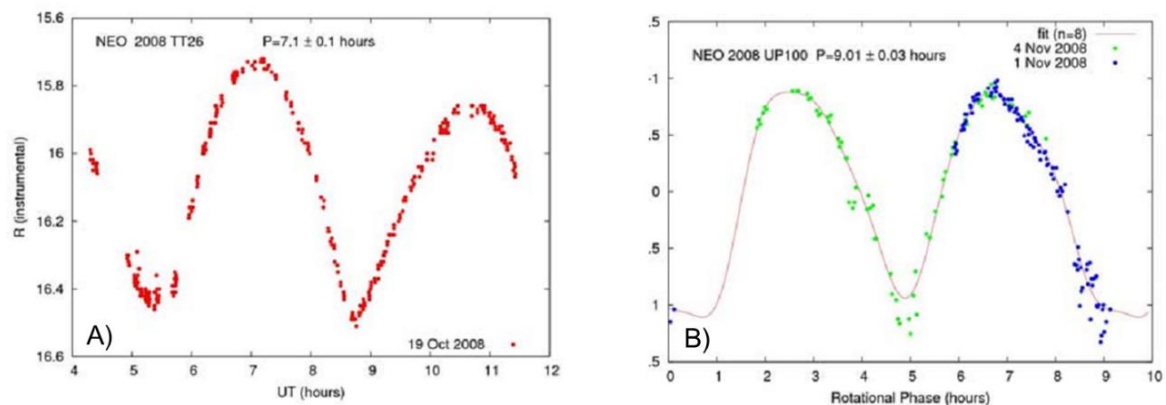
Figure 25 Preliminary light curves of A) NEO 2008 TT_{26} and B) 2008 UP_{100} indicating long rotation periods of over 7 hours for small NEOs having a diameter of only ~50-100 m [66].

2.1.6. Thermodynamic properties

The thermodynamic properties of an asteroid such as specific heat capacity, thermal conductivity, and sublimation enthalpy are also highly dependent on its composition as well as the micro-density and the micro-porosity, and therefore not immune to the epistemic uncertainties in the physical properties of the asteroid. These properties are often estimated from mid-infrared observations of the asteroidal surfaces by ground-based or space-based radar telescopes [75, 78] as well as from meteorite analogues [79]. Table 7 shows densities, specific heat capacities, and thermal conductivities of six meteorite samples: Abee, Campo del Cielo, Cold Bokkeveld, Cronstad, Lumpkin, and NWA 5515 [79]. These properties are measured and derived at 200 K. Cronstad (H5) and Lumpkin (L6) correspond to S-type's counterparts, Cold Bokkeveld (CM2) corresponds to a C-type's counterpart, and Campo del Cielo (IAB) corresponds to an M-type's counterpart.

Table 7 Thermodynamic characteristics of six meteorite samples: Abee, Campo del Cielo, Cold Bokkeveld, Cronstad, Lumpkin, and NWA 5515 [79].

Measured and derived properties at 200 K

Meteorite	Density (g/cm^3)	κ, 200 K (W/m/K)	c, 200 K (J/kg/K)
Abee (E4)	3.279	5.35	500
Campo del Cielo (IAB)	7.71	22.4	375
Cold Bokkeveld (CM2)	1.662	0.5	500
Cronstad (H5)	3.15	1.88	550
Lumpkin (L6)	2.927	1.47	570
NWA 5515 (CK4)	2.675	1.48	500

Throughout this thesis, however, these thermodynamic characteristics will be treated as constant values rather than uncertain properties and further details about the thermodynamic properties of three taxonomic classes (S-, C-, and M-type) are presented in Section 2.4. Such assumptions are simply due to the current insufficient understanding (i.e., incomplete or almost no statistical information) about the theoretical and practical asteroid thermodynamics and a rather complex correlation between the thermodynamic properties, asteroid mineralogy and physical properties [79]. Understanding and modelling the thermodynamic properties of the target hazardous asteroid is indispensable for some asteroid deflection techniques such as solar collector whose deflection efficiency is a function of the evaporation rate of the surface material. Interested readers should refer to the work by Zuiani *et al.* [80] which has put an emphasis on uncertainty quantification of the uncertain thermodynamic properties of the target asteroid.

2.2. Characterisation levels and corresponding uncertainties

There are three basic preliminary characterisation approaches to an identified hazardous body depending on the length of warning time: ground-based, space-based, and proximity characterisation approaches. Ground-based characterisation makes use of telescopic and following radar observations from the Earth whereas space-based characterisation leverages infrared satellites in space in addition to the ground-based observation options. These two characterisation scenarios would require only a few days during close Earth approaches of NEAs to complete [78], which means they could be possibly used simultaneously with the first discovery of a hazardous NEA by telescope. On the other hand, the proximity characterisation approach, which requires a precursor mission to the target NEA, would take at least 1¼ years to complete [54].

In theory, in-situ NEA surface characterisation is preferable to ground-based telescopic/radar or space-based infrared telescopic characterisation however, in practice, such proximity characterisation of the target body may not always be possible. The availability of precursor missions is subject to the orbit of the threatening NEA while, particularly for the moderate (10-20 years) warning time cases, quick preliminary characterisation is essential to ensure a wider mitigation campaign window (i.e. the period between the Earth departure of mitigation missions and the predicted Earth impact). The wider campaign window results in more mitigation campaign options and more efficient mitigation, even though the preliminary characterisation may remain incomplete without a precursor mission.

For example, given a ~10-year warning time, only ground-based telescopes and following radar observatories or, at most, space-based infrared telescopes would be utilised for preliminary characterisation whereas the proximity characterisation by precursor spacecraft would be available given a warning time of a few decades or so [26].

In any case of preliminary characterisation scenario, the physical properties of the threatening body will be, to a greater or lesser extent, subject to epistemic uncertainties, measurement errors, and modelling assumptions. The critical issue here is that preliminary mischaracterisation of the target body's fundamental physical characteristics could easily results in partial or complete failure of the mitigation campaign due to the incomplete information about the target body's characteristics.

2.2.1. Ground-based characterisation

The ground-based characterisation approach is a default and yet essential approach during the early stages of mitigation campaign planning. The accuracy of observational information by means of ground-based characterisation is based on the capability of ground-based telescopes and radar instruments on Earth, and thus the majority of physical parameters of the target object will remain highly uncertain [81]. Microscopic properties of a NEA can be estimated by analysing the surface colour and solar spectral reflectance while macroscopic characteristics such as mass and porosity are much more difficult to ascertain particularly when the object is only a few hundred metres or so in diameter. According to Müller *et al*. [82], ground-based telescopic observations with thermal infrared multimode instrument dedicated to 3-25 micron (mid-infrared) range have demonstrated higher performance in NEA characterisation than the radar observations (e.g., Arecibo and Goldstone) as the asteroid sub-surface/internal structures can be roughly estimated from thermal characterisation of the asteroid surface. However, in this work, such advanced ground-based mid-infrared characterisation is not considered to differentiate the ground-based characterisation approach from the space-based characterisation approach which makes use of infrared observations.

Figure 26 is the simplified diagram of the ground-based characterisation approach. The fundamental physical characteristics (mass, size, albedo, and momentum multiplication) for mitigation system design are derived from ground-based observational data, meteorite analogues of the NEA, and literature data regarding the macro porosity (i.e. large structural flaws inside the NEA). Crucially, the mass determination of an NEA is not directly available through ground-based observations but requires estimation of the bulk-density from meteorite analogues and literature data regarding the macroscopic characteristics. It is therefore inevitable that there would be major uncertainties in the preliminary characterisation, particularly in the mass (i.e., bulk density) determination in the case of ground-based characterisation. Geometric albedo determination is available through ground-based telescopic observations. The momentum multiplication, also known as momentum enhancement, can be estimated from the mass, bulk-density, and macro-porosity of the asteroid. The momentum multiplication represents the degree of momentum transfer enhanced by asteroidal ejecta escaped from the surface of the crater formation due to an impact on the asteroid. This parameter is one of the most important characteristics of the asteroid for deflection techniques such as kinetic impactor and nuclear interceptor. The

momentum multiplication coefficient is often designated as β, which will be explained further in detail in Chapter 3.
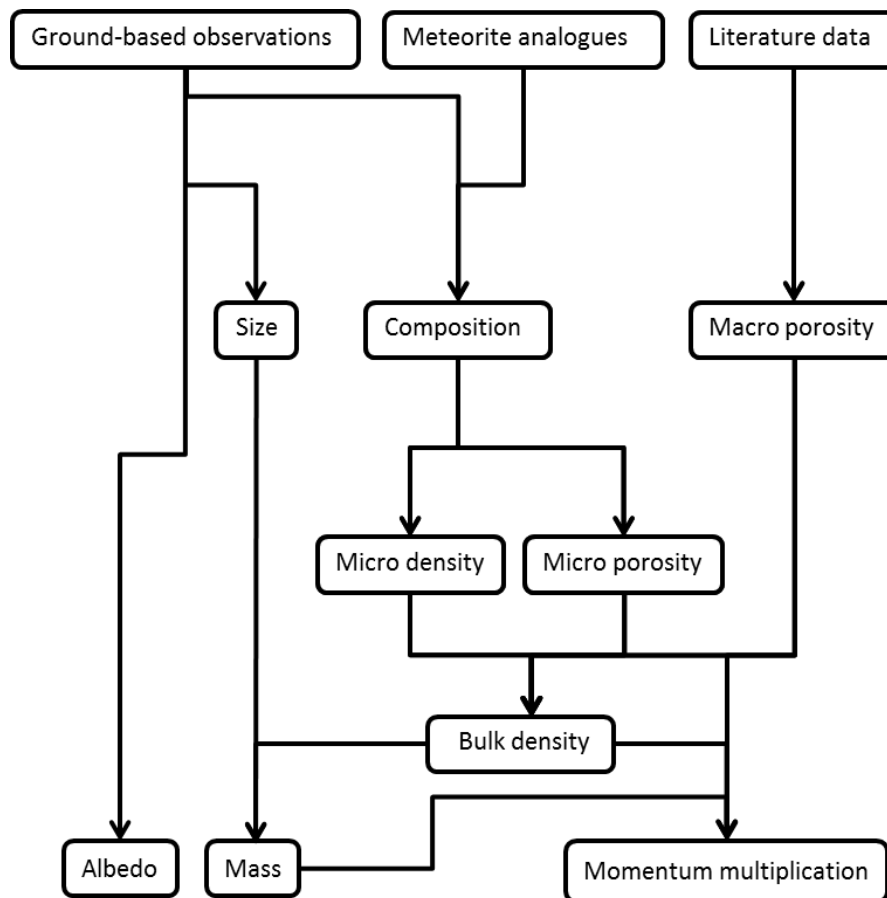
Figure 26 Ground-based characterisation diagram. Mass determination is available from the information about size and bulk-density of the asteroid. Macro-porosity determination is entirely dependent on literature data.

2.2.2. Space-based infrared characterisation

The space-based (infrared) characterisation approach is compatible with the ground-based characterisation approach but it is a more powerful form of preliminary characterisation approach. In this case, not only ground-based optical observation techniques but also space-based satellite observations are used, where the latter provides us with additional information about the surface thermal properties available from mid-infrared observations. For example, infrared astronomical satellites such as IRAS [83], AKARI [78], and NEOWISE [65] have successfully demonstrated the superior performance of mid-infrared observations to that of ground-based optical observations. Thermal inertia values fulfil a role to help us understand the surface roughness which can be, most importantly, used to identify the existence of a thick loose regolith carpet on the surface like Eros and to estimate the asteroidal interior structure: monolithic, heavily-fractured but coherent, or rubble piles made up of boulders

and pebbles like asteroid (25143) Itokawa, hence the macro-porosity. However, the microscopic characteristics will still be estimated by a spectrum analysis of the observed asteroid surface and from meteorite analogues.

The simplified diagram of the space-based infrared characterisation approach is shown in Figure 27. As can be seen, the only difference between the space-based and ground-based approaches is that the space-based one makes use of the mid-infrared data in order to estimate the macroscopic characteristics of the asteroid whereas the ground-based characterisation approach does not. The mid-infrared data provides us with better understanding of the surface roughness of the asteroid from which its internal structure (i.e., macro porosity) can be estimated. For this reason, the degrees of uncertainty of the ground-based and space-based (infrared) characterisation approaches are not significantly different as will be explained in Chapter 3, in comparison to the proximity-based characterisation approach.
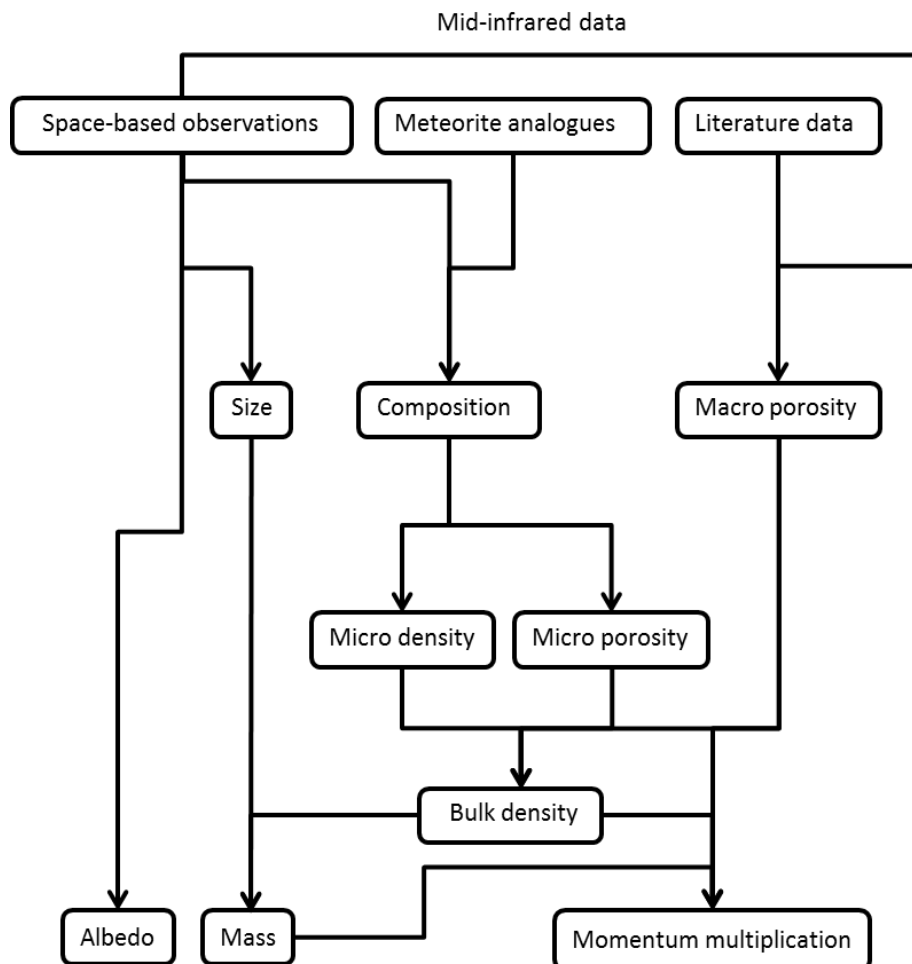
Figure 27 Space-based infrared characterisation diagram. Mass determination is available from the information about size and bulk-density of the asteroid. Macro-porosity determination is available from mid-infrared data and literature data.

2.2.3. Proximity-based characterisation

Proximity-based characterisation provides us with the best possible information about the target hazardous asteroid among the three characterisation approaches. In this case, the physical parameters of the asteroid will be determined directly through a precursor mission that is capable of sampling, examining the surface material, and capturing close-up images of the target body in proximity of the asteroid. Spacecraft-asteroid gravitational interaction allows us to directly determine the mass of the asteroid with a relative uncertainty of about 5% according to the mass determination of asteroid (25143) Itokawa by the Hayabusa spacecraft [69]. This in turn means that the bulk-density of the entire asteroid can be estimated from the sampled grain density, proximity mass determination, and size (i.e., asteroid volume V) determination through a close-up image analysis or simply from Equation (27). The bulk-density estimation from the proximity-based characterisation is more precise than the estimate inferred from remote observations of any kind associated with the uncertainty-based information about the spectrum of the asteroid surface and the corresponding meteorite analogues as well as the asteroid shape model.

$$\rho_{\text{bulk}} = 3M_a/V \qquad\qquad (27)$$

The simplified diagram of the proximity characterisation approach is shown in Figure 28 which illustrates how different the proximity-based characterisation approach is compared to the other two approaches. As can be seen, mass determination is available directly after the proximity observations by the spacecraft without any additional information such as the size and bulk-density of the asteroid. Also, the meteorite analogues corresponding to the asteroid surface spectrum are no longer necessary for the mineral composition determination. Furthermore, the albedo value of the asteroid is available both for geometric albedo and bond albedo. The bond albedo accounts for all of the light scattered from a body at all wavelengths and all phase angles, it is an important quantity to determine how much energy the asteroid body would absorb and emit. This, in turn, is crucial for defining the equilibrium temperature of the asteroid material, and most importantly, for a deflection technique such as a solar collector. The estimation of macro-porosity of the asteroid does not entail any literature data because the micro density, the micro porosity, and the bulk porosity are directly available from the proximity observational information acquired by spacecraft. Without going into details, these differences between three characterisation scenarios already imply that how important a precursor mission to the

identified hazardous asteroid will be during the early stages of mitigation campaign planning for credible asteroid characterisation and hazard mitigation.
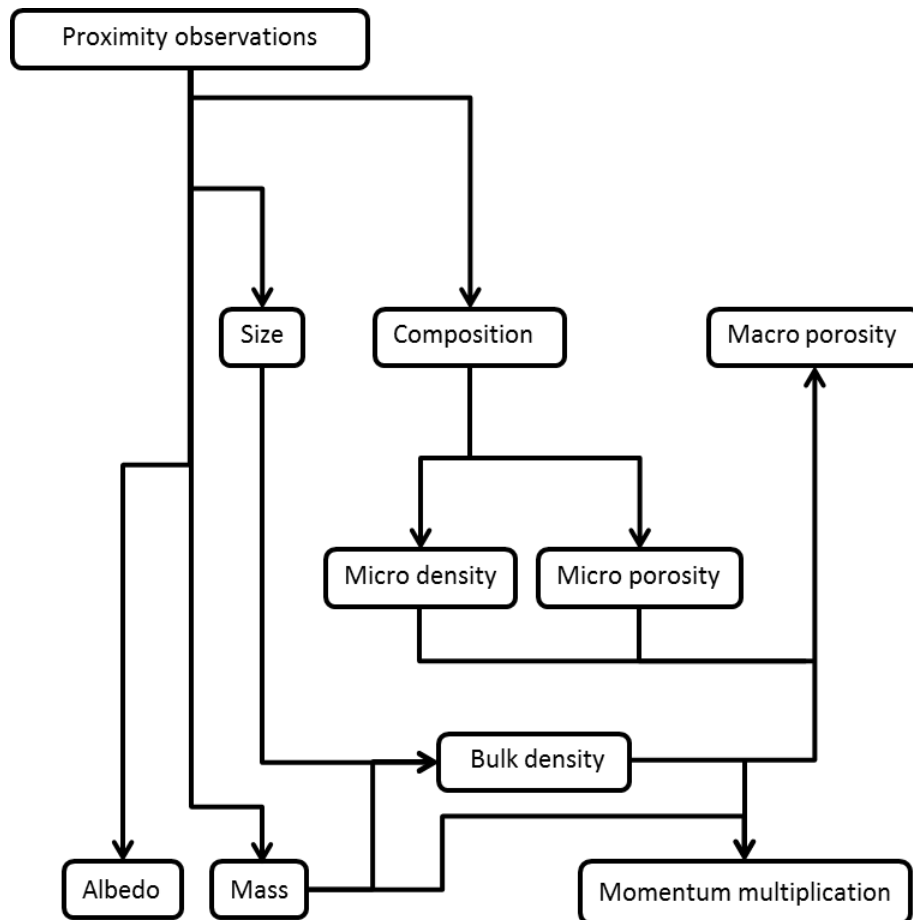
Figure 28 Proximity-based characterisation diagram. Mass determination is available directly from proximity observations. Macro-porosity determination is not dependent on ambiguous literature data unlike the other approaches.

2.3. Uncertainty quantification

In most literature about hazardous asteroid deflection techniques, uncertainties in the target object's physical characteristics are simply neglected or a system margin approach is used, either by assuming the worst-case combination of the NEA properties or by using a safety factor such that a necessary deflection is assured [48, 84, 85]. These approaches however may not always be the best option because both unexpected fragmentation of the target body and keyhole passage due to erroneous deflection are possible outcomes. Most importantly, the outcomes of any asteroid deflection attempt should be performed in a fairly controllable and predictable manner.

Meanwhile, representing the uncertain physical properties by conventional probabilistic means that require defining distribution functions is not suitable for NEA

characterisation particularly when there is a lack of knowledge or not enough information to assume a distribution function associated with the specific asteroid property. In this thesis, Dempster-Shafer theory (i.e., Evidence Theory) [59], which can quantify epistemic uncertainties without requiring any distribution assumption is used instead. As some examples of practical applications of Evidence Theory, Agarwal *et al*. [86] employed this theory to quantify uncertainties in multi-disciplinary systems analysis subject to epistemic uncertainty associated with the disciplinary design tools and input parameters while Croisard *et al*. [87] implemented this theory to preliminary space mission design based on uncertain information about the space system, demonstrating some advantages over traditional approaches.

In this section, the uncertainty quantification approach through Evidence Theory will be explained in detail and applied to the asteroid characterisation in order to quantify a variety of the inevitable uncertainties associated with the fundamental asteroid properties. Firstly, three different types of uncertainty are distinctly defined in Subsection 2.3.1. Mitigation system design is defined as multidisciplinary system design in Subsection 2.3.2. Following this, an overview of Evidence Theory, basic probability assignment (BPA) structures, and the algorithmic steps are presented in Subsections 2.3.3-0. Finally, BPA structures for the fundamental NEA characteristics are summarised in Subsection 2.3.6.

2.3.1. Types of uncertainty

When dealing with NEA characterisation or mitigation, we can encounter three different types of uncertainty – aleatory uncertainty, epistemic uncertainty, and error (i.e., numerical uncertainty) – which originate from different sources shown in Figure 29.
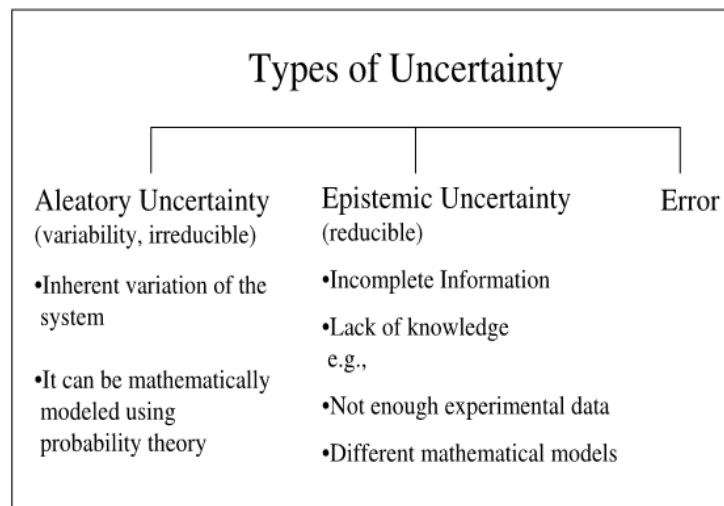
Figure 29 Different types of uncertainty [86].

In general, epistemic uncertainty arises when a system is not sufficiently characterised, certain characteristics of the system are neglected, or the physical model of the system is based on hypotheses rather than experiments. Current characterisation of the NEA population, including potentially hazardous asteroids, is insufficient, and hence epistemic uncertainty exist in our general knowledge of NEAs. This type of uncertainty can be reduced by collecting more credible information on the specific threatening NEAs or by improving general knowledge of the NEA population. Moreover, epistemic uncertainty also exists in design of low TRL components of a mitigation system such as the solar-pumped laser ablation system [80]. Unlike aleatory uncertainty, representation of epistemic uncertainty entails an appropriate quantification technique such as Evidence Theory [59].

Numerical uncertainty (i.e., errors) is a recognisable deficiency due to practical constraints on a system in general. The in-situ mass determination by the Hayabusa spacecraft, for example, had about 5% of measurement error which is thought to be due to the relatively small mass of Itokawa [69] – 190,000 times smaller than that of Eros, whose mass was determined within 0.05% [74]. The size determination of NEAs from the ground is also subject to the resolution of telescopic and radar images due to the practical constraints on the ground-based observational instruments. This type of uncertainty can be minimised by simply applying more accurate measurement techniques. Unlike the other types of uncertainty, the source of error is often known, such that error magnitudes can often be estimated in advance. Measurement errors in NEA size, rotation state, and shape determination could be as significant as the epistemic uncertainty in mass determination, however the hazardous asteroid is modelled as a spherical body throughout this thesis and these problems are not dealt with. Care must be therefore taken for the accuracy/applicability of the results in this work by the readers intending to compare their study on asteroid deflection techniques applied to more realistic misshapen NEAs for instance.

Aleatory uncertainty (also known as inherent uncertainty) represents a random variation in a system, inevitably present in every outcome of the system. For the case of kinetic impactor there will be, for instance, a certain amount of possibility of missing the target point on the NEA surface, or at worst the NEA itself due to the aleatory uncertainty in the precision of kinetic impact. Such practical limitations of the kinetic impactor are associated with the epistemic uncertainties and measurement errors in NEA size, rotation state, shape, centre of gravity, etc., and a very high-speed (10-20 km/s or >30 km/s for retrograde orbits) impact relative to a modest-sized object in space. For the case of solar collector, the acceleration of the target body (i.e., the surface material evaporation rate) will always fluctuate due to

among many factors, aleatory uncertainties in the solar flux, the asteroid surface condition and the mirror degradation with time. This type of uncertainty cannot be completely eliminated but they can be mathematically modelled using conventional probability theory, once a sufficient amount of statistical data is available. For example, the effects of aleatory uncertainties on asteroid deflection actions can be evaluated by means of Monte-Carlo simulation; however, applying a Monte-Carlo simulation to the mitigation campaign planning and optimisation approach considered in this study will substantially increase the cost of computation and thus the aleatory uncertainties of asteroid deflection is independently studied in Chapter 4.

Amongst the aforementioned types of uncertainty, epistemic uncertainty will be the most common causes of the uncertain physical properties of the target body, followed by measurement errors unless our general knowledge of NEAs is abundant and unbiased or a precursor mission is available.

2.3.2. Multidisciplinary system design

Hazardous NEA mitigation system design can be regarded as a multidisciplinary design (i.e., complex engineering system design) such that the orbital parameters, asteroid physical properties of the target body, and the deflection efficiency are all intrinsically coupled with each other. Figure 30 is a schematic diagram that describes such hazardous asteroid mitigation system design as a multidisciplinary system. The mitigation system design involves three basic vectors $\mathbf{p}$, $\mathbf{x}$, and $\mathbf{y}$ where

- $\mathbf{p}$ is a vector of design parameters representing fundamental properties of the hazardous NEA (e.g., orbital parameters, physical properties, etc.) and environmental parameters (e.g. gravity, solar constant, radiation pressure, etc.).

- $\mathbf{x}$ is a vector of mitigation system design variables (e.g. mass and impact velocity of kinetic impactor, mass and stand-off distance of nuclear interceptor, mirror size of solar collector, mass and stand-off distance of hovering gravity tractor, etc.).

- $\mathbf{y}$ is a vector of mitigation performance indicators of the campaign (e.g. mass of mitigation system, mission duration, deflection distance, confidence in deflection, etc.).
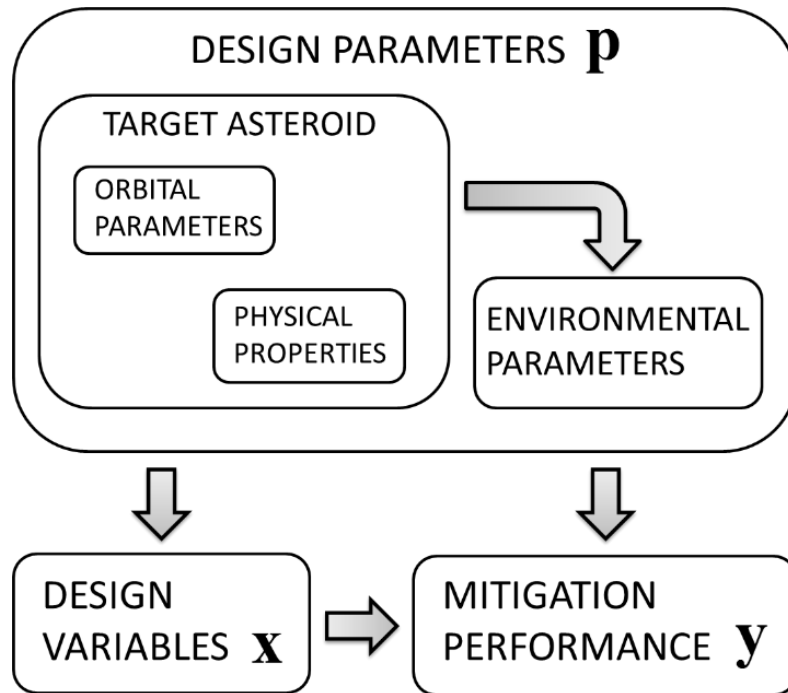
Figure 30 Hazardous NEA mitigation system design.

2.3.3. Evidence Theory

An uncertainty quantification technique – Evidence Theory also known as Dempster-Shafer theory [59] – is employed here, in order to quantify uncertainty-based information on NEA physical properties. Evidence Theory can deal with epistemic uncertainties and errors, when the amount of available information about a physical model/engineering system is limited.

For example, Evidence Theory has been recently applied to a preliminary space mission design: the optimal design of the mission BepiColombo by Croisard *et al*. in 2010 [87], and exhibited a number of advantages over conventional mission design approaches as follows:

A) Evidence Theory allows a more rigorous uncertain quantification than a conventional system margin approach, which is directly related to the source of uncertainty and the current uncertainty level.

B) A variety of design options corresponding to different performance and reliability levels are available.

C) Quantitative trade-off between performance and reliability is available for decision makers as well as engineers and designers.

D) The cost of iteration process between optimisation and reliability analysis is reduced or completely removed.

Evidence Theory makes use of two different uncertainty/probability measures called Belief (*Bel*) and Plausibility (*Pl*) as illustrated in Figure 31. Belief represents confidence in the truth of event $\mathcal{A}$ exclusive of the associated epistemic uncertainties whereas Plausibility represents confidence in the truth of event $\mathcal{A}$ inclusive of the associated epistemic uncertainties.
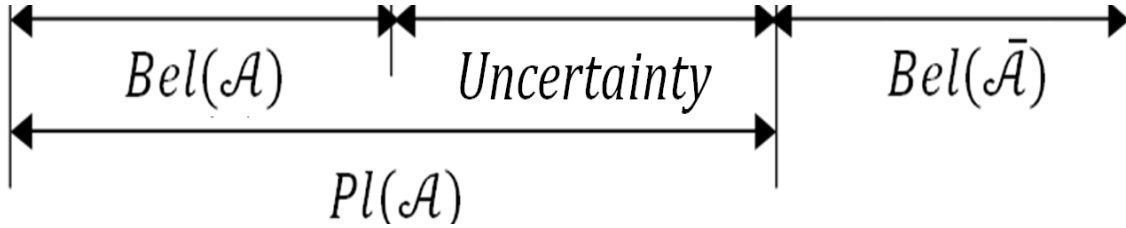
Figure 31 Belief and Plausibility [86].

Unlike evidential measures of conventional probabilistic means, the sum of the Belief measure that support the truth of event $\mathcal{A}$ and that in its negation is not necessarily unity as below.

$$Bel(\mathcal{A}) + Bel(\bar{\mathcal{A}}) \leq 1 \tag{28}$$

The basic probability measure used in Evidence Theory is known as the basic probability assignment (BPA). It is a function of m that maps the power set $(2^{\mathcal{U}})$ of the universal set $\mathcal{U}$ (also known as the frame of discernment) to [0, 1]. BPA $m(\mathcal{E})$ represents the degree of confidence in elementary proposition $\mathcal{E}$ (e.g. specific observation data associated with uncertainty and measurement errors). $m(\mathcal{E})$ satisfies the following three axioms:

$$m(\mathcal{E}) \geq 0 \text{ for any } \mathcal{E} \in 2^{\mathcal{U}} \tag{29}$$

$$m(\emptyset) = 0 \tag{30}$$

$$\sum m(\mathcal{E}) = 1 \text{ for all } \mathcal{E} \in 2^{\mathcal{U}} \tag{31}$$

where $\emptyset$ denotes an empty set. All the possible events which are subsets of the universal set $\mathcal{U}(\mathcal{E} \subset \mathcal{U})$ and have $m(\mathcal{E}) > 0$ are known as the focal elements. The set of all focal

elements induced by m is called a body of evidence, an example of which used in this thesis can be seen in Table 9.

The Belief is computed by summing the BPAs of the propositions that totally support an event while the Plausibility is determined by summing BPAs of all propositions which totally or partly support the event given as Equations (32) and (33), respectively. These scales pertain to each other while the sum of all the BPAs for proposition must add up to unity given as Equation (34).

$$Bel(\mathcal{A}) = \sum_{\mathcal{B}|\mathcal{B} \subseteq \mathcal{A}} m(\mathcal{B}) \tag{32}$$

$$Pl(\mathcal{A}) = \sum_{\mathcal{B}|\mathcal{B} \cap \mathcal{A} \neq \emptyset} m(\mathcal{B}) \tag{33}$$

$$Pl(\mathcal{A}) + Bel(\bar{\mathcal{A}}) = 1 \tag{34}$$

Evidence-based information from different sources (e.g., literature, observational data, experimental data, literature data, etc.) can be aggregated using existing rules of combination. In this study, the Dempster rule of combination [86] given by Equation (35) is applied to combine evidence from different sources. It is appropriate to apply, when there is some degree of consistency or sufficient agreement among the available evidence. However, it is not, for the cases where there is considerable inconsistency in the evidence. It is assumed that, as long as the asteroid class is known, there is certain agreement among information about the asteroid physical properties from different sources.

$$m(\mathcal{A}) = \frac{\sum_{\mathcal{B} \cap \mathcal{C} = \mathcal{A}} m_1(\mathcal{B}) m_2(\mathcal{C})}{1 - \sum_{\mathcal{B} \cap \mathcal{C} \neq \emptyset} m_1(\mathcal{B}) m_2(\mathcal{C})} \quad , \mathcal{A} \neq \emptyset \tag{35}$$

2.3.4. Basic probability assignment (BPA) structure

Epistemic uncertainty and parametric uncertainty in a given parameter are described as a set of intervals with associated BPAs. Figure 32 is a schematic representation of an example BPA structure for the uncertain parameter p_1. As can be seen in Table 8, the intervals of p_1 are non-overlapped with each other, however in general, they can be partially overlapped or even nested. They are usually obtained from observations and experiments as well as from literature data and hypotheses.
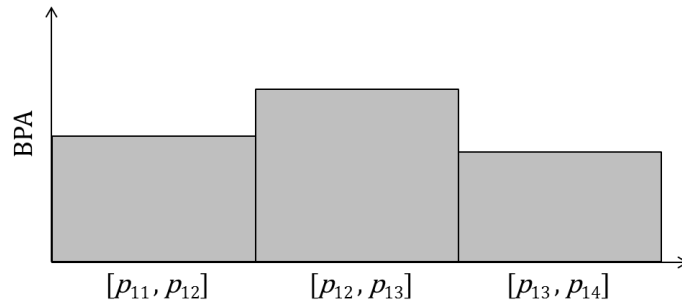
Figure 32 BPA structure for the uncertain parameter p_1.

Table 8 Intervals with associated BPAs of the uncertain parameter p_1.

Uncertain parameter	Interval	BPA
p_1	$[p_{11},\ p_{12}]$	m_{11}
	$[p_{12},\ p_{13}]$	m_{12}
	$[p_{13},\ p_{14}]$	m_{13}

2.3.5. Algorithmic steps

In this study, the following algorithmic steps are performed to derive Belief and Plausibility:

A) Collect all the necessary information on the asteroid characteristics from different sources and categorise it according to different characterisation approaches – ground-based, space-based, and proximity-based characterisation.

B) Determine the nominal physical properties of the NEA from the information collected in step A) and design a mitigation system based on this baseline for the nominal deflection distance b_{nom} within $b_\oplus < b_{\text{nom}} < b_{\text{safe}}$. The nominal deflection b_{nom} is a b-plane deflection that will be achieved through the given deflection mission to the NEA actually bearing the nominal physical properties.

C) Build the BPA structures by defining each uncertainty parameter as a set of intervals with the prescribed BPAs and, if necessary, combine the BPA structures of the same parameter from different sources by Dempster rule of combination/using Equation (35).

D) Compute the degree of confidence $m_c(C_i)$ associated with each distinct combination C_i of the uncertain parameters, where $i = 1, 2, 3, \dots, n$. $m_c(C_i)$ is simply the product of the BPAs associated with the uncertain parameters. The number of combinations n is proportional to the number of the parameters and that of intervals in each parameter.

E) Propagate $m_c(C_i)$ through the numerical simulation and compute lower and upper bounds of deflection outcome associated with each combination/combined proposition C_i, given the mitigation system defined in step B). Run over step D) and step E) for all the possible combinations.

F) Computed belief $Bel(b)$ and plausibility $Pl(b)$ of an arbitrary deflection b by Equations (32) and (33).

In step B), the mitigation system is designed based on the nominal physical properties instead of considering a system margin approach or the worst-possible combination of NEA characteristics (e.g. largest micro-density, smallest bulk-porosity, highest albedo, etc. of each taxonomic class). The reason for this is because changing the design parameters does not contributed to the inherent uncertainty in deflection outcome subject to the epistemic uncertainties in the NEA characteristics. Of course, it is obvious that, if the mitigation system is designed in consideration of the system margin, the system can provided a nominal deflection with the asteroid, given the worst-possible combination of NEA characteristics. The resultant deflection is however still ambiguous due to the epistemic uncertainties originating from the incomplete preliminary NEA characterisation.

2.3.6. BPA structures for asteroidal physical properties

The uncertain NEA physical properties, more specifically, micro density ρ_{mic}, micro porosity P_{mic}, bulk porosity P_{bulk}, and albedo p_v will be quantified respectively in the forms of BPA structures (i.e., a set of interval values with prescribed BPAs) in this section. The BPA structures for the S-type, C-type, and M-type asteroid models are given in Table 9. Each BPA structure consists of four physical properties for the ground-based, space-based, and proximity-based characterisation approaches. Ultimately, BPAs for all the possible combinations of the physical properties are derived through Evidence Theory. In the following sub-subsections, how the BPA structures for each taxonomic classification are built along with the corresponding supporting information used in this study will be briefly presented. Also, the constant design parameters are also provided in this section.

2.3.6.1. S-type asteroid

Microscopic physical parameters of S-type asteroids are derived by reference to its meteorite analogues – ordinary chondrites (OCs). The meteorite analogues of S-type asteroids were believed to be stony meteorites even before the Hayabusa spacecraft visited the S-type asteroid Itokawa. The Hayabusa mission finally provided direct confirmation that the characteristics of Itokawa's surface grains are consistent with characteristics of L, LL, and partly H chondrites [46]. Assuming the target asteroid is homogeneously composed of OCs, we can indirectly obtain the microscopic characteristics of the S-type asteroid model. Although, the Hayabusa mission revealed that asteroid (25143) Itokawa is most likely made of L and LL chondrites [6], we should not rule out the possible presence of subsurface metal-rich particles such as H chondrites buried inside the asteroid due to successive impact events. Since the majority of meteorite falls are stony meteorites, about 80% of which are OCs, the

amount of information on OCs is consequently most abundant among three types of meteorites corresponding to meteorite analogues of S, C, and M-types, respectively. BPA structures for micro-density ρ_{mic} and micro-porosity P_{mic} of the S-type asteroid model are given in Table 9. Those for ρ_{mic} are assembled by reference to 437 samples of H, L, and LL chondrites [88]. 691 OCs [89] are referred and aggregated with additional data on 291 OCs from different [23] literature sources by Dempster's rule of combination [86] to assemble the BPA structures for P_{mic}. It should be noted that the literature data of OCs are affected by considerable terrestrial weathering since most meteorites found on Earth spent long periods of time on the ground.

The abundance of S-type asteroids amongst the well-characterised asteroids [74] and a series of exploration missions to S-type asteroids also results in a better understanding of the macroscopic structures of S-type. BPAs for bulk-porosity, P_{bulk} of the S-type asteroid model are derived from the bulk porosities of only 7 existing S-type asteroids smaller than 100 km in diameter ranging 20-60% [74]. BPAs for albedo, p_v are derived from the observed geometric albedos of the 30 different S-type asteroids [83].

2.3.6.2. C-type asteroid

Microscopic physical parameters of C-type asteroids are derived by reference to its meteorite analogues – carbonaceous chondrites (CCs) which represent less than 5% of stony meteorite falls and, thus, the literature data of CCs is limited comparing to that of OCs. BPA structures for ρ_{mic} and P_{mic} of the C-type asteroid model are given in Table 9. The BPA structure for ρ_{mic} is compiled with reference to 11 CM chondrites [90]. Micro porosity P_{mic} is simply assumed to be 15.5-30.5% [88], which is consistent with the work of Flynn *et al.* [91]. This simple assumption is mainly due to insufficient or almost no available information on non-weathered micro porosities of CCs.

C-type asteroids are the second most abundant amongst discovered NEAs however, unlike S-type asteroids, in-situ exploration missions to C-type asteroids (e.g., Hayabusa 2 and OSIRIS-REx) are yet to be carried out. BPAs for P_{bulk} of the C-type asteroid model are derived from the bulk porosities of 8 existing C-type asteroids of various sizes ranging 30-70% [74]. BPAs for p_v are derived from observed geometric albedos of 18 different C-type asteroids[83].

2.3.6.3. M-type asteroid

Microscopic physical parameters of M-type asteroids such as (16) Psyche, (216) Kleopatra, (758) Mancunia, (785) Zwetana, and (6178) 1986 DA are derived by reference to its meteorite analogues – iron meteorites which represent less than 6% [13] of meteorite falls and, thus, the amount of information on iron meteorites is most limited. The compositions of some M-type asteroids are not always consistent with iron-nickel meteorite analogues while one of the smallest M-type asteroids, (6178) 1986 DA is a good example of a pure iron-nickel asteroid which is thought to be a remnant of the core of a fractured primitive body from the early solar system. Iron meteorites are often highly metallic but they do weather with time while less affected by terrestrial weathering than fragile chondrite meteorites. BPA structures for ρ_{mic} and P_{mic} of the M-type asteroid model are given in Table 9. Those for ρ_{mic} are assembled by reference to 21 iron-nickel meteorites [92]. Micro-porosity P_{mic} is simply assumed to be 0-1.2% [79]. This range is consistent with the iron-nickel meteorites of the Vatican collection with porosities of near zero [93].

The M-type classification is least abundant amongst the three asteroid types and, therefore, their physical properties are mostly unknown and yet to be explored by space missions. Unlike S-type and C-type asteroids, remote characterisation of M-type asteroids is not an easy task because spectrum analysis provides us less information than the other two types do. BPAs for P_{bulk} of the M-type asteroid model are derived from 7 existing M-type asteroids of various sizes ranging 0-40% [74]. BPAs for p_v are derived from observed geometric albedo of the 10 different M-type asteroids [83].

A total of 384 combinations of the physical properties with corresponding BPAs are derived for the S-type asteroid model and 64 combinations for the C-type and M-type. Table 10 shows the baseline physical properties (i.e., mean design parameters) for each taxonomic class, which will be referred to design a mitigation system throughout the thesis.

Table 9 BPA structures for the NEA physical properties of S-type, C-type, and M-type asteroids. A) Ground-based characterisation. B) Space-based characterisation. C) Proximity characterisation.

A)	S-type		C-type		M-type	
	Interval	BPA	Interval	BPA	Interval	BPA
ρ_{mic} (g/cm^3)	[3.23, 3.30]	0.31	[2.57, 2.60]	0.18	[7.59, 7.60]	0.05
	[3.30, 3.50]	0.29	[2.60, 2.70]	0.36	[7.60, 7.80]	0.19
	[3.50, 3.70]	0.33	[2.70, 2.80]	0.18	[7.80, 8.00]	0.62
	[3.70, 3.84]	0.07	[2.80, 2.86]	0.27	[8.00, 8.07]	0.14
P_{mic} (%)	[3.7, 5.0]	0.01	[15.5, 30.5]	1.00	[0.0, 1.2]	1.00
	[5.0, 7.5]	0.10				
	[7.5, 10.0]	0.30				
	[10.0, 12.5]	0.32				
	[12.5, 15.0]	0.22				
	[15.0, 16.3]	0.05				
P_{bulk} (%)	[16.4, 30.0]	0.43	[27.5, 40.0]	0.25	[0.0, 10.0]	0.43
	[30.0, 40.0]	0.14	[40.0, 50.0]	0.37	[10.0, 20.0]	0.14
	[40.0, 50.0]	0.29	[50.0, 60.0]	0.25	[20.0, 30.0]	0.14
	[50.0, 56.0]	0.14	[60.0, 67.8]	0.13	[30.0, 37.9]	0.29
p_v	[0.10, 0.15]	0.27	[0.04, 0.05]	0.33	[0.08, 0.11]	0.30
	[0.15, 0.20]	0.37	[0.05, 0.06]	0.44	[0.11, 0.13]	0.40
	[0.20, 0.25]	0.23	[0.06, 0.07]	0.17	[0.13, 0.16]	0.10
	[0.25, 0.28]	0.13	[0.07, 0.073]	0.06	[0.16, 0.17]	0.20

B)	S-type		C-type		M-type	
	Interval	BPA	Interval	BPA	Interval	BPA
ρ_{mic} (g/cm^3)	[3.23, 3.30]	0.31	[2.57, 2.60]	0.18	[7.59, 7.60]	0.05
	[3.30, 3.50]	0.29	[2.60, 2.70]	0.36	[7.60, 7.80]	0.19
	[3.50, 3.70]	0.33	[2.70, 2.80]	0.18	[7.80, 8.00]	0.62
	[3.70, 3.84]	0.07	[2.80, 2.86]	0.27	[8.00, 8.07]	0.14
P_{mic} (%)	[3.7, 5.0]	0.01	[15.5, 30.5]	1.00	[0.0, 1.2]	1.00
	[5.0, 7.5]	0.10				
	[7.5, 10.0]	0.30				
	[10.0, 12.5]	0.32				
	[12.5, 15.0]	0.22				
	[15.0, 16.3]	0.05				
P_{bulk} (%)	[21.4, 30.0]	0.43	[32.5, 40.0]	0.25	[2.86, 10.0]	0.43
	[30.0, 40.0]	0.14	[40.0, 50.0]	0.37	[10.0, 20.0]	0.14
	[40.0, 50.0]	0.29	[50.0, 60.0]	0.25	[20.0, 30.0]	0.14
	[50.0, 51.4]	0.14	[60.0, 62.5]	0.13	[30.0, 32.9]	0.29
p_v	[0.14, 0.15]	0.31	[0.041, 0.05]	0.33	[0.09, 0.11]	0.30
	[0.15, 0.20]	0.42	[0.05, 0.06]	0.44	[0.11, 0.13]	0.40
	[0.20, 0.25]	0.27	[0.06, 0.07]	0.17	[0.13, 0.15]	0.10
			[0.07, 0.071]	0.06	[0.15, 0.16]	0.20

C)	S-type		C-type		M-type	
	Interval	BPA	Interval	BPA	Interval	BPA
ρ_{mic} (g/cm^3)	[3.26, 3.30]	0.31	[2.59, 2.60]	0.18	[7.64, 7.80]	0.20
	[3.30, 3.50]	0.29	[2.60, 2.70]	0.36	[7.80, 8.00]	0.65
	[3.50, 3.70]	0.33	[2.70, 2.80]	0.18	[8.00, 8.04]	0.15
	[3.70, 3.76]	0.07	[2.80, 2.83]	0.27		
P_{mic} (%)	[8.2, 10.0]	0.35	[19.8, 26.3]	1.00	[0.0, 1.2]	1.00
	[10.0, 12.5]	0.39				
	[12.5, 13.2]	0.26				
P_{bulk} (%)	[34.4, 34.4]	1.00	[45.7, 45.7]	1.00	[13.1, 13.1]	1.00
p_v	[0.17, 0.20]	0.61	[0.049, 0.05]	0.43	[0.11, 0.13]	0.80
	[0.20, 0.21]	0.39	[0.05, 0.06]	0.57	[0.13, 0.131]	0.20

Table 10 Nominal physical properties for ground-based characterisation scenario. A) Ground-based characterisation. B) Space-based characterisation. C) Proximity characterisation.

A)	ρ_{mic} [g/cm³]	P_{mic} [%]	P_{bulk} [%]	p_v	M_a [10^9 kg]
S-type	3.45	10.66	36.17	0.19	3.17
C-type	2.71	23.00	47.36	0.05	2.05
M-type	7.87	0.60	17.55	0.12	9.32

B)	ρ_{mic} [g/cm³]	P_{mic} [%]	P_{bulk} [%]	p_v	M_a [10^9 kg]
S-type	3.45	10.66	36.12	0.18	3.17
C-type	2.71	23.00	47.34	0.05	2.05
M-type	7.87	0.60	17.45	0.12	9.33

C)	ρ_{mic} [g/cm³]	P_{mic} [%]	P_{bulk} [%]	p_v	M_a [10^9 kg]
S-type	3.45	10.89	34.35	0.19	3.26
C-type	2.71	23.00	45.71	0.05	2.11
M-type	7.87	0.60	13.14	0.12	9.84

Finally, the uncertainties in the fundamental physical parameters corresponding to the three characterisation approaches are summarised in Table 11. These uncertainties originate from the uncertain NEA physical properties shown in Table 9. As can be seen, a more rigorous but possibly more time-consuming characterisation approach results in smaller ranges of uncertainty in these fundamental physical properties for all the taxonomic classes.

Table 11 Uncertainties in the physical parameters – micro-density, micro-porosity, bulk-density, mass, and albedo – corresponding to the ground-based, space-based, and proximity characterisation approaches. They are represented in percentage relative to the nominal physical properties of each taxonomic class (see Table 10).

S-type	Ground-based	Space-based	Proximity
ρ_{mic}	–5.9-11.8%	–5.9-11.8%	–4.8-9.6%
P_{mic}	–7.0-5.6%	–7.0-5.6%	–2.5-2.5%
ρ_{bulk}	–36.1-45.7%	–28.8-36.8%	–5.4-9.0%
M_a	–36.1-45.7%	–28.8-36.8%	–5.4-9.0%
p_v	–46.4-50.0%	–23.8-31.7%	–10.0-10.0%

C-type	Ground-based	Space-based	Proximity
ρ_{mic}	–5.0-5.8%	–5.0-5.8%	–4.0-4.7%
P_{mic}	–7.5-7.5%	–7.5-7.5%	–3.3-3.3%
ρ_{bulk}	–41.3-45.6%	–32.3-35.5%	–4.0-4.7%
M_a	–41.3-45.6%	–32.3-35.5%	–4.0-4.7%
p_v	–26.5-34.1%	–23.8-31.7%	–10.0-10.0%

M-type	Ground-based	Space-based	Proximity
ρ_{mic}	–3.6-2.6%	–3.6-2.6%	–2.9-2.1%
P_{mic}	–0.6-0.6%	–0.6-0.6%	–0.6-0.6%
ρ_{bulk}	–27.3-24.5%	–21.5-20.8%	–3.0-2.0%
M_a	–27.3-24.5%	–21.5-20.8%	–3.0-2.0%
p_v	–28.6-42.9%	–23.8-31.7%	–10.0-10.0%

2.4. Constant design parameters

Other NEA physical parameters – opacity μ_0, specific heat capacity c, thermal conductivity κ, and sublimation enthalpy ΔH_{sub} at sublimation temperature T_{sub} – that are prerequisite to some of mitigation systems design are all available in Table 12 for different taxonomic classes: S-type, C-type, and M-type asteroids. These parameters are all predetermined in this study due to their inherent complexities in their uncertainty modelling, as well as for the sake of simplification.

2.4.1. Opacity

Opacity denoted by μ_0 represents the measure of impenetrability of the asteroid material to radiation (X-ray, gamma ray, and neutron), in other words, how nuclear energy is absorbed as it passes through the asteroid. μ_0 is dependent on the radiation type, the associated energy, and the material considered. Assuming that the radiant energy is 10 keV for X-ray, 2 MeV for gamma-ray and 14 keV for neutron radiation, μ_0 of different taxonomic classifications are calculated as shown in Table 12, These estimates are made for the mean chemical constituents of 30 OCs [94], 5 CCs [95], and 17 iron-nickel meteorites [92], referring the online database on radiation mass-absorption coefficients [96].

2.4.2. Specific heat capacity and thermal conductivity

The specific heat capacity, c and the thermal conductivity, κ of the S-type asteroid model are given as 850 J/kg/K and 1.7 W/m/K. These are estimated by taking the average of 800-900 J/kg/K and 1.4-2.0 W/m/K that represent c and κ of forsterite with porosity of 30% [97]. c and κ of the C-type asteroid model are given as 500 J/kg/K and 0.5 W/m/K, which are estimated by reference to the CC: Cold Bokkeveld (CM2) [79]. c and κ of the M-type asteroid model are given as 375 J/kg/K and 22.4 W/m/K, which are estimated by reference to the iron meteorite – Campo del Cielo (IAB) [79].

2.4.3. Sublimation enthalpy

The sublimation enthalpy denoted as ΔH_{sub} represents the energy required to evaporate the asteroid material per unit mass. The main mineral thought to be present in a typical S-type asteroid is olivine, which is consistent with what the Hayabusa mission has revealed through the in-situ grain sampling of asteroid Itokawa [46, 60]. Assuming that the dominant mineral is forsterite-rich olivine, the sublimation enthalpy of the S-type model is given as $\Delta H_{sub} =$

3.86 MJ/kg that is the sublimation enthalpy of forsterite (Mg_2SiO_4) at T_{sub} of around 1,800 K [98].

ΔH_{sub} of the C-type model is assumed to be equal to that of the S-type model in this study, since CCs, specifically, CM chondrites contain abundant hydrated minerals such as chrysotile [99] which is dehydrated and crystallised into forsterite when the temperature reaches around 1,000 K [100]. One of the dehydroxylation reactions of clino-chrysotile $Mg_3Si_2O_5(OH)_4$ is associated with the formation of the intermediate phase, the subsequent nucleation, and growth of forsterite Mg_2SiO_4 as described in Equations (36) and (37). The sublimation temperature of C-type is therefore assumed to be the same as that of S-type: $T_{sub} = 1,800$ K.

$$Mg_3Si_2O_5(OH)_4 \Rightarrow Mg_3Si_2O_7 + 2H_2O \tag{36}$$

$$2Mg_3Si_2O_7 \Rightarrow 3Mg_2SiO_4 + SiO_2 \tag{37}$$
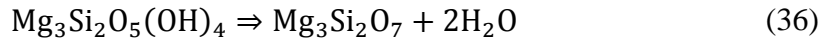
Iron (Fe) is the most predominant mineral in the M-type model assuming that the main constituent elements are Fe (92%) followed by Ni (5%), Co, and P [92]. The sublimation enthalpy of the M-type model is given as $\Delta H_{sub} = 6.26$ MJ/kg at T_{sub} of around 1,336 K, which is consistent with the sublimation enthalpy of iron (Fe) of a high degree of purity. This sublimation temperature is the ideal evaporation/condensation temperature of Fe [101].

Table 12 Opacity and thermodynamic property of asteroid. A) S-type. B) C-type. C) M-type.

A) Opacity			Thermodynamic property	
μ_0 (m²/kg)	X-ray	4.78	c (J/kg/K)	850
	Gamma ray	0.00448	κ (W/m/K)	1.7
	Neutron	0.00225	ΔH_{sub} (MJ/kg)	3.86
			T_{sub} (K)	1,800

B) Opacity			Thermodynamic property	
μ_0 (m²/kg)	X-ray	4.16	c (J/kg/K)	500
	Gamma ray	0.00474	κ (W/m/K)	0.5
	Neutron	0.00224	ΔH_{sub} (MJ/kg)	3.86
			T_{sub} (K)	1,800

C) Opacity			Thermodynamic property	
μ_0 (m²/kg)	X-ray	17.12	c (J/kg/K)	375
	Gamma ray	0.00424	κ (W/m/K)	22.4
	Neutron	0.00308	ΔH_{sub} (MJ/kg)	6.26
			T_{sub} (K)	1,336

2.5. Chapter summary

This chapter has put an emphasis on the preliminary characterisation of the asteroid physical properties that are essential to mitigation campaign planning. Three different levels (ground-based, space-based, and proximity) of characterisation have been defined. The uncertainty quantification technique: Evidence Theory has been introduced and applied to the uncertainty-based information about the asteroid characteristics in order to quantify the epistemic uncertainties. The BPA structures and the baseline design parameters for the asteroid physical properties, which will be referred to in the following chapters about further study on asteroid deflection missions and NEO hazard mitigation campaign planning, have been derived for different taxonomic classes and preliminary characterisation approaches. In addition, a series of estimates of the constant physical properties that are also prerequisite to mitigation system design have been provided in order to allow interested readers to reproduce the results of the thesis for comparison purposes.

3

3. Asteroid deflection techniques

"The risk that a Near-Earth Object hits us is low – but when it does, it may do a lot of damage. A NEO impact is the only natural threat which we have the technical capability to mitigate – so we should prepare for it."

— Detlef Koschny, *ESA's SSA programme*, 2009

This chapter presents the concepts and mathematical modelling of four asteroid deflection techniques – kinetic impactor (KI), nuclear interceptor (NI), solar collector (SC), and gravity tractor (GT) – which are divided into Section 3.1 for instantaneous deflection techniques (KI and NI) and Section 3.2 for slow-push deflection techniques (SC and GT). Section 3.3 provides a general assessment of the uncertainty in deflection efficiency of each technique subject to the uncertainty-based information about the fundamental NEA characteristics for the different preliminary characterisation scenarios.

3.1. Instantaneous deflection techniques

Instantaneous deflection techniques impulsively transfer linear momentum to an asteroid such that the velocity change of the asteroid results in a subtle orbital change, leading to a b-plane deflection. They are often more advantageous than slow-push deflection techniques in view of their quick velocity/orbital change but inevitably suffer from higher levels of uncertainty in the deflection efficiency and, more importantly, their deflection outcomes cannot be controlled as is the case for slow-push deflection techniques [49, 56]. Among the four deflection techniques considered, the KI and NI are instantaneous deflection techniques. Whenever instantaneous deflection approaches are concerned, the momentum multiplication factor β plays a very important role, and hence is detailed first in Subsection 3.1.1.

3.1.1. Momentum multiplication: β

Momentum multiplication β (i.e., momentum enhancement) represents the increase in momentum transferred to an object due to escaping ejecta as a crater is formed by an impact of a mass on the object's surface. The experimental results of hypervelocity impact on simulated planetesimal materials from the literature [102] have shown that fragmentation dispersion processes especially at impact velocities above 5 km/s. β makes a significant contribution to instantaneous deflection techniques that impart an instantaneous momentum transfer to the asteroid. Representation of β for a specific asteroid body becomes a challenging issue due to the modelling of an impact event on a small asteroid of different compositions and for different impact conditions. The study of Housen and Schmidt in 1983 [103] focused on constructing a model of crater ejecta using dimensional analysis and a theory of energy and momentum coupling in cratering events. This was then applied to deflection and fragmentation of NEAs by Ahrens and Harris in 1994 [35]. Here, two different approximate formulae of β are considered based on existing literature on β estimates.

3.1.1.1. Walker's lab experiment-based approximate formula of β

The momentum multiplication factor based on Walker's lab experiments [104] is a linear approximation. More precisely, the momentum multiplication β is inversely proportional to the target body's macro-porosity P_{mac} given by Equation (38).

$$\beta = \beta_0(1 - P_{\text{mac}}) \tag{38}$$

where β_0 is the baseline beta coefficient with values of 2.0 for relatively porous S-type and C-type asteroids and 5.0 for relatively coherent M-type asteroids. These values are within Holsapple's estimate of β (1.0-5.0) in his early work [105]. Equation (38) can be then rewritten as a function of the asteroid bulk-density ρ_{bulk} by substituting Equations (24) and (25), assuming constant ρ_{mic} and P_{mic} of the asteroid material, given by Equation (24)

$$\beta = \beta_0 \frac{\rho_{\text{bulk}}}{\rho_{\text{mic}}(1 - P_{\text{mic}})} = \beta_0 C_{\text{mic}}\rho_{\text{bulk}} \tag{39}$$

where $C_{\text{mic}} = 1/\rho_{\text{mic}}(1 - P_{\text{mic}})$ is the microscopic parameter coefficient which varies depending on the microscopic characteristics of the asteroid taxonomic class. The final forms

of Walker's lab experiment-based approximate for S-type, C-type, and M-type are given by Equations (40)-(42), respectively.

$$\beta = 0.65\rho_{bulk} \tag{40}$$

$$\beta = 0.96\rho_{bulk} \tag{41}$$

$$\beta = 0.64\rho_{bulk} \tag{42}$$

3.1.1.2. Holsapple's approximate scaling formula of β

Holsapple's momentum multiplication scaling formula is also derived from lab experiments, however, they are scaled up from the lab specimen size (10 cm) to the asteroid size (>100 m) [106]. There are two approximate forms for different types of target material – the weak strength porous (i.e., highly porous silicaceous rock) scaling form for S-type and C-type, and the asteroid strong rock (i.e., competent rock) scaling form for M-type.

Weak strength, porous (i.e., highly porous silicaceous rock) scaling form:

$$\beta = 1 + (3.3 \times 10^{-2})U^{0.2}\rho_{bulk}^{-0.1}\delta^{0.2}F_{esc} \tag{43}$$

Asteroid strong rock (i.e., competent rock) scaling form:

$$\beta = 1 + (6.5 \times 10^{-4})U^{0.65}\rho_{bulk}^{0.125}\delta^{0.2}F_{esc} \tag{44}$$

where U is the impact velocity, δ is the impactor density (e.g., density of the KI spacecraft) and is set to 3.0 g/cm^3, and the correction factor F_{esc} (the ratio of the momentum of an escaping ejecta mass element to the momentum of a total ejecta mass) is equal to 1.0 assuming all the ejecta will escape from hundred-metre sized asteroids according to Holsapple and Housen's work [106]. The tensile strength of the target asteroid is assumed to be 10 kPa for the porous asteroid scaling form and 10^3 kPa for the asteroid strong rock scaling form. Note that the actual tensile strength of an asteroid should be given as a function of the macro-porosity or bulk-density of the asteroid as well, however, such more rigorous modelling of asteroid tensile strength is unavailable with the limited amount of literature [104, 106], hence subject of another work.

Values of the momentum multiplication β represented by the two approximate formulae are given in Figure 33 as a function of ρ_{bulk} for three different asteroid taxonomic classes: S-type, C-type and M-type. Walker's lab experiment-based approximation shows a

linear increase in β for all the asteroid types whereas Holsapple's scaling approximation shows a subtle decrease in β for S-type and C-type and a very little increase in β for M-type, as the bulk-density increases. The former is due to the fact that β is simply represented as a linear function of the asteroid bulk-density whereas the latter is due to the tensile strength of the asteroid that is assumed to be constant with the asteroid macro-porosity. Walker's lab experiment-based approximation of β for S-type agrees with Walker's experimental results of β for granite.
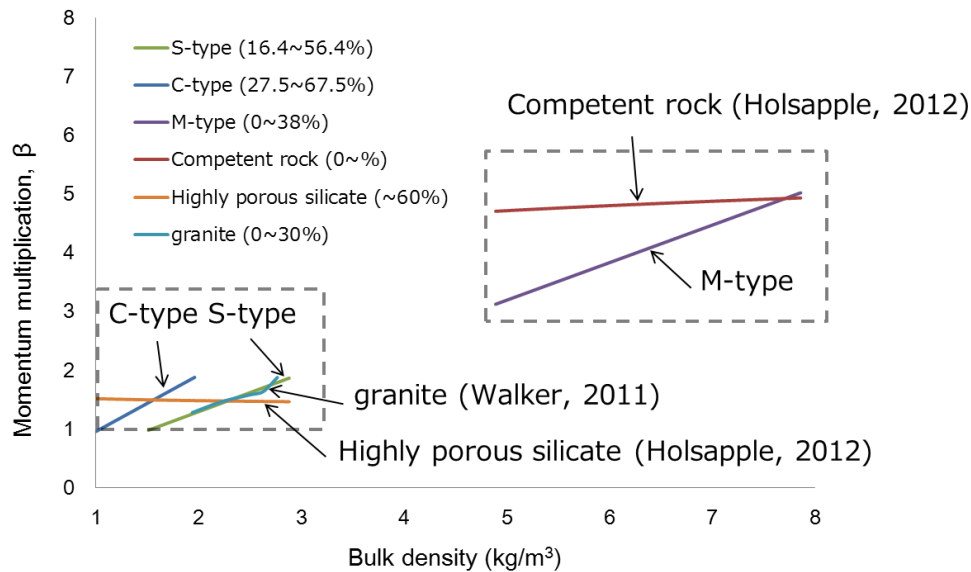
Figure 33 Walker's lab experiment-based approximation and Holsapple's scaling approximation of momentum multiplication factor β as a function of the bulk density of different rock types. The percentages represent bulk-porosities of S, C, and M-type and micro-porosities for competent rock, highly porous silicate, and granite.

Figure 34 shows β as a function of the impactor's velocity, where ρ_{bulk} of the highly porous silicate is assumed to be 2.2 g/cm^3 (typical bulk-density of S-type asteroids) and that of the competent rock is assumed to be 6.5 g/cm^3 (typical bulk-density of M-type asteroids) by reference to Table 10 in Chapter 2. As can be seen, the momentum multiplication of the M-type asteroid given by Holsapple's competent rock scaling form shows a steady increment as a function of the impactor's velocity whereas that of the S-type and C-type asteroids given by highly porous silicate scaling form indicates a very subtle or almost no increase of β as a function of the impactor's velocity. This means that, given the higher impactor's velocity, deflecting more coherent/denser asteroids (e.g., M-type) could be potentially as easy as, or in some cases, easier than deflecting more porous/less dense asteroids (e.g., S-type and C-type) of the same size. In other words, these results are clear evidence that a highly porous asteroid is good at absorbing energy from an impact as if a golf ball lands in a sand bunker without bouncing and dispersing the sand around.

However, as Holsapple himself clearly remarks in his work [106] "the cratering in the lab that is observed to be much different than for large (explosion) events makes one suspicious that scaling it up in size might give serious error," hence there is still a lot to be learned for this case of competent rock scaling. Furthermore, due to the limited amount of information on M-type asteroids and their meteorite counterparts (iron meteorites), the results of M-type asteroids could be profoundly biased by the epistemic uncertainties in the physical properties.
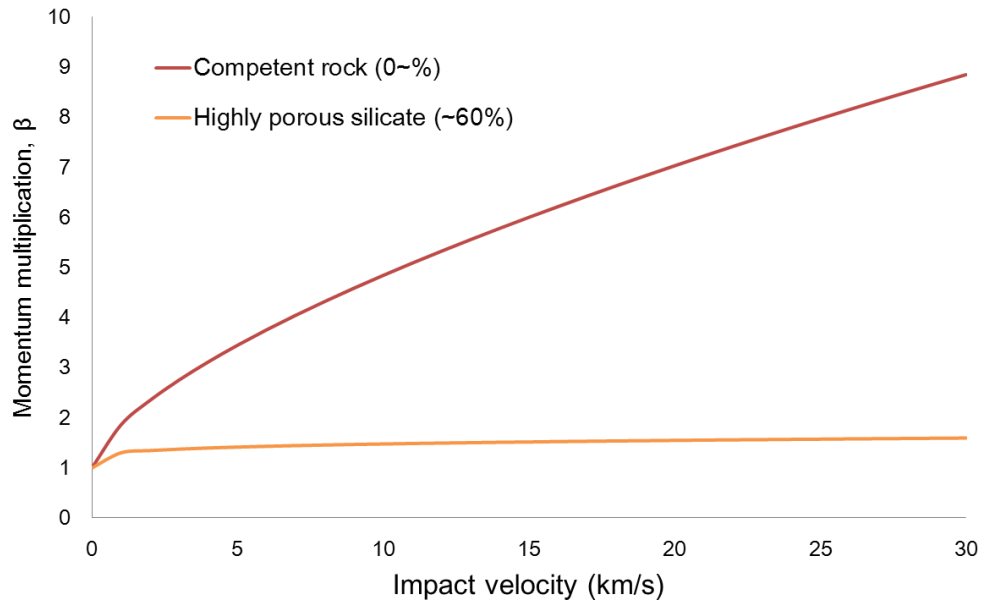
Figure 34 Momentum multiplication β as a function of impact velocity. β of the competent rock scaling form shows a steady increase with the impact velocity whereas that of the highly porous silicate scaling form remains almost constant with the impact velocity.

Walker's experiment-based approximate formula takes the asteroid taxonomic class and its macroscopic porosity P_{mac} into consideration but neither the impactor's velocity nor asteroid structural (i.e., tensile) strength is considered. Also, both impactor density and correction factor F_{esc} are ignored in this approximate formula of β. To begin with, it is quite doubtful that, without considering scaling of the model, such an approximation derived from small-scale lab experiments holds true for much larger-scale impact phenomena on an asteroid whose size is at least two or three orders of magnitude larger than Walker's experiment specimens.

Throughout this thesis, Holsapple's approximate formula of β is used instead of Walker's for all the numerical simulations while interested readers should refer to Appendix A.1 for a comparison study between two approximate formulae of β in terms of the effects on the deflection efficiency of the KI and NI.

3.1.2. Kinetic impactor: KI

The kinetic impactor: KI [35], which makes use of linear momentum transfer (i.e., impulsive velocity change) between the target asteroid and the KI spacecraft with high relative impact velocity, is one of the simplest instantaneous deflection methodologies, as illustrated in Figure 35. The KI concept has been actually demonstrated in space by NASA's Deep Impact mission to comet Tempel 1 in 2005 although the objective of the mission was to investigate the crater formation on the surface of Tempel 1. In order to efficiently transfer the impact energy to the asteroid as a linear momentum the KI should have the impact velocity vector $\mathbf{v}_{\mathrm{imp}}$ applied through the asteroid centre of mass (COM). The range of relative velocity achievable by various transfer orbits to NEAs is likely 10-20 km/s for a conventional chemical thruster module [26] and even higher than 30 km/s for retrograde orbits [107]. For reference, the impact velocity of NASA's Deep Impact spacecraft relative to Tempel 1 was about 10 km/s.
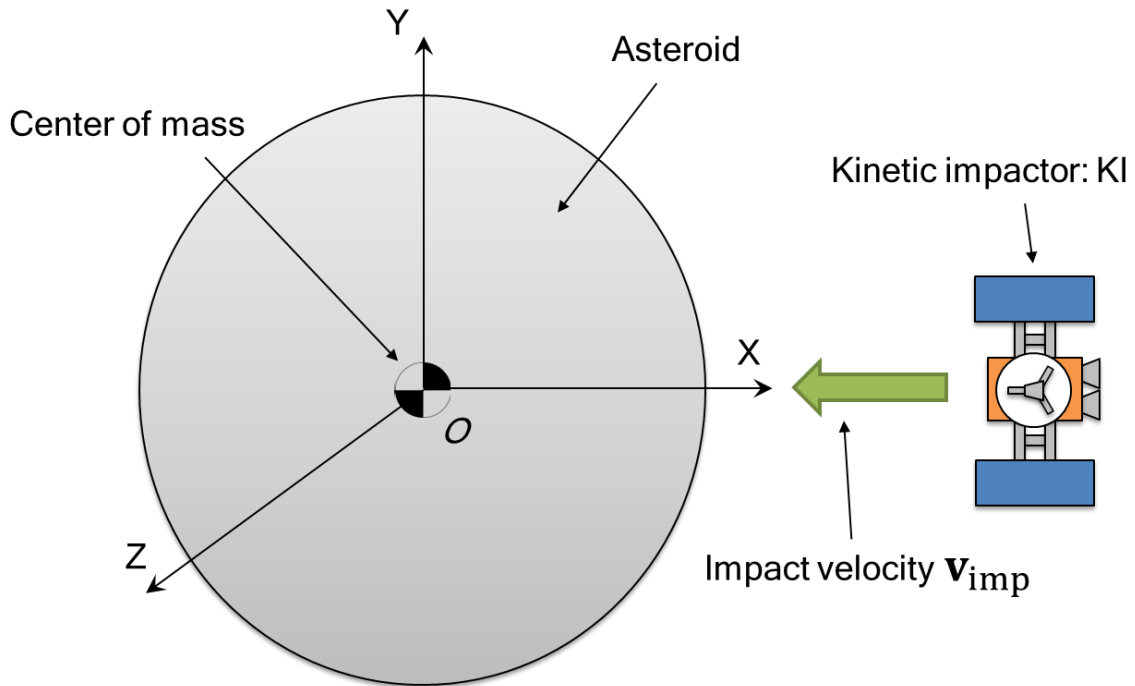
Figure 35 Simplified representation of KI model. The KI spacecraft aims to have the impact velocity vector applied through the asteroid COM for efficient linear momentum transfer. The impact velocity $\mathbf{v}_{\mathrm{imp}}$ is one of the three key parameters (the other two are asteroid mass and KI mass at the asteroid arrival) for the deflection efficiency of KI.

The instantaneous velocity change of the asteroid due to the KI: $\Delta\mathbf{v}$ is given as

$$\Delta\mathbf{v} = \beta \frac{m_{\mathrm{KI}}}{(M_a + m_{\mathrm{KI}})} \mathbf{v}_{\mathrm{imp}} \tag{45}$$

where m_{KI} is the KI mass at the kinetic impact time. As can be seen in Equation (45), the deflection efficiency of the KI is proportional to the impact velocity and the KI mass and inversely proportional to the asteroid mass. It can be seen however, that higher values of β will result in higher deflection efficiency. In other words, a more massive/cohesive asteroid is not necessarily more difficult to deflect than a less massive/more porous one.

Assuming that the x-axis in Figure 35 is tangential to the asteroid orbit and that the kinetic impact is successfully applied along that direction, it is commonly known that maximising the x-axis' component of $\mathbf{v}_{imp}$ results in an efficient orbit manipulation of the asteroid. A simple linear estimates by Ahrens and Harris [35] suggest $\Delta\mathbf{v}$ applied parallel to the orbit yields about 3 times larger deflection results than the same $\Delta\mathbf{v}$ applied transversally to a circularly orbiting body does.

Another large multiplication occurs if the kinetic impact takes place near the perihelion of an eccentric orbit, which has been clearly shown in Figures 15-20, Chapter 1. Most importantly, this basic principle holds true for all the deflection techniques: deflection attempts should take place when the asteroid is near its perihelion; however, some slow-push techniques (e.g., GT) may continue intercepting the asteroid even when the asteroid is away from the perihelion depending on their deflection efficiency and/or the warning time.

Figure 36 shows the KI spacecraft mass m_{KI} required to achieve 2½ $b_{\oplus}$ deflection distance on the 2036 b-plane for a 140-m sized (2011 AG$_5$ class) VI$_1$, given a 10-year warning time (i.e. mitigation window in which the kinetic impact takes place at the first perihelion epoch of the VI$_1$, on 9 October 2026). As can be seen in Figure 36-A), there are three curved surfaces for S-type, C-type, and M-type asteroids. Figure 36-B) is a contour plot version of Figure 36-A), which clearly indicates that a KI mission to an M-type asteroid outperforms that to an S-type asteroid: the required KI spacecraft mass for M-type is smaller than that for S-type, given the same $\mathbf{v}_{imp}$ and asteroid size. This implies that, for a deflection mission to an M-type asteroid whose orbit allows a relatively high impact velocity, the KI will become a more attractive alternative, considering the fact that the mass of an M-type asteroid could be an order of magnitude larger than that of an S-type or C-type asteroid. For reference, Figure 37 shows the results of m_{KI} for a 280-m sized (Apophis class) VI$_1$. m_{KI} required for 2½ $b_{\oplus}$ b-plane deflection is about one order of magnitude more than that is required for 140-m sized VI$_1$. Today's deep space transportation systems are however unable to launch a KI spacecraft of this scale, resulting in a KI mission to an Apophis class object infeasible, given the 10-year mitigation window.
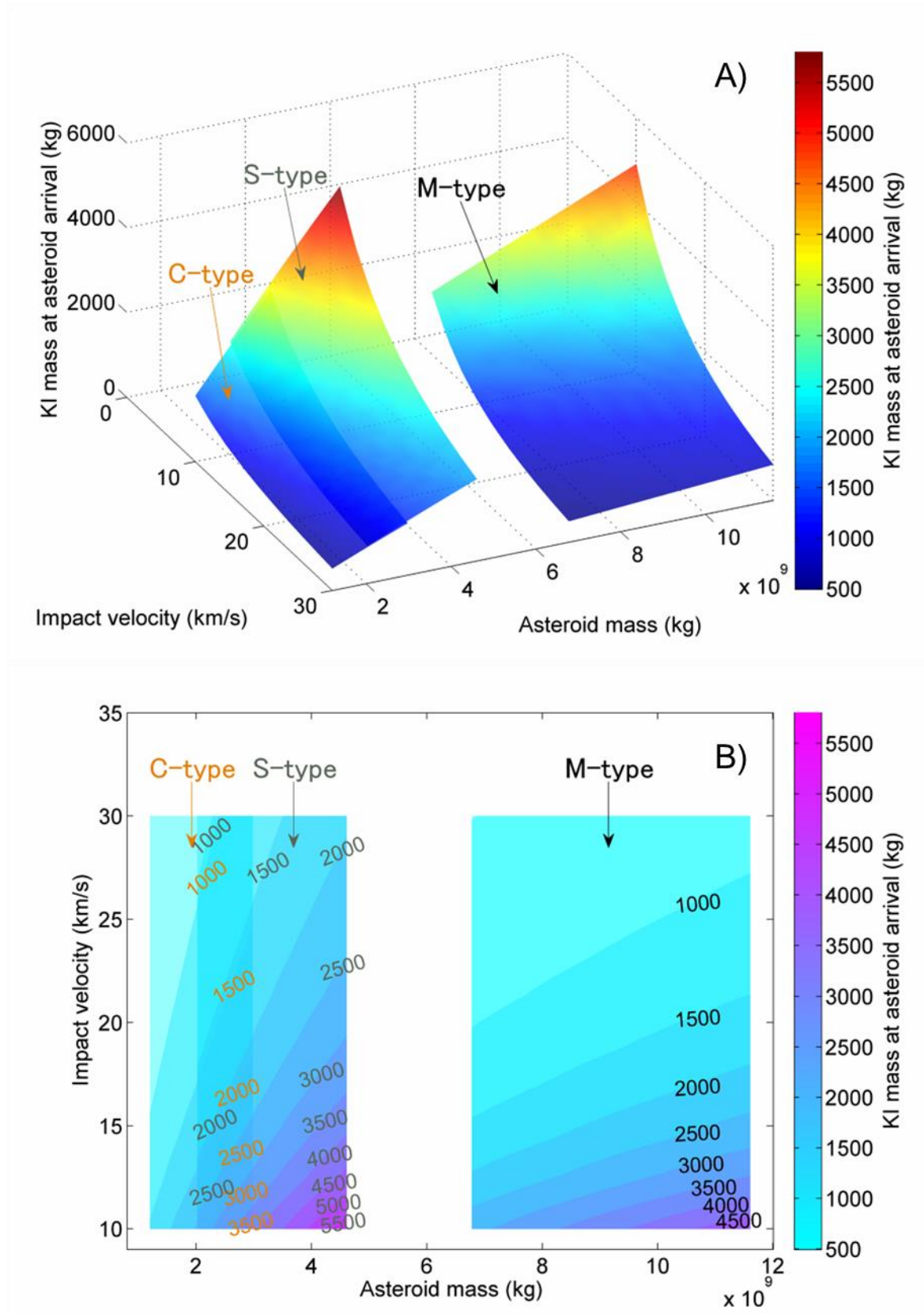
Figure 36 KI mass required to provide a 140-m sized VI₁ with $2\frac{1}{2}$ b$_\oplus$ deflection on the 2036 b-plane given 10 years of warning time before the impact epoch on 13 April 2036. The kinetic impact occurs on 9 October 2026, at the first perihelion of the VI₁ within the given mitigation window (i.e. 10-year warning time). A) Three-dimensional plot of the required KI mass for a range asteroid mass associated with each taxonomic class and kinetic impact velocity ranging between 10-30 km/s. B) Contour plot clearly shows that a KI mission an M-type asteroid outperforms that to an S-type asteroid: the required KI mass for M-type is smaller than that for S-type, given the same impact velocity and asteroid size.
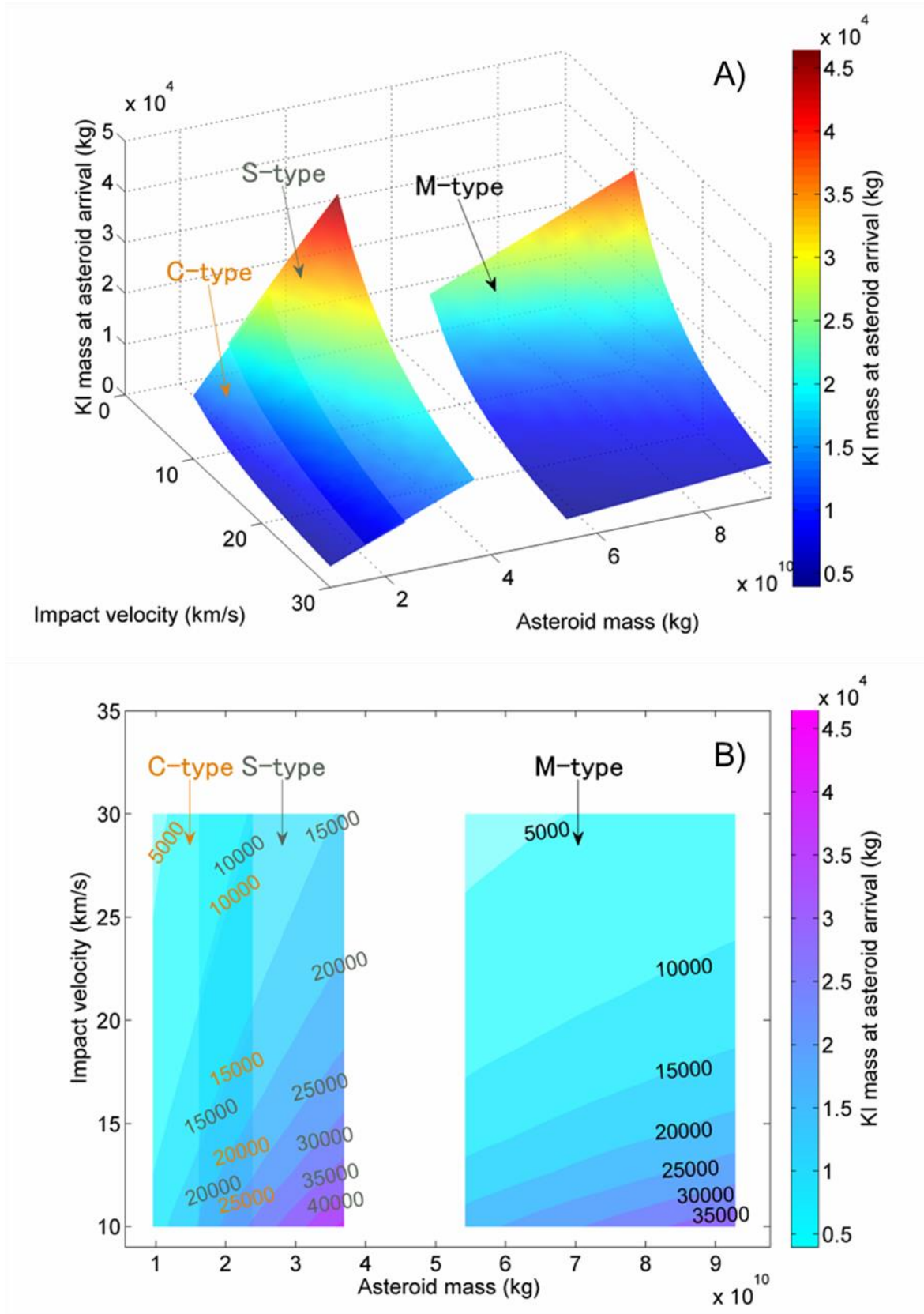
Figure 37 KI mass required to provide a 280-m sized VI$_1$ with 2½ b$_\oplus$ deflection on the 2036 b-plane given 10 years of warning time before the impact epoch on 13 April 2036. The kinetic impact occurs on 9 October 2026, at the first perihelion of the VI$_1$ within the given mitigation window (i.e. 10-year warning time). The required KI mass for a reasonable deflection of an Apophis-like asteroid of any taxonomic class becomes enormous (>15 tons at the asteroid arrival given a more realistic range of impact velocity: 10-15 km/s), resulting in the KI approach an infeasible deflection option unless a higher-velocity (>30 km/s) impact through a retrograde orbital transfer of the KI spacecraft is available [107].

3.1.3. Nuclear Interceptor: NI

The nuclear interceptor: NI deflection model used in this study is based on a stand-off explosion model [36] as illustrated in Figure 38. The stand-off model is, in theory, less sensitive to the uncertain physical properties and geometry of the target asteroid compared to a surface/sub-surface explosion model [35]. The impulsive velocity change δv due to the stand-off explosion of an onboard nuclear warhead is the sum of the δv due to the expelled debris of the NI spacecraft that extensively shower down on the asteroid's surface and radiation pressures of X-ray, neutron, and gamma ray generated by the stand-off blast given as below.

$$\delta v = \delta v_{debris} + \delta v_x + \delta v_n + \delta v_\gamma \tag{46}$$

δv_{debris} is derived by taking the linear momentum conservation of the impacting debris into account. δv_x, δv_n, and δv_γ are available through the integration of the radiation pressures over the sphere cap on the asteroid's surface that is irradiated by the stand-off nuclear explosion. In the following subsections, debris' contribution δv_{debris} is first detailed, followed by those of the radiation pressures.
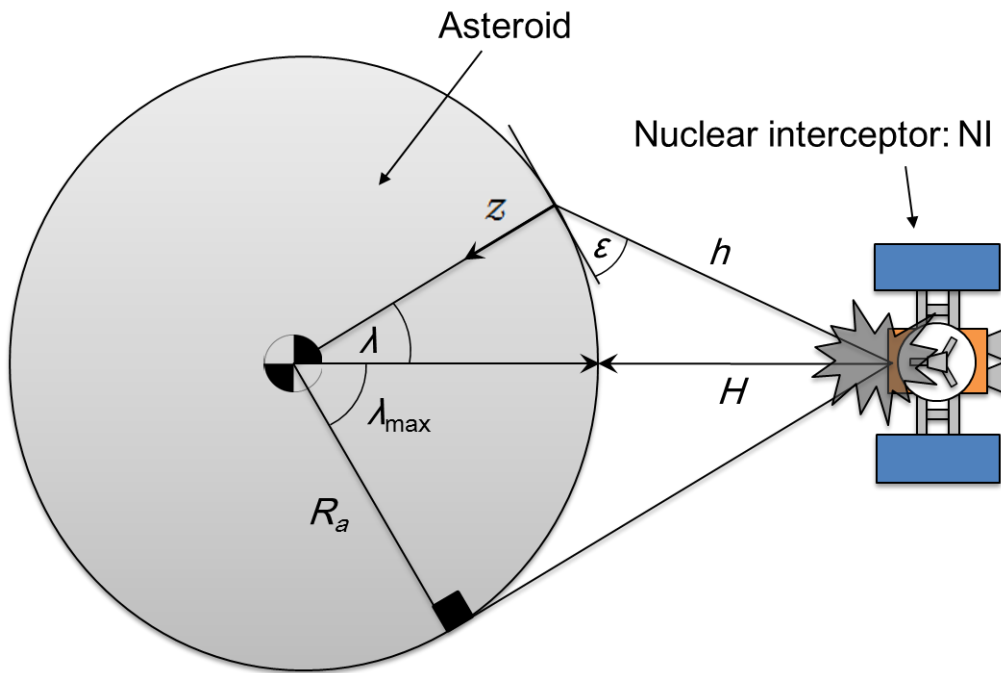
Figure 38 Simplified representation of stand-off NI model. The stand-off distance designated as H is one of the three key parameters (the other two are asteroid mass and NI mass at the asteroid arrival) for the deflection efficiency of the NI.

3.1.3.1. Debris

According to the work by Hammerling in 1995 [36], "the energy liberated in a nuclear explosion in space can be divided into that coming directly from the nuclear reactions and that from the heated case and weapon material." It is therefore assumed, throughout this thesis, that the nuclear explosion of the NI mitigation system scatters debris equally in all directions, a fraction of which will impinge on the target asteroid surface and transfer the linear momentum to the asteroid. The total mass of impacting debris that shower down on the surface of the asteroid m_{debris} is given by Equation (47).

$$m_{\text{debris}} = S m_{\text{dry}} \tag{47}$$

m_{dry} is the total dry mass of the NI spacecraft at the asteroid arrival and S is the ratio between the total area of the nuclear blast and the part of which impinging on the asteroid surface given as

$$S = \frac{1}{2} - \frac{\sqrt{H}}{2} \frac{\sqrt{H + 2R_a}}{R_a + H} \tag{48}$$

where H is the stand-off distance of the NI spacecraft with respect to the nearest surface of the asteroid (see Figure 38). The impacting velocity of the debris v_{debris} is described by Equation (49)

$$v_{\text{debris}} = \sqrt{\frac{2 f_{\text{debris}} E_t}{m_{\text{dry}}}} \tag{49}$$

where E_t is the total yield energy of the nuclear blast, and f_{debris} represents the proportion of kinetic energy in E_t. δv_{debris} can be derived by reference to the conservation of linear momentum.

$$\delta v_{\text{debris}} \approx \beta S_{\text{SC}} \frac{m_{\text{debris}} v_{\text{debris}}}{M_a} \tag{50}$$

β, S_{SC}, and M_a represent the momentum multiplication, the debris scattering factor, and the asteroid mass, respectively. The debris scattering factor is $2/\pi$ throughout this thesis, assuming a conventional estimate of 180-degree scattering of the debris centring on the epicentre of the nuclear explosion.

3.1.3.2. Radiation

The nuclear explosion of the NI mitigation system emits radiation equally in all directions, a fraction of which will impinge on the target asteroid surface, sublimate the surface material, and generate an artificial vaporised rock jet that accelerates the asteroid. The radiation contribution is ultimately a function of the radiant energy absorbed by the asteroid. Following the Beer-Lambert law of absorption, radiant energy absorbed per unit area dE_A is given by Equation (51)

$$dE_A = -\mu_0 E_A dm_A \tag{51}$$

where μ_0 is the opacity of the material (i.e., linear mass-absorption coefficient) that has been introduced in Section 2.4, Chapter 2. E_A is the received energy per unit area of the asteroid's surface. Mass per unit area dm_A is equal to the density of the asteroid ρ_a multiplied by a layer of the asteroid material of depth dz.

$$dm_A = \rho_a dz \tag{52}$$

The depth derivation of the energy per unit area E_A can be therefore given by Equation (53).

$$\frac{dE_A}{dz} = -\mu_0 \rho_a E_A \tag{53}$$

By integrating this over z, we can obtain the residual amount of the received energy per unit area at a given depth, designated as $E_A(z)$ which is given by Equation (54)

$$E_A(z) = E_A(0)e^{-\mu_0 \rho_a z} \tag{54}$$

where $E_A(0)$ is the energy per unit area on the surface of the asteroid, which is subject to the distance between the epicentre of the nuclear explosion and the asteroid's surface, designated as h. $E_A(z)$ induces the sublimation of material, where a portion of $E_A(z)$ is used in the sublimation process (i.e. in the form of sublimation enthalpy E_v). The remaining energy that is available in the form of kinetic energy accelerates the vaporised asteroid material to velocity v_e as below.

$$v_e = \sqrt{2(\mu_0 E_A(z) - E_v)} \qquad (55)$$

The variation of the linear momentum per unit area dp_A imparted to the asteroid due to this process is given by Equation (56).

$$dp_A = \rho_a v_e dz \qquad (56)$$

By integrating this from the surface of the asteroid to the maximum depth z_{max} at which the evaporation takes place, we can obtain the total linear momentum per unit area

$$P_A = \int_0^{z_{max}} dp_A dz \qquad (57)$$

where z_{max} can be computed by Equation (58).

$$z_{max} = \frac{1}{\rho_a \mu_0} \ln\left(\frac{\mu_0 E_A(0)}{E_v}\right) \qquad (58)$$

Taking the angle between the direction of the radiation and the direction tangential to the asteroid surface ε, the total linear momentum per unit area P_A can be rewritten as below.

$$P_A = \int_0^{z_{max}} \rho_a \sqrt{2\left(\mu_0 E_A(0)e^{-\frac{\mu_0 \rho_a z}{\sin\varepsilon}} - E_v\right)} dz \qquad (59)$$

The mass ablated from the asteroid's surface $m_{ablated}$ is given by Equation (60).

$$m_{\text{ablated}} = \int_0^{z_{\max}} \rho_a \mathrm{d}z \tag{60}$$

Equation (59) is integrated over the entire radiated surface represented by the surface area of a spherical cap S_{cap} given as a function of the asteroid central angle λ, where the integration is only dependent on λ.

$$S_{\text{cap}} = 2\pi R_a^2 (1 - \cos\lambda) \tag{61}$$

The total linear momentum P transferred to the asteroid is given by Equation (62)

$$P = \sqrt{8}\pi R_a^2 \rho_a$$
$$\times \int_0^{\lambda_{\max}} \left(\int_0^{z_{\max}} \sqrt{\left(\mu_0 \frac{f_{\text{radiation}} E_t}{4\pi[h(\lambda)]^2} e^{-\frac{\mu_0 \rho_a z}{\sin\varepsilon}} - E_v \right)} \mathrm{d}z \right) \sin\lambda \mathrm{d}\lambda \tag{62}$$

where δv_x, δv_n, and δv_γ are equal to the total linear momentum divided by the asteroid mass: P/M_a. The total linear momentum P transferred to the asteroid by radiation is different for each radiation type: $f_{\text{radiation}}$ in Equation (62) represents the proportion of radiation energy in E_t, which is different for each radiation type. h is simply given as a function of $\lambda \in [0 \ \lambda_{\max}]$ (see Figure 38). $\lambda_{\max}$ is the angle between the epicentre of the nuclear explosion and the horizon of the asteroid from the epicentre of the nuclear blast with respect to the asteroid body frame's centre, which is a function of the stand-off distance H.

Table 13 shows the released nuclear energy distribution of different radiation sources and kinetic energy, which is taken from the work by Hammerling [36] and based on the information in Glasstone [108]. For the case of the nuclear fission's energy distribution, 20% of the energy is available in the form of kinetic energy while the majority of the nuclear radiation is emitted in thermal X-rays. Momentum can be transferred by the multiple mechanisms: directly by means of the kinetic energy of the debris or, more efficiently, by ablation resulting from the absorption of gamma-rays, X-rays, and neutrons. According to the literature [36], the debris contribution can be neglected on the scale of a kilometre sized object but effective for a 200 m sized object. As previously discussed in Chapter 2, only a portion of this radiant energy is absorbed by the asteroid, which is subject to the opacity of

the target asteroid. In reality, the opacity of the target body as well as its mass is subject to the epistemic uncertainties in the physical properties; however, it is given as a constant value for the sake of simplicity in this study (see Table 12).

Table 13 Released energy distribution of different sources [36].

Source	X-ray	Neutron	Gamma ray	Kinetic	Others
Fission	70%	1%	2%	20%	7%
Fusion	55%	20%	1%	20%	4%

The nuclear energy of each radiation type is 10keV for X-ray, 2MeV for gamma ray, and 14MeV for neutron radiation [36]. Given the total radiation energy imparted on the surface of the target body and the kinetic energy imparted by the scattering debris, the instantaneous linear momentum transfer (i.e., velocity change δv) can be calculated through Equation (46). Assuming the yield-to-weight (YTW) ratio of the nuclear warhead is 0.1 ktons kg^{-1} by reference to the American 8-inch nuclear artillery shell W33 [109], the energy delivered by the explosion E_t can be computed as below

$$E_t = \text{YTW} \cdot m_{\text{wh}} \tag{63}$$

where m_{wh} is the onboard nuclear warhead mass given as a fraction f_{wh} of the NI spacecraft mass at the asteroid arrival, designated as m_{NI}. It is assumed that m_{wh} accounts for 30% of m_{NI} according to the literature [110] and also that m_{dry} is equal to m_{NI} because pre/post-deflection propellant is almost negligible or not required at all.

$$m_{\text{wh}} = f_{\text{wh}} m_{\text{NI}} \tag{64}$$

Figure 39 shows the NI spacecraft mass m_{NI} required to achieve $2\frac{1}{2}$ b$_\oplus$ deflection distance on the 2036 b-plane for a 140-m sized VI$_1$. The hazard scenario and interception epoch are exactly the same as those referred to in the previous subsection. In general, the results show that m_{NI} is 1-2 orders of magnitude smaller than m_{KI} for a reasonable deflection of any asteroid type. In this aspect, the NI seems to be the most efficient and yet feasible asteroid deflection approach among the all deflection techniques considered in this study although it will involve inevitable political challenges and require public

understanding and international cooperation before it could be counted on as an available asteroid deflection alternative.

As a reference, Figure 40 shows the results of an Apophis class, 280-m sized VI_1. m_{NI} could still fit in an order of a few hundred kilograms, given an optimal stand-off nuclear explosion. Moreover, m_{NI} for a larger body could be much smaller, given a higher YTW ratio than 0.1 ktons kg^{-1} which is too conservative for a nuclear warhead of this scale. In any case, the feasibility of the NI mission holds for a reasonable deflection of a 280-m sized asteroid of any taxonomic class, unlike the KI.

As a final remark on the NI deflection model, the stand-off distance H is one of the crucial factors of the stand-off NI deflection concept. An efficient instantaneous velocity change can be attained when the nuclear explosion occurs at a certain stand-off distance from the asteroid surface. It is often described by a simple form such that the optimum stand-off distance H_{opt} is equal to a fraction times the asteroid radius [35, 36]. However, as Sanchez *et al*. have previously pointed out in their work [48], this is unfortunately not always true: H_{opt} is actually a function of not only the asteroid radius (i.e., size) but also the asteroid's bulk-density (i.e., opacity) associated with its taxonomic class and the NI mass (i.e., nuclear yield of the onboard warhead) at the asteroid arrival.

Figures 41 and 42 represent the results of the instantaneous velocity change δv of the asteroid as a function of the stand-off distance for 140-m and 280-m sized VI_1, respectively. δv is normalised based on the maximum value that is attainable with the optimum stand-off distance: the optimum stand-off distance yields the total velocity change of 1.0 in these plots. The NI mass at the asteroid arrival m_{NI} is about 300 kg (i.e. 10 ktons of TNT). As mentioned above, the optimal stand-off distance is also a function of m_{NI}, however, this is only a matter of system design and not as significant as the other two crucial factors: the taxonomic class and asteroid size. In other words, the NI spacecraft mass can be computed once the taxonomic class and the equivalent diameter of the target body are estimated and the desired deflection distance on the b-plane is defined, simply by making a search for the smallest NI mass that can yield that deflection given its optimum stand-off interception. We can see in these figures that the optimum stand-off distance that yields the maximum velocity change is dependent on the target body's taxonomic class as well as the asteroid size. The results clearly show that, for the case of M-type, the debris contribution among the four components of the instantaneous velocity change is substantially large so that the optimal stand-off distance slightly decreases, compared with the cases of S-type and C-type. The NI

can take more advantage of the scattered debris impacting on an M-type asteroid than on an asteroid of the other two taxonomic classes. The only possible explanation for this is that the M-type's relatively high momentum multiplication β which could be a degree of magnitude greater than that of S-type or C-type according to the Holsapple's approximation of momentum multiplication factor β.

The NI's deflection efficiency change (i.e., optimal stand-off distance variation) with respect to the asteroid taxonomy has never been discussed in detail in the previous literature on the stand-off NI concept to the best of the author's knowledge. We expect that a high kinetic energy transfer might disrupt and disperse the object and result in secondary impact hazards of dispersed fragments to Earth depending on the target body's composition or taxonomic class. Not to mention, the same issue holds for the KI. If the asteroid does fragment, the mitigation mission might be still successful but the given asteroid deflection concept collapses and further detailed analyses on it (that will be provided later in this thesis) will make no sense at all. In order to address such an issue underlying the basis of the thesis, Subsection 3.1.4 will put an emphasis on a simplified analysis of the asteroid fragmentation and dispersion for both KI and NI deflection models, referring to the threshold specific energy Q_D^*: impact kinetic energy per target mass required to both shatter mechanical bounds and accelerate half the mass $0.5\,M_a$ to escape trajectories [111].
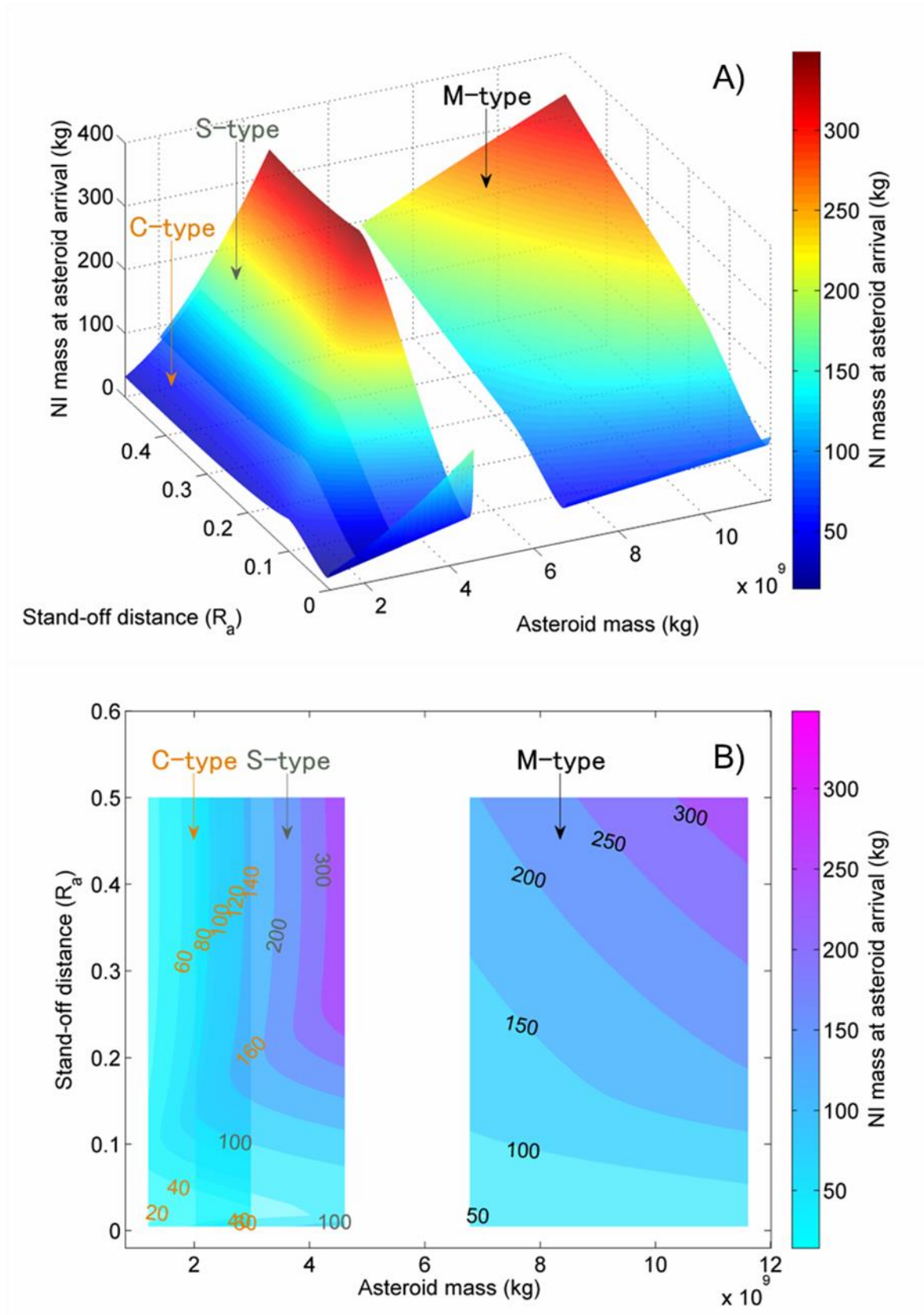
Figure 39 NI mass required to provide a 140-m sized VI$_1$ with $2\frac{1}{2}\ b_{\oplus}$ deflection on the 2036 b-plane given 10 years of warning time before the impact epoch on 13 April 2036. The nuclear interception takes place on 9 October 2026, at the first perihelion of the VI$_1$ within the given mitigation window (i.e. 10-year warning time).
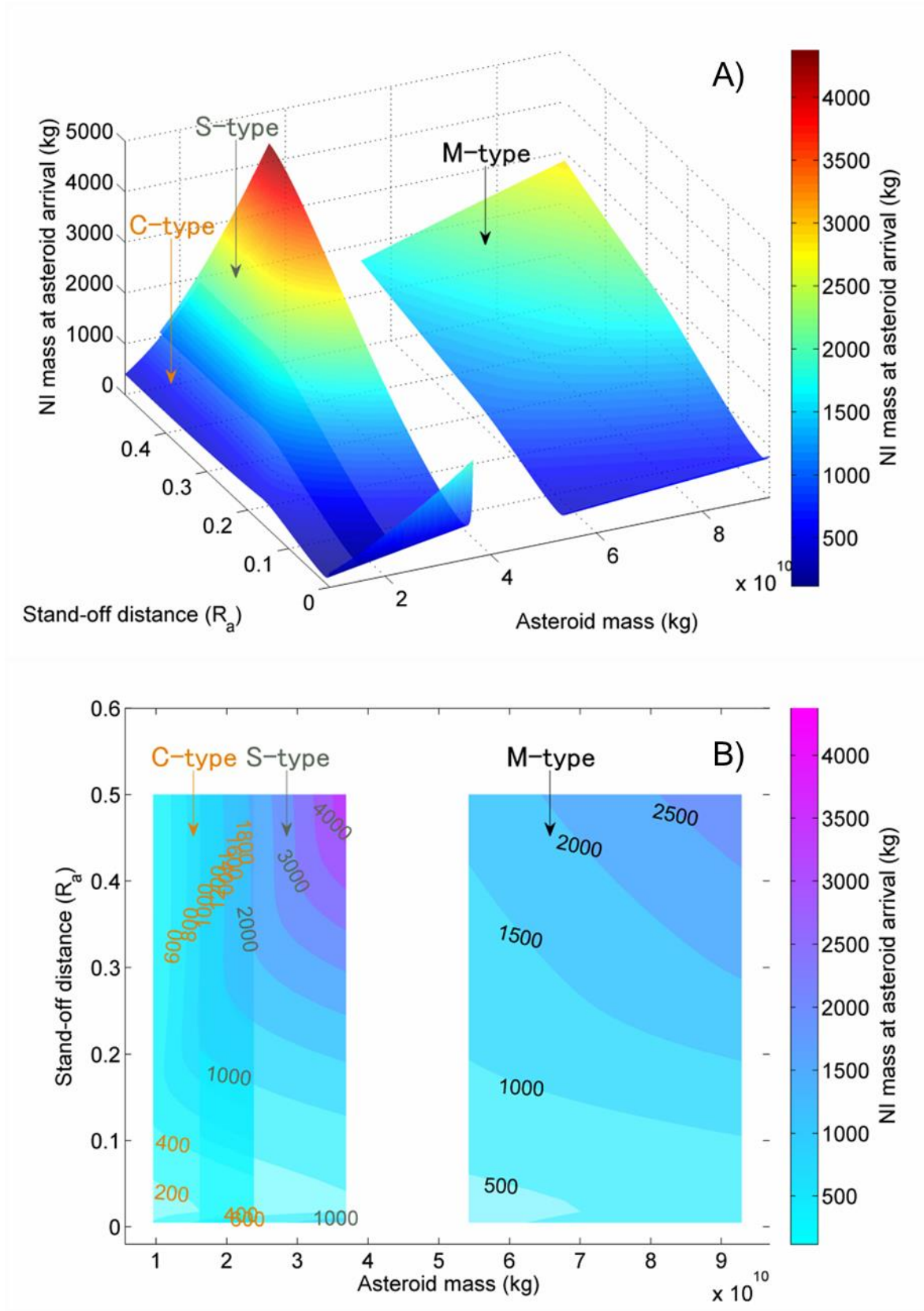
Figure 40 NI mass required to provide a 280-m sized VI₁ with 2½ b⊕ deflection on the 2036 b-plane, given the same hazard and mitigation scenario as Figure 39. Apparently, due to the conservative estimate of YTW, the NI mass resulted in a few tons for non-optimal stand-off scenarios but it could be technically smaller than 1000 kg, given a more realistic value of YTW for larger nuclear explosive packaging.
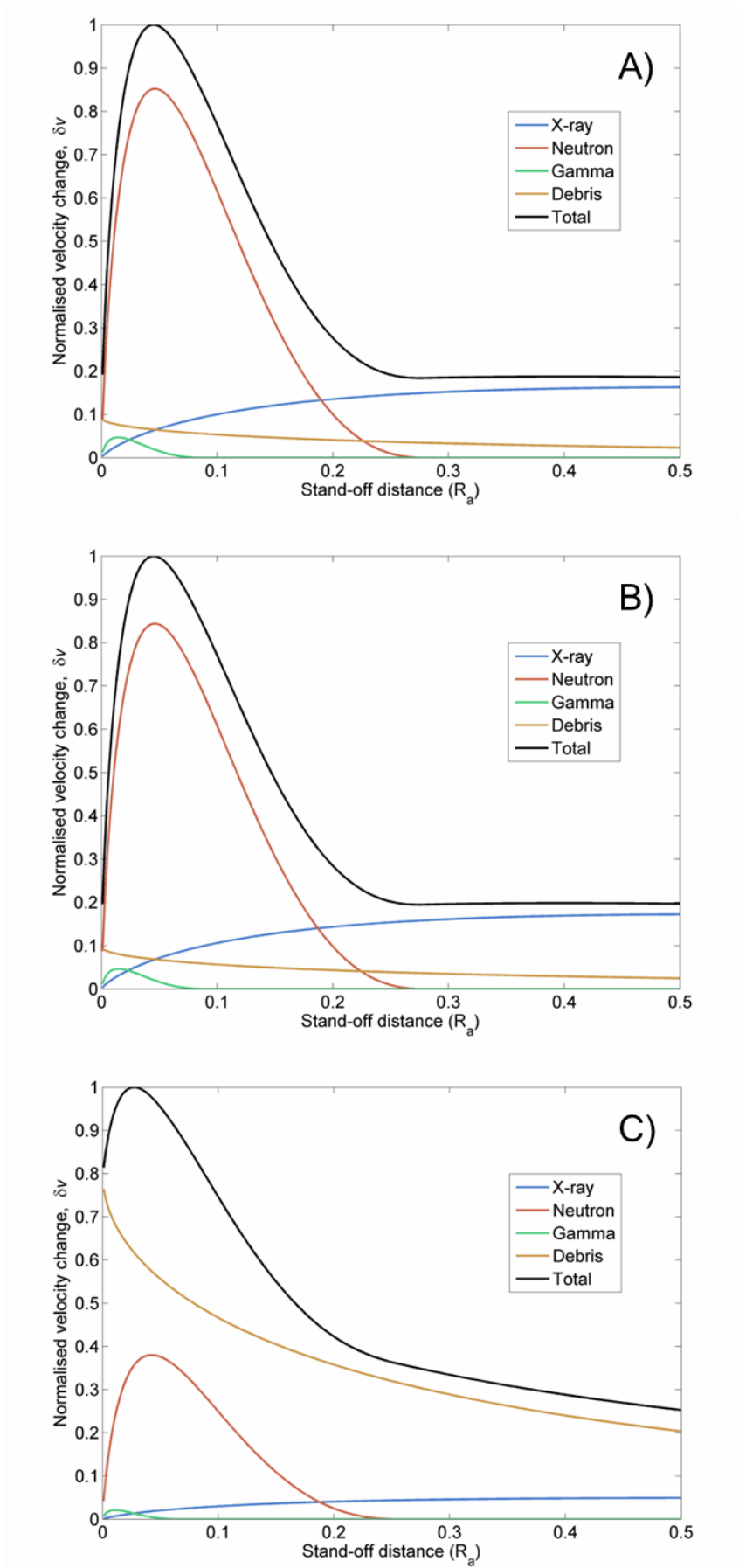
Figure 41 Normalised velocity change of 140-m sized VI₁ as a function of stand-off distance, provided by a 300-kg NI (equivalent to 10-ktons or 100-kg nuclear warhead) at the asteroid arrival. A) S-type. B) C-type. C) M-type. The optimal stand-off distance resides in <0.05 R_a.
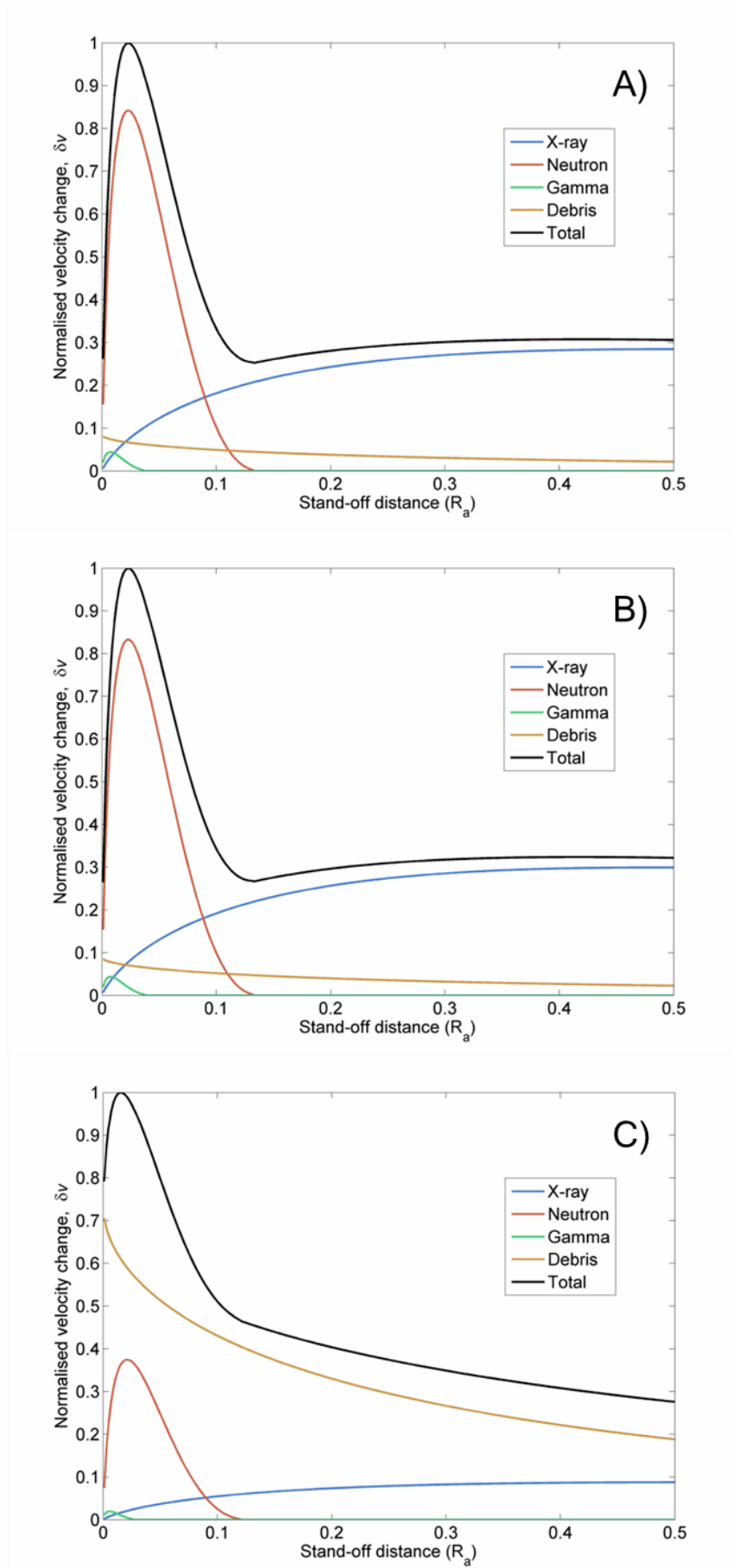
Figure 42 Normalised velocity change of 280-m sized VI₁ as a function of stand-off distance, provided by a 300-kg NI (equivalent to 10-ktons or 100-kg nuclear warhead) at the asteroid arrival. A) S-type. B) C-type. C) M-type. The optimal stand-off distance resides in <0.03 R$_a$.

3.1.4. Fragmentation and dispersion risk

Instantaneous deflection attempts of any kind are always associated with the risk of fragmentation and dispersion of the target asteroid. Ahrens and Harris noted in their work [35] that, given an interception/fragmentation of the target body ~75 days before intersection with Earth, most of the >10-m sized fragments will still stay on a collision course with Earth, while if the interception is performed well in advance (one or two orbits before the close Earth encounter), fragmentation and dispersal of the asteroid may not pose considerable secondary impact hazards of the dispersed fragments. In fact, several works on a near/sub-surface nuclear detonation aim for complete disruption and dispersion of the target body as this appears to be the only viable option for a large (>500 m in diameter) hazardous object and/or a relatively short warning time (months to a few years) hazard scenario [26, 35, 112]. However, this does not necessarily imply a successful mitigation mission from an engineering point of view, if the mission objective is merely to manipulate the object's orbit rather than to catastrophically fragment and disperse it. For this reason, it is indispensable to adequately evaluate the fragmentation and dispersion risk before going into any subsequent study on instantaneous deflection techniques.

Fragmentation and dispersion risks are often assessed by comparing the amount of kinetic energy imparted to a unit mass of the asteroid (specific kinetic energy) with the catastrophic disruption threshold (designated as Q_D^*) originally defined by Davis *et al*. [111]. Q_D^* (J/kg) is defined as energy per unit target mass required to both shatter mechanical bonds and accelerate half the mass to escape trajectories. Figure 43 represents a number of estimates of Q_D^* vs. R_a (asteroid radius in centimetre) which vary widely in literature [113]. According to the darker line (the summary of numerical outcomes for basalt spheres by Benz and Asphaug [114]) in Figure 43, Q_D^* is of the order of 100-1000 J/kg for hundred-metre sized objects. Unfortunately, this estimate is valid only if the target body is composed of basalt: Q_D^* is not only a function of the asteroid's size but also dependent on the target body's mineral composition (i.e., taxonomic class); however, as of today, little or no literature about such a complete and rigorous description of the critical specific energy Q_D^* is available to the best of the author's knowledge. We therefore assume that the estimate by Benz and Asphaug are adequate for the simplified analysis of asteroid fragmentation and dispersion required for this work. Nonetheless, the analysis will inform us how the specific kinetic energy changes according to the mitigation system design variables (impact velocity, stand-off distance, etc.).
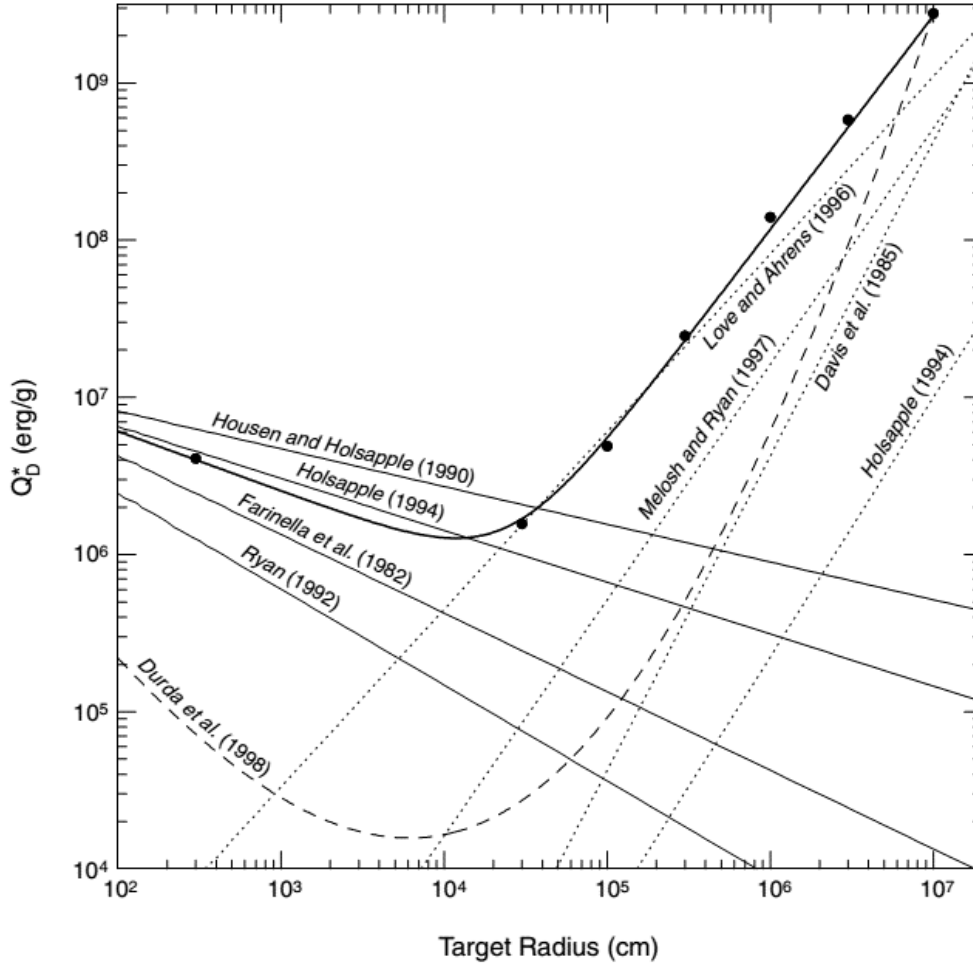
Figure 43 Values for the catastrophic disruption threshold Q_D^* of asteroids vary widely in literature. The darker line is the summary of numerical outcomes for basalt spheres by Benz and Asphaug [114]. The general trend for all models is that rocks get weaker with size because of size- and/or rate-dependent strength, and then get stronger once self-gravity dominates. For a collisionally-evolved population, objects to the right of the minimum (the strength-gravity transition) are likely to be shattered but not dispersed.

In order to determine whether a given instantaneous deflection attempt will fragment and disperse the target asteroid, the amount of kinetic energy imparted to a unit mass of the asteroid must be computed. This can be available by reference to the previous work by Sanchez *et al.* in 2008 [115], where the specific kinetic energy (designated as SKE) for the KI model and the specific absorbed nuclear energy (designated as SNE) for the NI model are defined. The KI model's SKE is available by solving Equation (65) whereas the NI model's SNE can be computed by solving Equation (66)

$$SKE|_{KI} = \frac{1}{2}\frac{m_{KI}v_{imp}^2}{M_a} = \frac{1}{2}\frac{(M_a + m_{KI})^2}{\beta^2 \cdot M_a \cdot m_{KI}}\Delta v \qquad (65)$$

$$SNE = \frac{E_t \cdot S}{M_a} \qquad (66)$$

where Δv, E_t, and S are given by Equations (45), (63), and (48), respectively. It should be noted that not all of the nuclear energy is in the form of kinetic energy but only the scattered debris' component of it is. The NI model's SKE is therefore given by Equation (67). Importantly, Equations (66) and (67) are a function of the stand-off distance H, through S.

$$SKE|_{\text{NI}} = \frac{f_{\text{debris}} \cdot E_t \cdot S}{M_a} = f_{\text{debris}} \cdot SNE \qquad (67)$$

Figure 44 shows a series of plots of specific kinetic energy ($SKE|_{\text{KI}}$) vs. kinetic impact velocity and the asteroid mass M_a for VI$_1$-VI$_6$. As can be seen, the risk of fragmentation and dispersion of the target body is dependent on the target asteroid orbit (i.e., required instantaneous velocity change) as well as its taxonomic class. The results are applicable to an asteroid of any size since $SKE|_{\text{KI}}$ is constant with target body's size. Most of the S-type and C-type virtual impactors will have fragmentation and dispersion risks given the same hazard scenario and mitigation mission requirements as what has been studied in Subsection 3.1.2 while VI$_2$ of any taxonomic class appears to be free of risk due to the lowest required velocity increment for the nominal b-plane deflection. On the other hand, a deflection attempt on VI$_3$ seems to pose a relatively high risk of fragmentation and dispersion due to the highest required velocity increment. M-type asteroids are more coherent and denser and since they have larger momentum multiplication than S-type and C-type asteroids are more immune to fragmenting and dispersing. This conclusions, however may be strongly biased by Holsapple's approximation of M-type's momentum multiplication factor β. Also, $SKE|_{\text{KI}}$ is proportional to the square root of the impact velocity, which implies that a higher velocity kinetic impact may not always be the best choice for a safe orbital manipulation of the Earth-threatening body. In any case, these results quantitatively agree well with the statement that a KI mission to a more cohesive body will be more efficient [106].

Figures 45 and 46 show a series of plots of specific kinetic energy ($SKE|_{\text{NI}}$) vs. stand-off distance and asteroid mass M_a for 140-m and 280-m sized VI$_1$-VI$_6$, respectively. Similar to Figure 44, the risk of fragmentation and dispersion of the target body varies according to the target asteroid's orbit or required instantaneous velocity change as well as its taxonomic class/composition. Again, most of the S-type and C-type virtual impactors will have higher fragmentation and dispersion risks than those of M-type. An optimal stand-off distance yields a smaller NI mass, hence a smaller nuclear yield and smaller $SKE|_{\text{NI}}$. Although the NI may, at first, appear to be a powerful and cost-effective asteroid deflection approach, its

deflection efficiency and the associated fragmentation and dispersion risk are very much dependent on the stand-off distance at the detonation of the nuclear explosive, which will be ambiguous to be assessed when the target body is non-spherical.
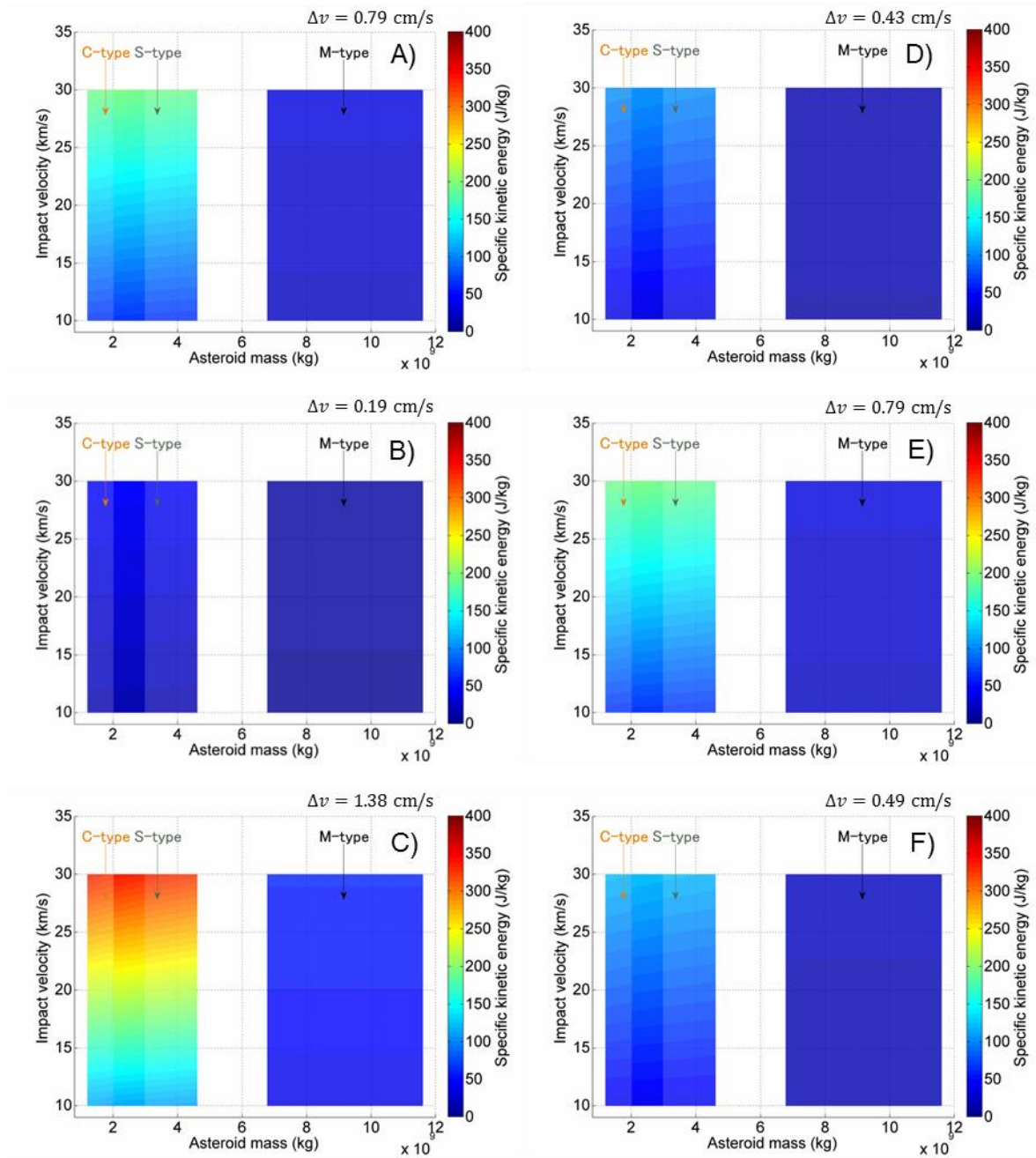
Figure 44 KI's specific kinetic energy ($\mathrm{SKE}|_{\mathrm{KI}}$) vs. impact velocity and asteroid mass for A)-F) $\mathrm{VI_1}$-$\mathrm{VI_6}$. The KI mass also varies according to the impact velocity such that the safe deflection distance, $2\frac{1}{2}\,\mathrm{b}_{\oplus}$ on the 2036 b-plane is achieved, given the same hazard and mitigation scenario as Figure 36 in Subsection 3.1.2. These results are valid for both 140-m and 280-m sized asteroids while 280-m sized asteroids may have, to some extent, smaller Q_D^*. The risk of fragmentation and dispersion of the target body fluctuates according to the target asteroid's orbit or required instantaneous velocity change $\Delta\mathrm{v}$ as well as its taxonomic class.
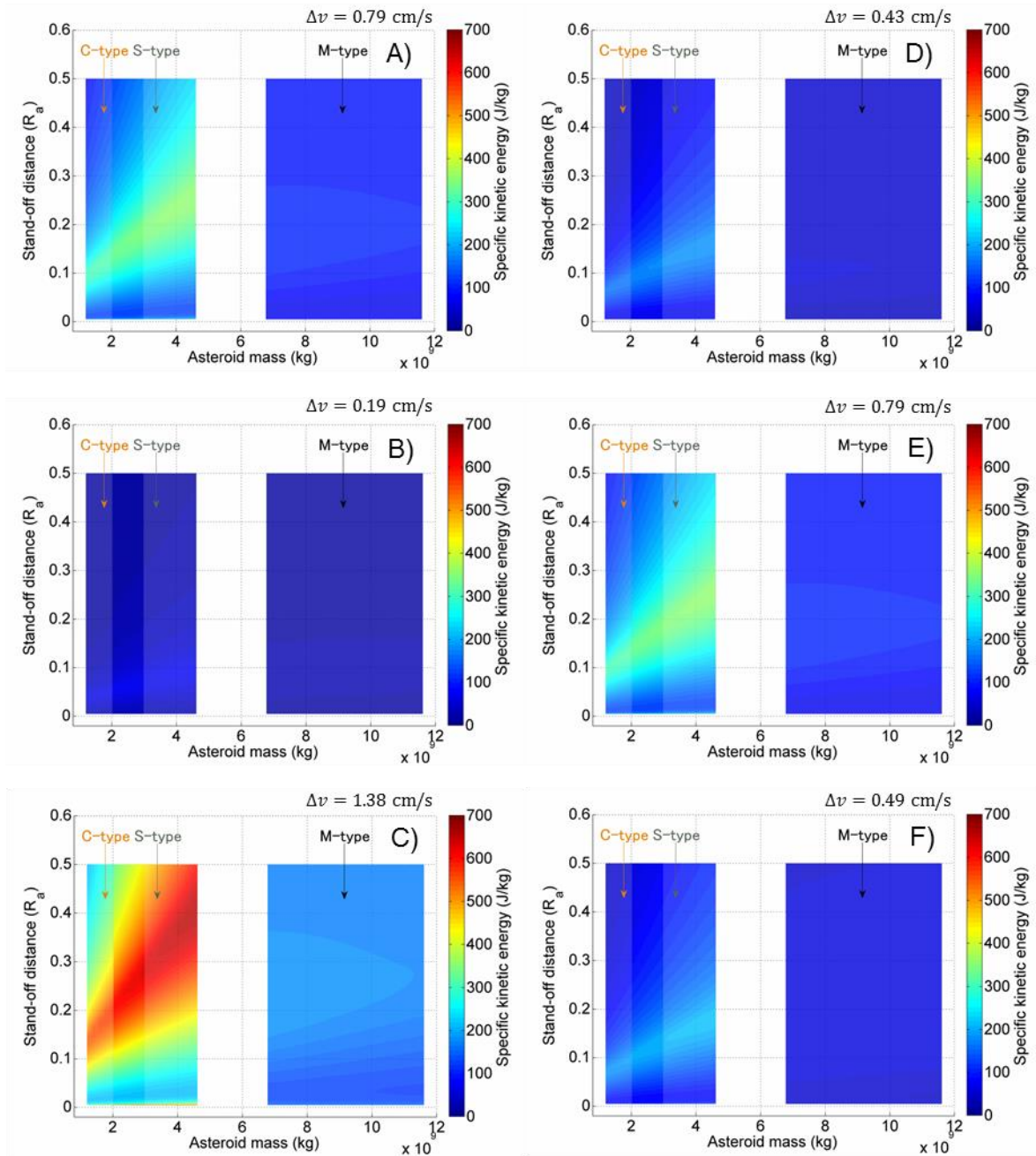
Figure 45 NI's specific kinetic energy ($SKE|_{NI}$) vs. stand-off distance and asteroid mass for A)-F) 140-m sized VI_1-VI_6. The NI mass also varies according to the impact velocity such that the safe deflection distance, $2½ b_\oplus$ on the 2036 b-plane is achieved, given the same hazard and mitigation scenario as Figure 39. Similar to the KI's results shown in Figure 44, the risk of fragmentation and dispersion of the target body is dependent on the required instantaneous velocity change Δv and the taxonomic class/composition of the target asteroid. What is more crucial here is the stand-off distance of the nuclear explosion. It appears to be that a more efficient NI mission associated with an optimal stand-off explosion yields smaller $SKE|_{NI}$, hence a smaller risk of fragmentation and dispersion.
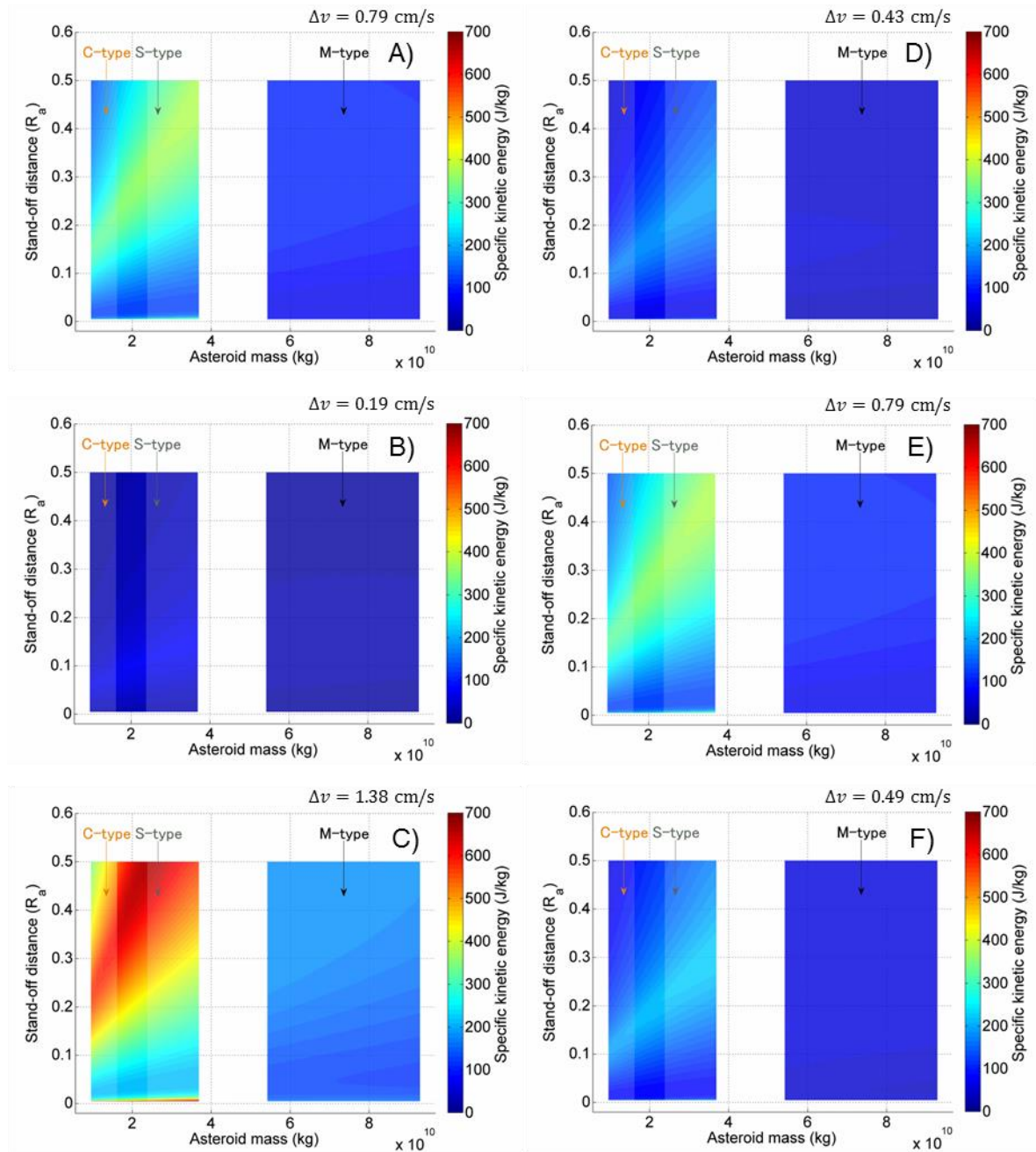
Figure 46 NI's specific kinetic energy ($\mathrm{SKE}|_{\mathrm{NI}}$) vs. stand-off distance and asteroid mass for A)-F) 280-m sized VI_1-VI_6. The NI mass also varies according to the impact velocity such that the safe deflection distance, $2\frac{1}{2}\,\mathrm{b}_\oplus$ on the 2036 b-plane is achieved, given the same hazard and mitigation scenario as Figure 40. Overall, the results are almost identical to Figure 45 while a slight shift of the colour map towards larger stand-off distance (upward direction) can be seen in each plot due to the difference in optimality of the NI's deflection efficiency.

3.2. Slow-push deflection techniques

Slow-push asteroid deflection techniques make use of a gradual orbital change through a continuous linear momentum transfer to the target asteroid. One of the advantages of slow-push techniques is that their deflection outcome is controllable however this is at the expense of longer deflection mission duration. Nevertheless, these approaches will still present uncertainty in their deflection efficiency due to the unknown asteroid properties. The uncertainty could be larger than that of instantaneous deflections due to the long-term propagation of the uncertainties over the mission duration. Among the four deflection techniques, the SC and GT are categorised as a slow-push technique.

3.2.1. Solar collector: SC

The SC model shown in Figure 47 is based on a pair of spacecraft comprising of a single inflatable solar collector (i.e., sunlight collector) and a thruster (i.e., concentrator/beam generator), originally proposed by Melosh [38] in 1994. A thrust force is generated by a vaporised rock jet emanating from the surface of the asteroid, as concentrated solar energy illuminates a spot of the asteroid surface, and sublimation of the surface material takes place. Recently, more advanced SC concepts such as the multi-collector configuration [116] have been proposed; however, applying the advanced concepts is irrelevant to the uncertainty analysis of the SC since they share the same ablation mechanism and sources of uncertainty.
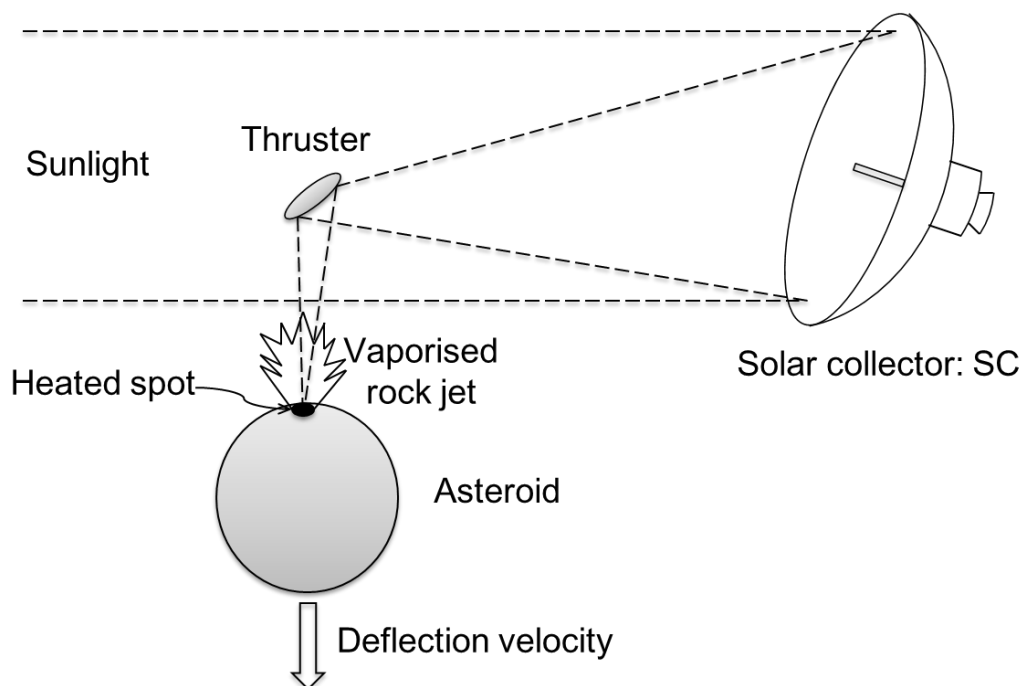

Figure 47 Simplified representation of SC model based on the concept originally proposed by Melosh [38]. Collected Sunlight is focused by the thruster which illuminates the asteroid surface, heats up the surface material, and generates an artificial vaporised rock jet.

For simplicity, a number of assumptions have been made on the SC model. The efficiency of the SC assembly is given as constant regardless of aleatory uncertainties in material characteristics due to degradation of the SC assembly. The mission duration of the SC is strictly bound by heliocentric distance, uncertainty propagation over the mission duration, and degradation of the SC assembly. In this chapter, it is assumed that the maximum mission duration is 30 days regardless of these factors for the sake of simplified analysis. It is assumed that the debris and gas are accelerated from the illuminated spot of the asteroid surface uniformly over a hemisphere, corresponding to a 180-degree plume cone with a conventional estimate of scattering factor of $2/\pi$.

Since the solar flux is inversely proportional to the square of the heliocentric distance, the efficiency of the SC is always higher when the asteroid and the nearby SC are closer to the perihelion. Given the asteroid's orbit, the warning time, and the mission duration, the SC mission start time t_{int} is optimised such that the b-plane deflection is maximised. Figure 48 represents the 30-day SC mission periods and orbital positions of VI_1-VI_6. The circular dots on the asteroid orbits represent where the deflection mission commences and the cross marks represent where it terminates. Table 13 shows the details (discovery dates, impact epochs of VI_1-VI_6, and mission durations) of these strawman SC missions to VI_1-VI_6.
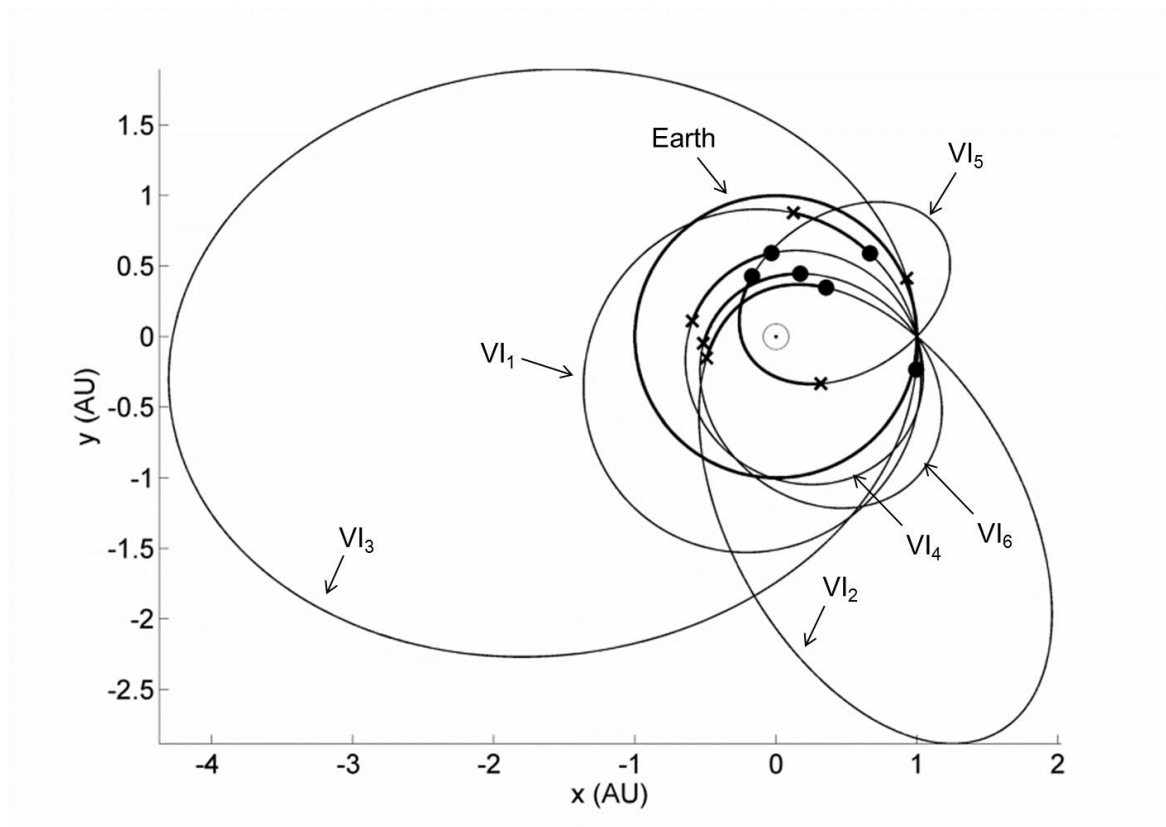

Figure 48 30-day SC mission periods and orbital positions of VI_1-VI_6. These mission durations are optimal in terms of deflection efficiency. The circular dots on the asteroid orbits represent where the deflection attempts start and the cross marks represent where they terminate.

Table 14 Discovery dates, impact epochs of VI₁-VI₆, and optimal 30-day SC mission periods given 10 years of warning time. The asteroid is approximately at its perihelion when it is the half-way point of the deflection mission duration.

Virtual impactor	Discovery date	Impact epoch	Mission duration
VI₁	2026/4/13	2036/4/13	2026/9/25-2026/10/25
VI₂	2026/4/13	2036/4/13	2026/11/25-2026/12/25
VI₃	2026/4/13	2036/4/13	2027/7/29-2027/8/28
VI₄	2026/4/13	2036/4/13	2026/8/16-2026/9/15
VI₅	2026/4/13	2036/4/13	2026/9/2-2026/10/2
VI₆	2026/4/13	2036/4/13	2027/2/2-2027/3/4

The deflection efficiency of the SC mission is dependent on the distance from the Sun, the size of the collector, the solar reflectivity of the collector, and the albedo of the asteroid surface. The received power density of the solar beam focused on the asteroid surface P_{solar} can be given by Equation (68).

$$P_{\text{solar}} = \eta_{\text{eff}} \frac{\varphi_s|_{\text{1AU}}}{R_{\text{SC}-\odot}^2} \frac{A_{\text{SC}}}{A_{\text{spot}}} (1 - p_v) \tag{68}$$

where η_{eff} is the efficiency of the SC assembly (i.e., solar reflectivity of the collector module), $\varphi_s|_{\text{1AU}}$ ($= 1367\,\text{W/m}^2$) is the solar flux at 1 AU, $R_{\text{SC}-\odot}$ is the SC's heliocentric distance which scales the solar flux at the given orbital position, A_{SC} represents the cross-section area of the reflective surface of the collector module perpendicular to the direction of the sunlight, A_{spot} is the area of the illuminated spot on the asteroid's surface, and p_v is the geometric albedo of the asteroid surface. The efficiency η_{eff} is assumed to be 90% by reference to literature [48, 117] whereas the concentration ratio of the SC assembly, designated as $\text{CR} = A_{\text{SC}}/A_{\text{spot}}$ is set to 2500. This value is equivalent to a diameter of the illuminated spot 50 times smaller than the diameter of the collector, which is assumed to be a conservative estimate of CR for the SC deflection model. For reference, the estimate of CR for a 100-m diameter concentrator was about 3900 in [117] whereas it was 2500 in [48].

Sublimation of the surface material takes place due to the net absorbed energy ΔQ which can be obtained by subtracting the radiation and conduction losses Q_{rad} and Q_{cond} from P_{solar} as below.

$$\Delta Q = P_{\text{solar}} - Q_{\text{rad}} - Q_{\text{cond}} \tag{69}$$

Energy loss due to conduction Q_{cond} can be computed by solving the differential equation for the surface temperature of the asteroid T

$$\frac{\partial^2 T}{\partial z^2} = \frac{c\rho_a}{\kappa}\frac{\partial T}{\partial t} \tag{70}$$

where c is the heat capacity (J/kg/K), $\rho_a = \rho_{\text{micro}}(1 - P_{\text{bulk}})$ is the asteroid bulk density, and κ is the thermal conductivity. These asteroid properties have been already detailed for each taxonomic class in Chapter 2. Referring to the initial conditions given by Equation (71) and the boundary condition given by Equation (72) and then applying a Laplace transformation to Equation (70), the temperature of the asteroid surface T can be computed by Equation (73)

$$T(z, 0) = 278\text{ K}, \quad T(0, t) = T_{\text{sub}} \tag{71}$$

$$\lim_{x \to \infty} T(z, 0) = T_0 \tag{72}$$

$$T(z, t) = T_0 + (T_{\text{sub}} - T_0) \cdot \text{erfc}\left(\frac{z}{2\sqrt{\kappa t / c\rho_a}}\right) \tag{73}$$

where T_0 is the initial temperature of the asteroid material, T_{sub} is the temperature of the illuminated spot of the asteroid surface which is equal to the sublimation temperature of the given asteroid material (see Table 12 in Chapter 2), and $\text{erfc}(f(z))$ is the complementary error function. The heat-flux loss by conduction $Q_{\text{cond}} = \kappa \cdot \partial T/\partial z$ on the surface of the asteroid ($z = 0$) can be then calculated by Equation (74), where a series expansion of the complementary error function $\text{erfc}(f(z))$ expressed by Equation (75) is used.

$$Q_{\text{cond}} = \frac{\partial T}{\partial z} = \frac{T_{\text{sub}} - T_0}{\sqrt{\pi t / c\kappa\rho_a}} \tag{74}$$

$$\text{erfc}\left(\frac{z}{2\sqrt{\kappa t / c\rho_a}}\right) = \frac{1}{\sqrt{\pi t / c\kappa\rho_a}}\left(z - \frac{z^3}{3 \cdot 1!} + \frac{z^5}{5 \cdot 2!} + \frac{z^7}{7 \cdot 3!} + \cdots\right) \tag{75}$$

The radiation heat loss Q_{rad} on the asteroid surface is defined according to the blackbody radiation formula given as Equation (76), where σ is the Stefan-Boltzmann constant, and ε_{bb} is the blackbody emissivity.

$$Q_{\text{rad}} = \sigma \varepsilon_{bb} T^4 \tag{76}$$

The net energy ΔQ absorbed by the illuminated asteroid surface will produce a flow of sublimated mass m_{exp}. A portion of this energy is used for the sublimation process and the other portion accelerates the sublimated mass m_{exp}. The expelled mass flow rate $\dot{m}_{\text{exp}}$ can be therefore given as

$$E_v \frac{dm_{\text{exp}}(t)}{dt} = \Delta Q \tag{77}$$

where E_v is the enthalpy of sublimation and $dm_{\text{exp}}(t)/dt$ is the flow rate of sublimated mass $\dot{m}_{\text{exp}}$. Expanding the terms in Equation (77) and solving for the mass flow rate gives Equation (78).

$$\dot{m}_{\text{exp}} = \frac{1}{E_v} (P_{\text{solar}} - Q_{\text{rad}} - Q_{\text{cond}}) \tag{78}$$

Integrating Equation (77) over the illuminated spot on the asteroid surface, the total sublimated mass flow rate can be computed by Equation (79). Note that a negative value of $\dot{m}_{\text{exp}}$ means that the absorbed energy is not sufficient to sublimate the asteroid surface material and thus the constraints of the integration have to be considered to avoid negative results.

$$\left(\dot{m}_{\text{exp}} \right)_{\text{total}} = \int_0^{y_{\text{max}}} \int_0^{x_{\text{max}}} \frac{1}{E_v} \left(\frac{(P_{\text{solar}} - Q_{\text{rad}})}{- \left(\sqrt{\frac{c \kappa \rho}{\pi}} (T_{\text{sub}} - T_0) \right) \sqrt{\frac{1}{t}}} \right) dx dy \tag{79}$$

The horizontal surface position x and the illumination time t can be related to the asteroid rotational velocity V_{rot}, such that $x = V_{\text{rot}} \cdot t$ and $dx = V_{\text{rot}} \cdot dt$. Equation (79) can be therefore rewritten as Equation (80), where the constraints of the integration t_{in} and t_{out} are the times at which a portion of the asteroid surface moves inside and outside the illuminated spot, respectively. The time that the portion of the asteroid surface spends under the spot beam is a function of the size and the angular rotation of the asteroid as well as the size of the illuminated spot which is available as a function of the size of the SC and the CR.

The SC mathematical model assumes an infinitely long rod of concentrated solar beam with the illumined spot of the asteroid surface at one end of it.

$$\left(\dot{m}_{exp}\right)_{total} = 2V_{rot} \int_0^{y_{max}} \int_{t_{in}}^{t_{out}} \frac{1}{E_v} \left(\frac{(P_{solar} - Q_{rad})}{-\left(\sqrt{\frac{c\kappa\rho}{\pi}}(T_{sub} - T_0)\right)\sqrt{\frac{1}{t}}} \right) dt dy \quad (80)$$

The average velocity of the expelled particles is determined by using the Maxwell distribution for particles of an ideal gas as below

$$\bar{v}_{exp} = \sqrt{\frac{8kT_{sub}}{\pi M_m}} \quad (81)$$

where M_m is the mass of a single molecule of Mg_2SiO_4 or Fe depending on the target asteroid material and k is the Boltzmann constant. Finally, the acceleration of the asteroid due to the sublimation $\mathbf{a}_{solar}$ is equal to the thrust produced by the sublimation process divided by the mass of the asteroid that varies as the sublimation progresses in time, corrected with a scattering factor ($S_{sc} = 2/\pi$), which accounts for the dispersion of the 180-degree plume cone.

$$\|\mathbf{a}_{solar}\| = S_{sc} \cdot \frac{\left(\dot{m}_{exp}\right)_{total} \cdot \bar{v}_{exp}}{M_a(t)} \quad (82)$$

Finally, the mass of the SC spacecraft m_{SC} is given by Equation (83) as a function of the collector's diameter d_{SC} by reference to the system mass breakdown and model for the solar concentrator "umbrella" shown in Figure 49 from the work of Gritzner and Kahle [117]. It is assumed that 30% of m_{SC} accounts for the SC assembly [110] and the other 70% of m_{SC} accounts for the thruster/beam generator, power subsystem, propulsion system, propellant masses, etc. The first term of Equation (83) accounts for the mass of the collector's aluminium-coated 90% reflectivity Mylar (18.9 g/m^2). The second term accounts for the mass of telescopic rods (2.4 kg/m), central boom (0.5 kg/m), and ropes (0.16 kg/m). The last one represents the total mass of eight 4-kg winches. Readers interested in more details on the configuration of the "umbrella" concept should refer to [117].

$$m_{SC} = \frac{10}{3}\left(18.9 \times 10^{-3} \cdot \pi \cdot \left(\frac{d_{SC}}{2}\right)^2 + 3.06 d_{SC} + 32\right) \tag{83}$$

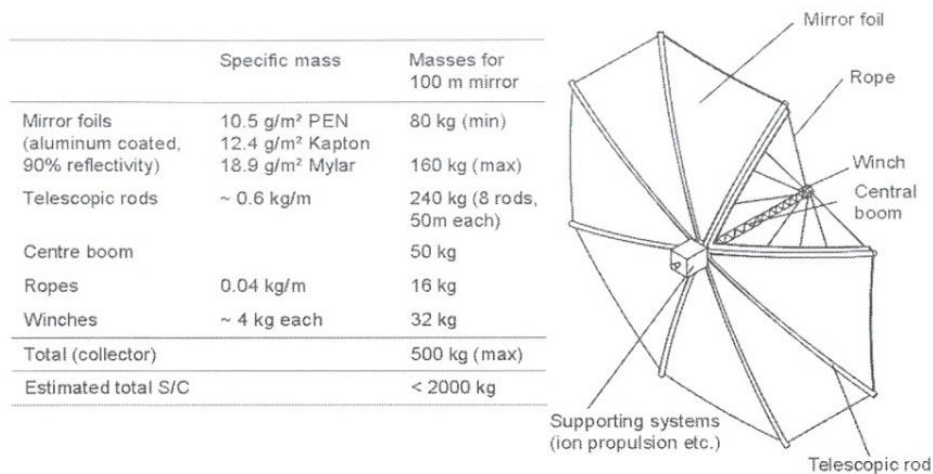|	Specific mass	Masses for 100 m mirror
Mirror foils (aluminum coated, 90% reflectivity)	10.5 g/m² PEN 12.4 g/m² Kapton 18.9 g/m² Mylar	80 kg (min) 160 kg (max)
Telescopic rods	~ 0.6 kg/m	240 kg (8 rods, 50m each)
Centre boom		50 kg
Ropes	0.04 kg/m	16 kg
Winches	~ 4 kg each	32 kg
Total (collector)		500 kg (max)
Estimated total S/C		< 2000 kg

Figure 49 System mass breakdown and model for solar concentrator "umbrella." As main material of the collector, mirror foils made of aluminium coated 90% reflectivity Mylar is considered as a conservative option in terms of mass [117].

Unlike the other three asteroid deflection alternatives (KI, NI, and GT), the SC is strongly influenced by the rotational state of the asteroid as it has to illuminate a spot of the rotating asteroid's surface and increase the illuminated spot temperature to a certain sublimation temperature in order to generate an artificial vaporised rock jet, hence the thrust force. It is therefore indispensable to determine whether sublimation will take place or not.

Since the composition of the asteroid is dependent on the target body's taxonomic class, we must first study how much temperature rise time is required for the sublimation of surface rocks. Figure 50 shows the illuminated spot temperature and a variety of heat flux variations with time for S, C, and M-types, given constant solar radiation power density of 2500 kW/m², where Q_{spot} varies in taxonomic class as each has a unique albedo value. The required time for a temperature increase that results in the surface rocks to be vaporised is about 2.0 seconds for S-type and 0.5 seconds for C-type whereas it takes about 12 seconds for M-type and about 20 seconds for a fraction of the supplied energy to be spent on the vaporisation process. This can be interpreted as the better heat conductivity of the metallic composition of M-type although the mineral composition model may be too much simplified. On the other hand, as the duration of illumination increases the fraction of energy for the evaporation of the M-type material substantially increases and reaches about 50% of the total energy after 100 seconds of illumination due to its low sublimation temperature: 1336 K. These results imply that an SC mission to an S-type or C-type asteroid will be more

advantageous in general while a slowly-rotating M-type asteroid could be easier to sublimate and to deflect than a fast-rotating one although the mass of M-type is generally larger than that of S-type or C-type with the exact same size.

To be more realistic, an asteroid could have finer grains/regolith of possibly different compositions with ten or hundred times smaller thermal conductivity between larger bare rocks on the surface that represent the asteroid's taxonomic type. Kahle *et al.* [118] previously stated in their work that, in case of an existing regolith layer, the evaporation rate would be two or three times higher while the degradation of the collector will progress much faster. Such cases are however out of the scope of this thesis, and hence not studied in detail.
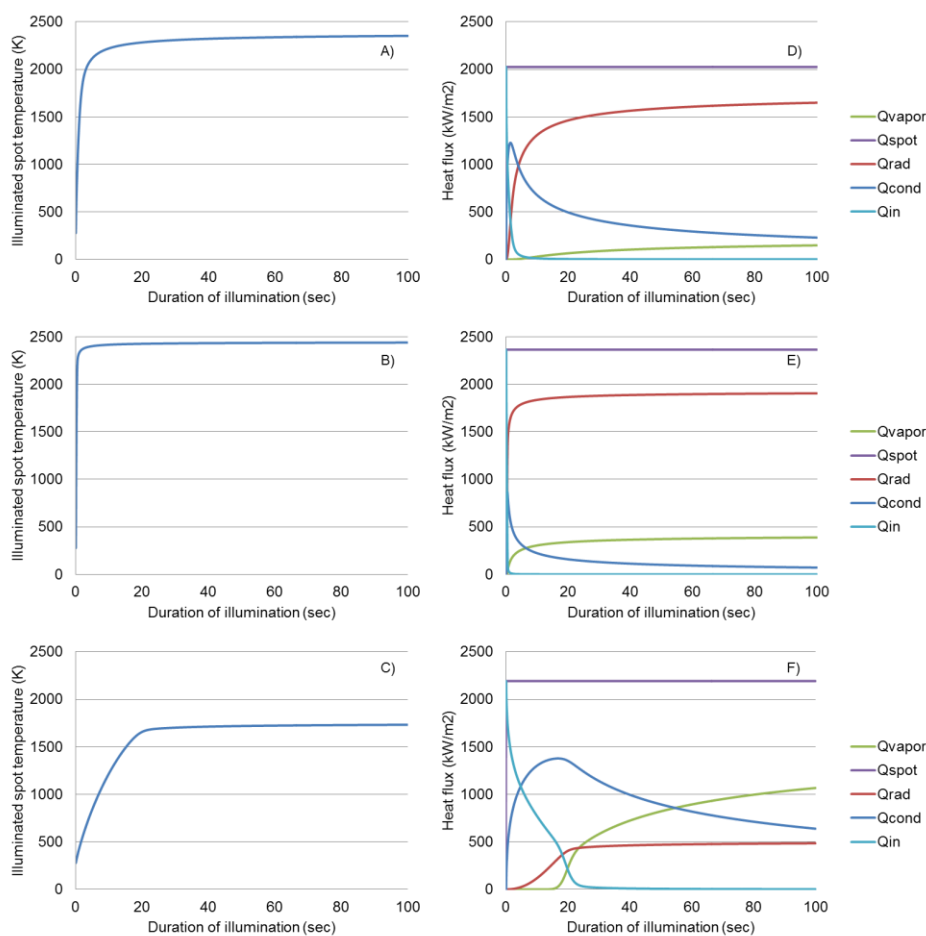
Figure 50 Illuminated spot temperature as a function of duration of illumination. A) S-type, B) C-type, and C) M-type. D)-F) show various kinds of heat flux time variations for S, C, and M-types, respectively. S-type and C-type reach the sublimation temperature of 1800 K in a matter of seconds whereas M-type requires about 12 seconds or so to reach the sublimation temperature of 1336 K. A certain level of the supplied energy is allocated for the vaporisation process of M-type after about 20 seconds of illumination due to its high heat conductivity; however, as the duration of illumination increases, the fraction of supplied energy used for the sublimation process becomes dominant, about 50% after 100 seconds of illumination.

These results must be then compared with the duration of illumination on a rotating body. Given the illuminated spot moving along the equator of the asteroid as it rotates, Figure 51 shows durations of illumination as a function of rotation period for various sized target objects for a 100-m diameter SC assembly with CR=2500. Two reference rotational periods – super-fast rotator (42.7 seconds) and spin barrier (2.2 hours: the speed limit imposed on the rotation of small rubble piles) – are shown as red and yellow vertical lines, respectively. The former refers to one of the discovered fast rotators: 2008 HJ [119] whereas the latter refers to the well-known rotational period threshold for <200-m sized asteroids [66]. Given the fact that most of the asteroids of this size complete one rotation in 0.1-10 hours [66, 76], the 100-m SC assembly succeeds in sublimating S-type and C-type, but may not be able to sublimate M-type if the rotational period is much shorter than the spin barrier. Throughout the thesis, it is assumed that the rotational period of the asteroid is 2.0 hours in order to take the worst-case and yet SC-applicable scenario into consideration. Finally, these results are subject to the SC assembly scale: for example, a larger collector diameter would lead to more rapid sublimation whereas the illumination spot size divided by rotation rate of the asteroid would affect the duration of illumination.
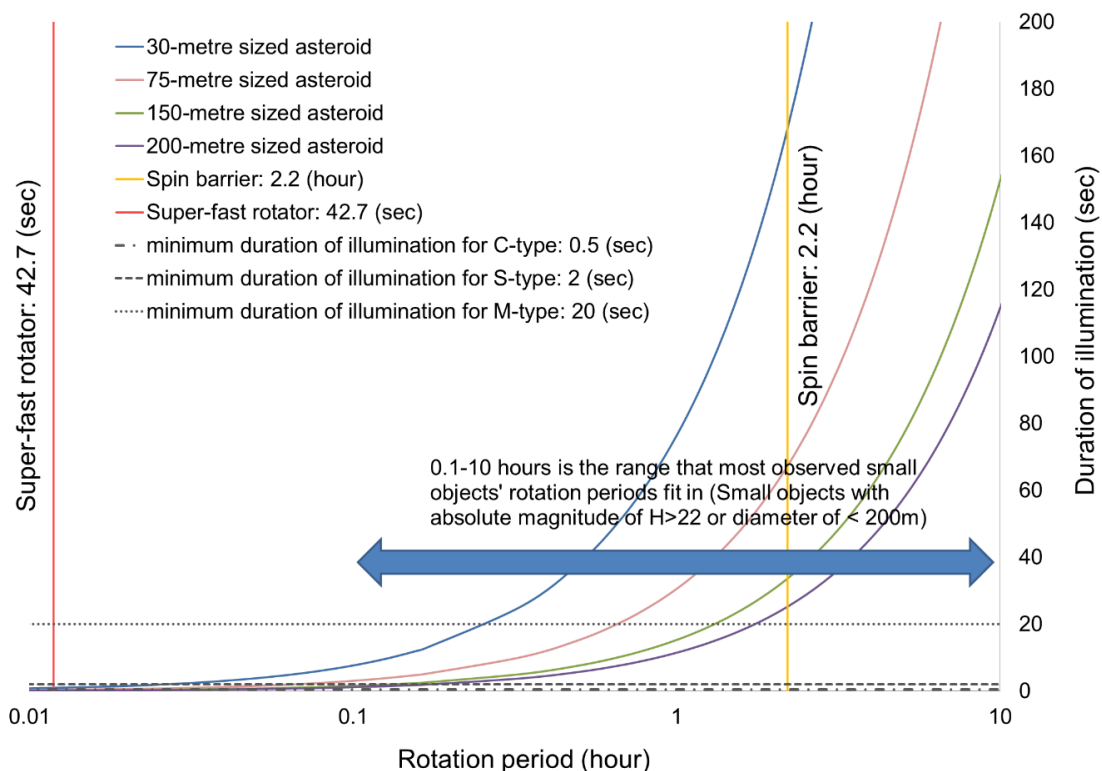
Figure 51 Duration of illumination for a 100-m diameter SC assembly with CR=2500, assuming that the illuminated spot moves along the asteroid's equator according to the rotation. For example, a 150-m sized asteroid rotates in 2 hours (slightly faster than the spin barrier) has a duration of illumination of about 30 seconds which is much longer than any minimum duration of illumination, hence enough to sublimate the surface material of any taxonomic class according to Figure 50. In case of a very unlikely event if the target object is a fast or even a super-fast rotator, the SC's efficiency will be substantially jeopardised or the SC technique itself will be completely out of commission for any taxonomic class.

Figures 52 and 53 show minimum collector size and SC mass requirements for $2\frac{1}{2}$ $b_\oplus$ b-plane deflection of 140 and 280-m sized VI_1, respectively. The specifications of the SC assembly (apart from the collector diameter which is given as a variable parameter here) are the same as the ones referred to previously in this section. The SC intercepts VI_1 for 30 days between 25 September 2026 and 25 October 2026 (see Table 14). The size/mass of the SC is given as a function of the mass and rotational state of the target asteroid.

Interestingly, the SC mass requirement for the 140-m sized VI_1's hazard scenario is relatively moderate in comparison with the instantaneous techniques, up to one order of magnitude smaller than the KI's mass requirement (for both S-type and C-type) and only a factor of two or three greater than that required for the NI mission (see Figures 36 and 39, respectively). Similarly as previously noted, an increase in the asteroid diameter results in an increase in the collector diameter or SC mass. However, if the rotational period is 1.0-2.0 hours (which is, in reality, more likely than a sub-hour rotational period), the required mass for the 280-m scenario is only about twice the mass required for the 140-m one and does not show the exponential mass increase seen in the KI. This implies that an SC mission is less dependent on the size of the target object than a KI mission; however, the SC is strongly subject to the heliocentric distance during the deflection mission. Also, it can be seen in both figures that deflecting a fast rotating M-type asteroid by means of the SC entails an order of magnitude greater size collector than that is required for the same amount of deflection of an S-type or C-type asteroid. This agrees with the results shown previously in Figure 50: sending an SC deflection mission to a fast-rotating M-type asteroid is not a particularly attractive option and so it is probably better to plan a KI mission in terms of its higher efficiency for the M-type scenario if an NI option is politically undesirable.

As a final remark on the SC deflection model, these results are only valid under the given assumptions; in reality, the asteroid will have an uneven shape and a rough surface composed of regolith and rocks of various sizes; the SC will be put in an artificial retrograde orbit about the self-rotating asteroid; and the collector degradation will occur due to the vapour deposition on it. This in turn results in focusing mismatch and inevitably jeopardising the pointing accuracy as also noted in [117]. However, in this thesis, these issues related with the efficiency of the SC technique will not be addressed as the ultimate goal of the thesis is rather a comprehensive analysis of mitigation missions as a part of mitigation campaign but not detailed study on each deflection mission concept. Readers interested in the details of the SC concept should refer to the available literature [38, 84, 116-118].

Figure 52 A) collector size and B) SC mass requirements for $2\frac{1}{2}\ b_\oplus$ b-plane deflection of 140-m sized VI₁. As long as the rotational period is more than 1.0 hour, an SC mission to the target asteroid of any taxonomic class is feasible given <1000-kg SC mass. In case of a very unlikely event if the target object is a fast or super-fast rotator, the SC's efficiency will be substantially jeopardised, resulting in a large SC mass of >2000 kg. For an SC mission to S-type and C-type, the mass at the asteroid arrival could be more or less equal to the Hayabusa spacecraft, about 500 kg while it could be as heavy as one of NASA's biggest deep space explorers ever sent, Cassini-Huygens (about 2500 kg) for the fast-rotating M-type scenario.
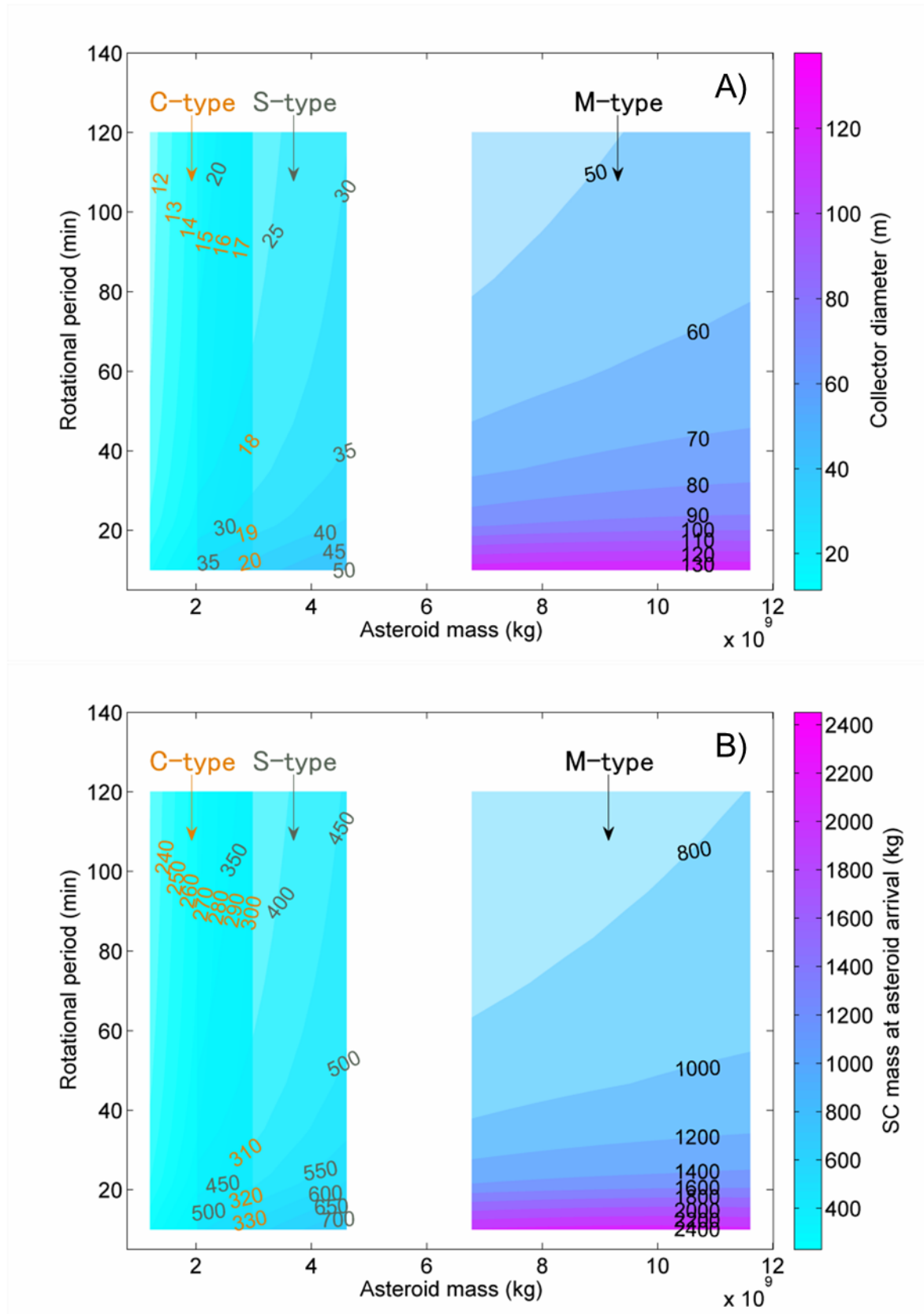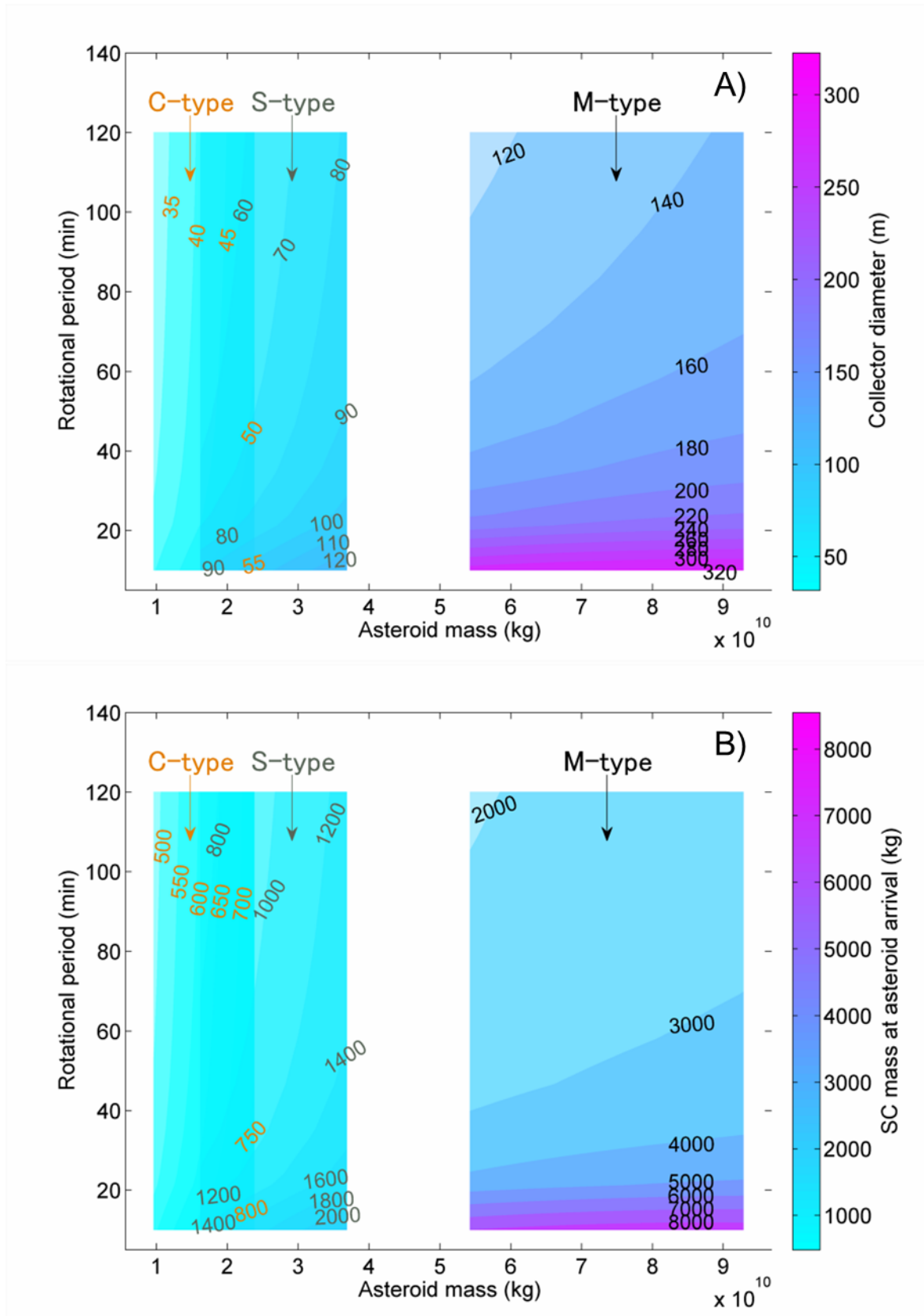
Figure 53 collector size and SC mass requirements for $2\frac{1}{2}$ $b_\oplus$ b-plane deflection of 280-m sized VI₁. Even a mission to a slower rotator (>1 hour) could entail the SC mass of 1 ton or more except for C-type. The SC mission to a C-type (least conductive and heavy among the three types) asteroid apparently results in the most efficient deflection. On the other hand, for the M-type scenario, it is no longer possible to achieve the desired deflection by a sub-ton SC mission even if the asteroid's rotational period is 2 hours or so.

3.2.2. Gravity tractor: GT

The first design concept of a GT was presented by Lu and Love in 2005 [41]. Figure 54 shows the simplified representation of the GT model based on their design concept. The principle of the GT is relatively simple in comparison with other deflection techniques. The spacecraft, so called the GT, hovers in close proximity to the asteroid such that the gravitational interaction between them triggers a gradual orbital change of the asteroid through a certain period of deflection mission (a year to a decade). The GT pulls the asteroid in parallel to the orbital direction of the asteroid to maximise the resultant b-plane deflection.
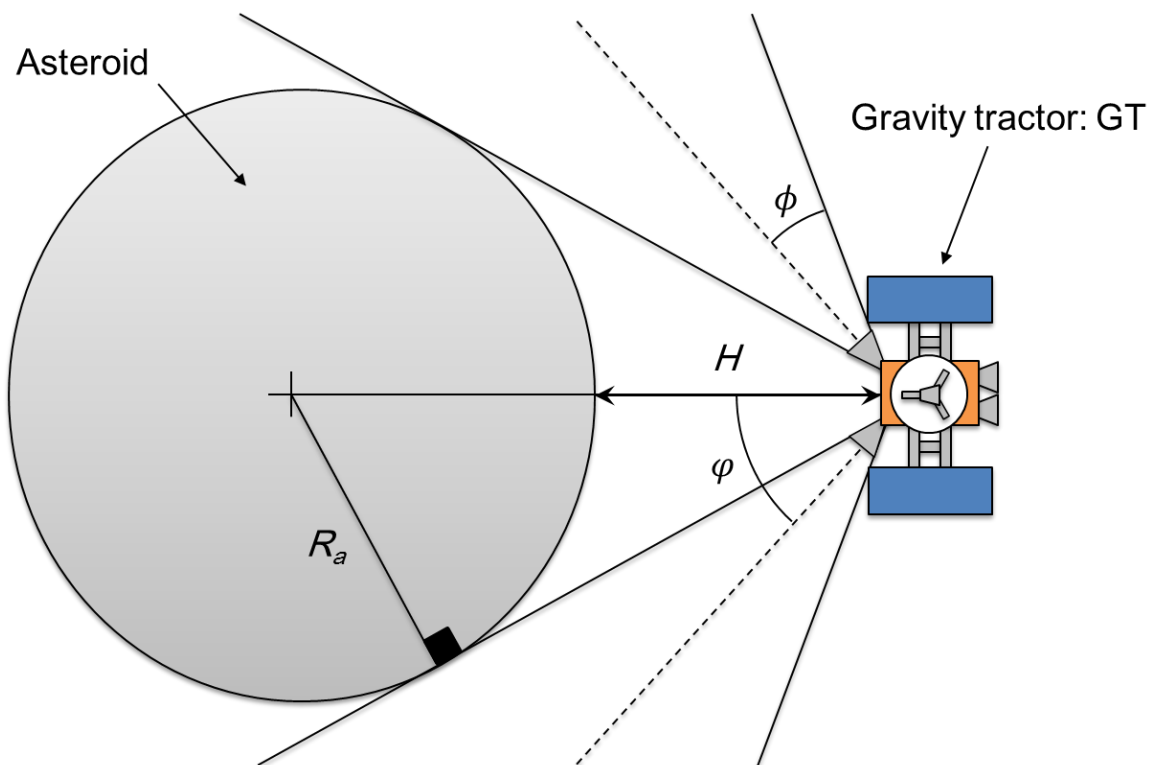
Figure 54 Simplified representation of GT based on the first concept proposed by Lu and Love in 2005 [41]. The GT spacecraft simply hovers in very proximity to the target asteroid in order to gravitationally attract the asteroid towards itself, resulting in a gentle orbital manipulation.

The GT will have a set of ion thrusters on the side of the spacecraft that is facing the asteroid as shown in Figure 54. These thrusters must be canted appropriately such that their exhaust plumes do not directly interfere with the asteroid, where the thruster canting angle φ is given by Equation (84). φ is dependent on the asteroid radius R_a, the distance between the GT and the asteroid's surface (stand-off distance H as shown Figure 54), and the half-angle of the exhaust cone (i.e., the divergence angle of the exhaust plumes of the ion thrusters) ϕ which is assumed to be 15 degrees according to the divergence angle of the flight-qualified ion thrusters: XIES onboard ETS-VI [120].

$$\varphi = \phi + \sin^{-1}\left(\frac{R_a}{R_a + H}\right) \tag{84}$$

Given the asteroid mass M_a, the GT spacecraft specifications, and the stand-off distance H, the total force F required for hovering at the constant position is given by Equation (85)

$$F = T_{\text{GT}} \cdot \cos\varphi = GM_a m_{\text{GT}}/(R_a + H)^2 \tag{85}$$

where T_{GT} is the total thrust force provided by the ion thrusters, G is the gravitational constant, m_{GT} is the GT's mass. The acceleration of the asteroid through the gravitational interaction $\mathbf{a}_{\text{GT}}$ can be described by Equation (86)

$$\|\mathbf{a}_{\text{GT}}\| = F/M_a = Gm_{\text{GT}}/(R_a + H)^2 \tag{86}$$

where m_{GT} is the sum of dry mass m_{dry} of the GT and propellant mass m_{prop}.

$$m_{\text{GT}} = m_{\text{dry}} + m_{\text{prop}} \tag{87}$$

The GT constantly uses propellant in order to maintain a hovering position in close proximity to the asteroid, hence m_{GT} (or m_{prop}) is a time variable and slowly decreases with time, resulting in a decrease of acceleration (i.e., gravitational pull) if the hovering altitude is kept constant as described in Equation (86). The mass of the GT spacecraft at any time t can be computed through Equation (88) which is derived from Equations (85) and (86), assuming a propellant consumption linearly proportional to the tractoring force F.

$$m_{\text{GT}}(t) = m_i \exp\left(\frac{-GM_a(t - t_{\text{int}})}{(R_a + H)^2 \cos\varphi I_{\text{sp}} g_0}\right) \tag{88}$$

where m_i is the initial GT's mass at the asteroid arrival time which is equal to the deflection mission start time t_{int}, assuming that the tractoring operation takes place immediately after the GT's asteroid arrival. I_{sp} is the ion engine's specific impulse and g_0 is the gravity acceleration on Earth. Dry mass m_{dry} is therefore given by Equation (89), where Δt is the gravitational tractoring duration the GT mission.

$$m_{\text{dry}} = m_i \exp\left(\frac{-GM_a\Delta t}{(R_a + H)^2\cos\varphi\, I_{\text{sp}}g_0}\right) \tag{89}$$

It is assumed that 50% of m_{dry} accounts for the power subsystem mass m_{ps} by reference to [110]. Given the initial GT mass m_i, $m_{\text{ps}} = 1/2\, m_{\text{dry}}$ is available as a function of the stand-off distance H and the GT mission duration Δt.

$$m_{\text{ps}} = \frac{1}{2} m_i \exp\left(\frac{-GM_a\Delta t}{(R_a + H)^2\cos\varphi\, I_{\text{sp}}g_0}\right) \tag{90}$$

The stand-off distance for the mission duration Δt can be found by solving Equation (91)

$$\frac{1}{2}\exp\left(\frac{-GM_a\Delta t}{(R_a + H)^2\cos\varphi\, I_{\text{sp}}g_0}\right)\cdot\frac{\xi}{\alpha}\cdot\cos\varphi - \frac{GM_a}{(R_a + H)^2} = 0 \tag{91}$$

where ξ is the specific thrust of the ion thrusters and α is the specific mass of the power subsystem (I_{sp}, ξ, and α that will be used in this thesis are shown in Table 15, respectively).

Table 15 Reference values of specific impulse I_{sp}, specific thrust ξ of the ion thrusters, and the specific mass α of the power subsystem on-board the GT spacecraft [48].

GT's specification	
I_{sp} (s)	3,000
ξ (N/kW)	0.034
α (kg/kW)	20

The deflection efficiency of the GT represented by b-plane deflection as a function of the tractoring duration and the stand-off distance is shown in Figure 55. Longer tractoring duration and a smaller stand-off distance lead to a larger resultant b-plane deflection; however, a stand-off distance too close to the asteroid surface results in an inefficient deflection because of an excessively large canting angle of the ion thrusters. As a consequence, there exists an optimal stand-off distance where the propellant consumption (i.e., the loss in GT mass) and the total applied gravitational tractoring force throughout the long-term GT mission duration are most balanced. The optimal stand-off distance is subject to the taxonomic class, asteroid size, and the tractoring duration. The deflection efficiency

for a more massive asteroid is smaller while its optimal stand-off distance becomes larger. On the other hand, optimal tractoring of a more porous asteroid leads to a much smaller stand-off distance and higher deflection efficiency; however, this could also result in unstable and complex tractoring operations of the GT spacecraft particularly when the target body is non-spherical or, at the worst, irregularly-shaped like asteroid (25143) Itokawa or (433) Eros.

Another element that must be taken into account is the specific mass α of the power subsystem onboard the GT spacecraft. The minimum required specific mass α_{min} for a given GT mission can be computed by Equation (92)

$$\alpha_{min} = \frac{m_{ps}}{P_{max}} \tag{92}$$

where P_{max} is the power subsystem's output required to provide the maximum thrust force that can counteract the gravity at the very beginning of the GT mission when the GT mass is equal to m_i. Figure 56 shows α_{min} corresponding to the GT missions shown in Figure 55. For example, 100 kg/kW (a conservative specific mass value of solar arrays operating near Earth [121]) does not generally suffice the optimal GT missions but 20 kg/kW (e.g., the specific mass of the flight proven SCARLET concentrator array onboard DS1 [122]) will suffice the optimal GT missions. Since α of 100 kg/kW is basically too conservative, it is assumed that α is 20 kg/kW throughout this thesis unless otherwise stated.

Figure 57 shows b-plane deflection distances achieved through a 1000-kg GT mission to VI$_1$ as a function of asteroid mass (i.e., bulk-density) and tractoring duration (1-10 years), given a 10-year warning time till the impact epoch 13 April 2036. Again, the deflection efficiency decreases as the asteroid size increases; however, it is notable that the deflection efficiency is not significantly affected by the uncertain asteroid mass of any type of asteroid particularly when the tractoring duration is relatively short, 3 years or so. The results indicate that the outcome of a GT mission to a not-well-characterised asteroid will not be substantially jeopardised due to the uncertain asteroid physical properties as long as the mission duration is relatively short. The GT is not as efficient as the other deflection alternatives but appears to be more insensitive to the ambiguous asteroid physical characteristics. This finding in turn implies that the GT mission is more suitable for a secondary deflection mission that provides some backup deflection before and after a primary instantaneous deflection mission. The main drawback of the GT is its required mass

for the asteroid-GT gravitational interaction: the GT mass could be easily larger than the required mass for a primary deflection mission and, crucially, a fraction of it will be simply a "deadweight" other than any prerequisite subsystems (e.g. ion thrusters, power subsystem, propellant, etc.).
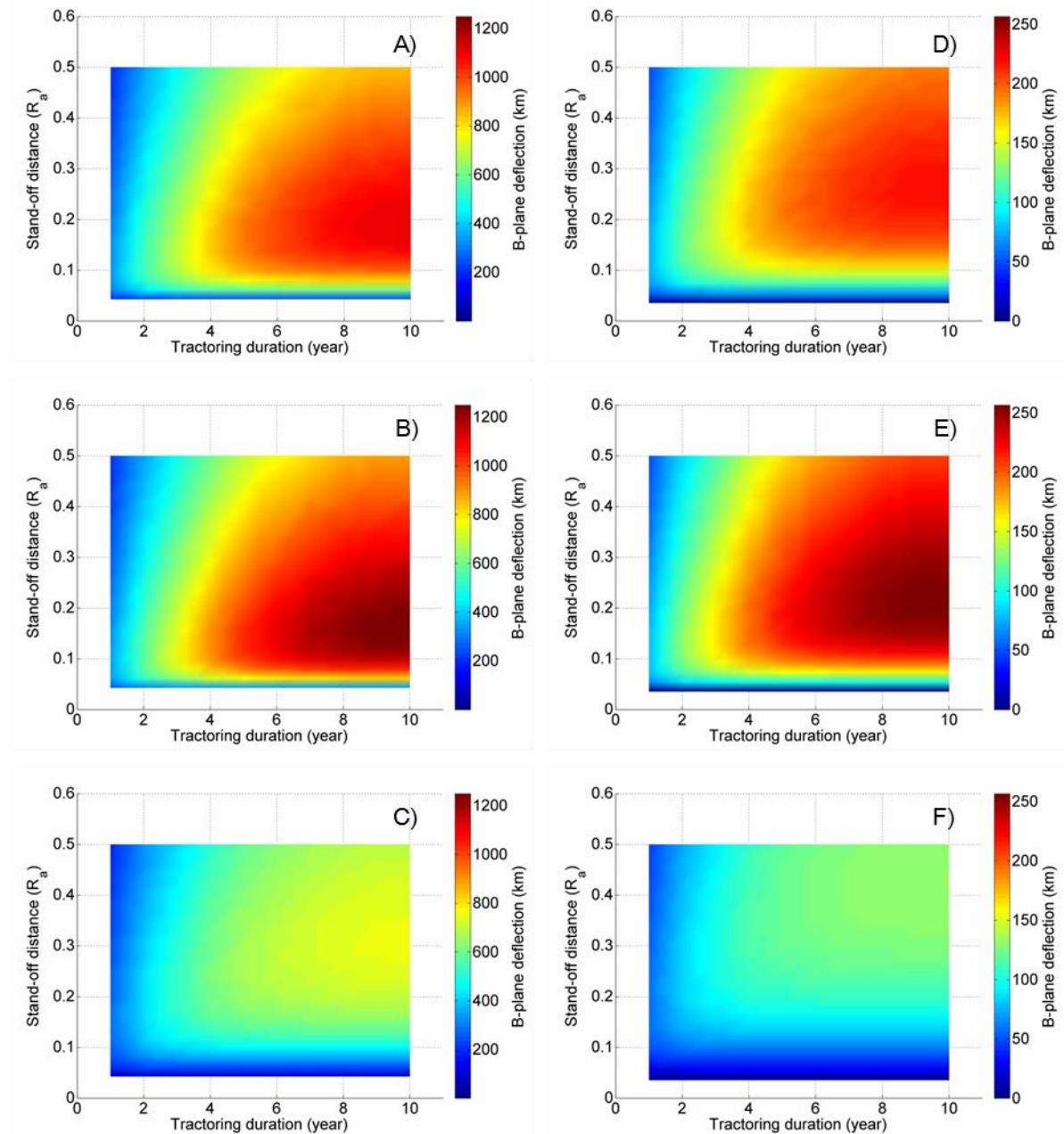

Figure 55 Deflection efficiency of a 1000-kg GT mission to VI₁ as a function of tractoring duration and stand-off distance, given a 10-year warning time till the impact epoch 13 April 2036. A) 140-m S-type. B) 140-m C-type. C) 140-m M-type. D) 280-m S-type. E) 280-m C-type. F) 280-m M-type. The GT mission begins on 13 April 2026 and lasts for 1-10 years. The bulk-density of each asteroid type refers to the baseline (see Table 10 in Chapter 2). The deflection efficiency is subject to the target asteroid's taxonomic class (i.e., bulk-density), tractoring duration, stand-off distance and its size. Increase in size results in substantial decrease in deflection efficiency similarly to the other deflection alternatives. Given a specific tractoring duration, an optimal stand-off distance H can be found, which yields the maximum deflection. Apparently, the larger the asteroid bulk-density or the mass is, the larger H can be, hence the safer and more stable the GT mission will be in exchange of lower deflection efficiency.

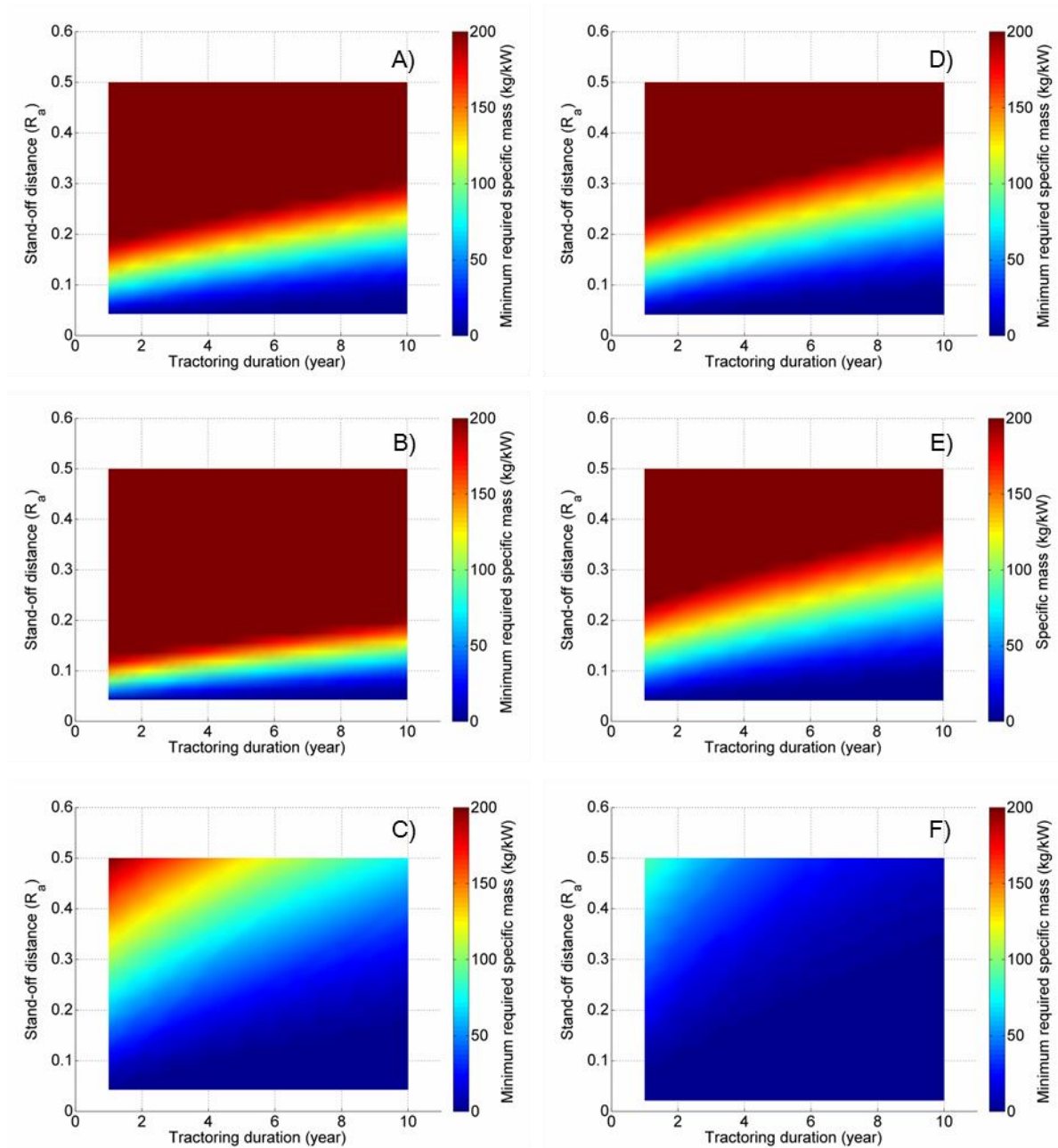**Figure 56 Specific mass α that is required for various GT missions shown in Figure 55. Given α of 20 kg/kW regardless of the Sun-asteroid distance, it will suffice supplying the required power for the optimal stand-off GT missions.**

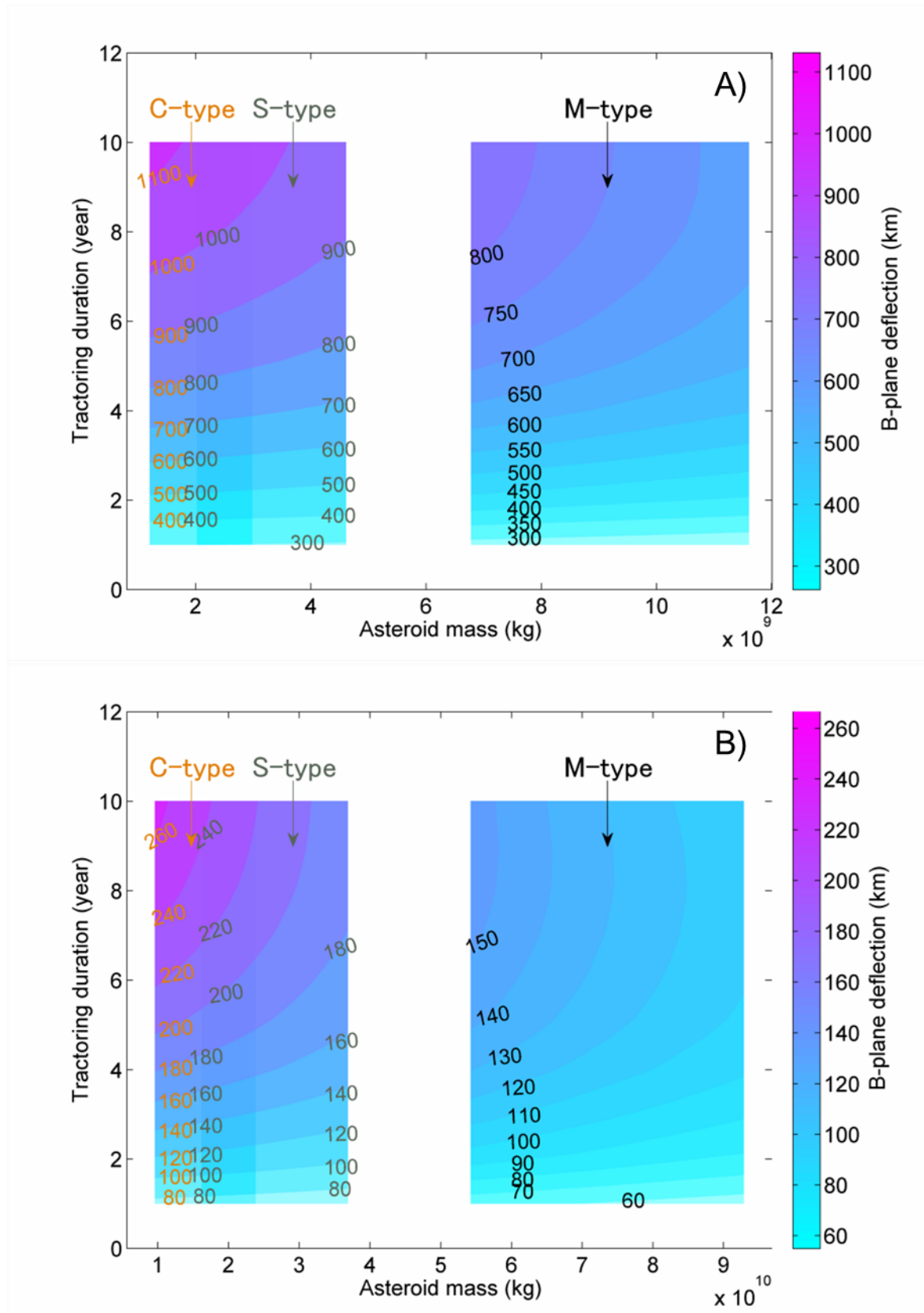**Figure 57 1000-kg GT mission to VI$_1$ as a function of asteroid mass (i.e., bulk-density) and tractoring duration, given a 10-year warning time till the impact epoch 13 April 2036. A) 140-m sized VI$_1$. B) 280-m sized VI$_1$. The deflection efficiency will not be substantially jeopardized by the ambiguity in asteroid mass of any asteroid type particularly when the tractoring duration is relatively short, about 3 years or so.**

As a final remark of the GT deflection model, in order to generate a sufficient asteroid-GT gravitational attraction, the GT hovering altitude/stand-off distance has to be a very small fraction of the asteroid radius [42]. An optimal hovering stand-off distance of the GT spacecraft has been also defined [48], where the resultant stand-off distances are often very close to the surface of the asteroid (<10 m) if the target body is hundred-metre sized in diameter. In reality, hovering in such close proximity to the asteroid could result in highly unstable spacecraft dynamics due to the inhomogeneous gravitational field about the target non-spherical and irregularly-shaped asteroid, which is, more importantly, associated with a certain risk of unexpected contact between the GT spacecraft and the asteroid [49, 123]. It is believed that such a collisional event has unexpectedly happened to the Hayabusa spacecraft when it attempted to touch down on the surface of asteroid (25143) Itokawa for sample collection for the first time [124]. However, since it has been assumed that the asteroid is a homogeneous spherical body here, detailed study of such spacecraft dynamics and stability in close proximity of the asteroid is not available.

3.3. Uncertainty in asteroid deflection

The main objective of this section is to quantitatively evaluate the uncertain deflection outcomes of the four asteroid deflection alternatives. The three different levels (ground-based, space-based infrared, and proximity) of preliminary characterisation as well as the three different taxonomic classes (S, C, and M-type) are taken into consideration in order to highlight the significance of information credibility about the target body's characteristics. Uncertainty in asteroid deflection (i.e., variation of b-plane deflection from the nominal deflection represented by the probabilistic measures: Belief and Plausibility) originates from the epistemic uncertainties in the preliminary asteroid characterisation which have been already detailed in Chapter 2. In reality, a feedback deflection action under epistemic and aleatory uncertainties is desirable such that mission failure, asteroid fragmentation, keyhole passage, etc. due to mischaracterisation of the target body can be avoided; however, in this study, every deflection mission is considered as a feedforward system for simplicity and thus the aleatory uncertainties or randomness of the deflection outcome is not taken into account.

Given the nominal physical properties and the virtual impactor, the mitigation mission can be designed for the desired nominal b-plane deflection. Similarly to the previous sections, an asteroid deflection mission here aims to achieve the nominal deflection of $2\frac{1}{2}\,b_{\oplus}$ on the 2036 b-plane. The nominal physical properties (see Table 10 in Chapter 2) are referred to as the design parameters (asteroid mass, bulk-density, albedo, etc.) in order to determine

the design variables (mitigation system specifications: KI, NI, GT mass, collector size, etc.). Although we could refer to the worst-possible asteroid physical properties (e.g., the upper bound value of uncertain asteroid mass) as the design parameters, such is merely a matter of system margin and does not have any influence on the uncertainty of deflection outcome (i.e., b-plane deflection) as will be shown later in this section. In other words, referring to the nominal physical properties as the design parameters can still help illustrate the effects of the epistemic uncertainties on the deflection outcomes. Care must be taken, however, when interpreting the meaning of the results shown in this section: the results are not particularly useful for efficiency analysis but they are merely for reliability analysis. For example, the GT system used to obtain the results assumed hugely massive GT spacecraft in order to provide the nominal deflection of $2\frac{1}{2}$ $b_{\oplus}$, given the 10-year warning time.

In order to compute the Belief and Plausibility measures of all the possible deflection outcomes, the BPA structures for all the combinations of the asteroid physical characteristics (see Table 4 in Chapter 2) have been referred to once again. The Belief of a b-plane deflection is equal to the sum of the BPAs of all the combinations of the physical properties that totally support the certainty of achieving that specific b-plane deflection distance whereas the Plausibility is the sum of the BPAs of all the combinations of physical properties that totally or partially support the certainty of achieving the same b-plane deflection distance.

Figure 58 shows two examples of Belief and Plausibility changes as a function of b-plane deflection achieved through the KI mission to an arbitrary virtual impactor under the ground-based (i.e., most uncertain) and proximity characterisation scenarios. Belief and Plausibility are represented as solid and dashed lines, respectively. The vertical green line denotes the nominal deflection distance of $2\frac{1}{2}$ $b_{\oplus}$, which is equal to the safe deflection distance b_{safe} (see Subsection 1.3.1 for more details). Figure 58-A) shows that the Belief measure of the nominal deflection (i.e., the chance of $b = b_{safe}$) is about 30-40% whereas the Plausibility measure is about 50-60%. The difference between the two probability measures for a specific deflection of b is that Belief represents the lower bound of the chance achieving that deflection whereas Plausibility represents the upper bound, which is affected by the uncertainty-based information regarding the target body characteristics. Moreover, the possible deflection range is dictated by the characterisation scenario: The more accurate the characterisation information of the target body is, the smaller the possible deflection range will be. Although proximity characterisation may, indeed, allow a substantially better prediction of the deflection outcome, sending a precursor mission would inevitably increase the total mitigation campaign cost.
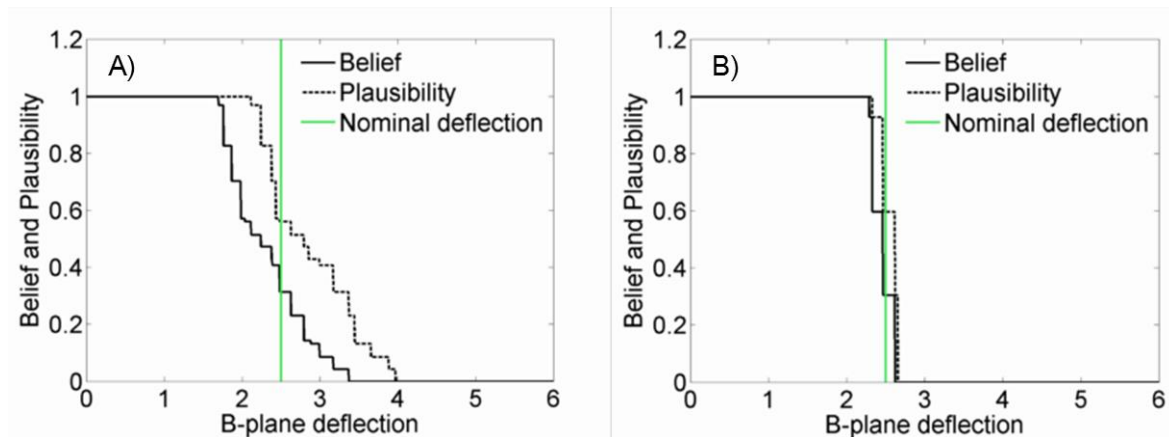
Figure 58 Examples of Belief and Plausibility changes a function of b-plane deflection achieved through the KI mission to an arbitrary virtual impactor under：A) Ground-based (i.e., most uncertain) characterisation scenario. B) Proximity characterisation scenario.

Figures 59 and 60 summarise all the computational results of Belief and Plausibility changes as a function of b-plane deflection achieved through the KI, NI, SC, and GT missions to an arbitrary virtual impactor. The results clearly show that no matter how much literature or engineering judgements one uses, there will always be a gap between Belief and Plausibility as long as there are epistemic uncertainties in preliminary characterisation. The Belief measure is found to be useful particularly for the credibility analysis of deflection missions as it informs the lower bounds of possible outcomes whereas the Plausibility measure informs the upper bounds. If the Belief measure of a b-plane deflection is non-unity, the chance of achieving that deflection is compromised. It appears to be that the differences in the results of the ground-based and space-based characterisation scenarios are very little whereas the results of the proximity characterisation scenario show clear differences in the degrees of uncertainty: these results quantitatively show the significance of the proximity characterisation approach to the deflection mission credibility. Also, the degree of uncertainty (i.e., the shapes of Belief and Plausibility lines) differs according to the physical properties that are related to the given deflection technique and also to the taxonomic class. In other words, each deflection technique has a different degree of uncertainty. For example, due to the substantial amount of epistemic uncertainties in albedo (see Table 11 in Chapter 2), the uncertainty range of b-plane deflection achieved through the SC is considerably wide as seen in Figure 60-C).

As can be seen in Figure 59-A), the results of the KI show that there is no substantial difference between the ground-based and space-based characterisation scenarios in terms of uncertainty in b-plane deflection for any taxonomic classes. The same holds for the results of the NI in Figure 59-B). For the case of the proximity characterisation scenario, the

uncertainty of both KI and NI missions are substantially reduced such that the resultant b-plane deflections are $2\frac{1}{2}$ $b_\oplus$ with uncertainty of ± 0.1-0.2 $b_\oplus$ (see Table 16). Furthermore, deflection efficiency of the KI or NI mission to the M-type asteroid results in smaller uncertainty for any characterisation scenarios, compared with the missions to the other two types. We believe that this is due to the strong correlation between the M-type's bulk-density and the momentum multiplication as well as the fact that the M-type asteroid has the smaller epistemic uncertainties in its microscopic characteristics than the other two (see Table 11 in Chapter 2). However, the amount of information or literature referred to in order to assemble the BPA structures for the M-type asteroid characteristics is least abundant among the three taxonomic classes and therefore the BPA structures are most likely biased. As a final remark on the KI and NI approaches, they have similar levels of uncertainty in deflection outcome even though their deflection efficiency is different. This is because they are both an instantaneous deflection technique and thus share the same fundamental deflection principle. It is obvious that the NI is the most efficient NEA deflection technique in terms of the YTW ratio among the four techniques but can never be the most accurate unless the target body is well-characterised through the proximity characterisation. Such a drawback of the NI may be minor and easily overcome by taking system margin into consideration and adjusting the standoff distance (i.e., trimming deflection leverage) before detonation, after pre-explosion, close observations of the target body by the NI spacecraft, itself.

The SC missions appear to be highly sensitive to the uncertain physical parameters (albedo in particular) as shown in Figure 60-C). Given the proximity characterisation scenario, there is a significant amount of uncertainty in deflection outcome (± 0.35 $b_\oplus$) for any taxonomic classes. As shown in Table 11 in Chapter 2, the uncertainty ranges of the albedo values are greater than any of the other physical parameters while the SC is the only deflection technique that is subject to the albedo of the target asteroid and hence there exists the largest uncertainty ranges in the SC's deflection efficiency among the four techniques.

Figure 60-D) clearly shows the smallest degree of uncertainty in deflection outcomes through the GT mission. These results indicate that the performance of GT is least dependent on the epistemic uncertainties in NEA physical characteristics, particularly on the uncertainty in mass. The reason for this is because the overall deflection efficiency of the GT system is dependent on the NEA mass, canting angle of ion thrusters, standoff distance, and the mission duration. Given the GT mission duration of 10 years and considering only one specific asteroid type, the optimal standoff distance, hence the canting angle of the ion thrusters slightly changes as the asteroid mass increases/decreases from the nominal value

within its uncertain range. The change in the canting angle, in turn, results in the change in the ion thrusters' output for hovering. For example, if the actual asteroid mass is smaller/larger than the nominal value, the standoff distance should be smaller/larger in order to provide the nominal deflection leverage ($F = m_{GT}/R^2$), which affects the canting angle, hence the required ion thrusters' output for hovering. As a consequence, the deflection efficiency does not substantially increase/degrease due to the smaller/larger asteroid mass with respect to the nominal value, but instead, remains alike (compared to the nominal deflection efficiency). However, given a full 10-year tractoring operation, the GT mass required for the nominal deflection of $2\frac{1}{2}\,b_\oplus$ will be too large (>10 tons) to be delivered to the asteroid by means of any currently-available deep space transportation systems. For this reason, the GT technique is more suitable as a secondary deflection mission as backup but cannot be considered as an option of primary deflection mission whose objective is to efficiently provide the nominal deflection in one quick attempt.

Table 16 shows that most of the outcomes of the KI and NI missions can, at least, provide the target asteroid with $b_\oplus$. On the other hand, the Belief of the SC missions under the ground-based and space-based characterisation scenarios are crucially compromised by the epistemic uncertainties such that the resultant b-plane deflections may not even reach $b_\oplus$, hence resulting in mission failure. However, the SC technique is, unlike the KI/NI, controllable throughout its deflection operation: the mission duration may be extended for additional month(s) or make another attempt at subsequent perihelion passage.

Table 16 Lower and upper bounds of 2036 b-plane deflection in $b_\oplus$ for different deflection techniques, characterisation scenarios, and taxonomic classes. A) KI. B) NI. C) SC. D) GT.

A)	S-type	C-type	M-type
Ground-based	1.70-3.97	1.70-4.38	2.05-3.33
Space-based	1.81-3.55	1.83-3.75	2.11-3.11
Proximity	2.29-2.66	2.38-2.61	2.45-2.57

B)	S-type	C-type	M-type
Ground-based	1.71-3.93	1.71-4.32	2.01-3.33
Space-based	1.82-3.52	1.84-3.71	2.11-3.12
Proximity	2.29-2.65	2.34-2.62	2.46-2.57

C)	S-type	C-type	M-type
Ground-based	1.11-5.23	1.60-4.60	1.46-4.54
Space-based	1.34-4.23	1.74-3.90	1.61-3.99
Proximity	2.15-2.85	2.35-2.63	2.35-2.74

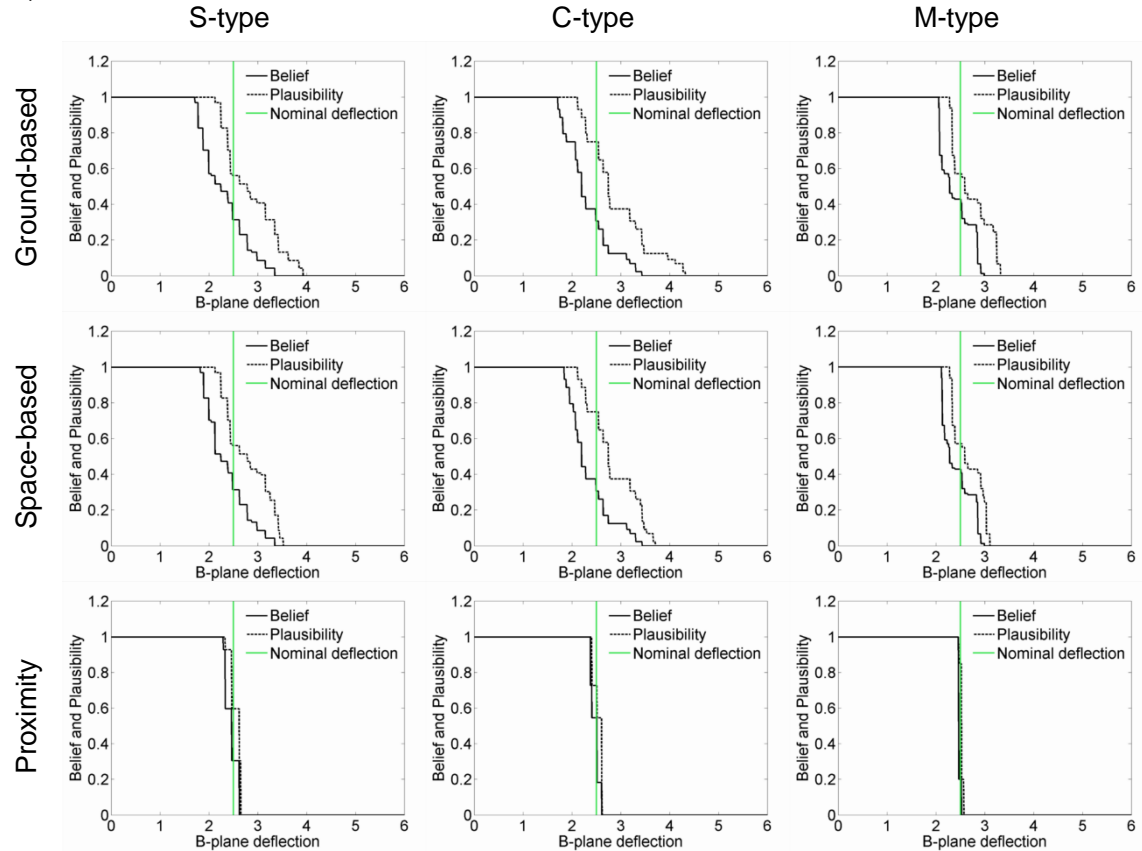| D)	S-type	C-type	M-type
Ground-based	2.32-2.81	2.38-2.85	2.25-2.86
Space-based	2.35-2.79	2.41-2.80	2.29-2.77
Proximity	2.48-2.56	2.49-2.54	2.48-2.54
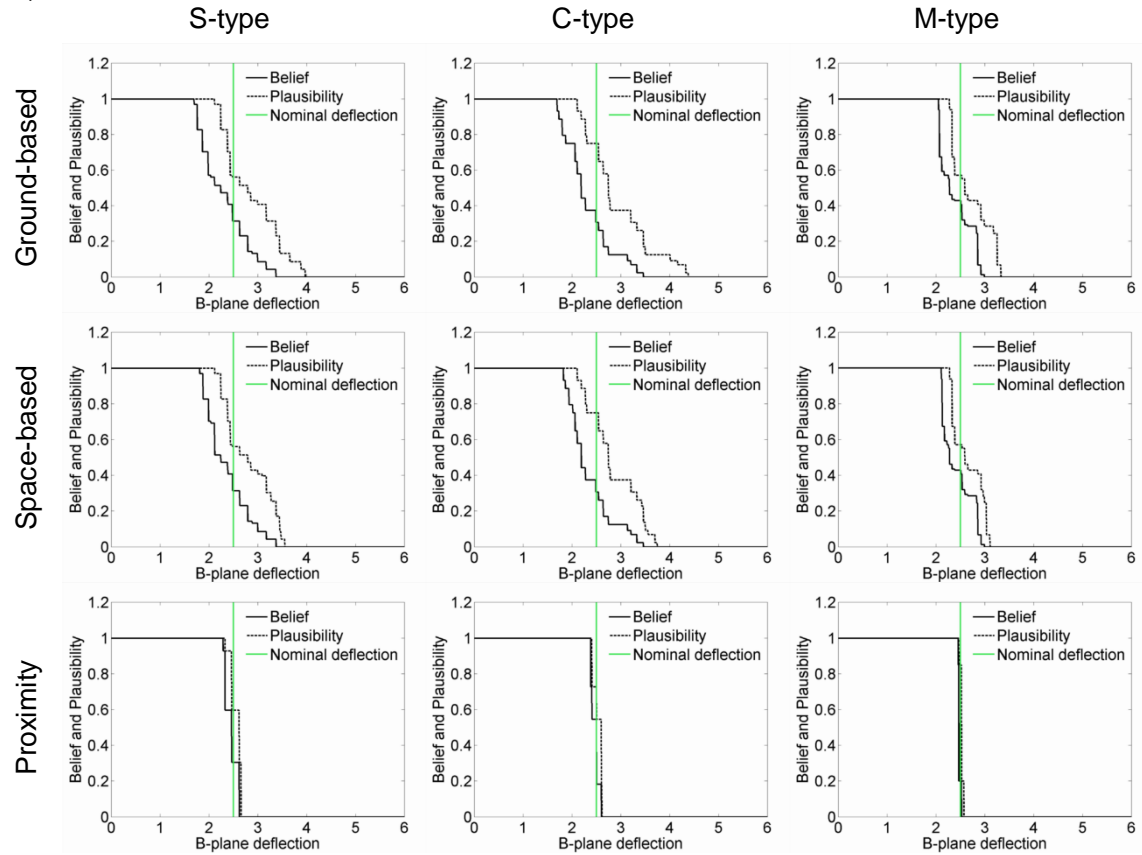
Figure 59 Belief and Plausibility vs. 2036 b-plane deflection in $b_\oplus$ (Earth-radius augmented for gravitational focusing) for different preliminary characterisation scenarios and taxonomic classes. A) KI. B) NI.
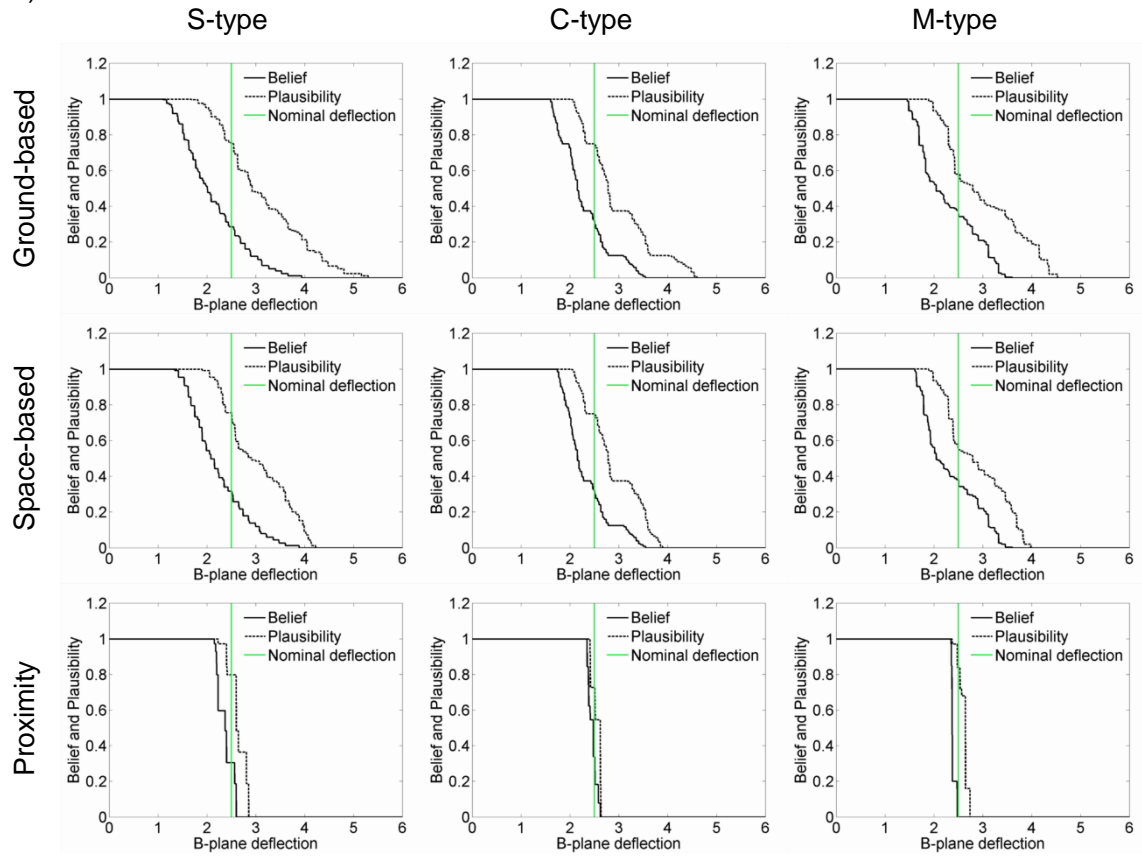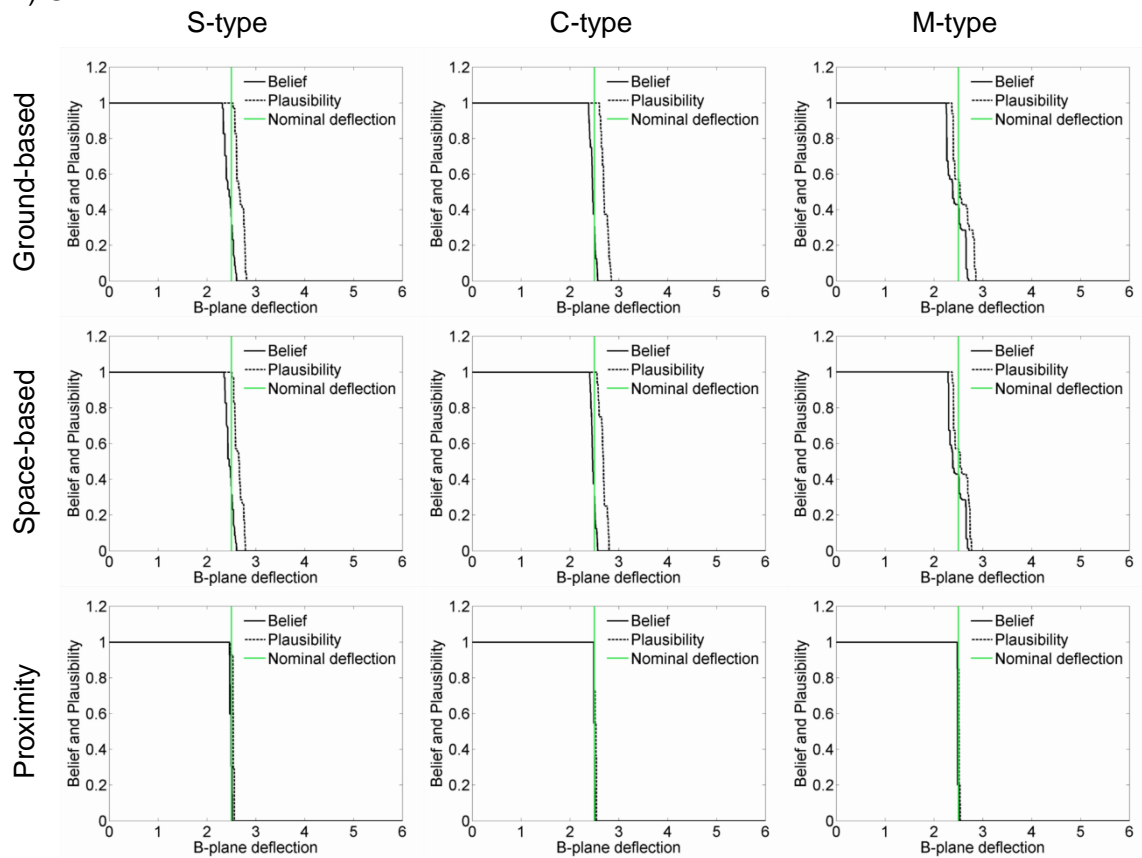
C) SC

D) GT

Figure 60 Belief and Plausibility vs. 2036 b-plane deflection in $b_{\oplus}$ (Earth-radius augmented for gravitational focusing) for different preliminary characterisation scenarios and taxonomic classes. C) SC D) GT.

3.4. Chapter summary

Mathematical models, design, and mitigation system requirements (e.g., system mass) of different deflection missions to VI_1 have been presented in Sections 3.1 and 3.2. Interested readers should refer to Appendix A.2 for the results of the other virtual impactors. In reality, planning of an asteroid deflection mission is not only a matter of required mitigation system mass at the asteroid arrival, and thus to be comprehensively studied as a part of the whole mitigation campaign. For instance, the KI does not have to rendezvous with the asteroid, hence little or no propellant is required at the NEA arrival. However, it needs high impact velocity parallel to the orbit of the asteroid at the interception, preferably near the perihelion while a more massive impactor is also essential to achieving a larger deflection. When the NI is concerned, it appears to be the most efficient deflection technique but there exists political challenges to overcome as it can be misused as a tactical weapon. The SC could be a relatively lightweight technique but its deflection outcome could be highly ambiguous due to the epistemic uncertainties in the asteroid characteristics and, more importantly, it is less efficient or disabled when the asteroid is away from the Sun. Section 3.3 has shown that the outcome of a deflection attempt of any kind will be more predictable if a precursor mission is sent during the early stages of mitigation campaign planning. However, in reality, such case would be rather rare, given today's limited hazardous object detection capability. This situation could be improved as more space telescope missions dedicated to NEO discovery such as the Sentinel mission by B612 are conducted. Finally, the leading reliability of GT missions to NEO has been demonstrated.

4

4. On the effects of NEO inhomogeneity and dynamics

"Make everything as simple as possible, but not simpler."

— Albert Einstein

A series of radar images of NEA 1999 RQ$_{36}$, namely (101955) Bennu, are shown in Figure 61 [125]. (101955) Bennu with a mean diameter of 560 m has potential Earth impact hazards associated with a series of close Earth approaches between 2169 and 2199. If NASA's OSIRIS-REx mission [34] is successful, this asteroid will be the second sub-kilometre near-Earth asteroid ever visited by a spacecraft after asteroid (25143) Itokawa was visited by JAXA's Hayabusa spacecraft. Although further observations will most likely eliminate the probability of Bennu's Earth impact hazards, a recent calculation found that the impact probability of (101955) Bennu on the approach in 2182 is about 1 in 1,000 chance [126]. This is one of the reasons why NASA's spacecraft OSIRIS-REx is to be sent to (101955) Bennu and to evaluate its impact risk by means of close proximity orbit tracking as well as to understand its physical properties by means of sampling return to the Earth. The mission will be launched in September 2016 and is expected to reach (101955) Bennu in October 2019.

The shape model of (101955) Bennu is available from the previous ground-based radar observations; however, Bennu's case is rather rare as a currently known PHO: most of the discovered PHOs are barely characterised for mass, shape, internal structure, etc. Given this limit imposed on our knowledge of the discovered PHOs, an asteroid deflection mission is most likely subject to the incomplete information about not merely the target body's fundamental physical properties (e.g., density, porosity, albedo, etc.) but also its shape and

rotation state (dynamics and geometry) as well as the inhomogeneity of internal density-distribution which may not be well-characterised from Earth.

This chapter will therefore put a particular emphasis on evaluation of the effects of NEO dynamics and inhomogeneity on asteroid deflection attempts and importantly to evaluate these effects on three asteroid deflection missions: the KI, GT, and SC, separately. The first section will focus on the KI mission and the following sections will focus on the GT and SC missions, respectively.
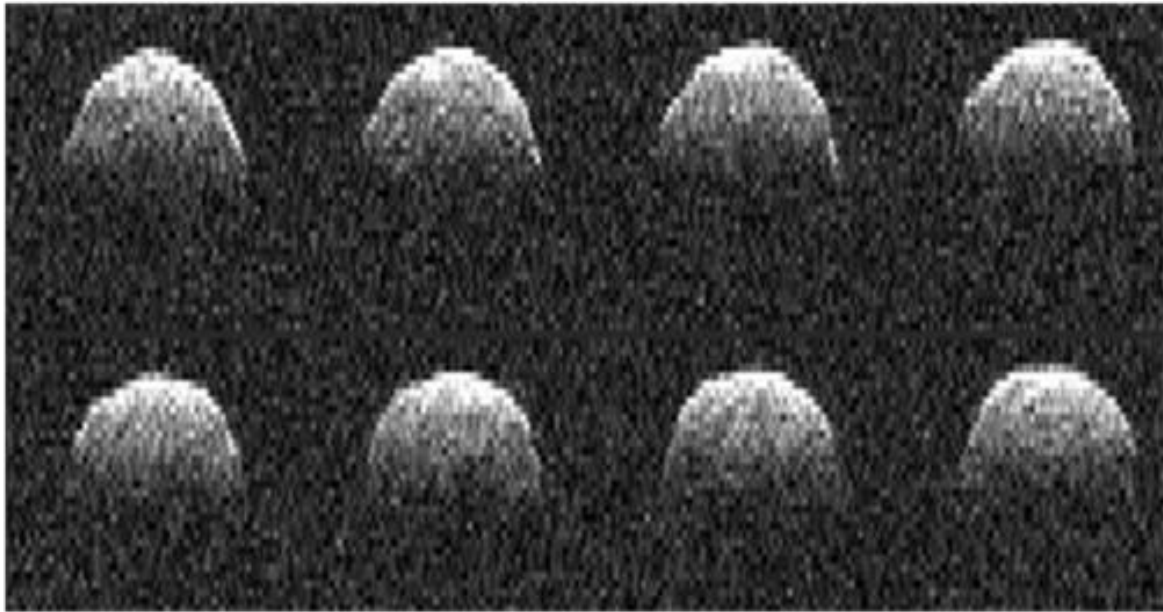

Figure 61 Goldstone radar Images of asteroid (101955) Bennu obtained when it approached close to the Earth in 23 September 1999 [125].

4.1. Effects of NEO inhomogeneity on KI mission

Figure 62 shows the simplified representation of a KI mission to a spherical asteroid with inhomogeneous density distribution. The offset distance between the centre of mass (COM) and centre of figure (COF) of the target asteroid shape projected on the target plane affects to some extent, the deflection efficiency of the KI mission. Hereinafter, we call this offset distance as a "COM offset". It is therefore essential to investigate the influence of the COM offset on the KI's deflection performance.

The KI's outcome is also subject to the precision of the terminal guidance system onboard the KI spacecraft. The CEP (circular error probability or circle of equal probability) [127] is introduced in order to represent the precision of the KI's terminal guidance system. The CEP can be defined as a circular miss distance on the target plane (see Figure 63) within

which 50% of the shots/kinetic impacts fall. In this study, a total of 10 different CEP: $0, 0.1, 0.2, ..., 1.0 \times R_a$ are taken into consideration. The CEP equal to $1.0 R_a$ means that 50% of the kinetic impacts will miss the target spherical body whereas the CEP equal to zero means that 100% of the kinetic impacts will fall on the COF on the target plane.
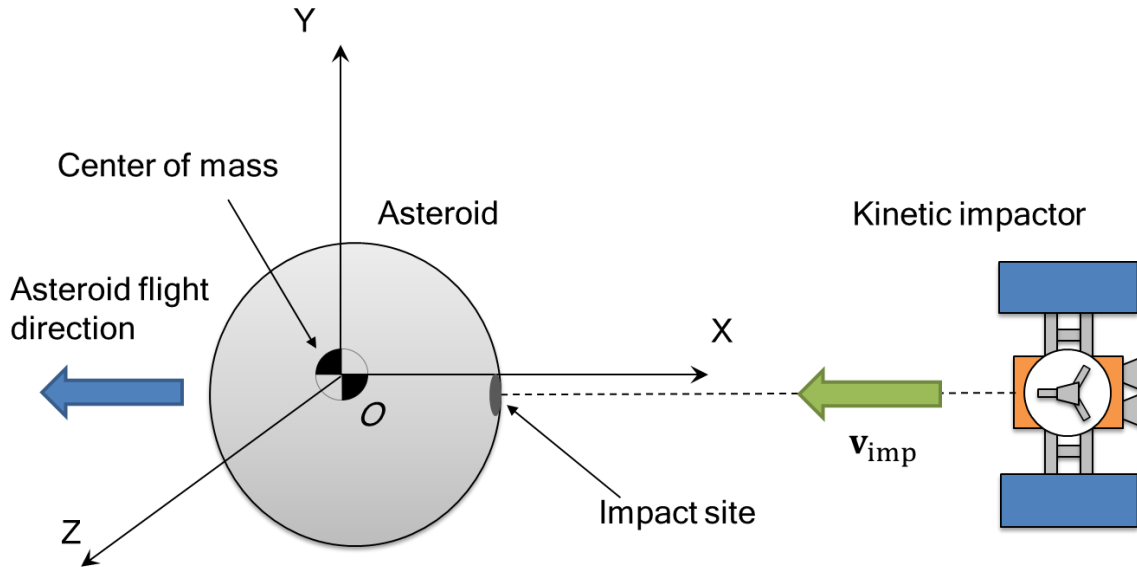

Figure 62 Simplified representation of the KI mission to a spherical asteroid with COM offset. Although the KI's impact velocity vector is parallel to the X-axis, it may not penetrate the COM due to the COM offset from the COF on the target plane (see Figure 63).
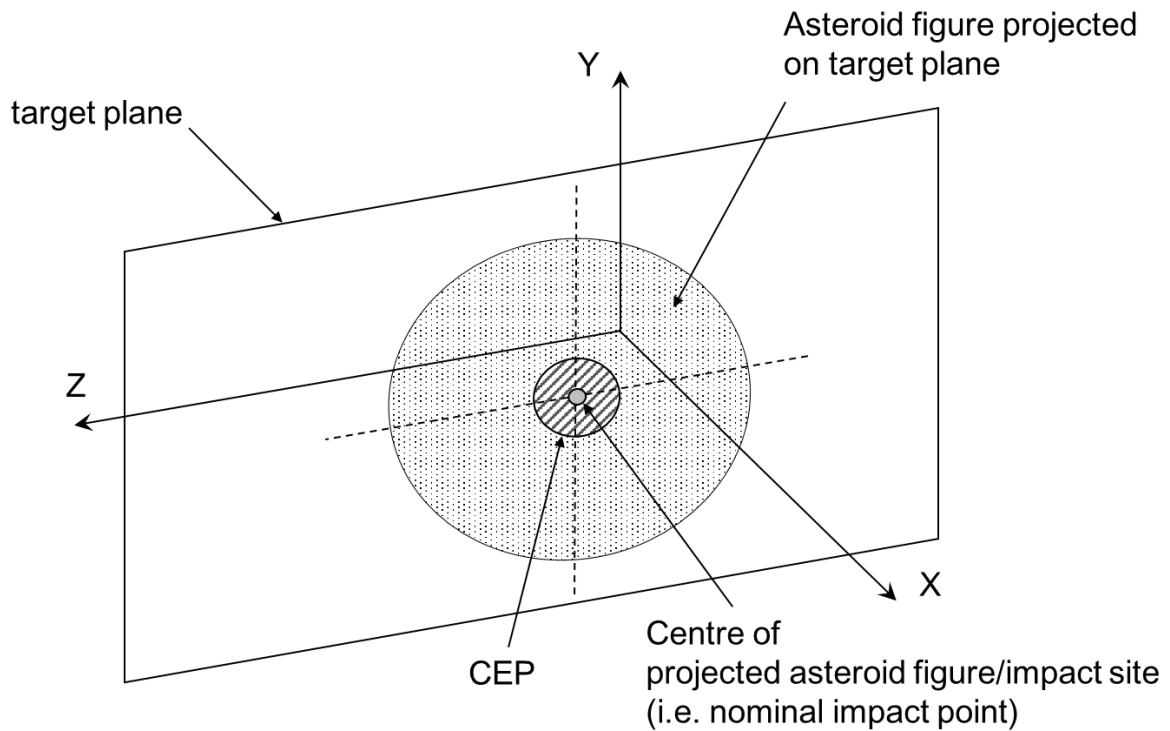

Figure 63 CEP (Circular Error Probability) and the spherical asteroid figure projected on the target plane (i.e. YZ-plane when the KI's impact velocity vector is parallel to the X-axis).

A tetrahedral finite element asteroid model is developed here in order to represent the internal density inhomogeneity of the target asteroid and the COM offset. The 3D surface and volumetric mesh generator for MATLAB/Octave: ISO2MESH 2013 [128] is used to generate the spherical asteroid composed of the total of 22,506 tetrahedral elements of different volumes, of which 2,982 elements are the surface elements. The density of each element is then assigned according to a given density distribution throughout the entire asteroid.

In order to represent COM offset distances of a variety of asteroid internal structures, three different asteroid density distribution models are taken into consideration: the simple homogeneous density distribution model, the inhomogeneous density distribution model, and the inhomogeneous density distribution model with partly different (i.e., metallic) composition.

These distribution models present a denser region of the asteroid, known as the neck region. This higher density region in sub-kilometre asteroids has been confirmed by the Hayabusa mission [129] although Itokawa is non-spherical. In this study, it is assumed that finer grains are accumulated in the neck region due to local gravity variations such that this region is denser than the main body of the asteroid even though the asteroid model is given as a sphere body. The neck region is modelled as a kind of disk with thickness of half the asteroid-radius (e.g., 35 m for the spherical asteroid with 140 m in diameter) and tip tapered according to the spherical surface of the asteroid. The neck region's disk is normal to the Z-axis and its centre exists somewhere between $\pm$ 38.5 m along the Z-axis. The COM of the asteroid therefore mainly shifts in the Z-axis direction. The centre position is randomly determined according to the uniform distribution. This existence of the neck region results in a COM offset that can be as large as $\pm$ 12 m along the Z-axis for the inhomogeneous density distribution model with partly different composition. $\rho_{body} = 2.20$ g/cm^3 and $\rho_{neck} = 2.20, 3.21,$ or 6.49 g/cm^3 (the density distribution type) are randomly assigned to each finite element according to the normal distribution with $3\sigma = 0.80$ g/cm^3. For reference, the COM offset of highly- asteroid (25143) Itokawa was measured to be 14 ± 7 m in terms of minimum distance from the COF and 21 ± 12 m in terms of distance along the x-axis towards Itokawa's head [130].

Due to the differences in density distribution, we can identify three different patterns of gravitational slope of the asteroid. The gravitational slope is the angle between the local gravity vector and the normal to the asteroid surface. Figure 64 shows the gravitational slope

of each density distribution for the 140-m sized spherical asteroid. Figure 64-A) is the simple homogeneous density distribution model, Figure 64-B) is the inhomogeneous density distribution model, and Figure 64-C) is the inhomogeneous density distribution model with partly different (i.e., metallic) composition. In these plots, the redder the surface colour is, the higher the gravitational slope is.

In order to perform a statistical analysis of KI missions to the asteroid with random COM offset for a wide range of CEP between 0-1.0R_a, a Monte-Carlo simulation with the total trial number of 3000 is applied. For each trial, the densities of the finite elements are redistributed according to the selected one of the three aforementioned density distribution models, hence the asteroid mass and the COM offset vary for every trial. Note that the CEP is constant per run so that the simulation must be run 10 times for the different size of CEP. Figure 65 is a simple flow diagram of the integral part of the KI's Monte-Carlo simulation where the mass M_a, COM offset $\mathbf{R}_{\mathrm{COM}}$ with respect to the origin of the asteroid figure O_{COF}, and MOI $\mathbf{I}_a$ of the asteroid are computed in order to derive the deflection by KI. If the CEP is zero, the outcome (i.e., impulsive velocity change) of each KI trial is completely subject to the COM offset and mass of the asteroid.

The impulsive velocity change achieved through the KI mission can be computed by Equation (93)

$$\begin{bmatrix} \Delta v_{\mathrm{X}} \\ \Delta v_{\mathrm{Y}} \\ \Delta v_{\mathrm{Z}} \end{bmatrix} = \beta \frac{m_{\mathrm{KI}}}{(M_a + m_{\mathrm{KI}})} \cdot \hat{\mathbf{r}}_{\mathrm{imp}} \times \mathbf{v}_{\mathrm{imp}} \cdot \hat{\mathbf{r}}_{\mathrm{imp}} \tag{93}$$

where $\hat{\mathbf{r}}_{\mathrm{imp}}$ is the normalised impact point vector of the KI with respect to the COM. If the kinetic impact takes place on the YZ-plane/parallel the X-axis

$$\mathbf{v}_{\mathrm{imp}} = [v_{\mathrm{KI}} \quad 0 \quad 0]^{\mathrm{T}} \tag{94}$$

else if it does on the XY-plane/parallel the Z-axis

$$\mathbf{v}_{\mathrm{imp}} = [0 \quad 0 \quad v_{\mathrm{KI}}]^{\mathrm{T}} \tag{95}$$

where v_{KI} is the KI spacecraft's terminal approach velocity parallel to either X-axis or Z-axis. Here, it is assumed that the KI spacecraft approaches parallel to the flight direction of the asteroid, which yields an optimal deflection outcome.
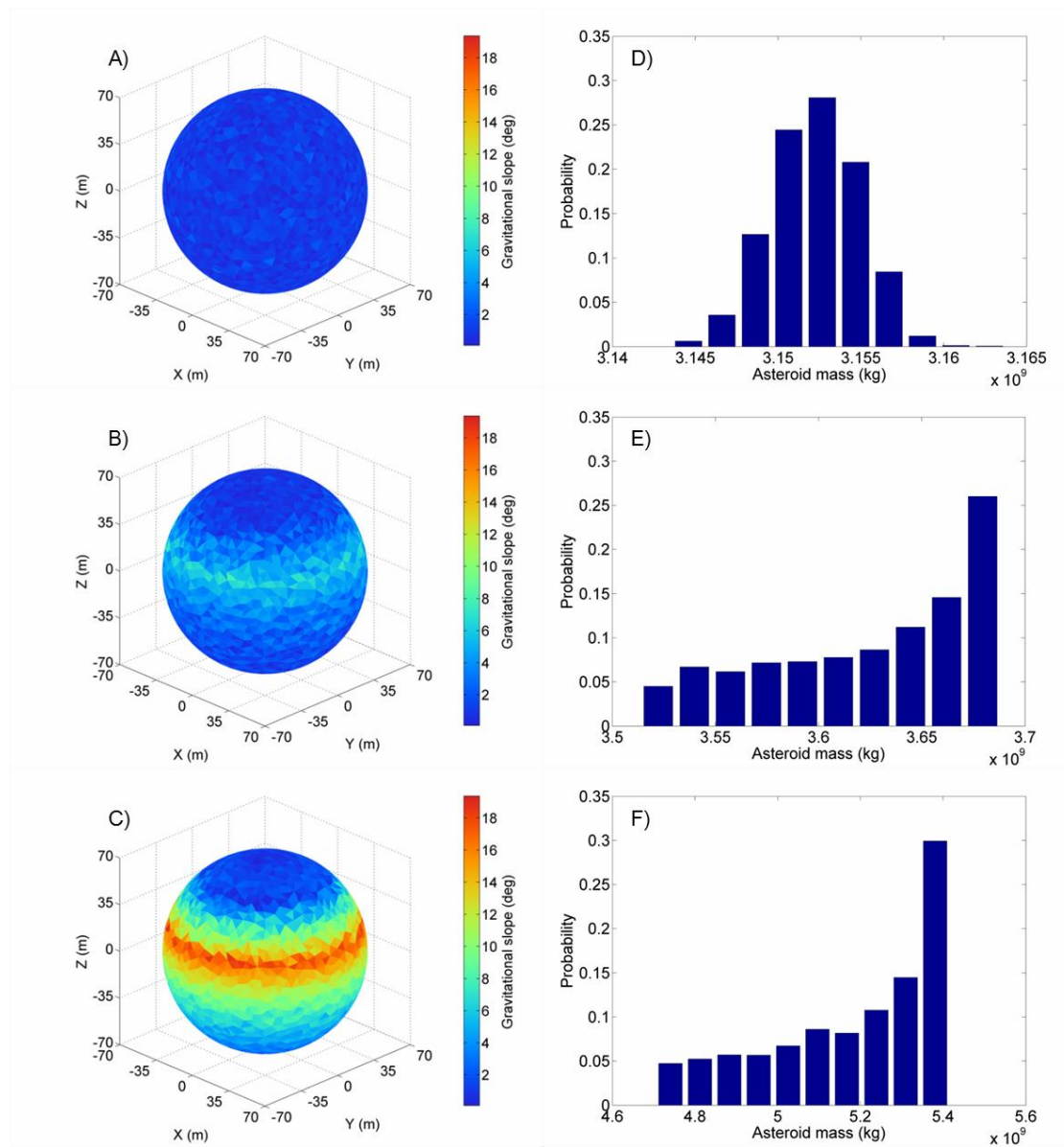

Figure 64 Three different models of spherical asteroid with homogeneous/inhomogeneous density distribution. Examples of gravitational slopes of A) homogeneous S-type model, B) inhomogeneous S-type model, and C) partly metallic (M-type composition in neck region) Inhomogeneous S-type model. D) Asteroid mass and associated probability for model A). E) Asteroid mass and associated probability for model B). F) Asteroid mass and associated probability for model C). E) and F) show that the asteroid mass' probability distributions are not in the form of normal distribution due to the existence of the denser neck region.
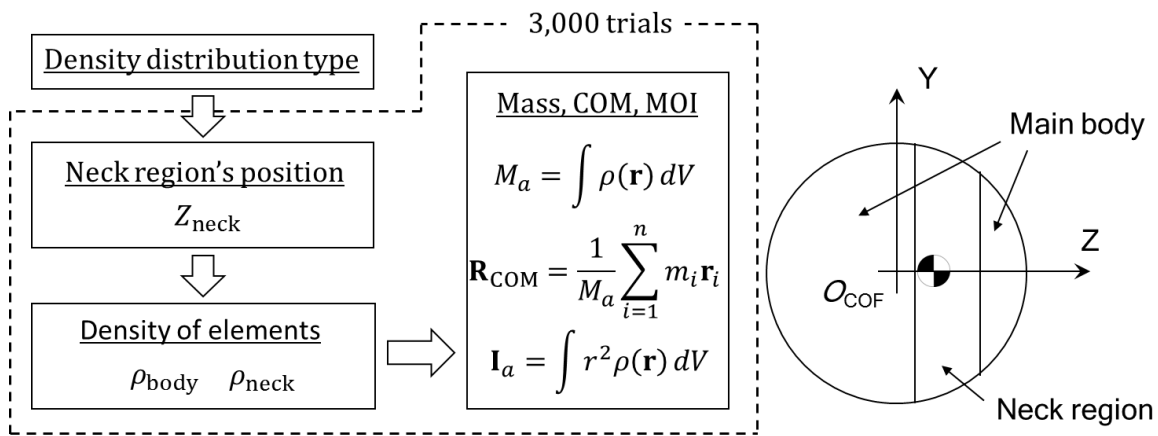
Figure 65 Flow diagram of the Monte-Carlo simulation for KI mission.

4.1.1. Results of Monte-Carlo simulation

Figures 66-68 show the results of the Monte-Carlo simulation of the KI missions to VI_1. The simulation is performed for two different case scenarios: the kinetic impact on the YZ-plane and the XY-plane such that the effect of the COM offset can be evaluated for both best and worst case scenarios. All the results in Figures 66-68 are given in the form of impulsive velocity change components along the three axes: Δv_X, Δv_Y, and Δv_Z with corresponding probabilities. The KI mass m_{KI} is set to 1000 kg and its impact velocity is set to 10 km/s with respect to the COM of the target asteroid. The momentum multiplication β is computed for the density of the specific asteroid finite element that is hit by the KI spacecraft, assuming that the KI spacecraft's bulk density is equal to 3.0 g/cm³. The probability distributions in Figure 67-C) and Figure 68-C) appear to be a bit peculiar but they can be interpreted as the products of the uniform distribution of the neck region's location, the inhomogeneous density, COM offset, and the asteroid mass's non-normal distribution shown in Figure 64-E) and F).

These results clearly indicate that the CEP (i.e., the accuracy of the KI's terminal guidance) basically dictates the KI's outcome: in most cases, the components of the velocity change normal to the impact direction are about three orders of magnitude smaller than that parallel to the impact direction. However, particularly when the CEP is near-zero (implying a highly accurate terminal guidance) and the density distribution is highly inhomogeneous like Figure 64-C), the effect of the COM offset becomes non-negligible as can be seen in Figure 68-G) and H). In some cases, the components of the velocity change normal to the impact direction could be only one order of magnitude smaller than that parallel to the impact

direction (see Figure 67-C) and Figure 68-C)). These results, however may not hold true in the case of a KI mission to an elongated and/or uneven asteroid.

As a final remark of Section 4.1, the angular momentum/velocity of the asteroid will be also affected by kinetic impact. Figure 69 clearly shows that the angular velocity increment through the kinetic impact is greatly affected by the CEP value and can be, at worst, about 4.0×10^{-3} deg/s for the case of the homogeneous asteroid model, which is only one degree of magnitude smaller than the initial angular velocity of the asteroid (2.5×10^{-2} deg/s given a rotation period of 4 hours) shown in Figure 69. Note that the angular velocity increment does not necessarily take place about Z-axis as shown in Figure 69, since the actual kinetic impact point can be anywhere inside the uncertain impact site on the YZ-plane in this case. As model above, the probability distribution of kinetic impact along the radial direction with respect to the COF takes normal distribution whereas that along the tangential direction is uniform. It can be seen that the case of the homogeneous density model (see Figure 69-A)) results in slightly larger angular velocity increment with respect to the cases of the two inhomogeneous density asteroid models (see Figure 69-B) and C)). This is however simply due to the differences in target mass: The less massive the target asteroid is, the faster it can be spun up by kinetic impact. We therefore conclude that the angular momentum change due to the kinetic impact can modify the rotational state of the asteroid while it is greatly subject to the CEP value or the KI's terminal guidance accuracy.

Other than the uncertain COM offset distance, the CEP or the accuracy of a kinetic impact is affected by multiple factors in reality: the precision limit of the terminal guidance system onboard the KI spacecraft, the visible surface region of the asteroid from the KI spacecraft (i.e., phase angle with respect to the sun), etc. The results of this section have shown that the effects of the uncertain COM offset distance could be trivial in most cases but these factors that affect the CEP could dictate outcomes of KI missions in practice.

Furthermore, unexpected events such as dispersal and shape modification of the asteroid due to spin-up of the asteroid may be trigged by a kinetic impact with a substantial offset distance from the COM of the asteroid figure plotted in the target plane. Outcomes of a kinetic impact near the very edge of the asteroid is also unknown. For instance, it could shave off a part of the target body rather than spinning up it and, more importantly, result in a smaller linear momentum transfer than expected.
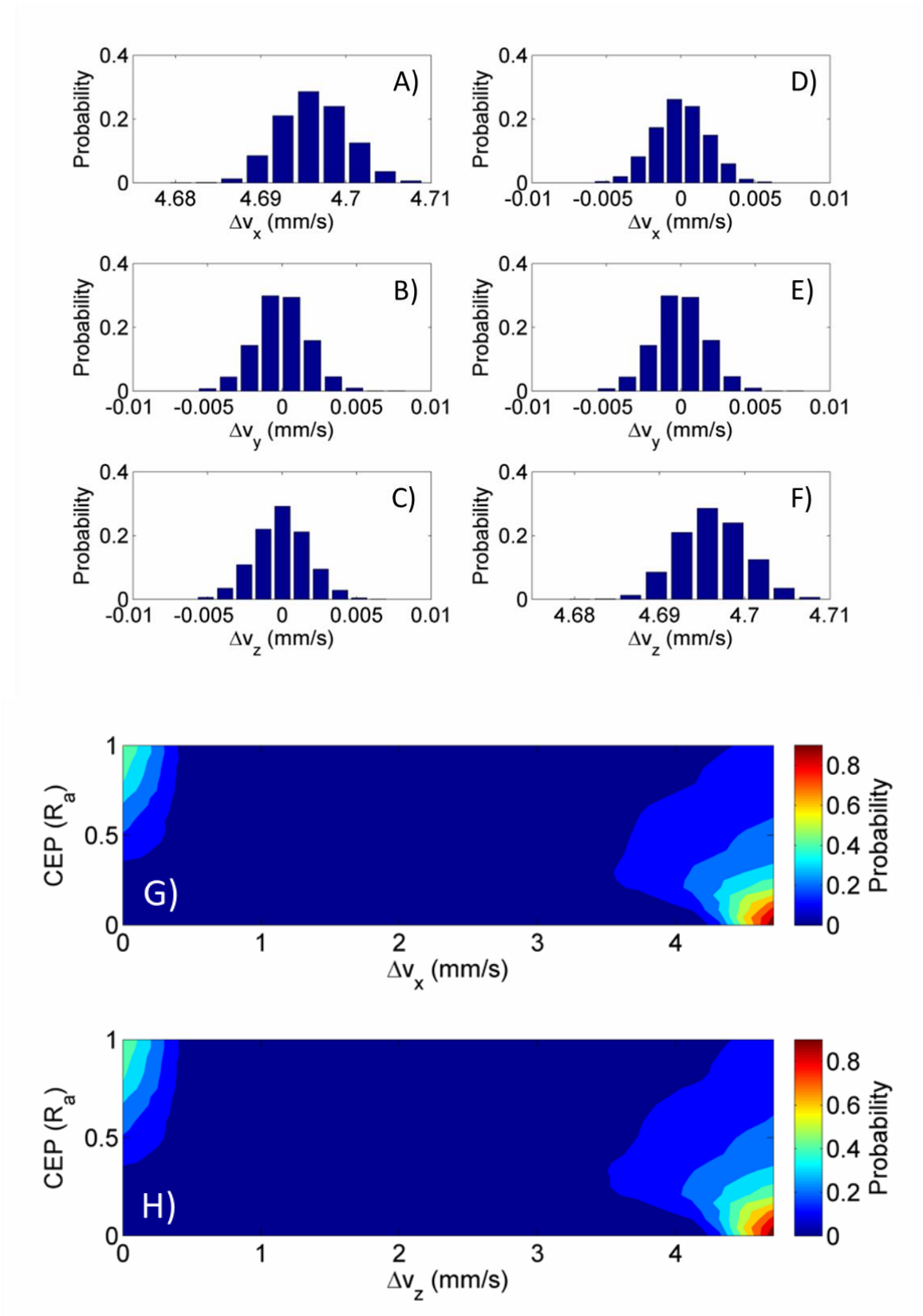
Figure 66 Instantaneous velocity changes A) Δv_X, B) Δv_Y, and C) Δv_Z achieved through the kinetic impact on YZ-plane with CEP=0. D) Δv_X, E) Δv_Y, and F) Δv_Z are the results of the kinetic impact on XY-plane with CEP=0. The target asteroid's density is based on the homogeneously distributed model. G) and H) show the instantaneous velocity changes along X and Z axes for the YZ-plane and XY-plane impact scenarios as a function of CEP, respectively.

Figure 67 Instantaneous velocity changes A) Δv_X, **B)** Δv_Y, **and C)** Δv_Z **achieved through the kinetic impact on YZ-plane with CEP=0. D)** Δv_X, **E)** Δv_Y, **and F)** Δv_Z **are the results of the kinetic impact on XY-plane with CEP=0. The target asteroid's density is based on the inhomogeneously distributed model. G) and H) show the instantaneous velocity changes along X and Z axes for the YZ-plane and XY-plane impact scenarios as a function of CEP, respectively.**
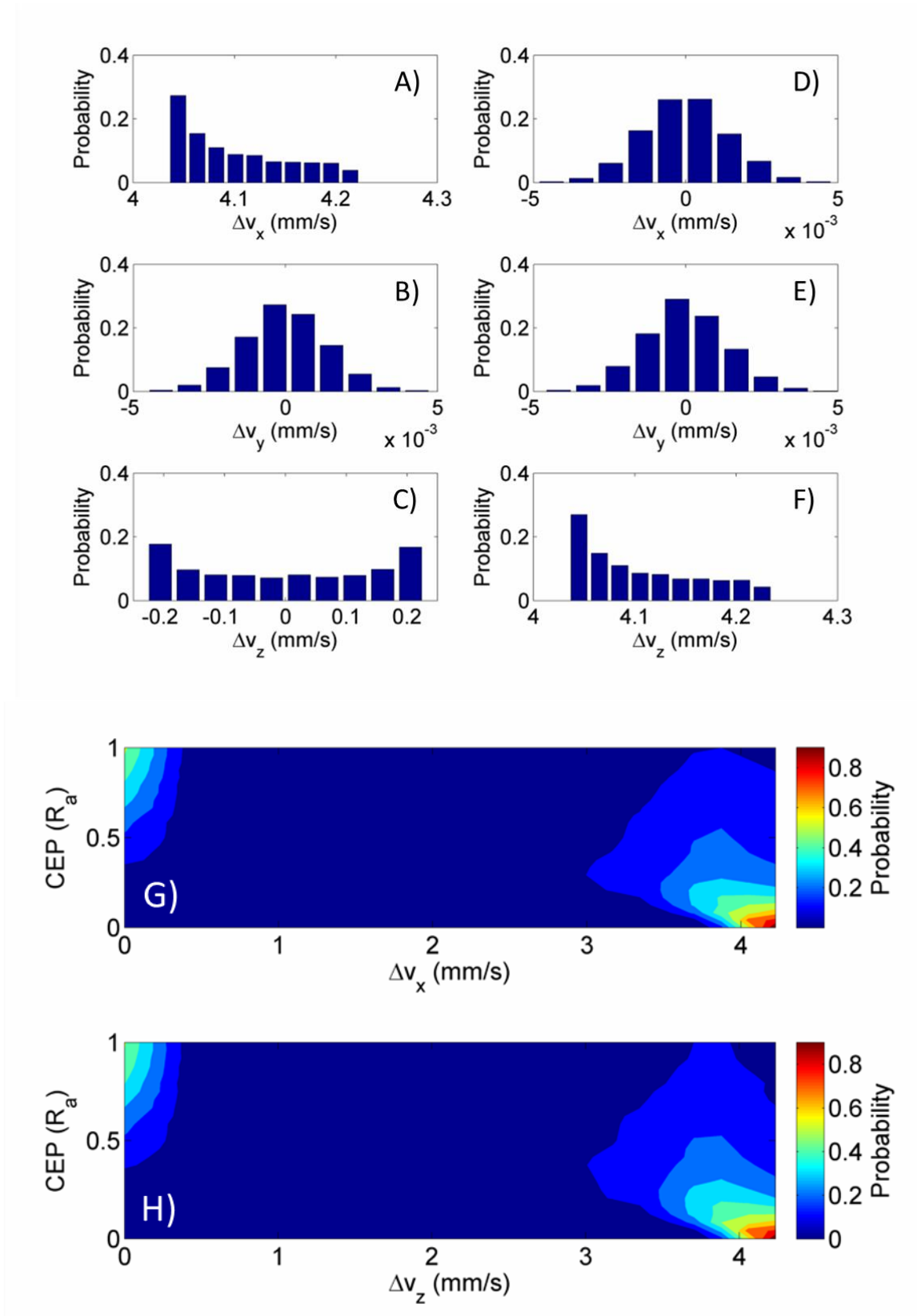
Figure 68 Instantaneous velocity changes A) Δv_X, **B)** Δv_Y, **and C)** Δv_Z **achieved through the kinetic impact on YZ-plane with CEP=0. D)** Δv_X, **E)** Δv_Y, **and F)** Δv_Z **are the results of the kinetic impact on XY-plane with CEP=0. The target asteroid's density is based on the inhomogeneously distributed model with partly metallic composition. G) and H) show the instantaneous velocity changes along X and Z axes for the YZ-plane and XY-plane impact scenarios as a function of CEP, respectively.**
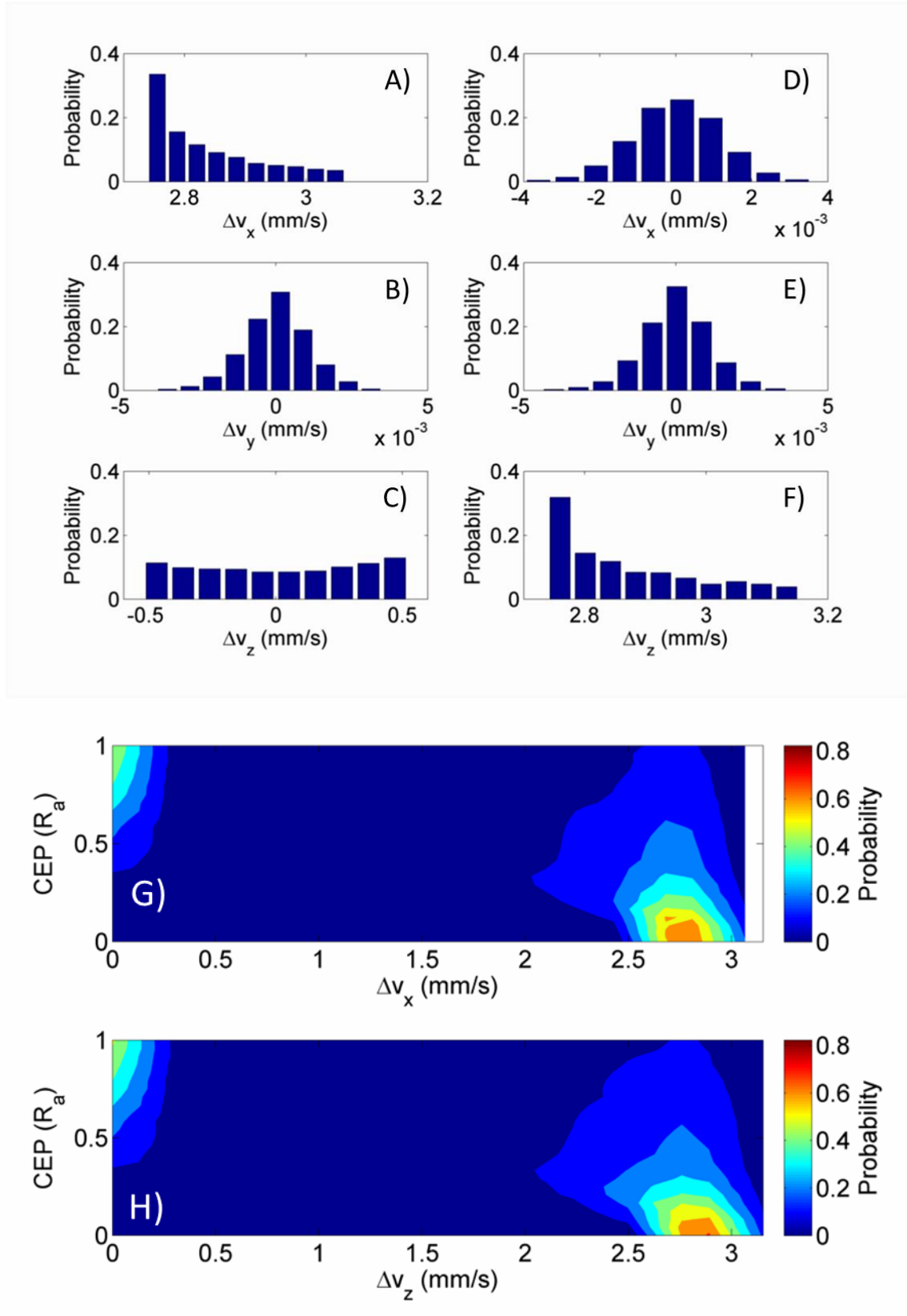
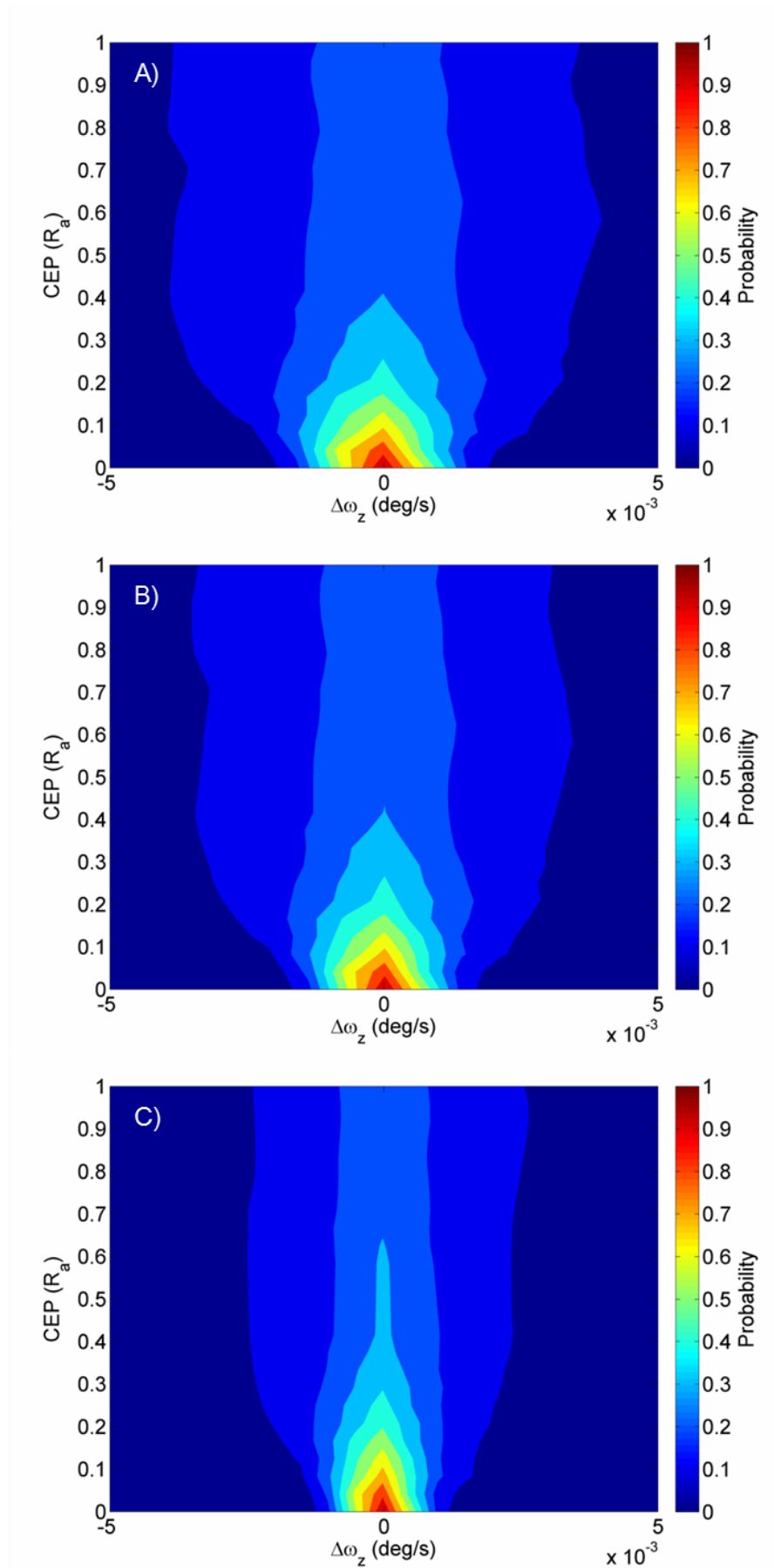**Figure 69 Angular velocity increment $\Delta\omega_z$ about the Z-axis due to the kinetic impact parallel to the X-axis on the asteroid rotating once every 4 hours (i.e., at 2.5×10^{-2} deg/s) about the Z-axis. A) Homogeneous density distribution model. B) Inhomogeneous density distribution model. C) Inhomogeneous density distribution model with partly different (i.e., metallic) composition.**

4.2. Effects of irregularly-shaped asteroid on GT mission

In this section, the effects of irregularly-shaped/elongated asteroid on GT spacecraft dynamics during its tractoring operation are investigated. A GT mission simply makes use of the gravitational interaction between the target body and the spacecraft hovering in proximity to it. Although accurate determination of the fundamental asteroid characteristics is prerequisite to mitigation system design including GT spacecraft, our knowledge of them during the early stages of mitigation campaign planning could be highly ambiguous due to the limits imposed on the preliminary characterisation opportunities and capability as pointed out in the previous work by Sugimoto *et al.* [56]. Due to this simple deflection mechanism, the GT mission is likely less sensitive to the epistemic uncertainties in the fundamental asteroid characteristics (e.g., bulk-density, volume, porosity, etc.) as shown in Chapter 3.

Recent work by Sugimoto *et al.* has quantitatively demonstrated the certainty of the GT's deflection outcome which stands out from the other deflection techniques studied here [57]. However, this does not mean that the GT approach is superior to the others in any case. The deflection efficiency of the GT (i.e., deflection yield to mass ratio) is the lowest among the deflection approaches under analysis. Moreover, although it may seem that the GT spacecraft is free from the influence of the asteroid physical/geometric features apart from the mass, the GT spacecraft will inevitably experience perturbation motions due to the non-uniformity of the asteroid gravity field due to the combination of its spin state and irregular shape. In theory, the closer to the asteroid the GT spacecraft is, the larger the gravitational pull but also the perturbation motions will be and therefore it is indispensable to evaluated the effect of asteroid inhomogeneous gravity on the GT spacecraft. For reference, the influence of the solar radiation pressure (SRP) is also taken into consideration in this section as another cause of perturbations of the GT spacecraft in space.

The shape of VI_1 is based on the shape model of asteroid (433) Eros. The gravitational field of VI_1 is computed through the spherical harmonics expansions of Eros' shape model which is scaled to the equivalent diameter of 140 m, assuming that its bulk density is identical to that of Eros (2.67 g/cm^3) [131]. VI_1 is therefore a highly elongated S-type asteroid with an axial ratios of 3:1:1 (286m: 93m: 93m) and its gravitational field is inhomogeneous as shown in Figure 70. The stationary part of the asteroid's gravitational potential U at any point $P(r, \varphi, \lambda)$ on and above the asteroid's surface is conveniently expressed on a global scale by summing up over degree and order of a spherical harmonic

expansion. The spherical harmonic coefficients represent, in the spectral domain, the global structure and irregularities of the gravitational potential field or of the gravitational field of the asteroid. The equation relating the spatial and spectral domain of the gravitational potential U is given by Equation (96)

$$U(r, \varphi, \lambda) = \frac{GM_a}{r}\left[\bar{C}_{00} + \left(\frac{R}{r}\right)^l \sum_{l=1}^{l_{max}} \sum_{m=0}^{l} \bar{P}_{lm}(sin\varphi)(\bar{C}_{lm}cosm\lambda + \bar{S}_{lm}sinm\lambda)\right] \quad (96)$$

where r, φ, and λ are spherical asteroid-centric/asteroid body coordinates of the computation point: radius, latitude, and longitude, respectively. R is the reference length or the mean semi-major axis of the asteroid (e.g. 133 m for 140-m sized asteroid). $GM_a = 2.56 \times 10^{-10}$ km^3/s^2 is Newton's gravitational constant multiplied by the mass of the asteroid. l and m represent degree and order of the spherical harmonic. The size of the model is 15×15 (i.e. $l = m = 15$). $\bar{P}_{lm}$ are the fully normalised Legendre functions. $\bar{C}_{lm}$ and $\bar{S}_{lm}$ are the spherical harmonic coefficients of the asteroid. Finally, the $\bar{C}_{00}$-term is close to 1 and scales the value GM_a. All the values of normalised spherical harmonic coefficients of the reference shape model of asteroid (433) Eros are available in Appendix A.3.

It is assumed that VI$_1$ will make a close Earth encounter on 13 April 2036 in a similar way as the hazard scenario considered in the previous chapters; however, the encounter here is just an Earth flyby event rather than an Earth impact event. Although VI$_1$ does not pose an Earth impact risk on 13 April 2036, there is a non-negligible chance of keyhole passage that will put it on a subsequent Earth impact trajectory. The objective of a hazard mitigation mission here is therefore to manipulate the orbit of VI$_1$ and place it in a safe spot (i.e., safe harbour) on the 2036 b-plane, given a 10-year warning time from the earliest time of mission commencement of 13 April 2026 till the Earth encounter epoch of 13 April 2036. We also assume that there is no uncertainty in pre-deflection and post-deflection orbital determination of VI$_1$ although there will be inevitably a certain amount of uncertainty in reality. This is because the accuracy of small body orbital determination is limited by the available observation opportunities and methodologies, which are out of the scope of this thesis. In general, it can be very ambiguous, leaving an uncertainty ellipse on the b-plane with semi-major axis of several hundred kilometres, even if tracking of the spacecraft in proximity to the target body is available according to the JPL's report on the GT mission analysis in 2008 [49].
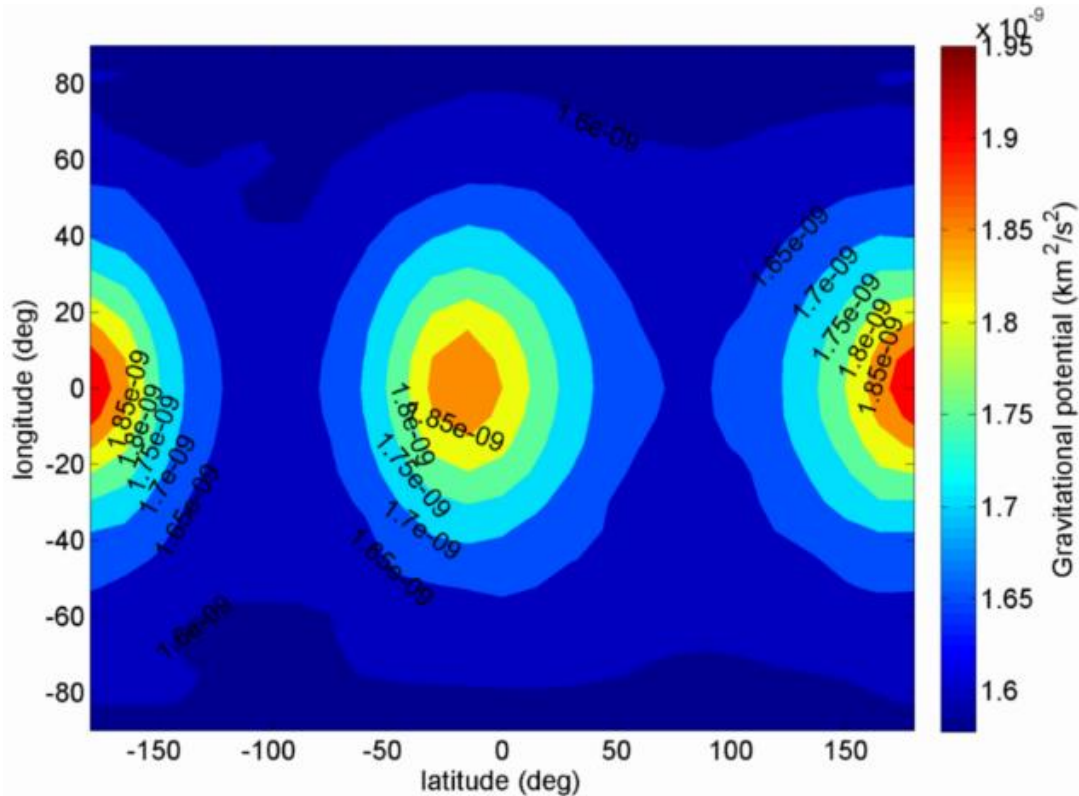
Figure 70 Gravitational potential mapped on a 153-m radius sphere that circumscribe the entire figure of VI$_1$. The horizontal and vertical axes represents the latitude and longitude of each point on the 153-m radius sphere, respectively. There are two regions where the gravitational potential is high (shown in redder colour). These regions correspond the protruding parts of the elongated asteroid.

4.2.1. Modelling of GT mission to irregularly-shaped asteroid

Figure 71 shows a simplified representation of the GT mission to an elongated asteroid. The coordinate system is defined such that the X-axis is always parallel to the flight/orbital direction of the asteroid, the Y-axis is perpendicular to the flight direction on the orbital plane, and the Z-axis (the rotational axis of the asteroid) completes the right-handed coordinate system. Similar to the original concept proposed by Lu and Love [41], the GT spacecraft has a set of ion thrusters equipped on one side of it facing the target asteroid. Each one of these ion thrusters must be canted such that the ion exhaust does not impinge on the asteroid surface. In order to minimise this canting angle φ and maximise the component of the thrust parallel to the gravitational force at given altitude H (distance between the GT spacecraft and the nearest asteroid surface as shown in Figure 71), a tri-axial ellipsoid that circumscribes the rotating target asteroid's baseline shape must be taken into consideration. Assuming that the asteroid is rotating around the Z-axis, the size of this ellipsoid is given by 143m: 143m: 47m and therefore the ion thrusters are canted on the XY plane/along the Z-axis. The divergence angle of ion beam ϕ must be also taken into account. Here, ϕ is

assumed to be 15 degrees according to the divergence angle of the flight-qualified ion thrusters: XIES onboard ETS-VI [120].
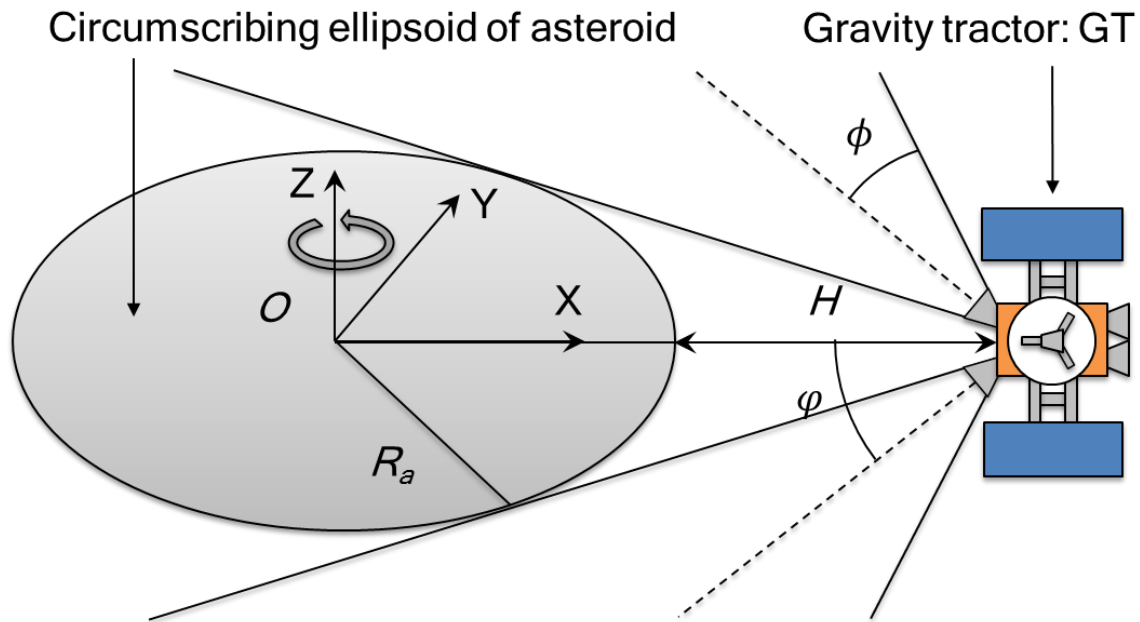

Figure 71 Simplified representation of GT mission to an irregularly-shaped asteroid.

4.2.2. Gravity and SRP about irregularly-shaped asteroid

There are two sources of perturbation that affect a hovering GT spacecraft in proximity to the asteroid: the asteroid gravity and the SRP. Figure 72 shows the gravity change over one asteroid rotation, given a rotational period of 4 hours. Figure 73 shows the SRP change as a function of the orbital time the heliocentric distance of the asteroid. The SRP on the GT spacecraft is here computed by reference to $C_R = 1.28$ which is the estimate of the SRP coefficient of the Hayabusa spacecraft [132]. The equation of motion of the GT spacecraft in proximity of the asteroid is given by Equation (97).

$$m_{GT} \cdot \mathbf{a} = \mathbf{F}_g + \mathbf{F}_{SRP} \tag{97}$$

where the asteroid gravity force $\mathbf{F}_g$ and the SRP $\mathbf{F}_{SRP}$ acting on the GT spacecraft are given by Equations (98) and (99), respectively.

$$\mathbf{F}_g = m_{GT} \frac{U}{\|\mathbf{r}\|} \cdot \hat{\mathbf{r}} \tag{98}$$

$$\mathbf{F}_{SRP} = P_{SRP} \cdot A_R \cdot C_R \cdot \hat{\mathbf{R}}_{GT-\odot} \tag{99}$$

$P_{SRP} = 4.56 \times 10^{-6} \cdot \left\| \mathbf{R}_{GT-\odot} \right\|^2$ N/m² is the solar radiation pressure at a given heliocentric distance $\mathbf{R}_{GT-\odot}$ in astronomical unit, $A_R = 25.28$ m² is the reference surface of the GT spacecraft that is facing the Sun direction, and $\widehat{\mathbf{R}}_{GT-\odot}$ is the normalised heliocentric distance vector of the GT spacecraft. A_R of 1000-kg GT spacecraft is given by scaling A_R of the 500-kg Hayabusa spacecraft [132].
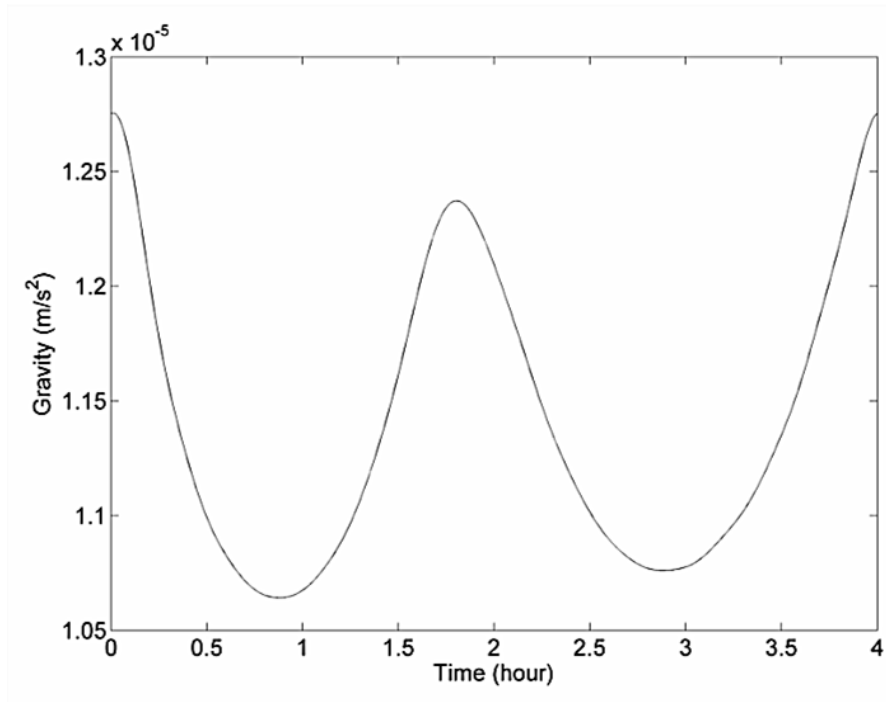

Figure 72 Gravity change over one asteroid rotation, given X= 153 m (i.e., *H*=10 m) and Y=Z=0.
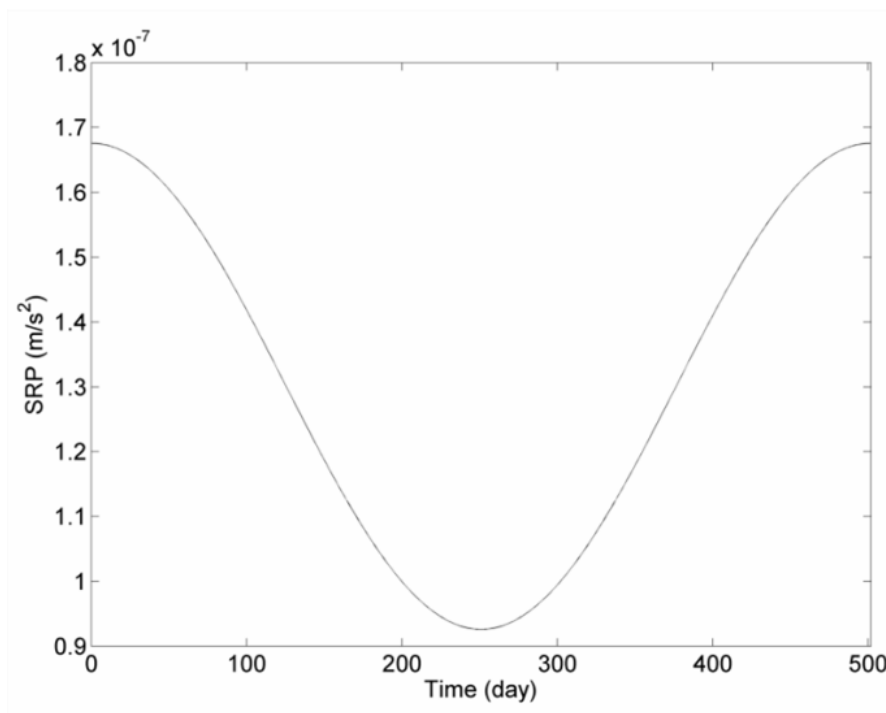

Figure 73 Acceleration change due to the SRP over one asteroid orbit of about 500 days.

Both the asteroid gravity and the acceleration due to the SRP change with time; however, the acceleration due to the SRP is 2-3 orders of magnitude smaller than the gravitational acceleration and therefore almost negligible as long as the GT spacecraft hovers in close proximity (e.g., 10 m or so in altitude) to the target body. Hovering at such a small altitude may however cause instability and collisional risk of the GT spacecraft.

Previous work by Broschart and Scheeres [123] has found out that, for the case of inertial hovering about a misshapen object, there exists instability in the radial direction while the transverse directions are always stable. The perturbation along transverse directions is 2-3 degrees of magnitude smaller than the asteroid gravity (see Figures 72 and 73) and so can be most likely counteracted with scheduled attitude control of the spacecraft with onboard ion/chemical (e.g., hydrazine) thrusters. On the other hand, the perturbation along the radial direction must be counteracted by adjusting the thrust level of the ion thrusters onboard the GT spacecraft as it hovers above the rotating irregularly-shaped asteroid. The thrust component parallel to the gravitational pull is assumed to be always equal to the fluctuating gravity throughout the tractoring operation in this study although such a continuous thrust control may not be realistic. However, since this study does not put an emphasis on the spacecraft dynamics, guidance and control, further detailed analysis of the perturbation motions are omitted here.

Figure 74 shows the deflection efficiency of the 1000-kg single GT as a function of the tractoring duration (1-10 years) and the stand-off distance of the GT spacecraft measured from the COM of the asteroid. It can be seen that a higher b-plane deflection is attainable with longer tractoring duration and, more importantly, a hovering altitude of about 10-20 m results in an optimal deflection. Although hovering at this altitude may not be technically challenging, as flight-proven by the Hayabusa mission [124], it might not be desirable from a mission safety point of view. In fact, if something goes wrong with the GT spacecraft (e.g., trouble with ion engines, momentum wheels, etc.) during the tractoring operation, it is most likely to collide with the asteroid and the asteroid deflection mission by GT will be compromised particularly when there is only one GT spacecraft sent to the target hazardous asteroid. It is therefore recommendable to design more redundant mission concepts of the GT deflection approach, however which is out of scope of this doctoral thesis.
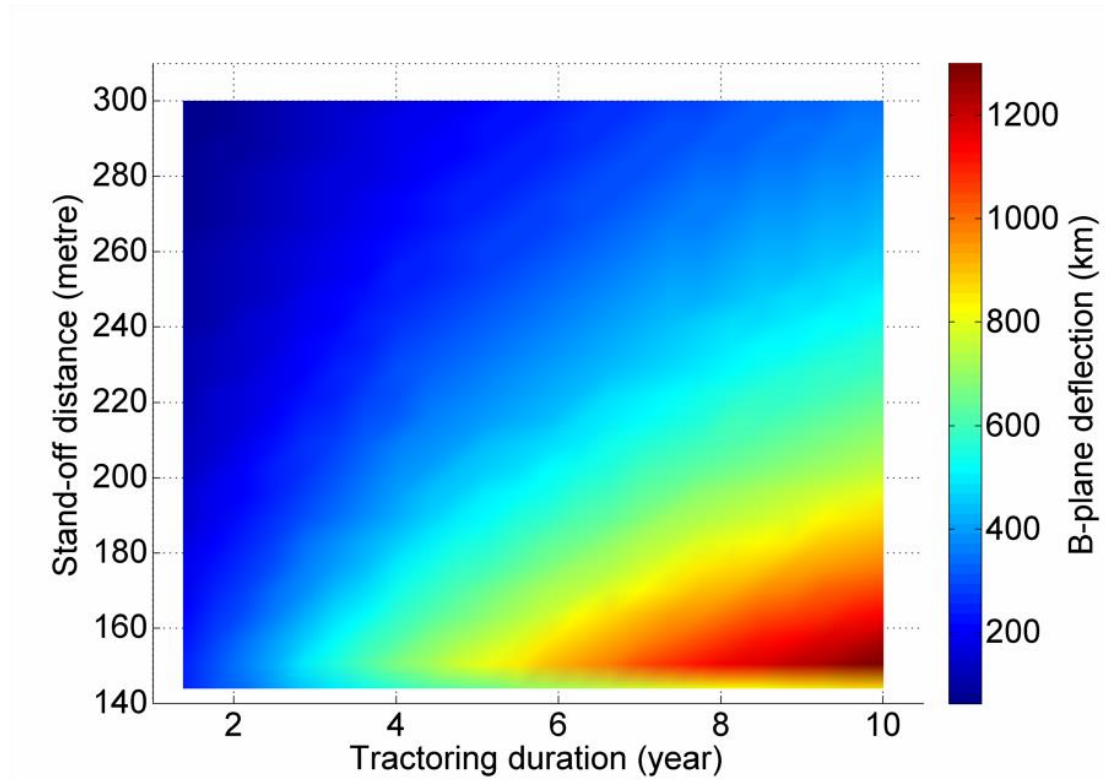
Figure 74 Deflection efficiency as a function of the tractoring duration and the stand-off distance (measured from the asteroid COM) for single 1000-kg GT mission. There are a specific stand-off distance where the deflection is maximised. However, when the optimal stand-off distance is concerned, the GT spacecraft has to hover about 10 m above the asteroid's protruding region, which may substantially compromise the safety of the operation over the long-term GT mission duration.

4.3. Effects of rotation and shape on SC mission

Here, the deflection efficiency of the SC mission is briefly evaluated as a function of asteroid shape and rotation, where an ellipsoidal asteroid body with equivalent diameter of 140 m, eccentricity of 0-0.9, and the rotational period of 0-2.0 hours are assumed. Figure 75-A) is a simplified representation of the SC mission to the ellipsoidal asteroid. Figure 75-B) illustrates the solar beam from the SC illuminating the asteroid surface, the rock jet normal to the surface, and the angle θ between them. Assuming that the asteroid is rotating around the Z-axis, the deflection force at a given moment is given as $T\cos\theta$, where T is the thrust force applied to the asteroid by rock jet. T can be computed by reference to the SC model previously defined in Chapter 3, which is, importantly, dependent on the rotational velocity. The total deflection applied to the asteroid by the SC mission can be obtained through the numerical integration over the SC mission duration (e.g. 30 days). Note that, in this specific study, the efficiency of the SC assembly (collector's reflectivity) that has been also discussed previously is not taken into account as a part of SC deflection efficiency. This means that the

efficiency here is literally given as a function of the eccentricity and the rotational period of the ellipsoidal asteroid.
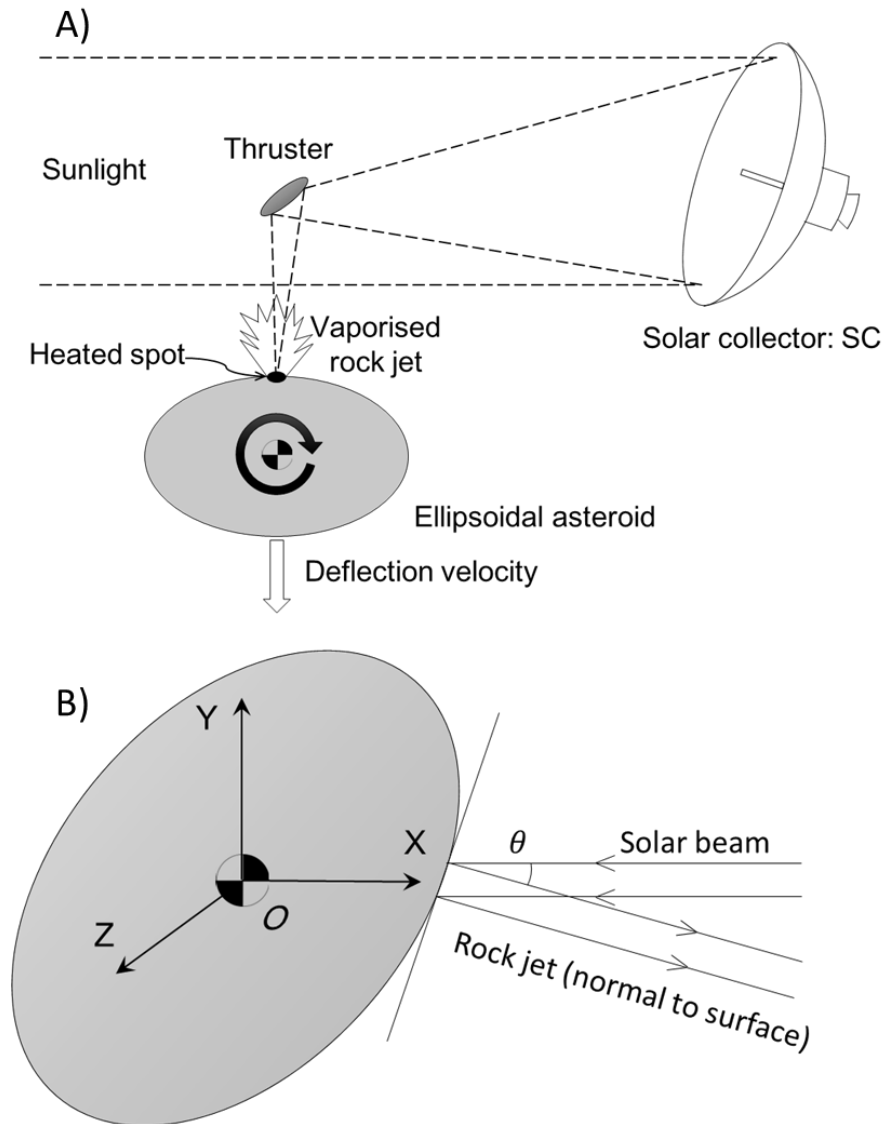

Figure 75 SC mission to an ellipsoidal asteroid. A) Simplified representation of the mission. B) The solar beam from the SC illuminating the asteroid surface, the rock jet normal to the surface, and the angle θ between them. Note that this model does not take the surface roughness into account.

Figure 76 shows the results of numerical analyses of the SC deflection efficiency for three different asteroid types: A) S-type, B) C-type, and C) M-type. The efficiency is given in the form of normalised deflection efficiency with respect to the maximum deflection efficiency (=1.0) which is achievable when the eccentricity is zero and the rotational period is 120 min for each asteroid type. For this reason, the results cannot be used for a comparison analysis of the efficiency of three cases. As can be seen, the deflection efficiency of SC missions drops down to <50% with the rotational period of <60 min for S-type, <10 min for C-type, and <100 min for M-type whereas it shows a gradual fall as a function of the

eccentricity from 0.4 to 0.9 and a sudden fall with the eccentricity of >0.9. Regarding the asteroid type, the SC mission to C-type is the most insensitive to the rotational period, followed by those to S-type and M-type in order, which agrees with the results in Chapter 3.
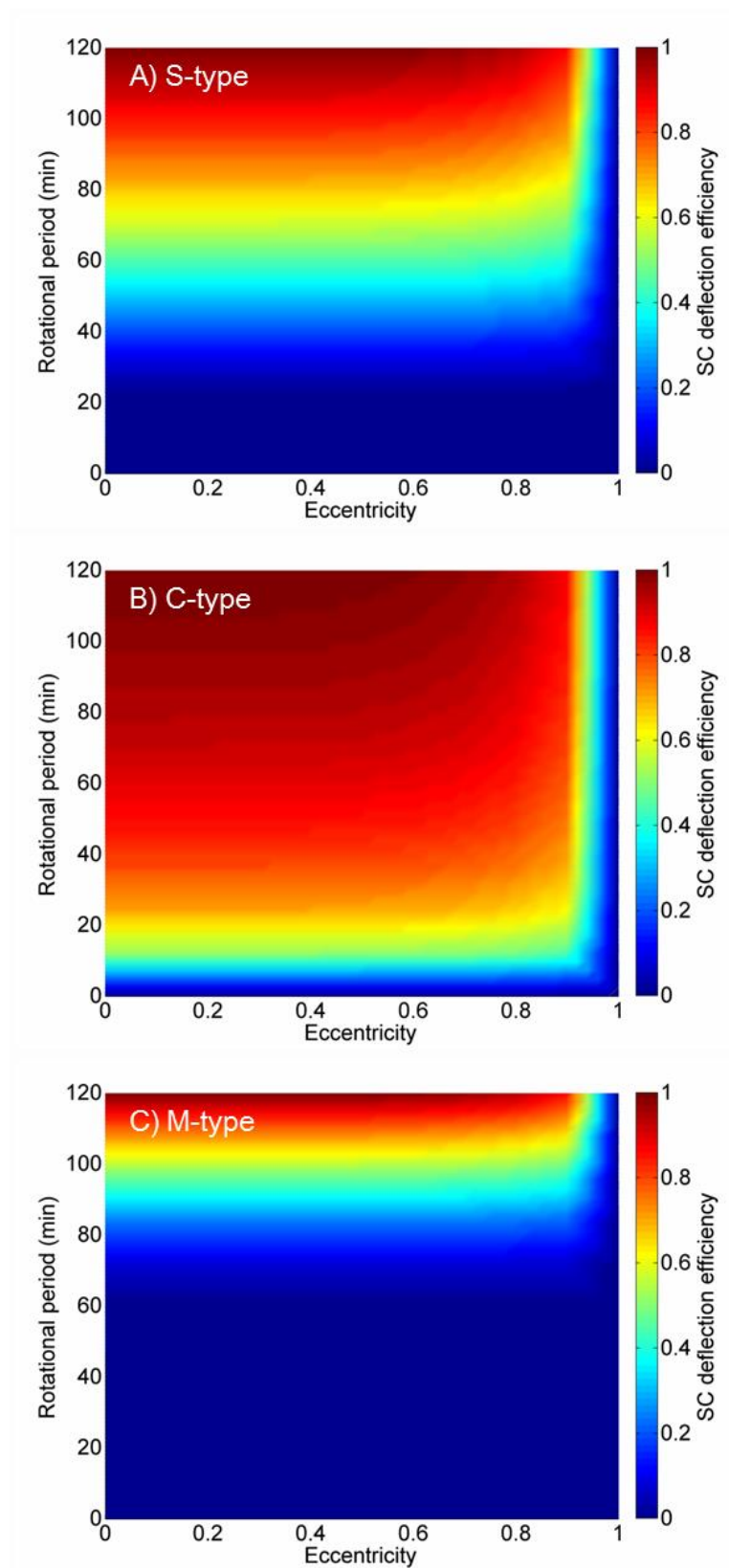

Figure 76 Normalised SC deflection efficiency with respect to the maximum deflection given to the asteroid with rotational period of 120 minutes and zero eccentricity. Note that these plots cannot be compared in terms of the actual deflection performance for three cases.

4.4. Chapter summary

This chapter has emphasised the effects of asteroid dynamics and inhomogeneity on the two specific asteroid deflection techniques: the KI and GT. The results have shown that the COM offset due to the inhomogeneity of the internal density distribution does affect the KI's deflection outcomes when the CEP is zero. In other words, we can conclude that the KI mission outcomes are basically dictated by the accuracy of the terminal guidance control as long as the target body is spherical or the asteroid mass and its shape are well-characterised. However, this conclusion may not hold if the target body is an irregular body and not well-characterised. The results of the GT missions to the irregular asteroid have shown that the gravity variation with time will be the main source of perturbation. Note that the effect of the SRP on the spacecraft will become a concern only when the spacecraft is not in close proximity of the asteroid. The analyses of SC missions to the ellipsoidal asteroid model have shown that the SC deflection efficiency will be dependent on the rotation and shape of the target body. Most importantly, if the target body is highly elongated (i.e., highly eccentric), the efficiency could be profoundly compromised due to the swaying motion of vaporised rock jet from the asteroid surface. It is therefore recommended to accurately control the direction of the solar beam towards the asteroid surface during the deflection (i.e., sublimation) operations in order to provide the rocket jet in a desired direction parallel to the orbital direction of the asteroid. Regarding the rotational period, as long as it is a couple of hours, the SC deflection efficiency will not be significantly affected by the rotational state of the asteroid; however, if the target body is identified to be a fast-rotator the efficiency could be seriously compromised.

5

5. Towards designing a credible mitigation campaign

"The dinosaurs became extinct because they didn't have a space program. And if we become extinct because we don't have a space program, it'll serve us right!"

— Larry Niven

Mitigation campaigns should be accurately planned in order to accomplish a successful deflection even if the preliminary NEA characterisation is based on ground-based telescope/radar observations which often provide only very ambiguous information about important NEA characteristics. Sending multiple spacecraft of one specific type of deflection technique (e.g., the multiple solar mirror concept of Maddock *et al.* [116] or the multiple GT concept of Foster *et al.* [133]) can increase the deflection efficiency as well as the redundancy of the given deflection mission. However, such mitigation missions are inevitably subject to the uncertain performance of the deflection technique and thus the mitigation campaign could be profoundly compromised due to not only the epistemic uncertainties in the NEA characteristics but also aleatory/practical uncertainty of the technique itself (e.g. the terminal guidance precision of a KI mission, the sublimation efficiency of an SC mission, etc.).

Sending multiple asteroid deflection missions of different techniques is one of the possible approaches to the design of a credible mitigation campaign. Here, we consider a dual-deflection mitigation campaign that combines the KI/NI/SC as a primary deflection mission and the GT as a secondary deflection mission in order to overcome the limits imposed on the single asteroid deflection approach and to make the given mitigation campaign more credible. The primary deflection mission makes use of an

instantaneous/quasi-instantaneous (e.g., a week/month-long deflection by SC) deflection technique whereas the secondary deflection mission makes use of a slow push deflection technique. The final outcome of the given mitigation campaign is therefore determined by the secondary deflection mission which performs its slow-push deflection according to the instantaneous outcome of the primary deflection mission that could be fully successful, partly successful, or at worst, complete failure. In addition to this, the secondary deflection mission should be capable of preventing the NEA from passing an undesired subsequent Earth impact keyhole on the 2036 b-plane due to the unexpected b-plane deflection of the primary mission.

The use of the GT as a backup deflection mission for the secondary impact keyhole avoidance has been first suggested by Yeomans *et al*. in the JPL report in 2008 [49]. Such combined mitigation strategies have been also studied as a part of the NEOShield project [134]. Yeomans *et al*. [49] pointed out in the report that tracking of the GT spacecraft would provide precise information about the asteroid orbit (as well as its characteristics through in-situ observations) before and after the primary deflection mission and also after the GT's NEA orbit manipulation. Their study however, assumed the range of the momentum enhancement factor β of the NEA $(1 < \beta < 5)$ in order to evaluate the possible range of the outcome of the primary deflection achieved through the KI instead of considering the uncertainties in the NEA physical characteristics.

Dual-deflection mitigation campaign planning involves trade-offs between a series of competing aspects (total mitigation systems mass, mission duration, deflection distance, confidence in deflection/campaign credibility, etc.). They are to be optimised to minimise the launch costs of NEA mitigation systems and total campaign duration while maximising the mitigation efficiency (i.e., deflection distance on the b-plane of the Earth encounter) and the confidence in successful mitigation campaign (i.e. Belief of the nominal deflection distance).

5.1. Dual-deflection mitigation campaign

As stated above, the dual-deflection mitigation campaigns studied here consist of a primary KI/NI/SC mission and a secondary GT mission, which are designated as KI-GT, NI-GT, and SC-GT campaigns, respectively. Figure 77 shows an example of KI-GT campaign under the 20-year warning time scenario. The hazardous NEA in Figure 77 is VI_1 so it is an Apollo asteroid with a diameter of 140 m. The transfer orbits of the KI and GT are determined by

solving a conventional two-body Lambert's problem. A chemical propulsion system of $Isp = 300\ s$ is used as a kick stage at the Earth departure and also at the terminal approach to the target NEA to accelerate or decelerate the spacecraft. For the case of KI-GT campaign, two missions are sent to the NEA separately and therefore take two different trajectories. This allows the KI mission to take advantage of a higher relative velocity at the encounter with NEA while allowing the GT mission to rendezvous with the NEA without consuming an excessive amount propellant at NEA arrival. For this reason, the GT's arrival could be earlier than the KI's arrival, in which case the GT will be operational before and after the KI mission. On the other hand, for the case of NI-GT/SC-GT campaign, the two missions are sent together to the target NEA in a similar fashion to the interceptor stack concept (see Figure 78) proposed by Adams *et al.* [54]. All the dual-deflection mitigation campaigns will nevertheless be designed and optimised in the same manner with respect to the aforementioned configurations. In any scenario, it is assumed that, after the NEA rendezvous, the GT mission would start tractoring the NEA if its mass were identified to be substantially larger than the nominal value through in-situ characterisation by spacecraft. In this chapter, the upper bound of the uncertainty in NEA mass shown in Table 11 is assumed to be true, which means that the GT will start tractoring as soon as its NEA rendezvous. In practice, the GT will stop tractoring and stay away from the NEA when the primary deflection (KI/NI/SC) takes place for safety reasons; however, such detailed operations are omitted in this study.
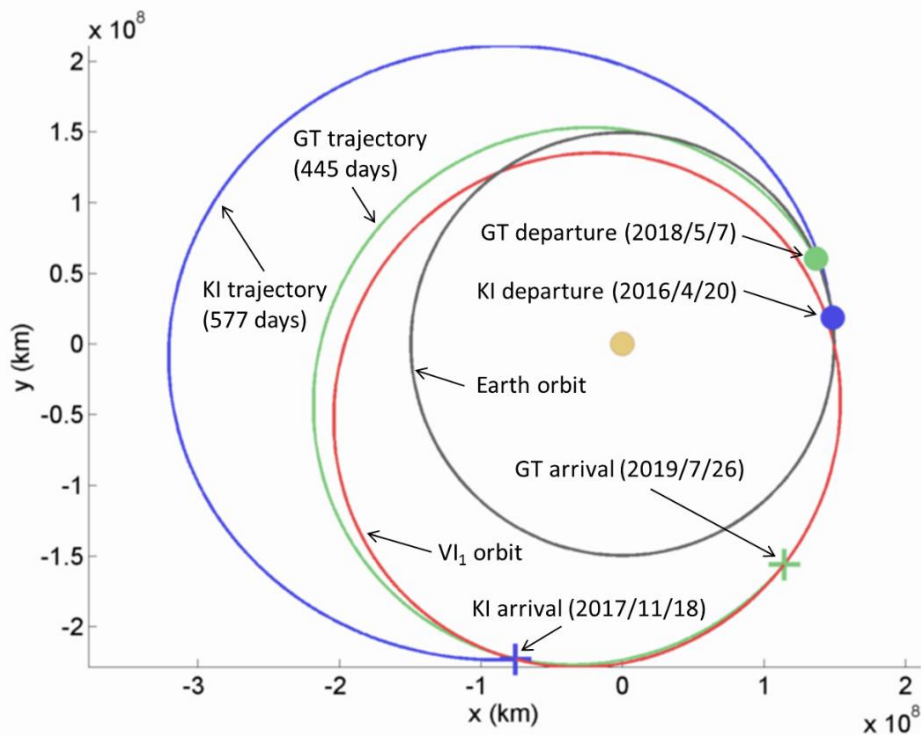

Figure 77 Example of KI-GT campaign against VI$_1$. The warning time (i.e., mitigation campaign window) is set to 20 years between 2016-2036 but the rest of the hazard scenario is the same as previously defined in Section 1.4, Chapter 1.
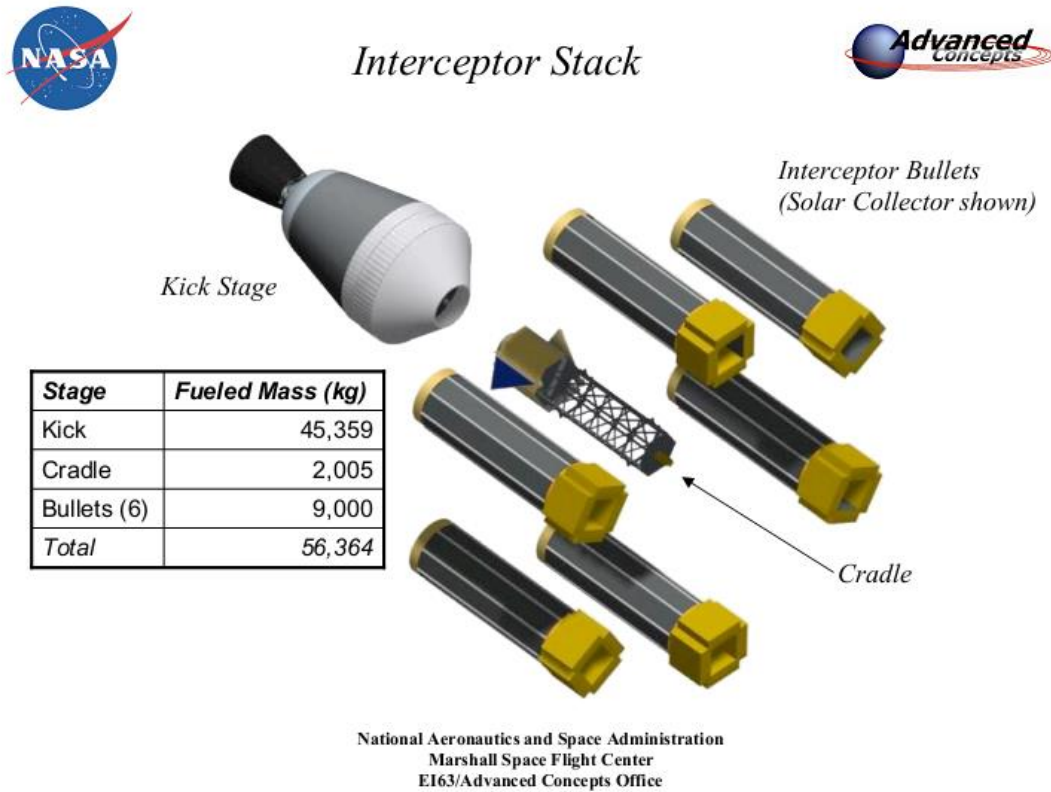
Figure 78 Conceptual diagram of the interceptor stack proposed by Adams et al. [54]. Each bullet has its own mitigation system.

Here once again, we refer to the three basic vectors of design parameters **p** (NEO physical properties), mitigation system design variables **x** (mitigation system specifications), and mitigation performance indicators **y** (resultant b-plane deflection, campaign duration, and confidence in a successful mitigation campaign, etc.) previously defined in Section 2.3 in Chapter 2. The system design variables in vector **x** and their bounds for KI-GT/NI-GT/SC-GT campaign are shown in Table 17. m_1 and m_2 are the mass of primary and secondary mitigation systems at NEA arrival, respectively. t_1 and tof_1 are the Earth departure time and the flight time of the primary deflection mission whereas t_2 and tof_2 are the Earth departure time and the flight time of the secondary deflection mission, where the latter two are required only for KI-GT campaign planning. The primary deflection mission start time t_{int1} must be also defined for the NI-GT/SC-GT campaign as the two mitigation systems will be sent together such that the NEA arrival time may not be always optimal for t_{int1} of the given primary deflection mission. Note that $\Delta\mathbf{v}_{\mathrm{imp}}$ ($= \Delta v_{\mathrm{imp}} \cdot \hat{\mathbf{v}}_{\mathrm{imp}}$) is the impact velocity increment in addition to the terminal NEA encounter relative velocity $\mathbf{v}_{\mathrm{imp}}$ at NEA arrival of the KI mission. Finally, Δt_{GT} and Δt_{SC} are the durations of time for the GT mission and the SC mission, respectively, where T_a is

one orbital period of the given virtual impactor. The maximum value of the SC mission duration Δt_{SC} is therefore one asteroid orbit at most; however, such a long SC mission duration is usually not necessary as will be shown later in this chapter.

Table 17 Minimum and maximum values of design variables x for a KI-GT/NI-GT/SC-GT campaign. The warning time (i.e., mitigation campaign window within which a mitigation campaign is launched and completed) is set to 20 years between 2016-2036. T_a is the orbital period of the target NEA.

x	KI-GT	NI-GT	SC-GT
m_1 (kg)	100-10000	0-300	0-300
m_2 (kg)	100-10000	100-10000	100-10000
t_1	2016/4/13-2036/4/13	2016/4/13-2036/4/13	2016/4/13-2036/4/13
tof_1 (day)	30-1000	30-1000	30-1000
t_2	2016/4/13-2036/4/13		
tof_2 (day)	30-1000		
t_{int1}		$(t_1 + tof_1)$-t_{MOID}	$(t_1 + tof_1)$-t_{MOID}
Δv_{imp} (km/s)	0-100		
Δt_{GT} (year)	0-20	0-20	0-20
Δt_{SC} (T_a)			0-1

The dual-deflection mitigation campaign optimisation problem requires an assessment of the figures of merit (i.e., the mitigation performance indicators) in vector **y** that characterise the performance and the confidence in a successful mitigation campaign. Seven figures of merit in vector **y** are described in Table 18. m_0 is the total mitigation systems mass at the Earth departure stage (EDS), which is equal to the sum of m_{EDS1} and m_{EDS2}: the masses of two mitigation systems at the EDS. m_0 should be as small as possible to reduce the cost of the mitigation campaign. The upper bound of m_0 is set to 100 tons, which is, in practice, too large to be launched by a single heavy-lift launch vehicle (HLV) available today such as Atlas V or Delta IV [135]. It is therefore assumed that substantially heavy mitigation systems are launched and put into Earth orbit separately by multiple HLVs. In the cases of NI-GT and SC-GT campaigns, those are combined together in space before the EDS. Nonetheless, this study does not put emphasis on planning of mitigation campaigns available today: 100-ton mitigation systems at the EDS are not realistic in terms of their launch costs. t_{f1} and t_{f2} are the asteroid arrival time of the mitigation system(s) and the campaign completion time (i.e., GT termination time), respectively. t_{f1} is desirable to be as late as possible such that more time can be spent on decision-making of mitigation campaign enforcement. t_{f2}, on the other hand, should be as early as possible such that an additional mitigation campaign can be launched, if necessary. Not to mention, t_{f1} can be no later than t_{f2}. b_{nom} is the nominal deflection on the b-plane and desired to be as large as possible

within the range of $1{,}000 \text{ km} \leq b_{\mathrm{nom}} \leq 32{,}000 \text{ km}$. The lower bound of b_{nom} refers to the safe amount of deflection (1000 km on the b-plane) that is required to put the b-plane uncertainty ellipsoid off the secondary impact keyholes [49] whereas the upper bound is approximately equal to a b-plane deflection of 5.0 Earth-radii which is simply twice the safe deflection distance defined previously in Chapter 1 in order to consider mitigation campaigns with safer deflection into account. Bel_{nom} and Pl_{nom} are the Belief and Plausibility measures of nominal deflection distance. Higher Belief is simply an indication of higher confidence in successful mitigation. Finally, b_{trim} is the post primary mission trim deflection achieved through the GT mission, which indicates the trim deflection capability of the given dual-deflection mitigation campaign for secondary impact keyhole avoidance. The maximum deflection distance of this trim maneuverer is set to 1000 km on the b-plane.

Table 18 Figures of merit of dual-deflection mitigation campaign for different scenarios: KI-GT, NI-GT, and SC-GT. The smaller these figures are, the more optimal the given mitigation campaign is. Note that the arrival time of the mitigation system(s) t_{f1} is to be maximised as a later primary deflection completion time allows the planetary defense framework to delay the decision-making of the campaign as long as possible.

y	Description
m_0	Total mitigation systems mass at EDS ($= m_{\mathrm{EDS1}} + m_{\mathrm{EDS2}}$)
$-t_{\mathrm{f1}}$	Primary deflection completion time
t_{f2}	Secondary deflection completion time
$-b_{\mathrm{nom}}$	Nominal deflection achieved through dual-deflection campaign
$-Bel_{\mathrm{nom}}$	Belief of nominal deflection b_{nom}
$-Pl_{\mathrm{nom}}$	Plausibility of nominal deflection b_{nom}
$-b_{\mathrm{trim}}$	Trim (post-primary) deflection achieved through by GT mission

Minimising the above-mentioned figures of merit inevitably entails a multi-objective optimisation problem. Following the conventional approach of Pareto optimal optimisation [48], the fast and elitist multiobjective genetic algorithm NSGA-II [136] is used to compute Pareto optimal design points of dual-deflection mitigation campaigns. A total of 2400 solutions for **y** from a hundred of generations are numerically computed in MATLAB. Detailed information about the multiobjective genetic algorithm is omitted in this thesis and thus readers interested in the algorithm should refer to the work of NSGA-II developed by Deb *et al*. [136].

5.2. Results and discussion

A series of optimisation results of the KI-GT, NI-GT, and SC-GT campaigns are presented in Subsections 5.2.1-5.2.3, respectively. Note that these results are only for VI_1 and thus interested readers in the other scenarios (VI_2-VI_6) should refer to Appendix A.5.

5.2.1. KI-GT campaign

The Pareto-optimal results of KI-GT campaigns against 140-m sized S-type VI_1 characterised under the ground-based characterisation scenario are shown in Figures 79-82. In Figures 79 and 80, the Pareto-optimal solutions for the campaigns are plotted for KI Earth departure time vs. total mitigation system mass at EDS (t_1 vs. m_0) and GT termination time vs. total mitigation system mass at EDS (t_{f2} vs. m_0), respectively. These are sorted by eight different levels of Belief measure Bel_{nom} hence, there exists A)-H) for the respective levels of Belief measure. The colours of the dots represent the degrees of nominal deflection distances ranging between 0.0-5.0 Earth-radii.

Figure 79 shows that many optimal mitigation campaigns with large nominal deflection are concentrated in the KI Earth departure time t_1 around the year 2018 while there are quite a few of them available early in 2020 particularly with smaller Belief of nominal deflection. This appears to be due to the amplification effect of the VI_1 perihelion passage on asteroid deflection attempts that happens approximately every 1.38 years, and more importantly, the relative position of the Earth and VI_1 at the KI's EDS, t_1. This amplification effect is evident also for the results of the other virtual impactors (see Appendix A.4). As the Belief of the nominal deflection increases, the number of solutions for the optimal mitigation campaigns decreases, which is simply because a KI-GT campaign with higher degree of Belief requires a larger fraction of the total mitigation system mass m_0 for the secondary deflection mission (i.e. more massive GT spacecraft at the EDS m_{EDS2} for a larger post-KI deflection). In order to allocate an enough post-KI deflection through the GT mission, the KI Earth departure time is severely limited to the year 2018's time frame as shown in Figure 79-H). As a consequence, m_0 becomes substantially larger than that of the campaigns with lower level of Belief. This in turn means that, if the campaign credibility is not prioritised, quite a few optimal solutions offer a relatively light-weight (20-40 tons) and late-term KI-GT campaigns (in 2025 or later) which satisfy the safe b-plane deflection distance of $2\frac{1}{2}\ b_\oplus$ (4.16 Earth-radii) as shown Figure 79-A).

Figure 80-A) shows that there are optimal mitigation campaigns of various nominal deflection distances within a wide range of campaign completion time/GT termination time between 2018-2036 whereas Figure 80-H) shows that a high confidence mitigation campaign with a high nominal deflection results in a late campaign completion, 2026 or later. However, it can be seen that t_{f2} close to the year 2036 does not necessarily result in an effective mitigation campaign in terms of the nominal deflection distance. This can be interpreted as the inefficiency of GT missions close to the impact/Earth encounter epoch in the year 2036.

Figure 81 shows the ratio of KI and GT masses at EDS. It can be seen that dual-deflection mitigation campaigns with large nominal deflection and high confidence level require a larger fraction of the total mass m_0 for the GT mission than the KI mission. Again, this should be due to the inefficiency of GT as a deflection technique with respect to the KI.

When the secondary impact keyhole passage avoidance is considered, Figure 79 shows that the year 2033 will be the last launch opportunity for an effective keyhole mitigation campaign against VI_1. Although the dots around the year 2033 are mostly dark blue, these dual-deflection mitigation campaigns can still provide the nominal deflection distance of >1000 km which is more than enough to avoid secondary impact keyhole. In addition, the avoidance of undesired keyhole passage due to the primary deflection can be fulfilled, counting on the reserved trim deflection b_{trim} by the post-KI deflection achieved through the GT mission (see Figure 82). Not surprisingly, the earlier the KI interception is, the larger b_{trim} can be. The periods of time to obtain b_{trim} range from months to years and they are, of course, proportional to the nominal deflection and the confidence level of each campaign.

Particularly in the case of the KI-GT campaign scenario against VI_1, the GT rendezvous with the NEA could be before/after the KI arrival/interception time depending on the KI-GT campaign's mission sequence. The former case is found to be highly beneficial as it enables proximity characterisation of the NEA as well as the precise guidance of the KI by GT spacecraft. The GT might start tractoring immediately after the NEA rendezvous before the KI arrival/impact, however, this is not always the case, for example, if the in-situ NEA physical characterisation determines that the actual NEA mass is less heavy than its expected nominal value. In that case, the GT mission can provide an extra deflection to the outcome of the primary deflection which will be likely larger than the nominal value.

Figures 83 and 84 show comparison among the KI-GT mitigation campaigns against VI_1 of three different taxonomic classes: S, C, and M-types. The results correspond to

$Bel_{nom} = 1.00$. These results indicate that there are no significant differences between them; however, it seems that the optimality of the KI interception (i.e., preferable Earth departure time for a larger nominal deflection) is slightly dependent on the taxonomic class of the target asteroid as can be seen in Figure 83-A)-C). The optimal ratio of KI and GT masses varies according to the taxonomic class (see Figure 84-A)-C)). The KI mass for the dual-deflection mitigation campaigns against the M-type asteroid accounts for a larger fraction of total mitigation system mass compared with the other two scenarios. The post-KI trim deflection (see Figure 84-D-F)) is not entirely free of the asteroid taxonomic class either. Not surprisingly, the GT mission to the M-type/heaviest asteroid results in the least post-KI deflection efficiency even if the mitigation campaign takes place early in the 20-year mitigation window, around 2018.

As a final remark on the KI-GT campaign scenario, in practice, not only the NEA arrival but the Earth departure of the KI could be later than the GT arrival at the NEA, depending on the available launch window, warning time, NEA orbit, etc. This is actually a critical issue of the KI mitigation system design as the primary deflection mission because the GT spacecraft may be able to conduct preliminary characterisation of the NEA at the proximity characterisation level even before the Earth departure of the KI mission; however, the feasibility study of such a precursor characterisation mission by GT followed by a KI mission is out of scope of this thesis.
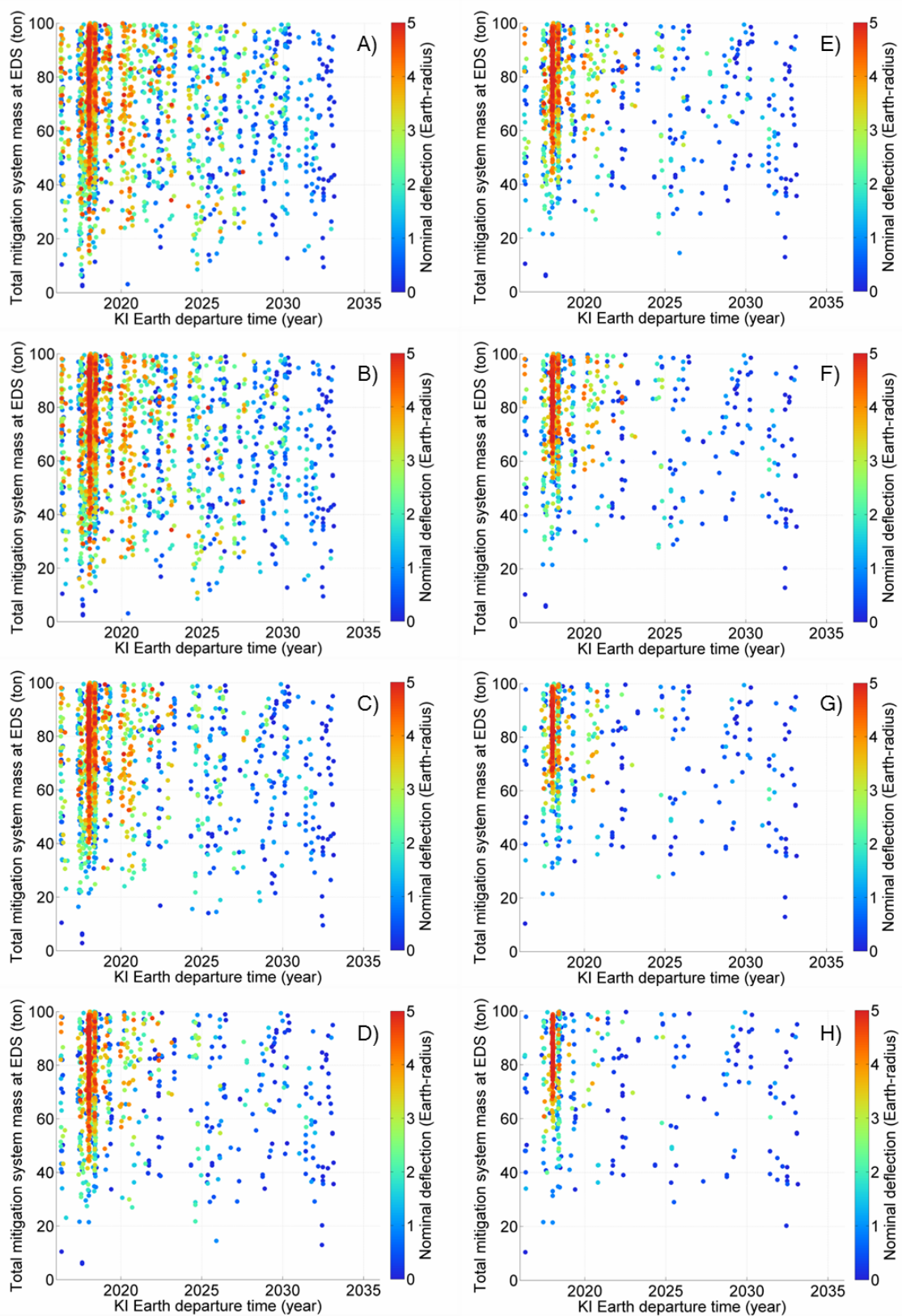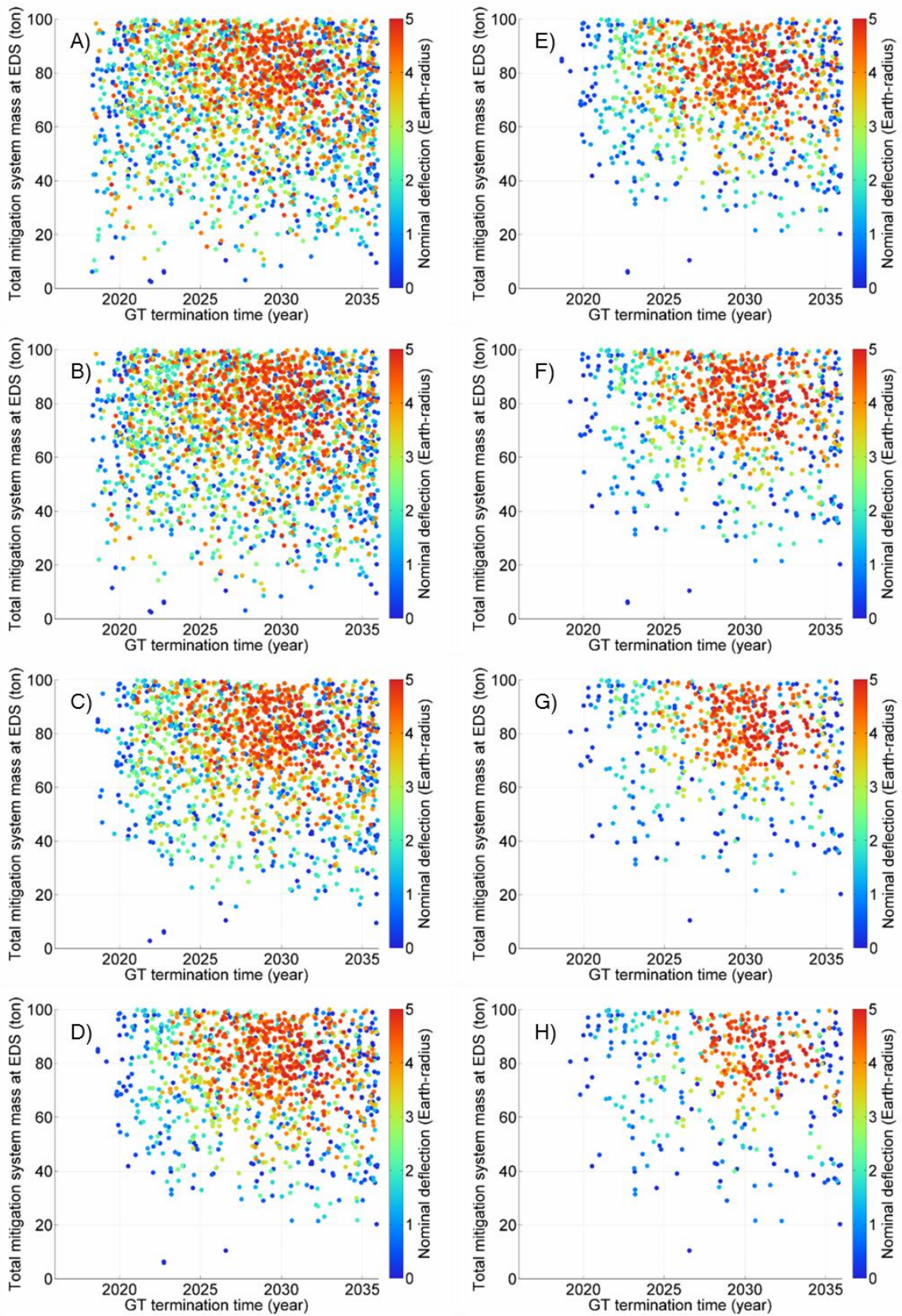
Figure 79 Pareto-optimal solutions for KI-GT campaigns against S-type VI₁ plotted for KI Earth departure time vs. total mitigation system mass at EDS. The colours of the dots represent the degrees of nominal deflection distances between 0.0-5.0 Earth-radii. A) $\text{Bel}_{\text{nom}} \geq 0.47$. **B)** $\text{Bel}_{\text{nom}} \geq 0.51$. **C)** $\text{Bel}_{\text{nom}} \geq 0.56$. **D)** $\text{Bel}_{\text{nom}} \geq 0.57$. **E)** $\text{Bel}_{\text{nom}} \geq 0.70$. **F)** $\text{Bel}_{\text{nom}} \geq 0.83$. **G)** $\text{Bel}_{\text{nom}} \geq 0.97$. **H)** $\text{Bel}_{\text{nom}} = 1.00$.

Figure 80 Pareto-optimal solutions for KI-GT campaigns against S-type VI₁ plotted for the GT termination time vs. total mitigation syst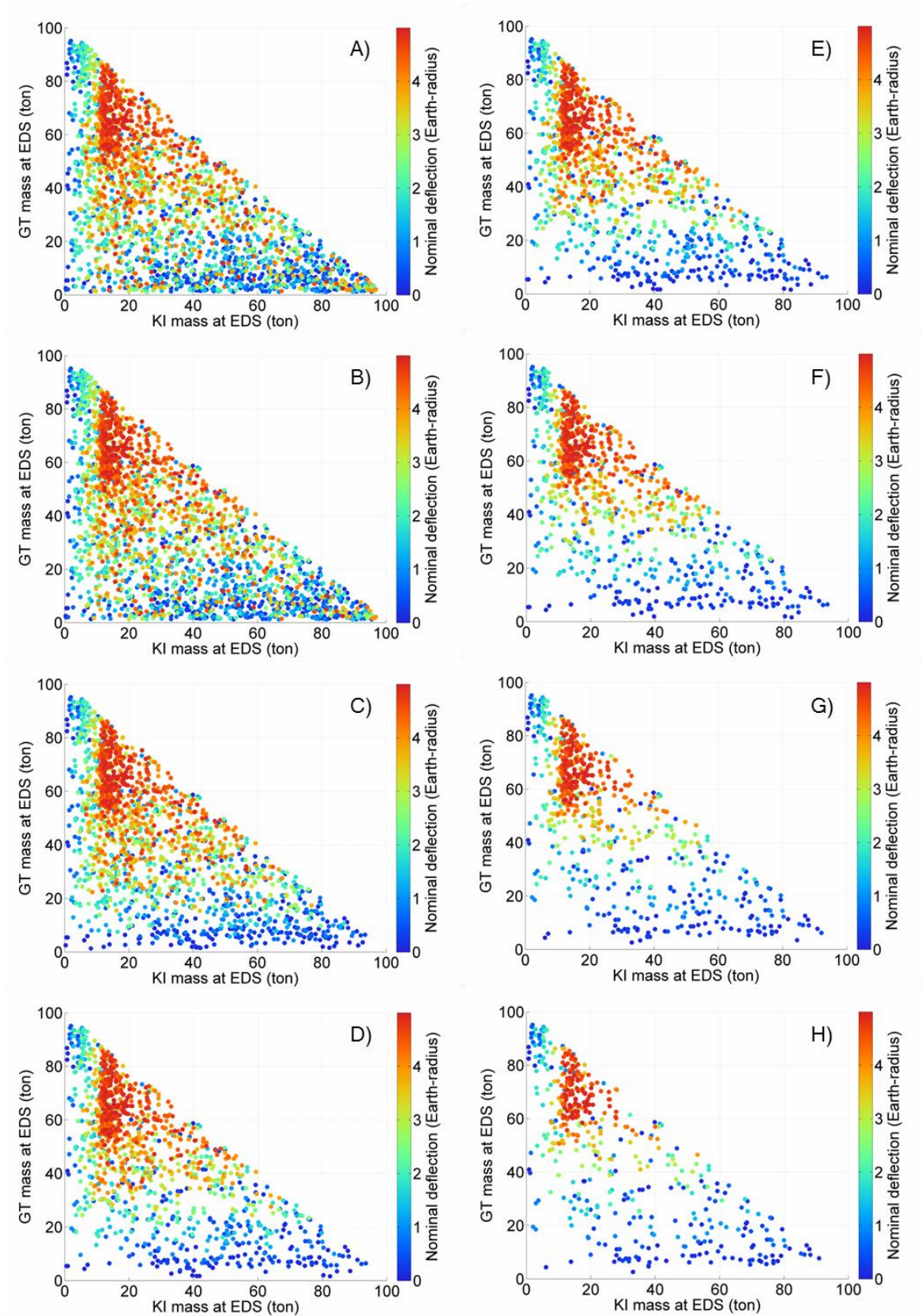em mass at EDS. A) $Bel_{nom} \geq 0.47.$ **B)** $Bel_{nom} \geq 0.51.$ **C)** $Bel_{nom} \geq 0.56.$ **D)** $Bel_{nom} \geq 0.57.$ **E)** $Bel_{nom} \geq 0.70.$ **F)** $Bel_{nom} \geq 0.83.$ **G)** $Bel_{nom} \geq 0.97.$ **H)** $Bel_{nom} = 1.00.$

Figure 81 KI mass vs. GT mass at EDS. A) $Bel_{nom} \geq 0.47.$ **B)** $Bel_{nom} \geq 0.51.$ **C)** $Bel_{nom} \geq 0.56.$ **D)** $Bel_{nom} \geq 0.57.$ **E)** $Bel_{nom} \geq 0.70.$ **F)** $Bel_{nom} \geq 0.83.$ **G)** $Bel_{nom} \geq 0.97.$ **H)** $Bel_{nom} = 1.00.$
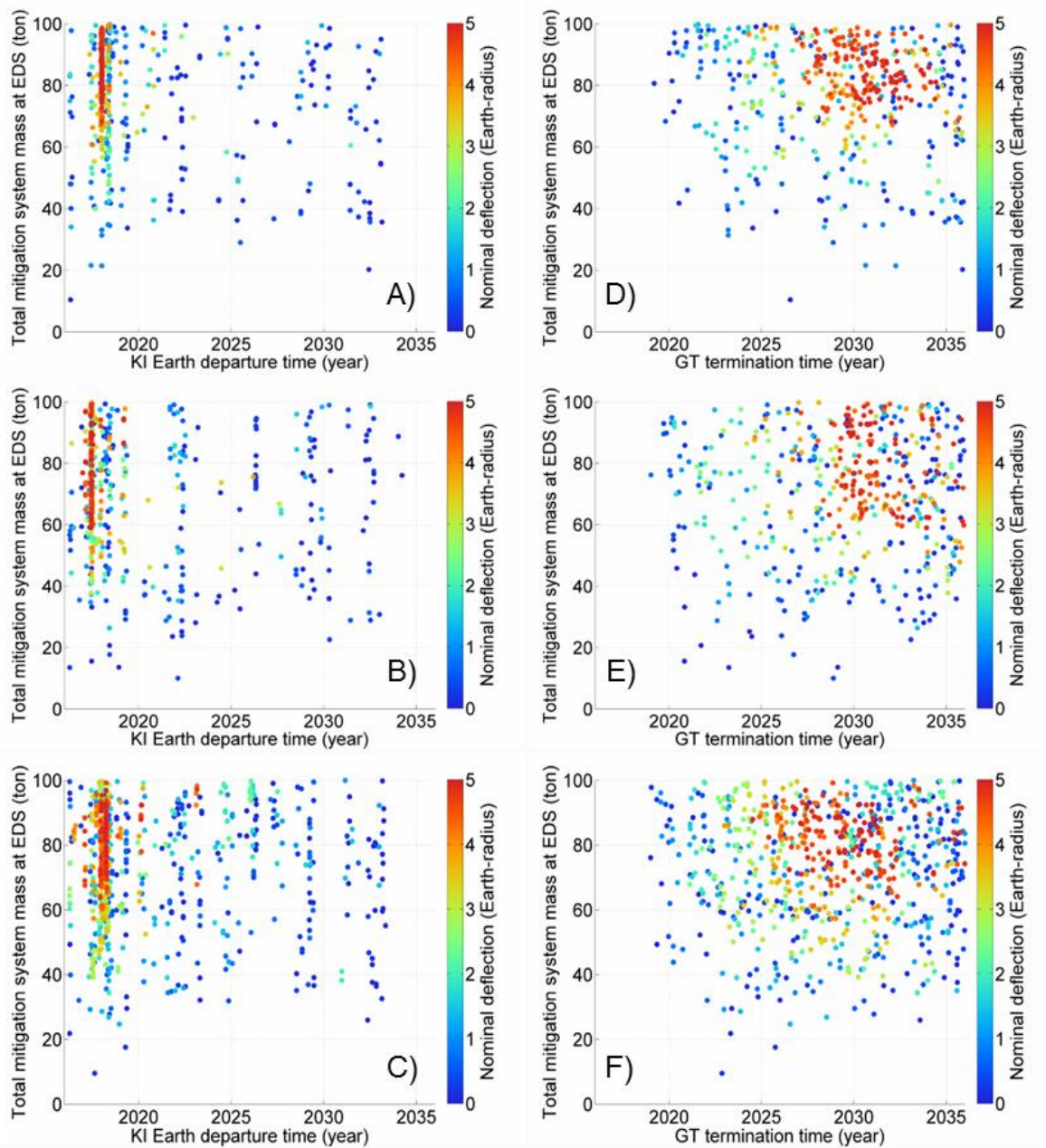
Figure 82 Post-KI deflection by GT. A) Bel$_\text{nom} \geq 0.47$. B) Bel$_\text{nom} \geq 0.51$. C) Bel$_\text{nom} \geq 0.56$. D) Bel$_\text{nom} \geq 0.57$. E) Bel$_\text{nom} \geq 0.70$. F) Bel$_\text{nom} \geq 0.83$. G) Bel$_\text{nom} \geq 0.97$. H) Bel$_\text{nom} = 1.00$.
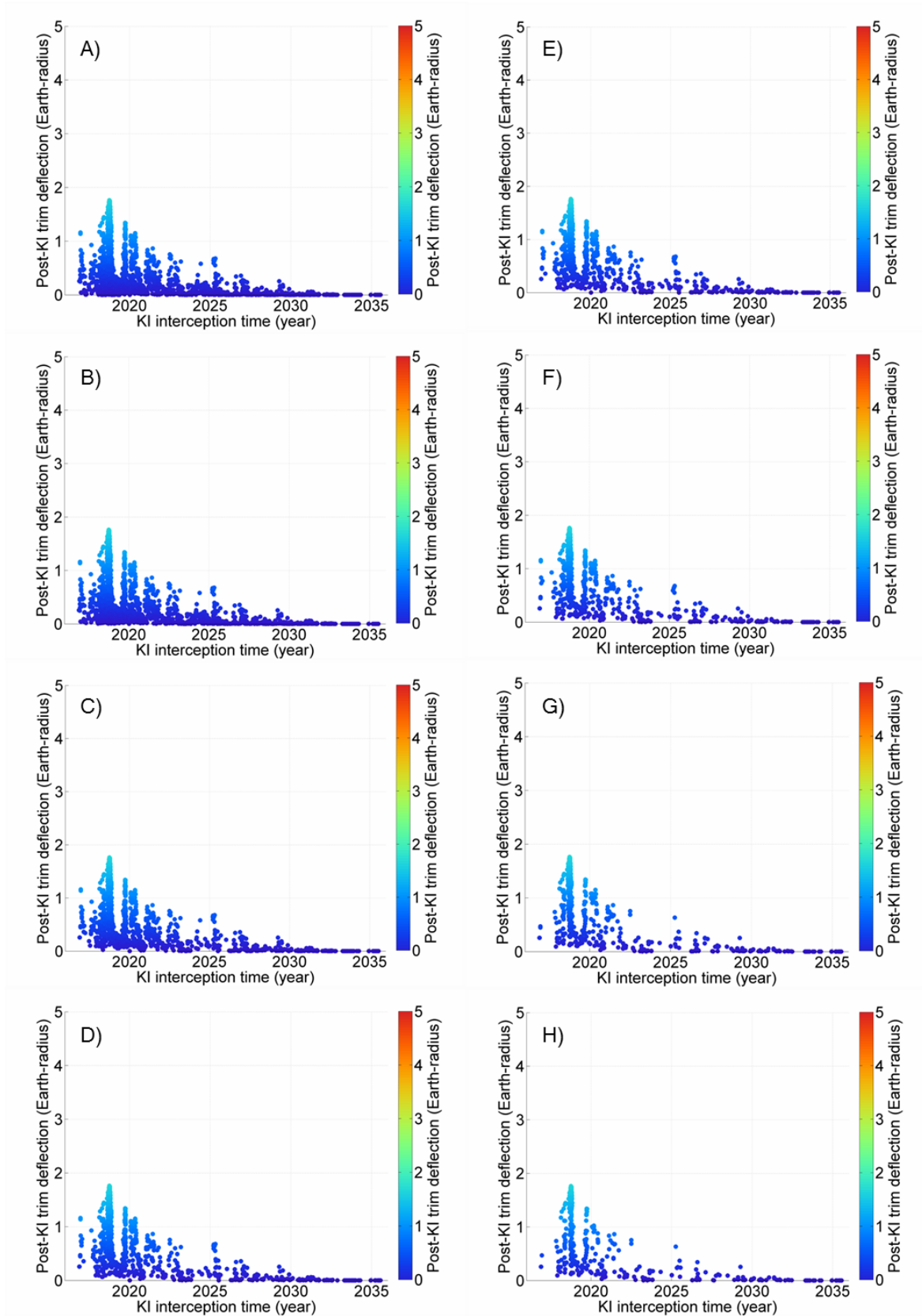
Figure 83 Comparison among the campaigns against three taxonomic classes: S, C, and M-types. These are results correspond to $\mathrm{Bel_{nom}} = 1.00$. The plots on the left-hand side show KI Earth departure time vs. Total mitigation system mass at EDS. A) S-type. B) C-type. C) M-type. The plots on the right-hand side show GT termination time vs. total mitigation system mass at EDS. D) S-type. E) C-type. F) M-type.
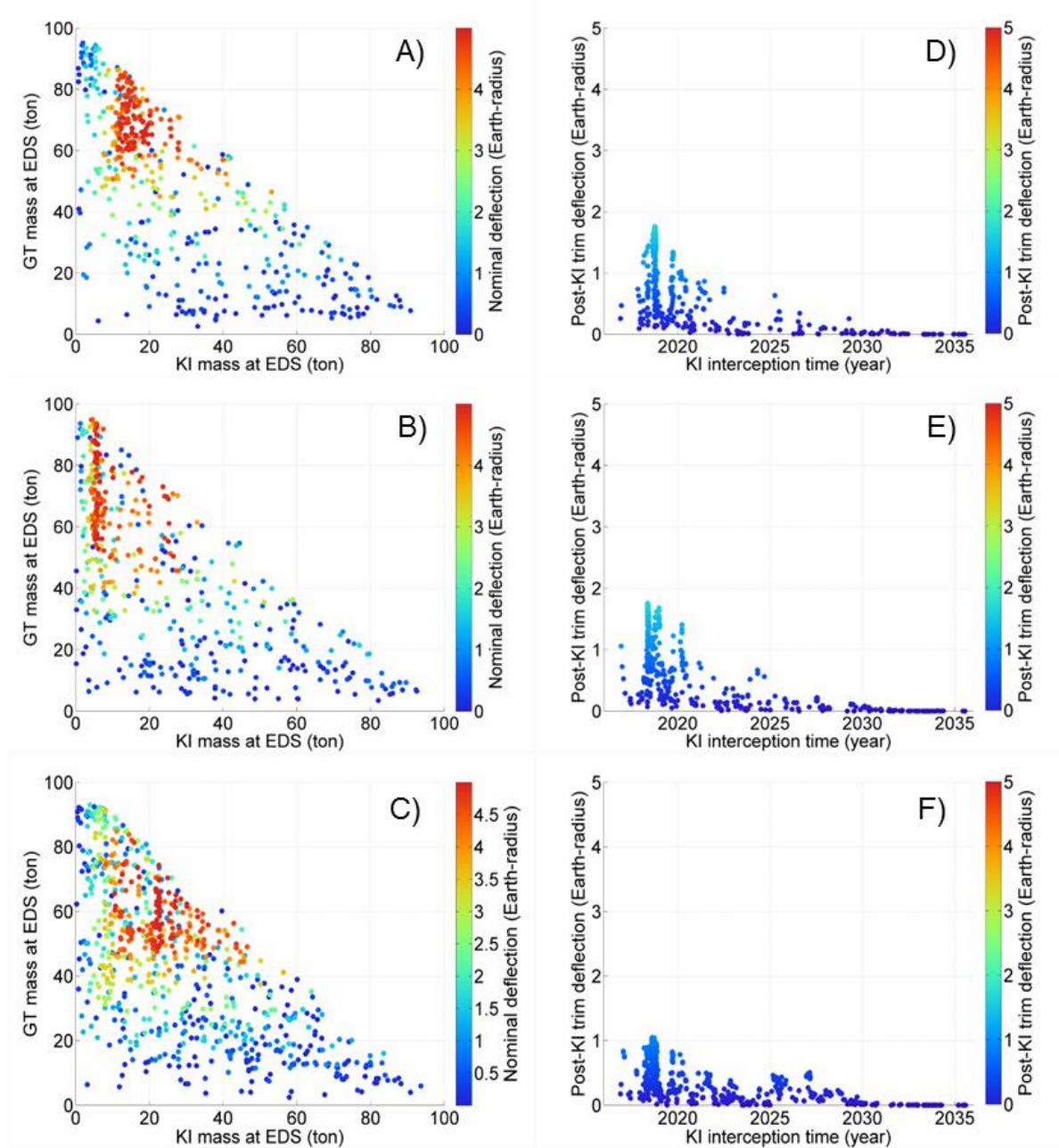
Figure 84 Comparison among the campaigns against three taxonomic classes: S, C, and M-types. These are results correspond to $\mathrm{Bel_{nom}} = 1.00$. The plots on the left-hand side show KI mass at EDS vs. GT mass at EDS. A) S-type. B) C-type. C) M-type. The plots on the right-hand side show KI interception time vs. Post-KI trim deflection. D) S-type. E) C-type. F) M-type.

5.2.2. NI-GT campaign

The Pareto-optimal results of NI-GT campaigns against 140-m sized S-type VI_1 characterised under the ground-based characterisation scenario are shown in Figures 85-88 in a similar fashion as the results of KI-GT campaign scenario presented in the previous subsection.

Figure 85 clearly shows that the NI-GT mitigation campaign scenario has more distinct optimality in terms of the NI-GT mitigation campaign launch window than the KI-GT mitigation campaign scenario. This might be explained by the fact that both NI and GT mitigation systems are delivered to the target asteroid as a single interceptor stack and rendezvous with it together and therefore optimal launch windows are more limited than the KI-GT scenario. This can also be seen for the results of the other virtual impactors shown in Appendix A.4. As the Belief of the nominal deflection increases, the number of solutions for such optimal mitigation campaigns decreases more noticeably than the KI-GT scenario, again because of the limited launch opportunities for the interceptor stack carrying the two mitigation systems. An NI-GT campaign with higher degree of Belief requires a larger mass for the GT while the mass required for the NI mostly remains below 300 kg.

A late-term Earth departure of the interceptor stack within the 20-year timeline results in considerable reduction of the deflection efficiency and, as a consequence, regarded as non-optimal by the multi-objective optimisation program used in this study. For this reason, the interceptor stack's Earth departure time is severely limited particularly when a higher degree of Belief is concerned. On the other hand, if the campaign credibility is not prioritised, quite a few optimal solutions offer a relatively light-weight (10-30 tons) and late-term (2028~) NI-GT campaigns which satisfy the safe b-plane deflection distance of $2\frac{1}{2}\, b_{\oplus}$ (4.16 Earth-radii) as shown in Figure 85-A). Also, Figure 85-D) shows that the year 2029 will be the last launch opportunity for an effective mitigation campaign against VI_1 if the NI-GT mitigation campaigns with $Bel_{nom} \geq 0.57$ are concerned. Although the dots around 2029 are mostly dark blue, they can still achieve the nominal deflection distance of >1000 km.

Figure 86-A) appears similar to Figure 80-A), showing optimal mitigation campaigns of various nominal deflections within a wide range of campaign completion time between 2018 and 2036. Figure 86-H) is also similar to Figure 80-H), indicating that a mitigation campaign with high Belief and nominal deflection results in a late campaign completion time.

Figure 87 shows the ratio of NI and GT masses at the NEA arrival instead of those at the EDS because they depart the Earth and sent to the target asteroid together. It can be seen that NI-GT mitigation campaigns require a very large fraction of the total mass for the GT mission. This is simply due to the inefficiency of the GT as a deflection technique with respect to the NI which has the highest YTW ratio among the four deflection techniques.

Similar to the KI-GT scenario, undesired keyhole passage due to the primary deflection can be avoided, assuming that b_{trim} is achieved through the post-NI GT mission (see Figure 88). It is interesting to see that there are no dots in Figure 88 after the year 2031 if the NI-GT mitigation campaigns with $Bel_{\text{nom}} \geq 0.57$ are concerned. Again, this is due to the limited launch opportunities of the NI-GT interceptor stack spacecraft.

Figures 89 and 90 compare the NI-GT mitigation campaigns against VI_1 of three different taxonomic classes: S, C, and M-types. The results correspond to $Bel_{\text{nom}} = 1.00$. Almost the same coloured dot patterns can be seen in Figure 89-A)-C). On the other hand, Figure 89-D)-F) show that the completion time of an NI-GT mitigation campaigns is, to some extent, subject to the taxonomic class of the target asteroid. The optimal ratio of NI and GT masses ratio also varies according to the taxonomic class (see Figure 90-A)-C)). The NI mass for the case of M-type appears to require a higher fraction of total mitigation system mass compared to the other two taxonomic classes. This can be interpreted as the lower deflection efficiency of the NI mission to the M-type asteroid due to the larger asteroid mass of M-type. The post-NI deflection (see Figure 90-D)-F)) is not entirely free of the asteroid taxonomic class either. Not surprisingly, the GT mission to the M-type asteroid results in the least both pre-NI and post-NI deflection efficiency.

As a final remark on the NI-GT campaign scenario, an NI-GT mitigation campaign generally outperforms a KI-GT mitigation campaign. However, it still requires a relatively heavy GT spacecraft in order to achieve a high Belief/confidence level on the nominal deflection equal to or close to the safe b-plane deflection. In reality, both NI and GT deflection missions should take place after the target asteroid is carefully characterised by spacecraft. This will substantially reduce the epistemic uncertainties in the fundamental NEA characteristics such as the mass, density, porosity, shape, etc. If that is the case, the NI mission can refer to the actual physical properties of the target body and regulate the NI deflection yield by changing the stand-off distance such that the nominal deflection can be achieved without the help of the post-NI deflection by GT mission for instance.
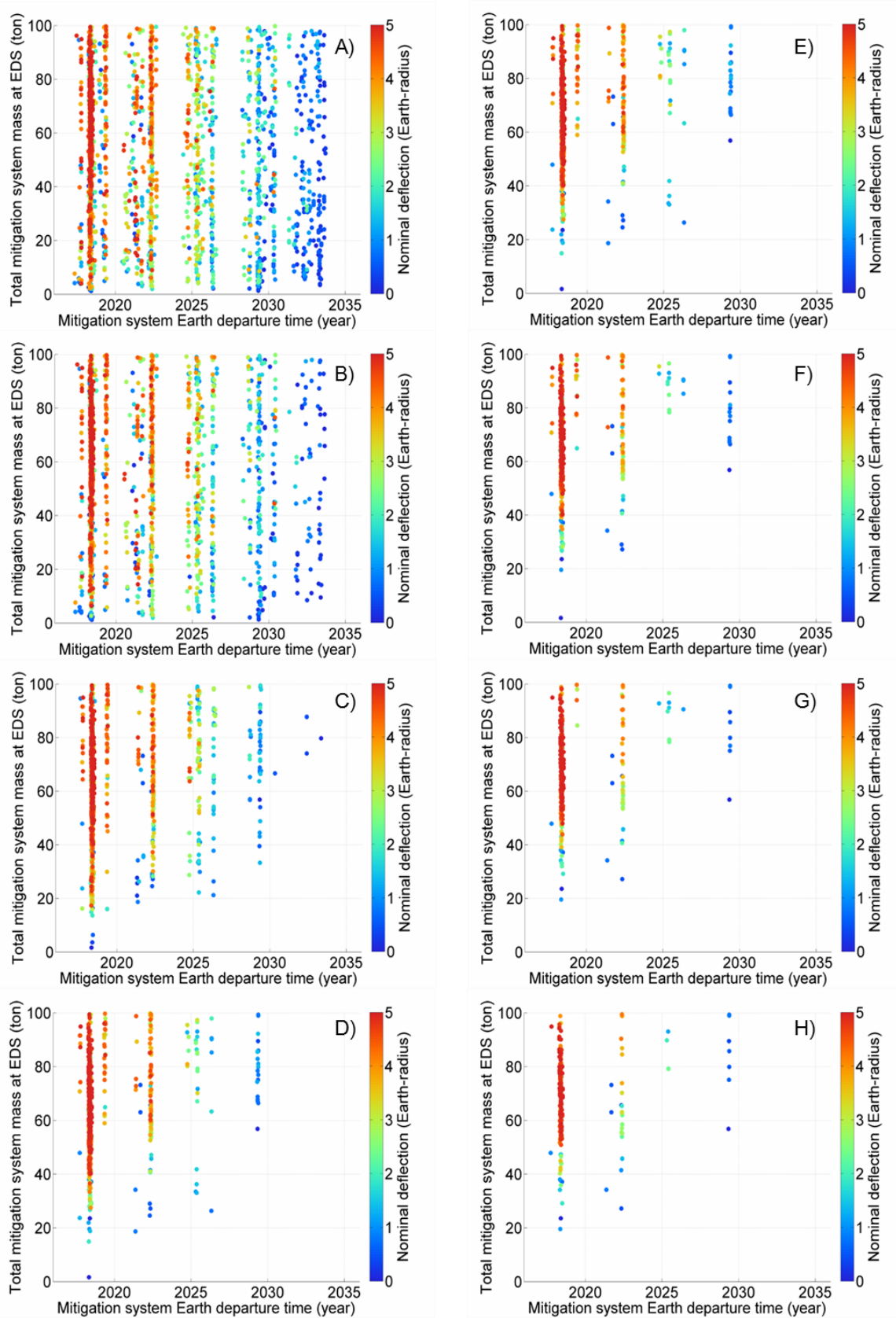
Figure 85 Pareto-optimal solutions for NI-GT campaigns against S-type VI₁ plotted for mitigation system Earth departure time vs. total mitigation system mass at EDS. The colours of the dots represent the degrees of nominal deflection distances between 0.0-5.0 Earth-radii. A) $\text{Bel}_{\text{nom}} \geq 0.47$. B) $\text{Bel}_{\text{nom}} \geq 0.51$. C) $\text{Bel}_{\text{nom}} \geq 0.56$. D) $\text{Bel}_{\text{nom}} \geq 0.57$. E) $\text{Bel}_{\text{nom}} \geq 0.70$. F) $\text{Bel}_{\text{nom}} \geq 0.83$. G) $\text{Bel}_{\text{nom}} \geq 0.97$. H) $\text{Bel}_{\text{nom}} = 1.00$.
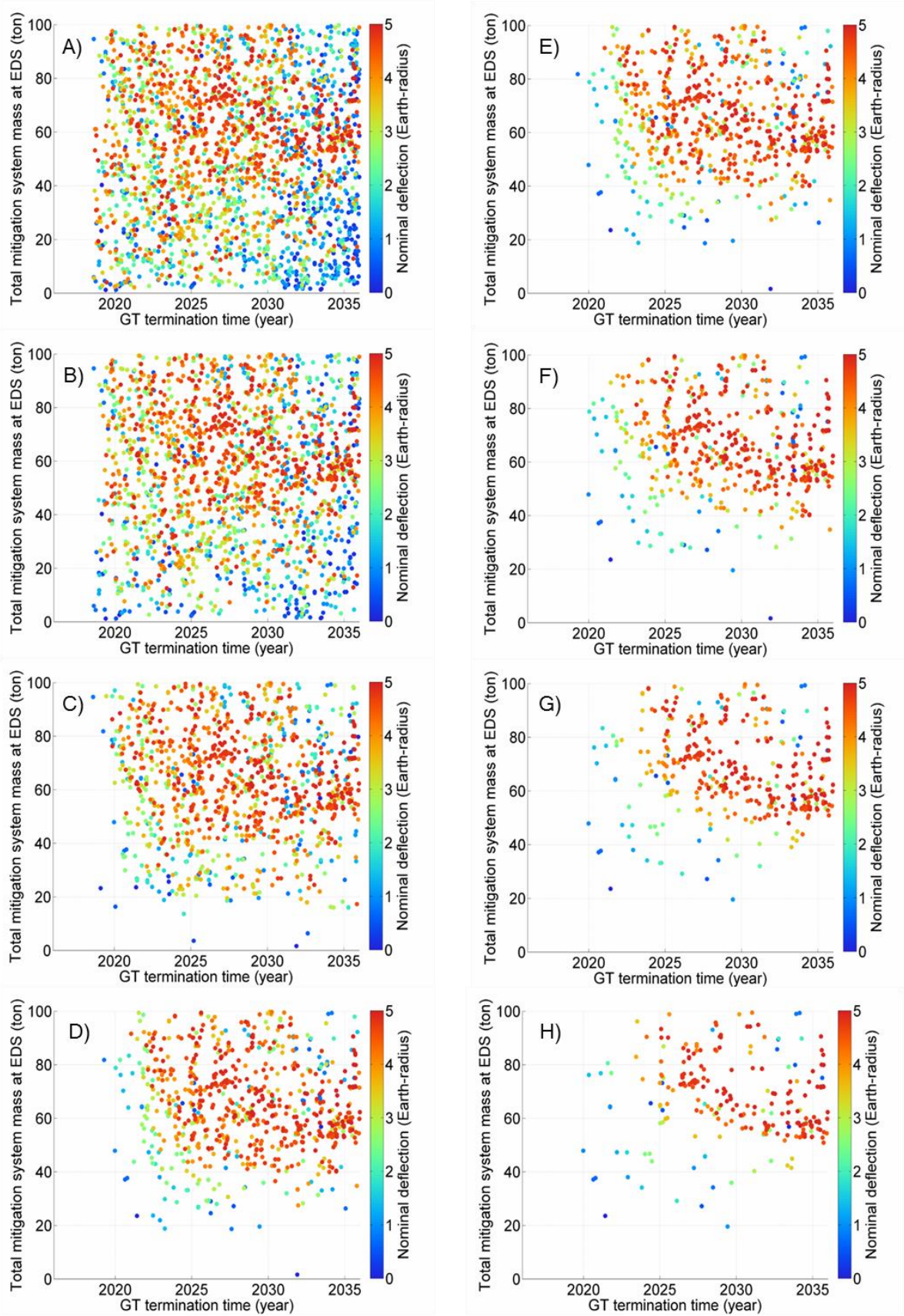
Figure 86 Pareto-optimal solutions for NI-GT campaigns against S-type VI$_1$ plotted for the GT termination time vs. total mitigation system mass at EDS. A) $\text{Bel}_{\text{nom}} \geq 0.47$. **B)** $\text{Bel}_{\text{nom}} \geq 0.51$. **C)** $\text{Bel}_{\text{nom}} \geq 0.56$. **D)** $\text{Bel}_{\text{nom}} \geq 0.57$. **E)** $\text{Bel}_{\text{nom}} \geq 0.70$. **F)** $\text{Bel}_{\text{nom}} \geq 0.83$. **G)** $\text{Bel}_{\text{nom}} \geq 0.97$. **H)** $\text{Bel}_{\text{nom}} = 1.00$.
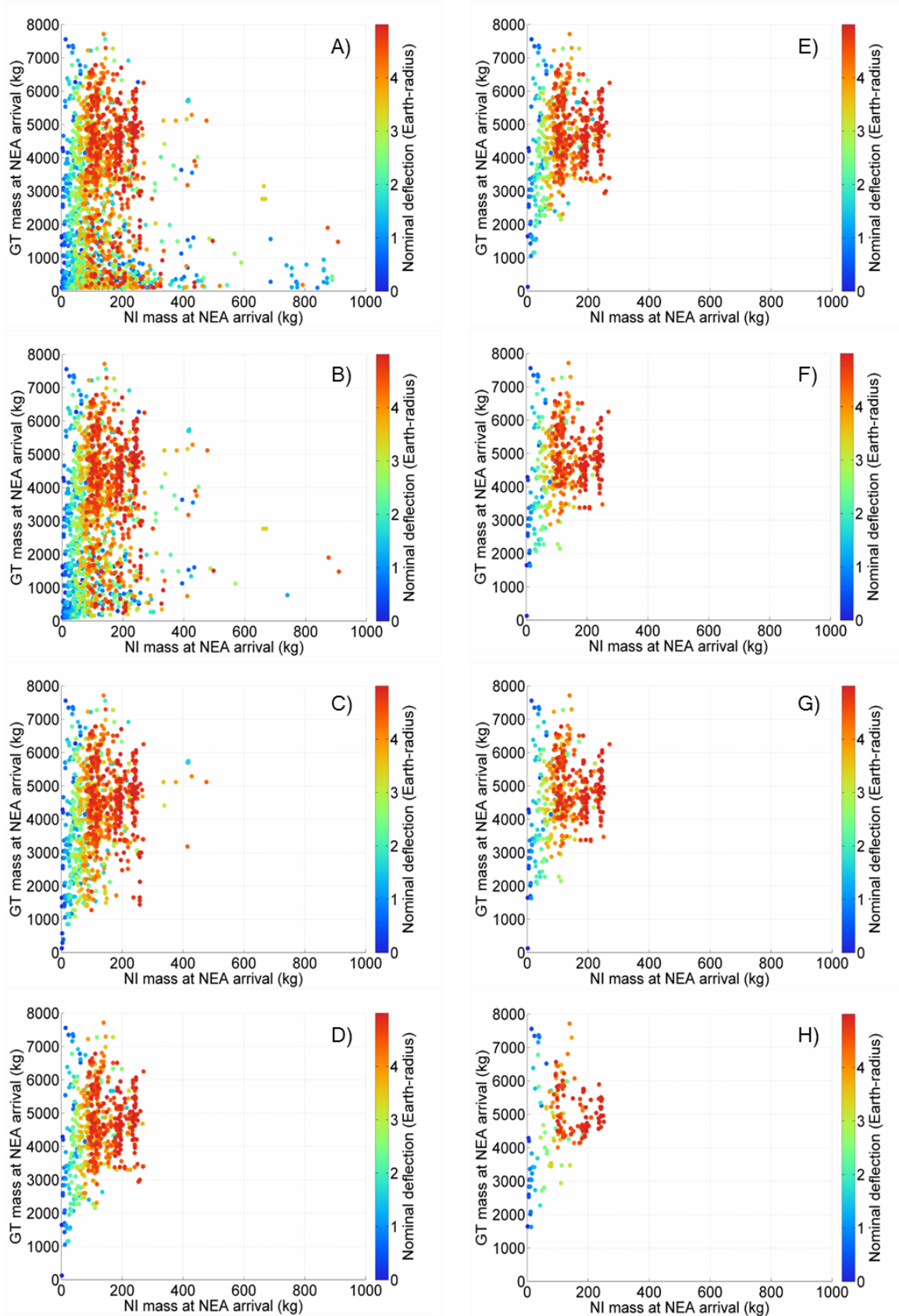
Figure 87 NI mass vs. GT mass at NEA arrival. A) $Bel_{nom} \geq 0.47.$ **B)** $Bel_{nom} \geq 0.51.$ **C)** $Bel_{nom} \geq 0.56.$ **D)** $Bel_{nom} \geq 0.57.$ **E)** $Bel_{nom} \geq 0.70.$ **F)** $Bel_{nom} \geq 0.83.$ **G)** $Bel_{nom} \geq 0.97.$ **H)** $Bel_{nom} = 1.00.$
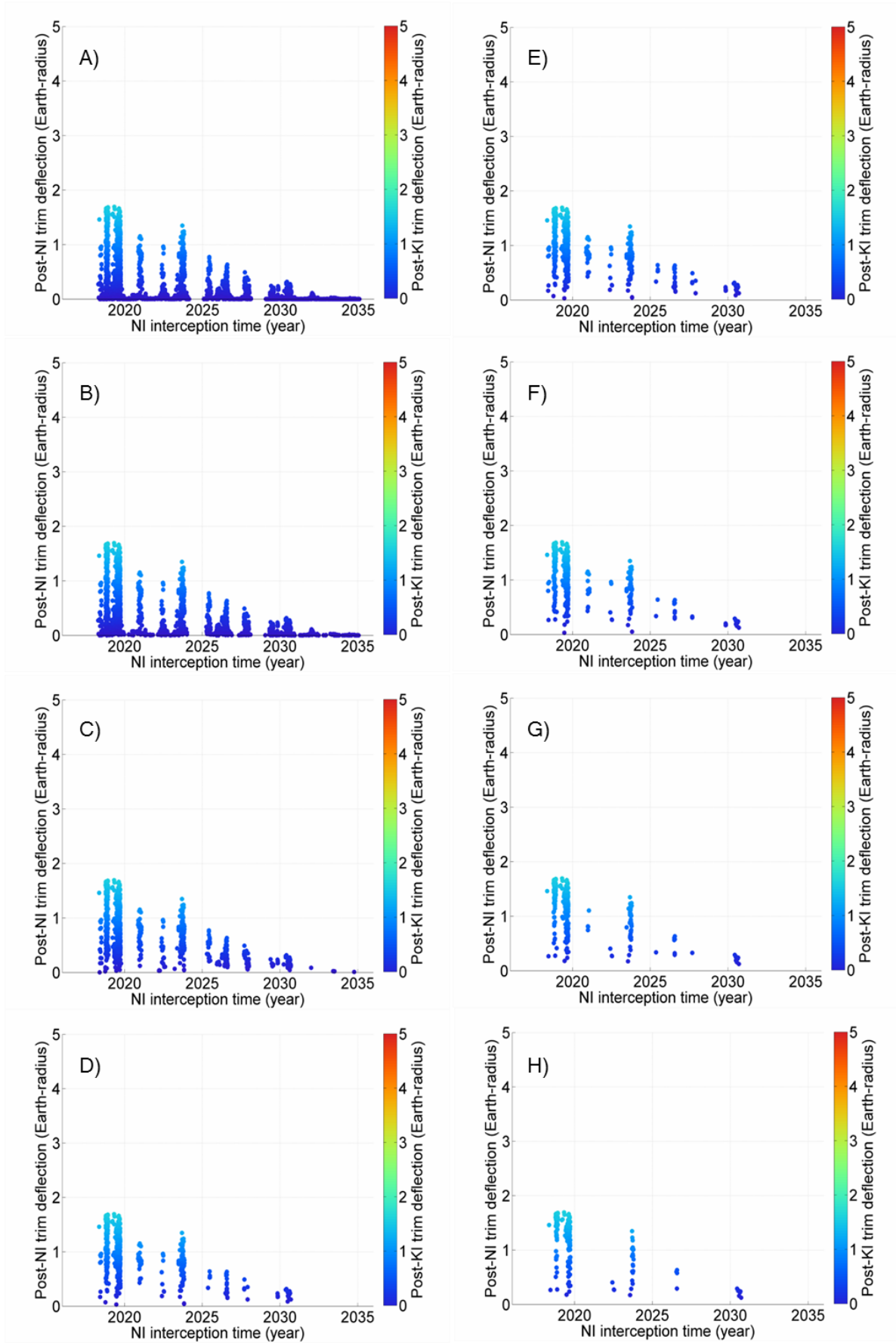
Figure 88 Post-NI deflection by GT. A) $Bel_{nom} \geq 0.47.$ **B)** $Bel_{nom} \geq 0.51.$ **C)** $Bel_{nom} \geq 0.56.$ **D)** $Bel_{nom} \geq 0.57.$ **E)** $Bel_{nom} \geq 0.70.$ **F)** $Bel_{nom} \geq 0.83.$ **G)** $Bel_{nom} \geq 0.97.$ **H)** $Bel_{nom} = 1.00.$
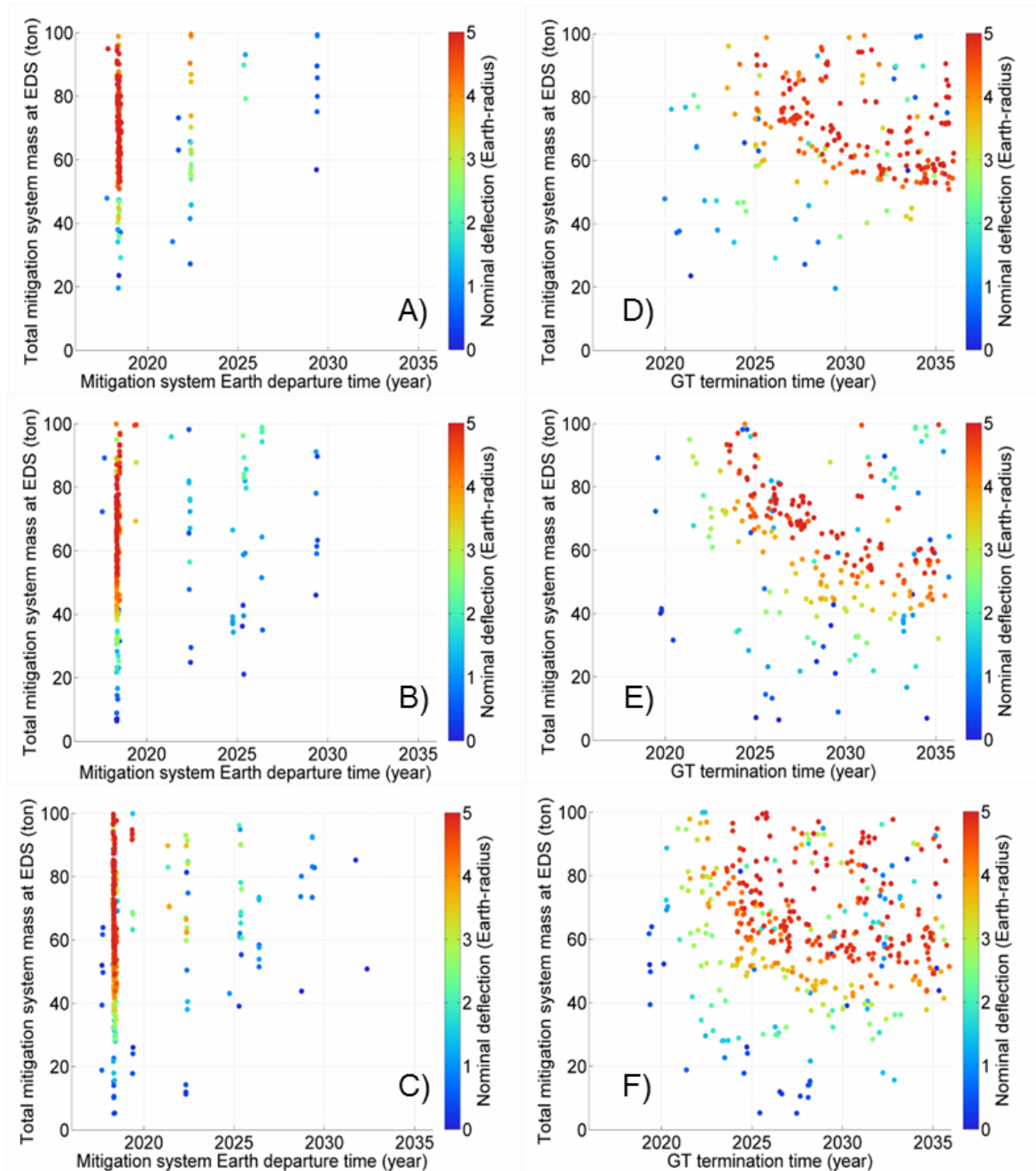
Figure 89 Comparison among the campaigns against three taxonomic classes: S, C, and M-types. These are results correspond to $\mathbf{Bel_{nom}} = \mathbf{1.00}$. The plots on the left-hand side show mitigation system Earth departure time vs. Total mitigation system mass at EDS. A) S-type. B) C-type. C) M-type. The plots on the right-hand side show GT termination time vs. total mitigation system mass at EDS. D) S-type. E) C-type. F) M-type.
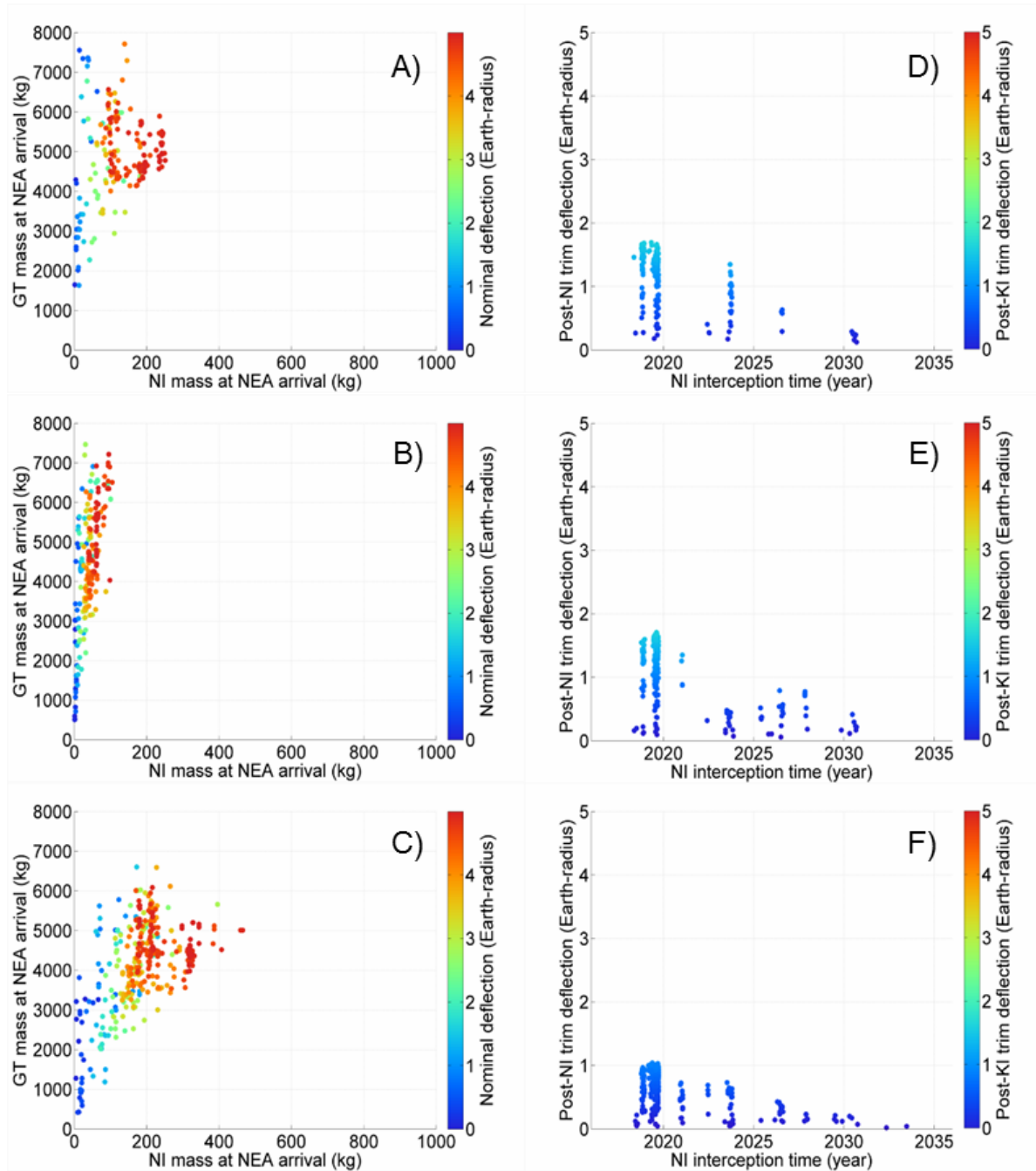
Figure 90 Comparison among the campaigns against three taxonomic classes: S, C, and M-types. These are results correspond to $Bel_{nom} = 1.00$. The plots on the left-hand side show NI mass vs. GT mass at NEA arrival. A) S-type. B) C-type. C) M-type. The plots on the right-hand side show NI interception time vs. Post-NI trim deflection. D) S-type. E) C-type. F) M-type.

5.2.3. SC-GT campaign

The Pareto-optimal results of SC-GT campaigns against a 140-m sized S-type VI_1 characterised under the ground-based characterisation scenario are shown in Figures 91-94.

Figure 91 shows that most of the optimal mitigation campaigns with large nominal deflections (i.e., redder dots) require the SC to have an Earth departure time t_1 around the year 2018 while the campaigns that depart after 2018 become much less efficient in terms of nominal deflection leverage. Particularly when a higher value of Belief measure is concerned, the availability of mitigation campaigns with reasonable nominal deflection after 2018 is strictly limited as can be seen in Figure 91-H). According to Figure 94, the optimal mitigation campaigns available around the year 2018 are associated with a relatively large fraction of the resultant b-plane deflection achieved through the GT mission. This can be interpreted as the large effects of the epistemic uncertainties in NEA physical properties on the SC deflection efficiency as shown in Chapter 3.This is also true for the results of the other virtual impactors as shown in Appendix A.4. On the other hand, if the campaign credibility is not prioritised, some optimal solutions after the year 2025 offer a relatively light-weight (20-40 tons) SC-GT campaign which satisfies the safe b-plane deflection distance of $2\frac{1}{2}$ $b_{\oplus}$ (4.16 Earth-radii) as can be seen in Figure 91-A).

Similar to the KI-GT and NI-GT mitigation campaigns, Figure 92 shows that there are optimal mitigation campaigns of various nominal deflection distances within a wide range of campaign completion time between 2020 and 2036. The Pareto-optimal SC-GT mitigation campaign with the earliest completion time can be found around the year 2020 which is approximately two years later than those for the KI-GT and NI-GT mitigation campaign scenarios around the year 2018. This can be explained by the fact that the SC mission takes a few weeks to months before it completes the deflection attempt.

Figure 93 shows the ratio of SC and GT masses at NEA arrival. It can be seen that SC-GT mitigation campaigns generally require larger fraction of the total mitigation system mass for the GT mission than for the SC mission. This is due to the inefficiency of the GT as a deflection technique in comparison with the SC which is one of the most efficient deflection techniques among the four deflection techniques considered in this doctoral thesis. If a higher value of Belief measure is concerned, the GT mass becomes substantially larger than the SC mass. This is again due to the inefficiency of the GT as an asteroid deflection technique as well as due to the large uncertain outcome of the SC mission. It is therefore

highly desirable to improve the deflection efficiency of the GT mission or simply to send more than a single SC mission to the target asteroid for the SC-GT campaign scenario.

If only the secondary impact keyhole passage is concerned, Figure 91 shows that the year 2029 will be the last launch opportunity for an effective mitigation campaign against VI_1. In addition, the avoidance of undesired keyhole passage due to the primary deflection can be fulfilled, counting on the deflection b_{trim} by post-SC deflection achieved through the GT mission (see Figure 94). It seems that large b_{trim} is provided through the GT mission when the SC mission takes place in the year 2019 and thus the mitigation campaigns are more efficient than the late-term ones.

Figures 95-96 show comparison analysis of the dual-deflection mitigation campaigns against VI_1 for three different taxonomic classes: S, C, and M-types. The results correspond to $Bel_{nom} = 1.00$. These results indicate that there are no significant differences between them in terms of the optimality of the EDS time (i.e., coloured dot patterns) as shown in Figure 95-A)-C). However, the optimal SC-GT campaigns against C-type VI_1 appears to be more efficient than the other two SC-GT campaign scenarios for S-type and M-type in terms of the total mitigation system mass at EDS. This is due to the fact that the SC mission to the C-type asteroid is more efficient than that to the S-type or M-type asteroid due to C-type's lowest asteroid mass and albedo among the three taxonomic classes. Similar to what has already been observed for the other two mitigation campaigns, Figure 95-D)-F) show that the SC-GT mitigation campaigns against the M-type asteroid require a considerable amount of GT mass in order to achieve a high level of campaign credibility. The optimal ratio of SC and GT masses at the NEA arrival also changes according to the taxonomic class (see Figure 96-A)-C)) as already highlighted for the other two campaign scenarios. Again, the SC mass for the case of C-type appears to be substantially smaller than those of the other KI-GT and NI-GT dual-deflection mitigation campaigns against C-type VI_1, which is due to the highest deflection efficiency by means of the SC mission to the C-type asteroid. The post-SC trim deflection through the GT mission (see Figure 96-D)-F)) is generally not immune to the asteroid taxonomy. Interestingly, Figure 96-D) shows that the SC-GT mitigation campaigns against S-type VI_1 have a larger fraction of deflection achieved through the GT mission in comparison with the other SC-GT campaigns against C-type and M-type VI_1 shown in Figure 96-E) and F). This finding implies that the optimal combination of the SC and GT missions (i.e., the ratio of deflection by each mission) is greatly dependent on the taxonomic class of the asteroid for the SC-GT mitigation campaign scenario.
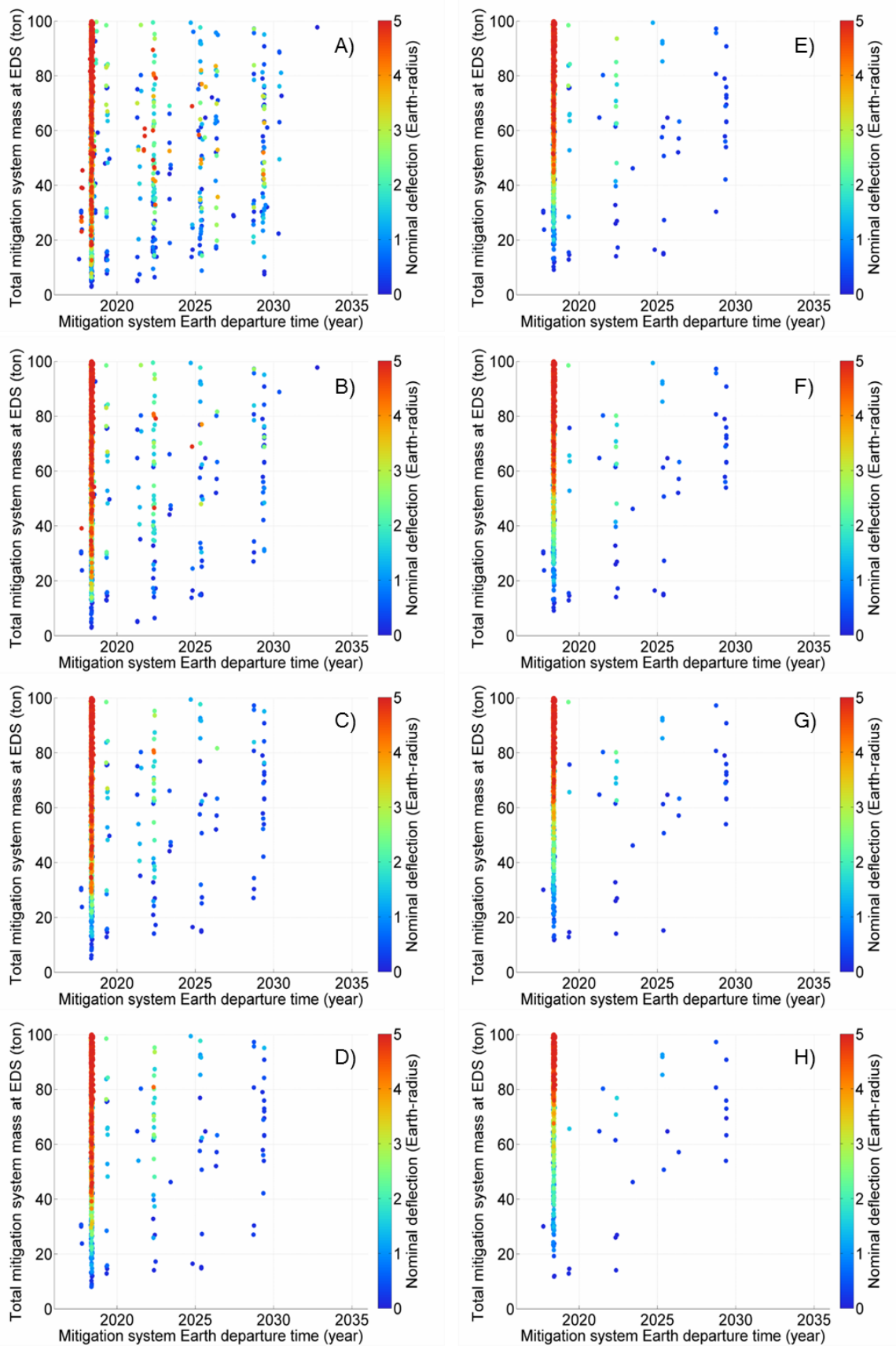
Figure 91 Pareto-optimal solutions for SC-GT campaigns against S-type VI$_1$ plotted for mitigation system Earth departure time vs. total mitigation system mass at EDS. The colours of the dots represent the degrees of nominal deflection distances between 0.0-5.0 Earth-radii. A) Bel$_{nom} \geq 0.47$. B) Bel$_{nom} \geq 0.51$. C) Bel$_{nom} \geq 0.56$. D) Bel$_{nom} \geq 0.57$. E) Bel$_{nom} \geq 0.70$. F) Bel$_{nom} \geq 0.83$. G) Bel$_{nom} \geq 0.97$. H) Bel$_{nom} = 1.00$.
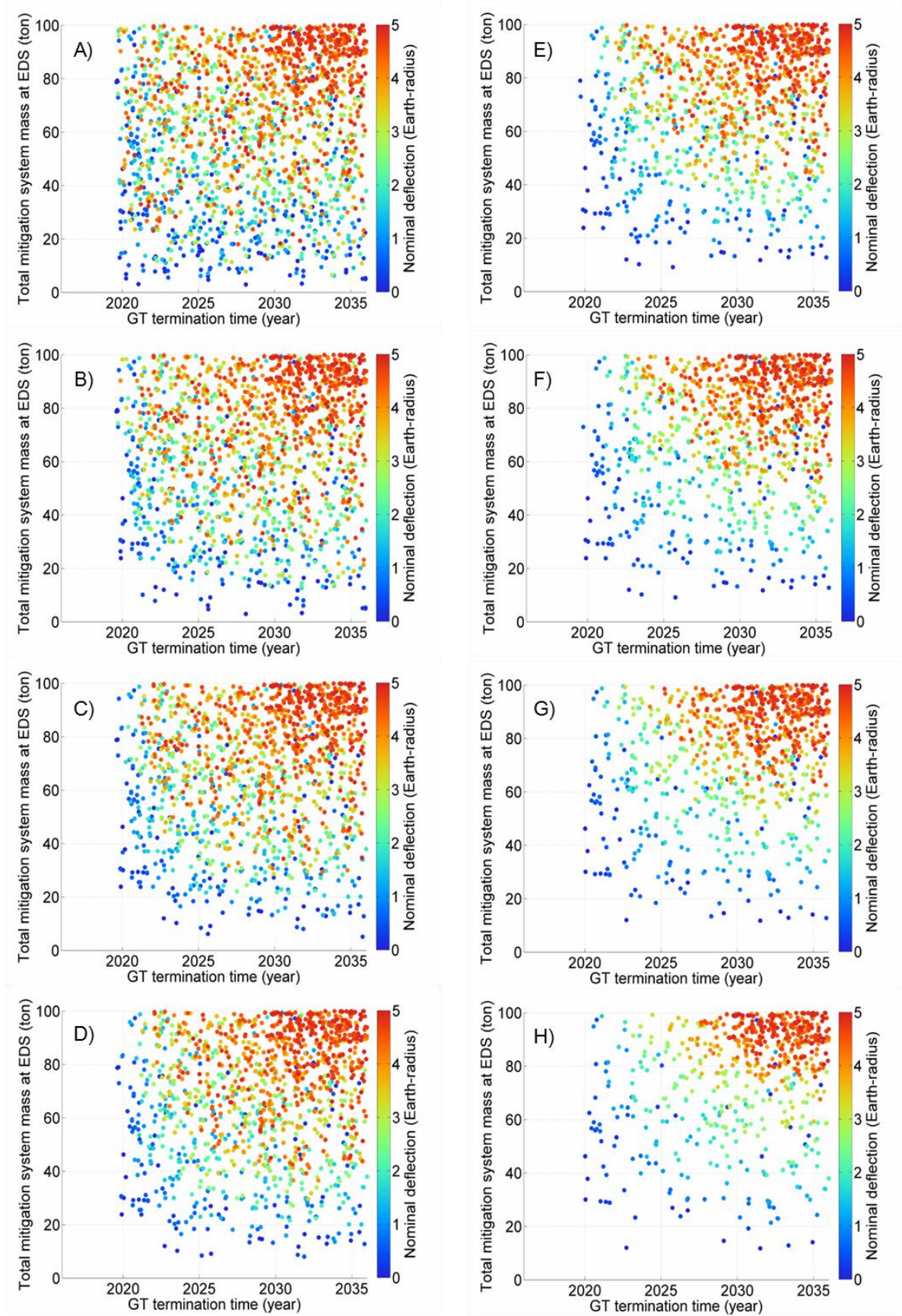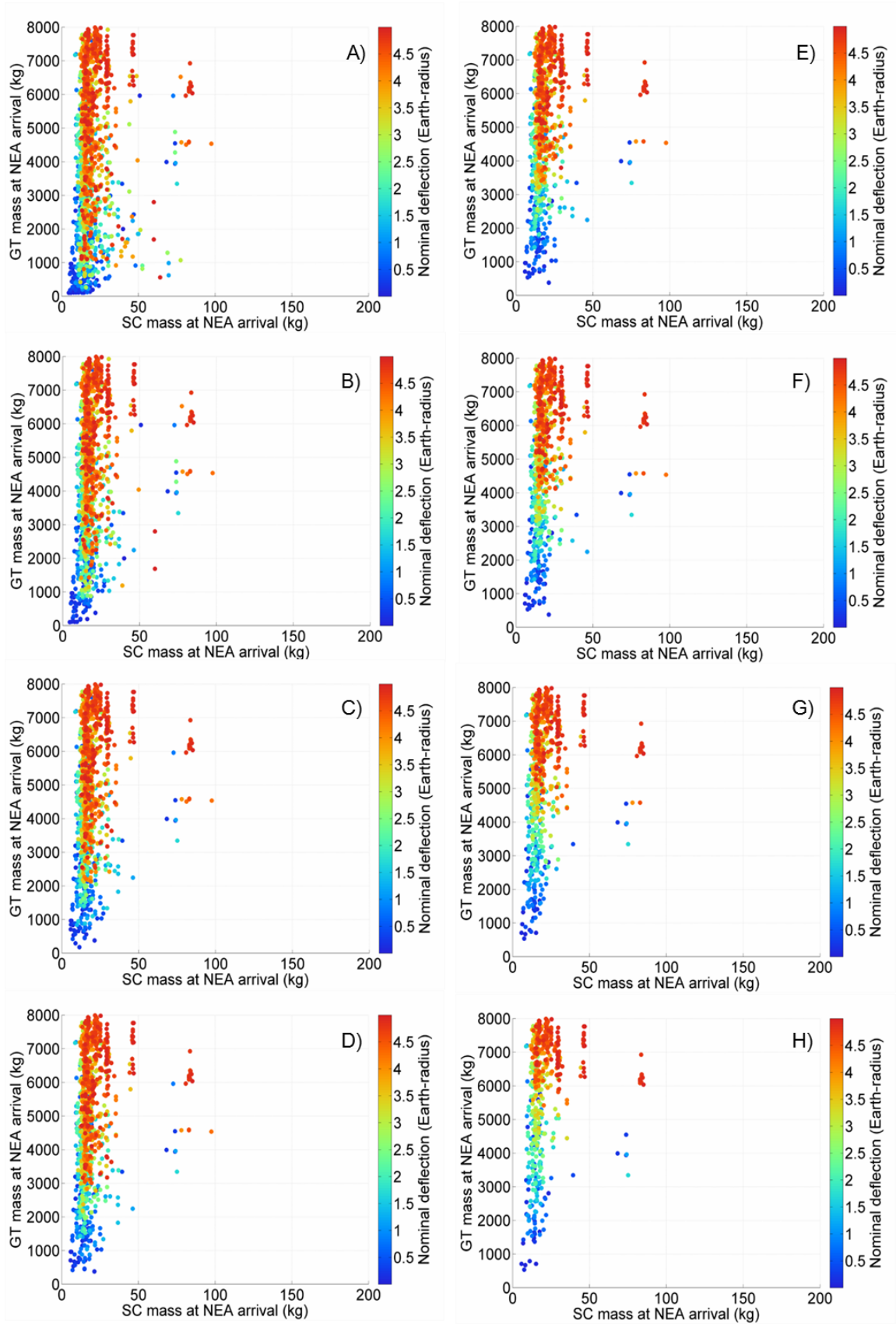
Figure 92 Pareto-optimal solutions for SC-GT campaigns against S-type VI$_1$ plotted for the GT termination time vs. total mitigation system mass at EDS. A) $\text{Bel}_{\text{nom}} \geq 0.47.$ **B)** $\text{Bel}_{\text{nom}} \geq 0.51.$ **C)** $\text{Bel}_{\text{nom}} \geq 0.56.$ **D)** $\text{Bel}_{\text{nom}} \geq 0.57.$ **E)** $\text{Bel}_{\text{nom}} \geq 0.70.$ **F)** $\text{Bel}_{\text{nom}} \geq 0.83.$ **G)** $\text{Bel}_{\text{nom}} \geq 0.97.$ **H)** $\text{Bel}_{\text{nom}} = 1.00.$

Figure 93 SC mass vs. GT mass at NEA arrival. A) $Bel_{nom} \geq 0.47$. **B)** $Bel_{nom} \geq 0.51$. **C)** $Bel_{nom} \geq 0.56$. **D)** $Bel_{nom} \geq 0.57$. **E)** $Bel_{nom} \geq 0.70$. **F)** $Bel_{nom} \geq 0.83$. **G)** $Bel_{nom} \geq 0.97$. **H)** $Bel_{nom} = 1.00$.
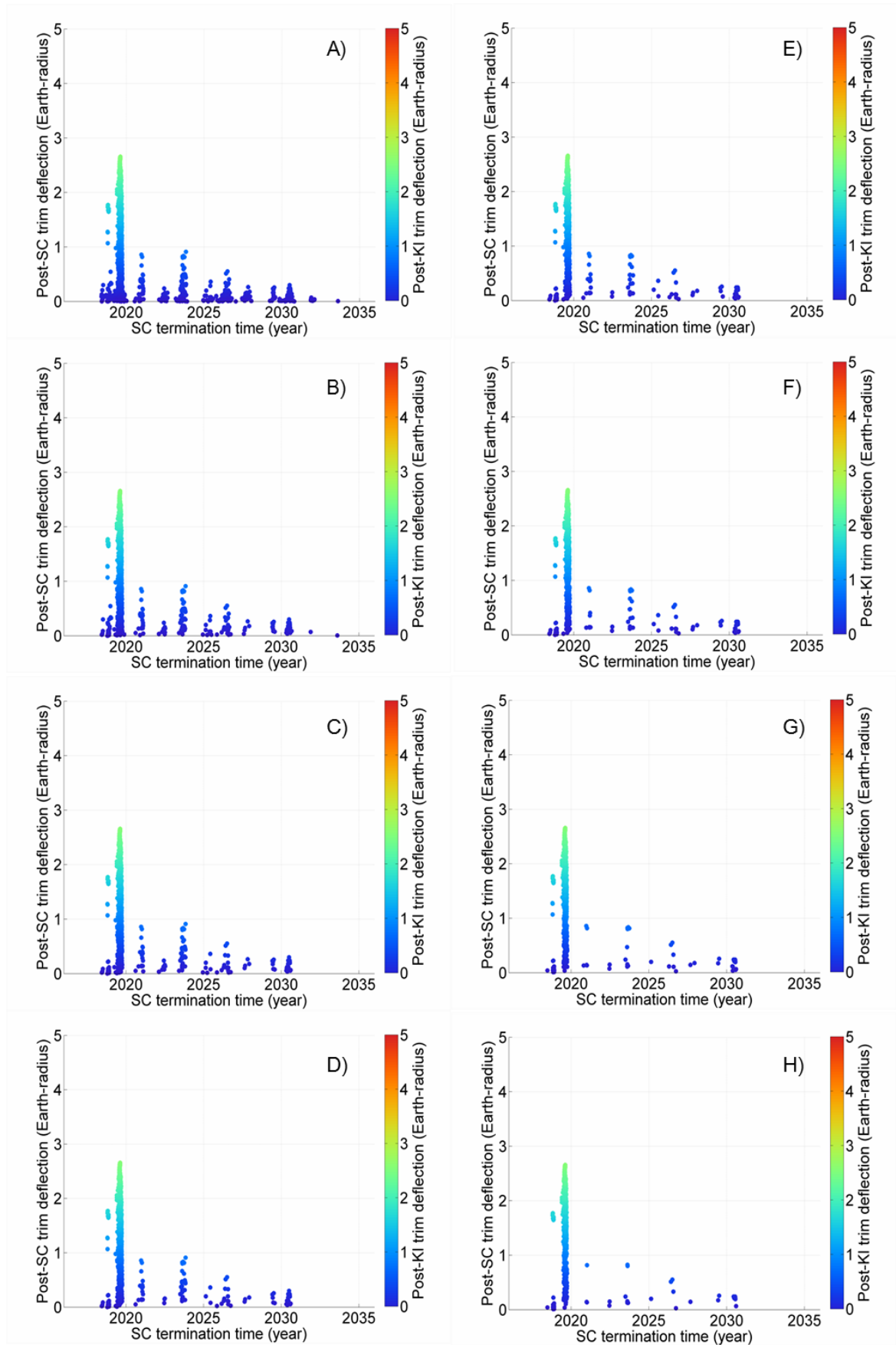
Figure 94 Post-SC deflection by GT. A) $\mathrm{Bel_{nom}} \geq 0.47.$ **B)** $\mathrm{Bel_{nom}} \geq 0.51.$ **C)** $\mathrm{Bel_{nom}} \geq 0.56.$ **D)** $\mathrm{Bel_{nom}} \geq 0.57.$ **E)** $\mathrm{Bel_{nom}} \geq 0.70.$ **F)** $\mathrm{Bel_{nom}} \geq 0.83.$ **G)** $\mathrm{Bel_{nom}} \geq 0.97.$ **H)** $\mathrm{Bel_{nom}} = 1.00.$
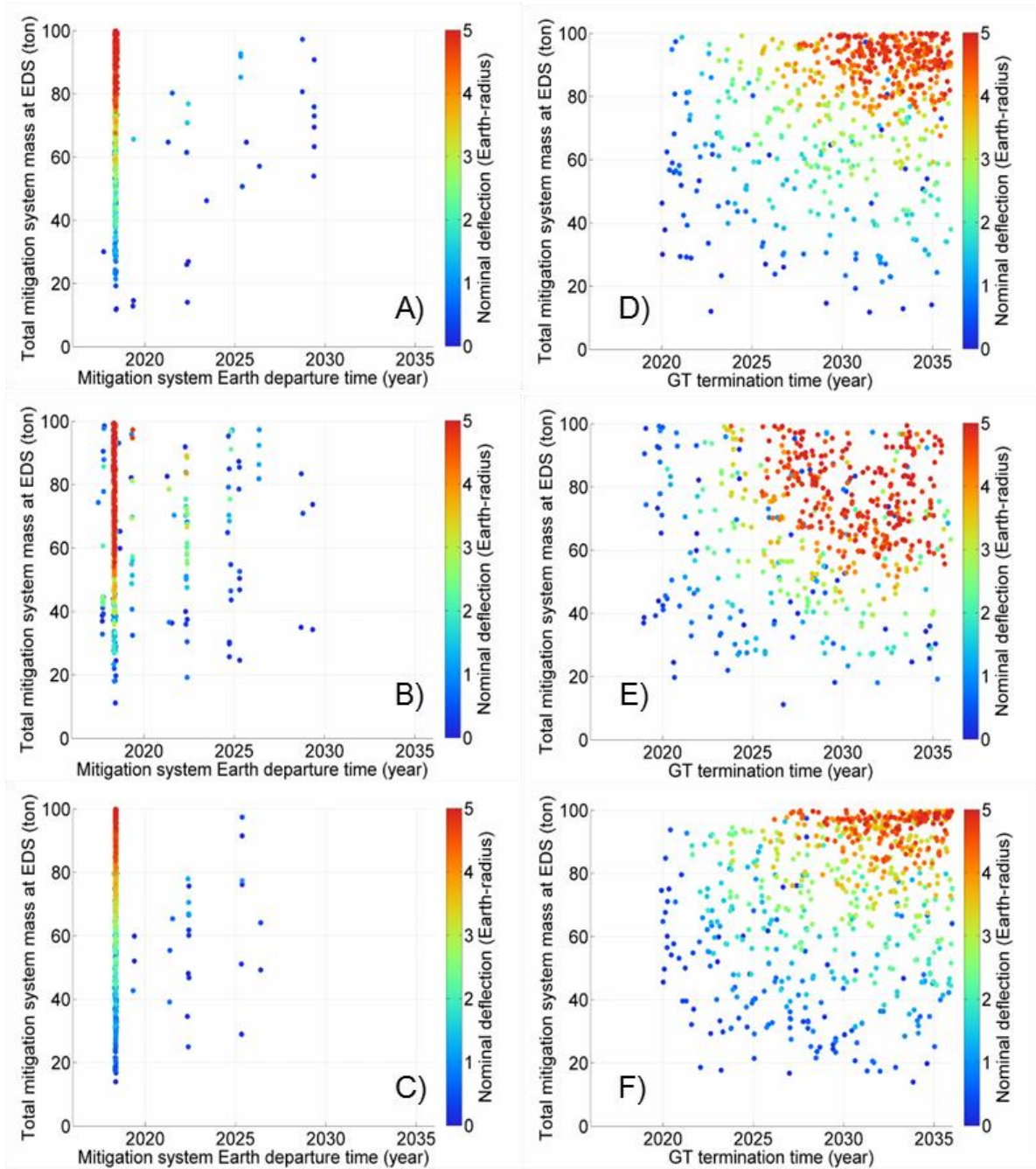
Figure 95 Comparison among the campaigns against three taxonomic classes: S, C, and M-types. These are results correspond to $\mathrm{Bel_{nom}} = 1.00$. The plots on the left-hand side show mitigation system Earth departure time vs. Total mitigation system mass at EDS. A) S-type. B) C-type. C) M-type. The plots on the right-hand side show GT termination time vs. total mitigation system mass at EDS. D) S-type. E) C-type. F) M-type.
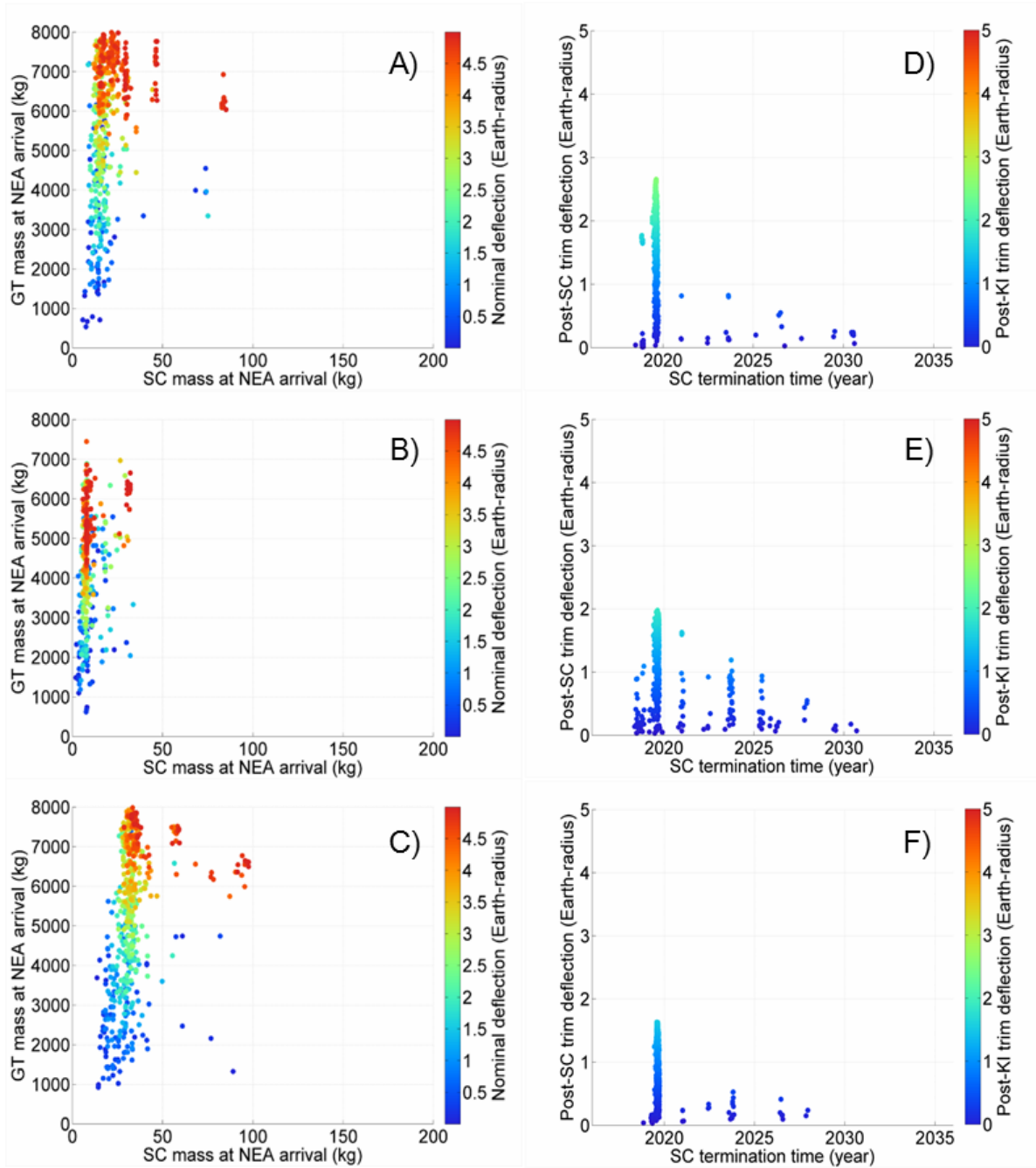
Figure 96 Comparison among the campaigns against three taxonomic classes: S, C, and M-types. These are results correspond to $Bel_{nom} = 1.00$. The plots on the left-hand side show SC mass at NEA arrival vs. GT mass at EDS. A) S-type. B) C-type. C) M-type. The plots on the right-hand side show SC termination time vs. Post-SC trim deflection. D) S-type. E) C-type. F) M-type.

5.3. Chapter summary

This chapter has emphasised the development of an innovative hazardous NEA mitigation campaign planning approach under the uncertain information of the fundamental asteroid characteristics. In particular, a possible approach – dual-deflection mitigation campaign consisting of primary and secondary deflection missions – has been studied in detail. In order to evaluate the campaign credibility/confidence level of each deflection mission subject to the uncertain NEA characteristics, the uncertainty quantification technique called Evidence Theory is used once again. The results of the dual-deflection mitigation campaigns have shown that dual-deflection mitigation campaign planning entails a series of competing requirements and constraints that must be assessed in order to achieve a mitigation campaign with optimal performance (i.e., deflection outcome or b-plane deflection) and high confidence (Belief) in successful deflection.

Given the GT as a secondary deflection mission, the Belief of a nominal deflection can be improved, to a certain degree, by years of tractoring operations before and after a primary deflection mission; however the GT's deflection efficiency is not as high as the other deflection techniques, resulting in a large total mitigation systems mass for any dual-deflection mitigation campaign with a high Belief value/confidence level. It should be noted, however, that this does not necessarily mean that the GT must always start intercepting the target body immediately after the NEA rendezvous and keep tractoring as scheduled but the actual operation of the GT is still subject to the in-situ NEA characterisation as well as the uncertain outcome of the primary deflection.

Given a 20-year warning time, a mitigation campaign with a completion time (i.e., GT termination time) of approximately half the warning time seems to be more optimal than a longer-term mitigation campaign or a campaign with a larger total mitigation system mass [48]. This appears to be due to the deflection efficiency reduction with time (see Figure 15 in Chapter 1) and the exponential increase in the launch costs of the mitigation systems for a late-stage mitigation campaign.

Possible secondary impact keyhole passage due to an undesired outcome of primary deflection mission can be avoided by a relatively light-weight GT in a dual-deflection mitigation campaign. However, the GT mass at the EDS tends to be still larger than that of any primary deflection mission due to its mass (deadweight) requirement to achieve an effective gravitational interaction. This makes the GT mitigation technique less attractive as

a secondary deflection mission option even though its deflection efficiency is mostly immune to the epistemic uncertainties in the NEA characteristics.

Finally, this particular mitigation campaign planning approach presented here could be useful for the near-term hazardous NEA mitigation campaigns where we might have to tap into our incomplete knowledge of NEAs for mitigation campaign design. The approach enables the selection of the best possible combination of deflection missions from a catalogue of various possible mitigation campaign options, without compromising the campaign credibility. However in the long-term future, further knowledge of the NEA population and specific NEAs and PHOs will have steadily accumulated and improved thanks to a number of forthcoming NEA survey and exploration missions such as NEOSSat, Sentinel, Hayabusa 2, and OSIRIS-REx as well as the recently announced NASA's near-term NEA redirect mission that will also involve human exploration of the captured asteroid for in-situ characterisation.

6

6. Conclusions

"Nothing is more fatal to the progress of the human mind than to presume that our views of science are ultimate, that our triumphs are complete, that there are no mysteries in nature, and that there are no new worlds to conquer."

— Sir Humphrey Davy

This doctoral thesis is the conclusion of the three year research study on asteroid hazard mitigation, and more specifically on hazard mitigation campaign planning and credibility analysis. The work focused on preliminary characterisation of the hazardous object, mitigation mission analysis under the epistemic uncertainties in the fundamental asteroid characteristics, and dual-deflection mitigation campaign planning that takes the campaign credibility into account. The author believes that the results presented in this doctoral thesis will be found to be beneficial to the planetary defense community as well as general readers interested in this field. The following paragraphs summarise the major research findings.

Chapter 1 sets the scene for NEOs and their Earth impact hazards. The current statistics on the NEO population show that the near future Earth impact hazards may occur due to smaller (140 m or smaller in diameter) asteroids rather than kilometre sized objects that can cause a catastrophic devastation to the Earth's environment. A series of important terminologies in the field of planetary defense such as b-plane deflection, keyhole, MOID, etc. were defined to familiarise the readers whose background is not planetary defense. In order to exercise more realistic NEO hazard mitigation campaign planning and analysis throughout this thesis, six different virtual Earth menacing asteroids of various orbits: VI_1-VI_6 were introduced.

Chapter 2 put an emphasis on preliminary characterisation of an identified hazardous NEA. Here, three different levels (ground-based, space-based, and proximity levels) of preliminary characterisation approaches were defined. Evidence Theory, used to quantify the epistemic uncertainty of the NEA properties, appears more appropriate than conventional uncertainty quantification techniques, especially during the early stages mitigation campaign planning when our knowledge of the target hazardous body is most likely limited only to ground-based characterisation level. Unlike a typical system margin approach, Evidence Theory allows engineers or decision makers to take the confidence level of a given deflection technique into consideration, which means that they can elaborately design or select the primary deflection mission as well as complementary missions to reduce the risk of mission failure. Each characterisation approach has a unique set of asteroid physical properties with epistemic uncertainties, which is summarised as a list of the physical properties with associated basic probability assignments (BPAs). Note that the BPA structures were assumed by combining all the available information from different literature sources of the discovered NEOs and meteorite characteristics such that they are inevitably biased to some extent.

Chapter 3 focused on the mathematical modelling of four different asteroid deflection techniques: KI, NI, SC, and GT and the evaluation of the effects of epistemic uncertainties on their deflection outcomes (i.e. b-plane deflection). Asteroid deflection methodologies have been traditionally assessed in terms of a variety of criteria including system configurations, mission timelines, launch capabilities, required warning times subject to TRLs, etc. Reliability however has not been taken into consideration as an important criterion until this work. We demonstrated that different asteroid deflection missions have different uncertainty levels subject to the epistemic uncertainties in the physical properties of the target asteroid and found that the mission reliability could be profoundly compromised in some cases. The results indicate that a more rigorous characterisation scenario (e.g., proximity characterisation) allows us to estimate the outcome of an asteroid deflection attempt with higher confidence level. The GT is generally inefficient and not competitive with the other three techniques; however, its deflection outcome is more predictable and thus could be a good option as a back-up deflection mission and/or orbital trim manipulation for keyhole avoidance. It should be noted however it is questionable to make a complete and fair comparison between the different deflection techniques since this study makes a number of assumptions and simplifications in the mathematical models of the deflection techniques. In addition, most of the asteroid deflection techniques studied here are still at the theoretical development level and require further development at the technological level.

Chapter 4 covered the study on the effects of NEO dynamics and inhomogeneity particularly on the outcomes of KI, GT, and SC deflection missions. The results show that the accuracy of the deflection achieved through a KI mission is subject to not only the physical properties of the asteroid but also to the KI's terminal guidance precision. If the terminal guidance of the KI is ideal (i.e., if the CEP is zero), the outcome of the KI mission (i.e., impulsive velocity change) will be governed by the density distribution/COM offset from the centre of asteroid figure and, of course, by the asteroid mass. Also, it was clearly shown that the b-plane deflection through a GT mission will not be entirely free of the effects of the asteroid inhomogeneity and dynamics as the GT spacecraft will inevitably experience perturbations due to the gravity fluctuation as the asteroid rotates, particularly when the GT spacecraft hovers in close proximity to the target body (e.g. 10-20 m from the protruding ends of an irregularly-shaped, elongated asteroid). Solar radiation pressure will however not be a major cause of orbital perturbations of the GT spacecraft about the asteroid when the spacecraft is close to the asteroid although it will be an issue when further away from the asteroid (i.e. free of the asteroid's gravitational field). Finally, the analysis of the SC mission to the rotating ellipsoidal asteroid has revealed that the SC deflection efficiency is dependent on the eccentricity and rotational velocity of the asteroid of any type. A fast rotational velocity could profoundly compromise the efficiency while the effect of the eccentricity of the asteroid on the SC deflection efficiency will not be as significant as that of the rotational state unless it is highly elongated (eccentricity of >0.9).

In Chapter 5, an approach of multiple deflection campaigns: dual-deflection mitigation campaigns was studied in detail. Dual-deflection mitigation campaigns were designed by optimising the mission cost, duration, deflection efficiency, and most importantly, the campaign credibility (i.e. the confidence level on the success of the given mitigation campaign). Pareto-optimal solutions for the dual-deflection campaigns consisting of KI/NI/SC and GT missions (designated as KI-GT, NI-GT, and SC-GT campaigns) were derived through the multi-objective optimisation approach. Among the three campaign options, the NI-GT campaigns generally outperform the other two options due to the highest YTW ratio of the NI mission. However, although the launch windows for the optimal SC-GT campaigns are strictly limited to the early-stages about the year 2018 in the 20-year warning time, they can be as competitive as the optimal NI-GT mitigation campaigns for some cases. The KI-GT campaigns are generally inferior to the other two options due to the high KI mass requirement for the KI mission; however, it is still advantageous that the outcome of the KI mission is instantaneous as well as the NI mission unlike the slow-push SC mission. In summary, the results of this chapter show that the dual-deflection mitigation

campaigns would be found to be advantageous particularly if the target asteroid's fundamental physical characteristics are not well-characterised during the early stages of mitigation campaign planning. However, they also shed light upon the fatal inefficiency of the GT mission concept as a secondary/back-up deflection mission for direct impact hazard mitigation, resulting in the substantial increase in the total campaign launch costs. The concept may be applicable to keyhole avoidance since b-plane deflection leverage required for a few hundred metre sized keyhole avoidance could be several orders of magnitude smaller than that required for 1.0 $b_\oplus$ for instance.

A

Appendices

A.1. Momentum multiplication approximation

All the results here are associated with the momentum multiplication approximation by Walker's experiment-based linear approximation formula that has been previously introduced and compared with Holsapple's approximation formula in Chapter 3. The KI mass requirements shown in Figures 97 and 98 correspond to those shown in Figures 36 and 37 whereas the NI mass requirements shown in Figure 99 and 100 correspond to those shown in Figures 39 and 40, respectively. The normalised velocity changes by NI shown in Figures 101 and 102 correspond to those shown in Figures 41 and 42. Finally, the SKE shown in Figures 103-105 corresponds to that shown in Figures 44-46.

Firstly, unlike Holsapple's momentum multiplication approximation, Figures 97 and 98 show that Walker's experiment-based linear approximation results in less density/asteroid mass dependency of the KI mass required for the safe deflection. This can be interpreted as a result of the two different approximation formulae of the momentum multiplication β. The same features can be seen in Figures 99 and 100 for the NI. However, the results of M-type show substantially (i.e., an order of magnitude) larger NI mass required for the same amount of deflection in comparison with those of Holsapple's momentum multiplication approximation particularly when the stand-off distance is non-optimal (e.g. 0.5 asteroid-radii). Figures 101-C) and 102-C) clearly show that the scattering debris contribution to the instantaneous velocity change is not as significant as that has been shown in Figures 41-C) and 42-C). Again, this is due to the two different approximation formulae of β. The SKE also becomes substantially large when the target body is M-type for Walker's experiment-based linear approximation due to the increase in required NI mass when the stand-off distance is non-optimal.

As a final remark on the momentum multiplication approximation, mathematical modelling of both KI and NI deflection techniques requires an accurate formulation of the momentum multiplication factor β, which is not an easy job as it has been described in Chapter 3. As a hazardous asteroid deflection technique, both KI and NI have a relatively high TRL; however, their deflection outcomes (i.e., instantaneous velocity changes) are highly dependent on the actual value of β of the target asteroid as well as the given approximation formula of β. It is therefore desirable to send a demo mission to a non-hazardous NEO and check if these high TRL deflection techniques work as expected. If not, it will still allow us to refine the deflection techniques and redefine the approximation of the momentum multiplication β directly based on the deflection demonstration mission results.
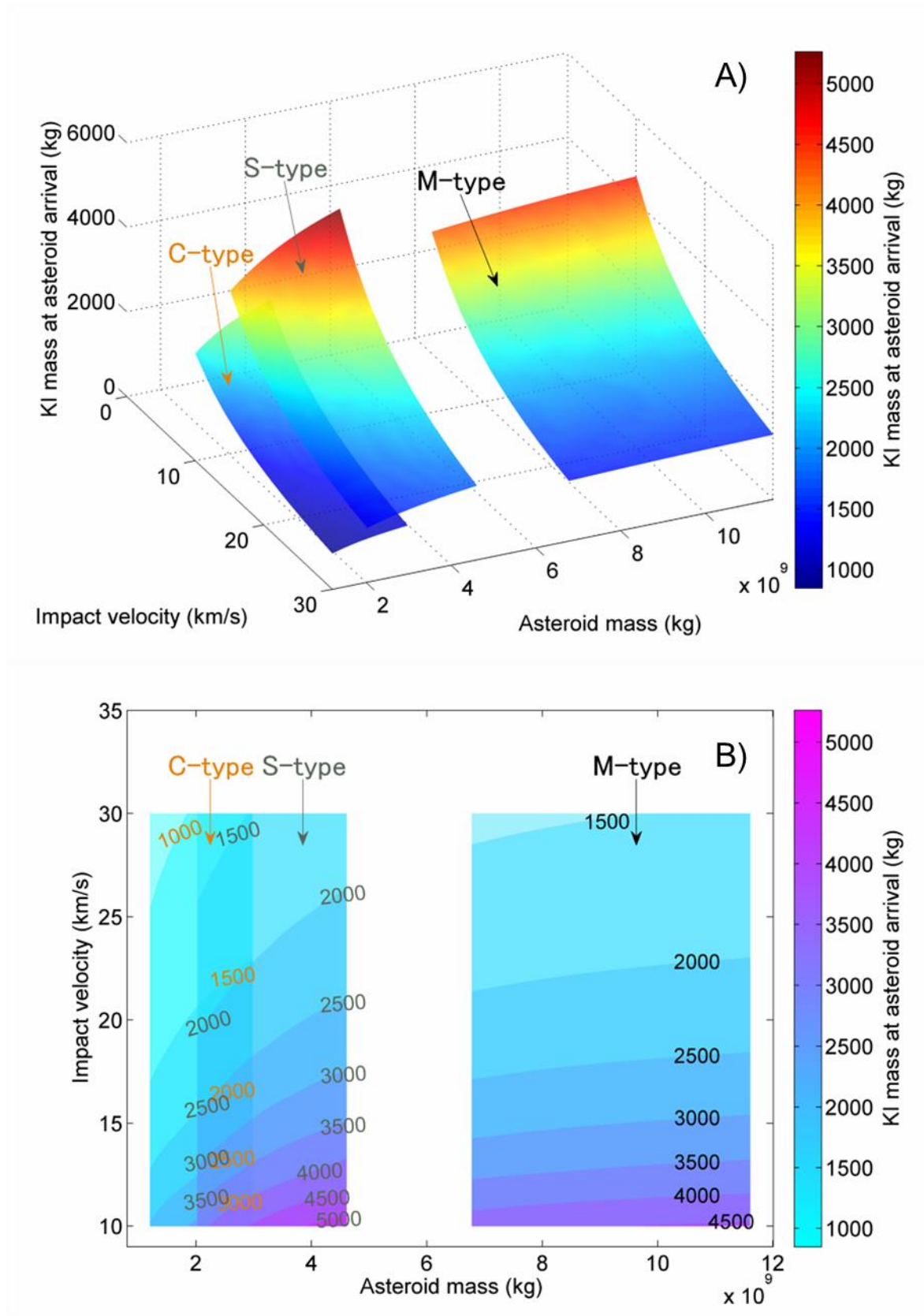
Figure 97 KI mass required to provide a 140-m sized VI$_1$ with $2\frac{1}{2}$ b$_\oplus$ deflection on the 2036 b-plane given 10 years of warning time before the impact epoch on 13 April 2036. The kinetic impact occurs on 9 October 2026, at the first perihelion of the VI$_1$ within the given mitigation window (i.e. 10-year warning time). A) Three-dimensional plot of the required KI mass for different asteroid mass associated with three taxonomic classes and kinetic impact velocity ranging between 10-30 km/s. B) Contour plot clearly indicates that the KI against an M-type asteroid outperforms that against an S-type asteroid: the required KI mass for M-type is smaller than that for S-type, given the same v_{imp} and asteroid mass.
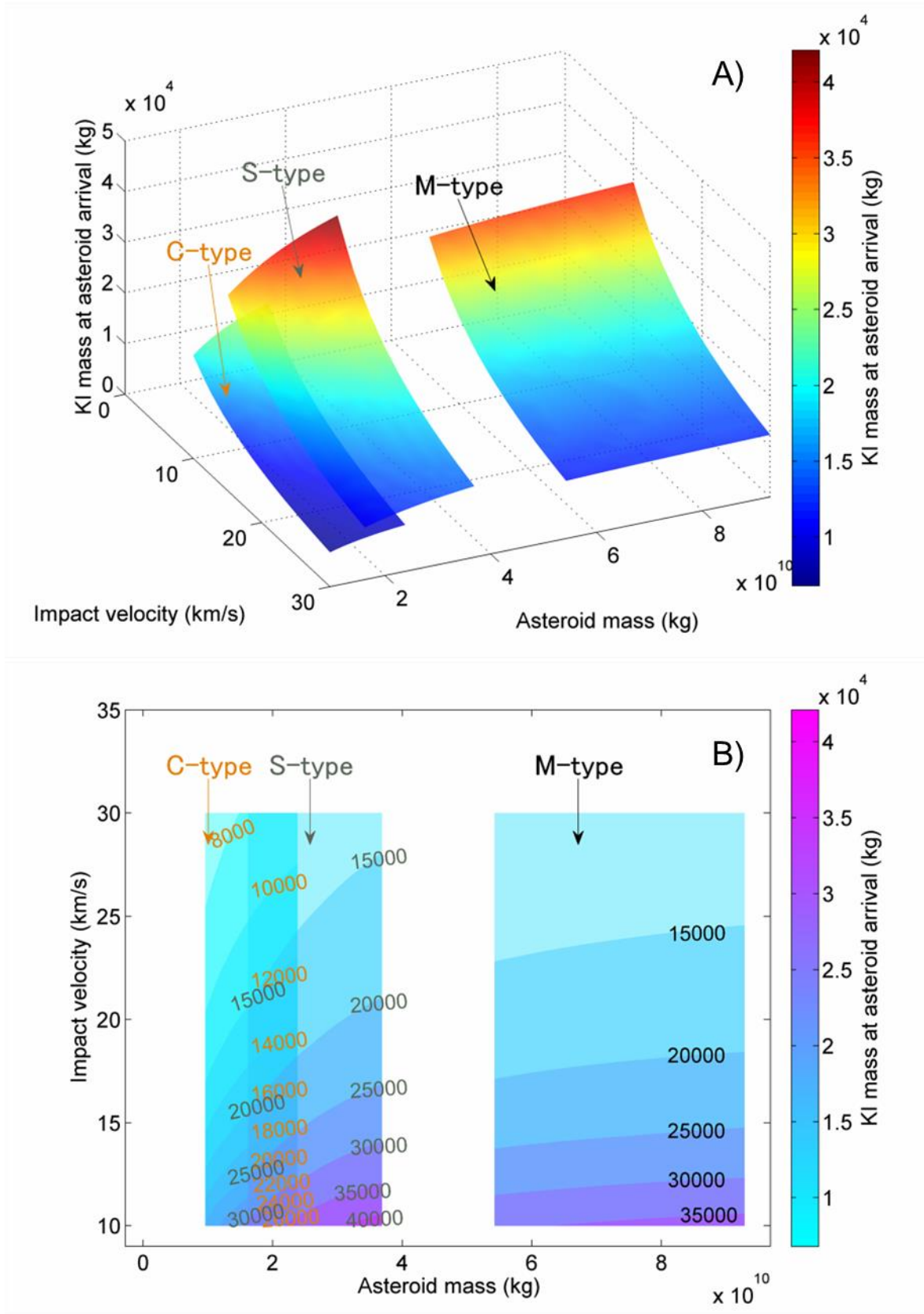
Figure 98 KI mass required to provide a 280-m sized VI$_1$ with 2½ b$_\oplus$ deflection on the 2036 b-plane given 10 years of warning time before the impact epoch on 13 April 2036. The kinetic impact occurs on 9 October 2026, at the first perihelion of the VI$_1$ within the given mitigation window (i.e. 10-year warning time). The required KI mass for a reasonable deflection of an Apophis-like asteroid of any taxonomic class becomes enormous (>10 tons at the asteroid arrival) given reasonable impact velocity of 10-15 km/s, resulting in the KI approach an unrealistic deflection option unless a higher-velocity (>30 km/s) impact through a retrograde orbital transfer, etc. is available [107].
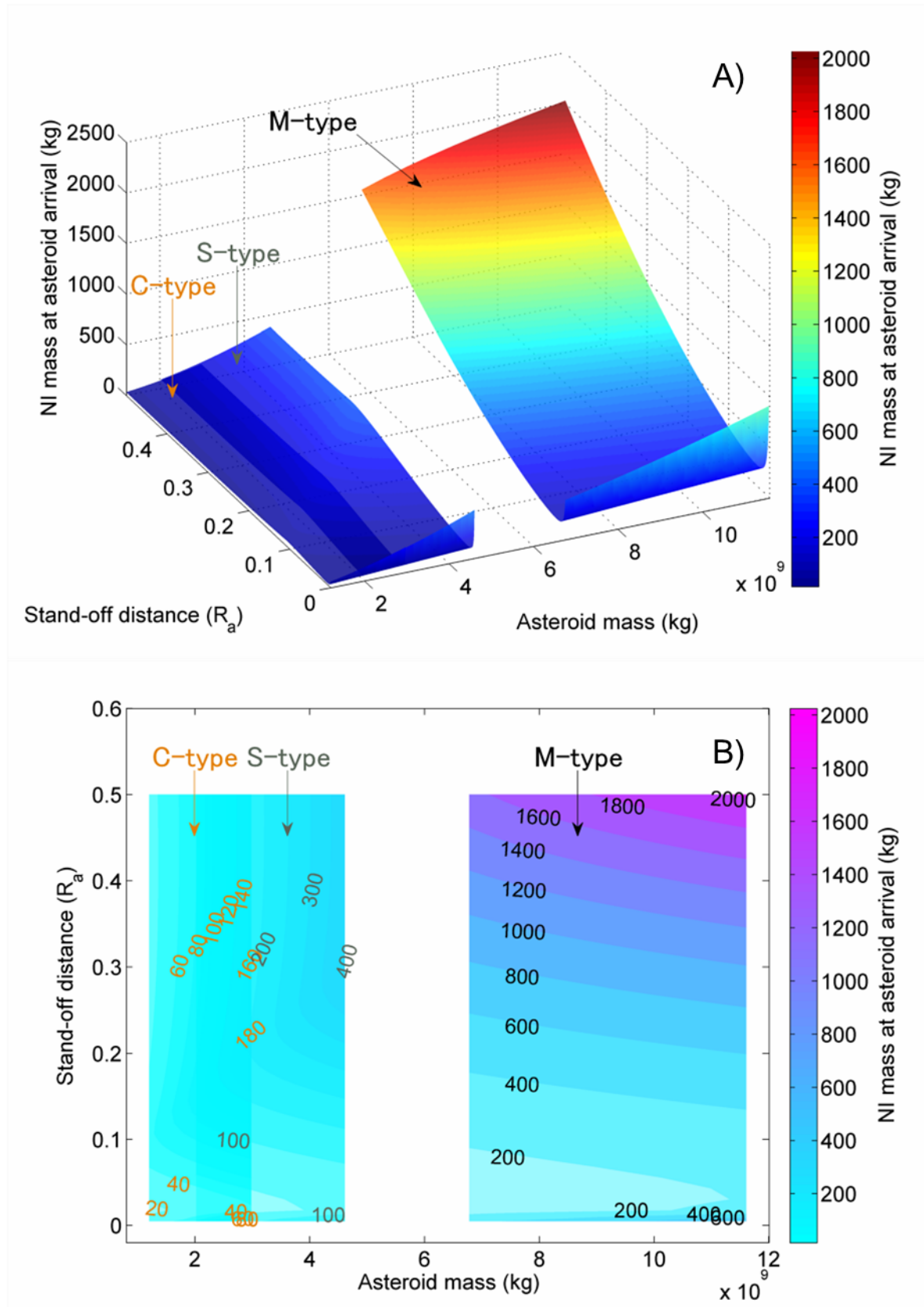
Figure 99 NI mass required to provide a 140-m sized VI₁ with 2½ b⊕ deflection on the 2036 b-plane given 10 years of warning time before the impact epoch on 13 April 2036. The nuclear interception takes place on 9 October 2026, at the first perihelion of the VI₁ within the given mitigation window (i.e. 10-year warning time).
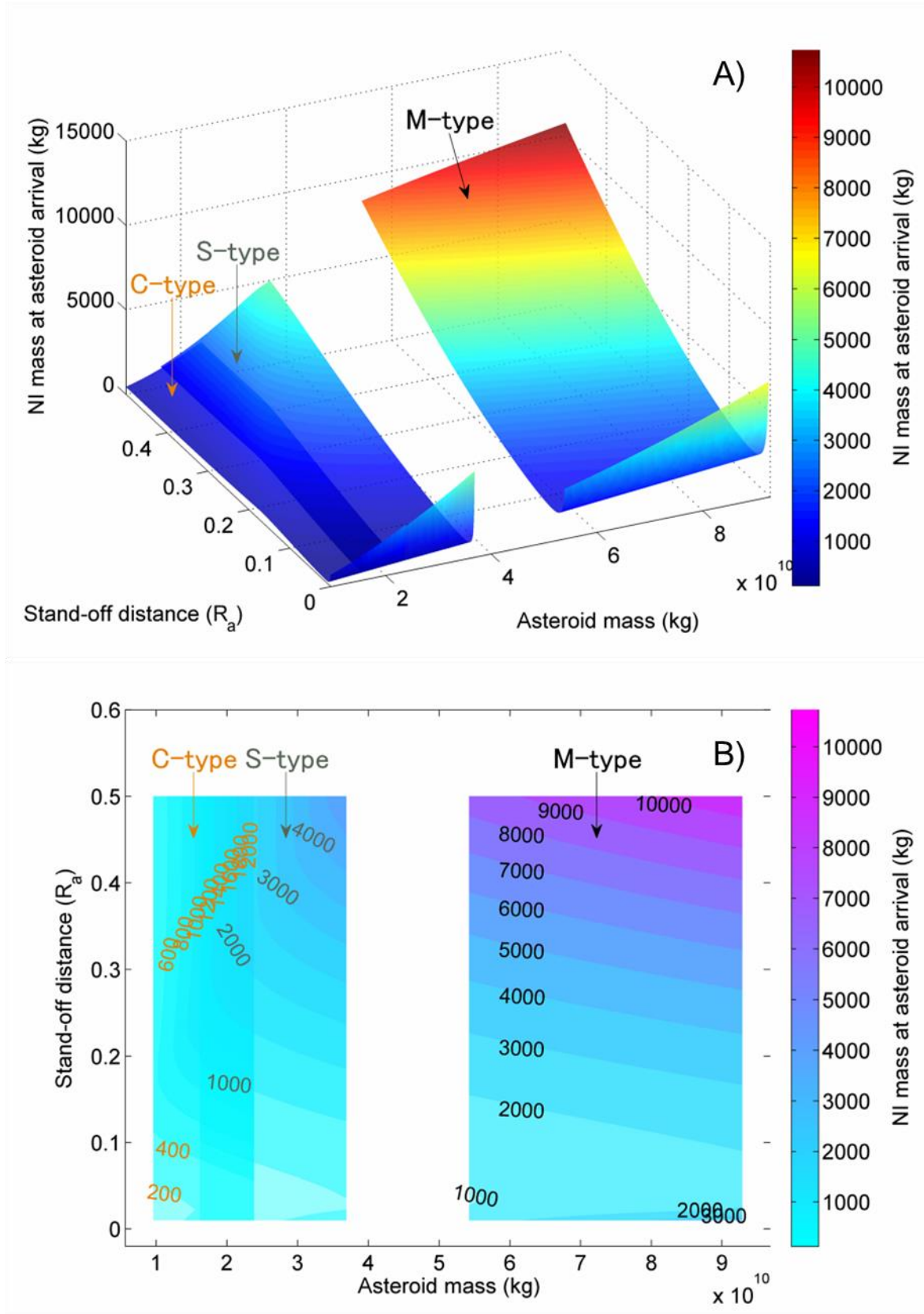
Figure 100 NI mass required to provide a 280-m sized VI$_1$ with 2½ b$_\oplus$ deflection on the 2036 b-plane. Apparently, due to the conservative estimate of YTW, the NI mass resulted in a few tons for non-optimal stand-off scenarios but it could be technically smaller than 1000 kg, given a more realistic value of YTW for larger nuclear explosive packaging.
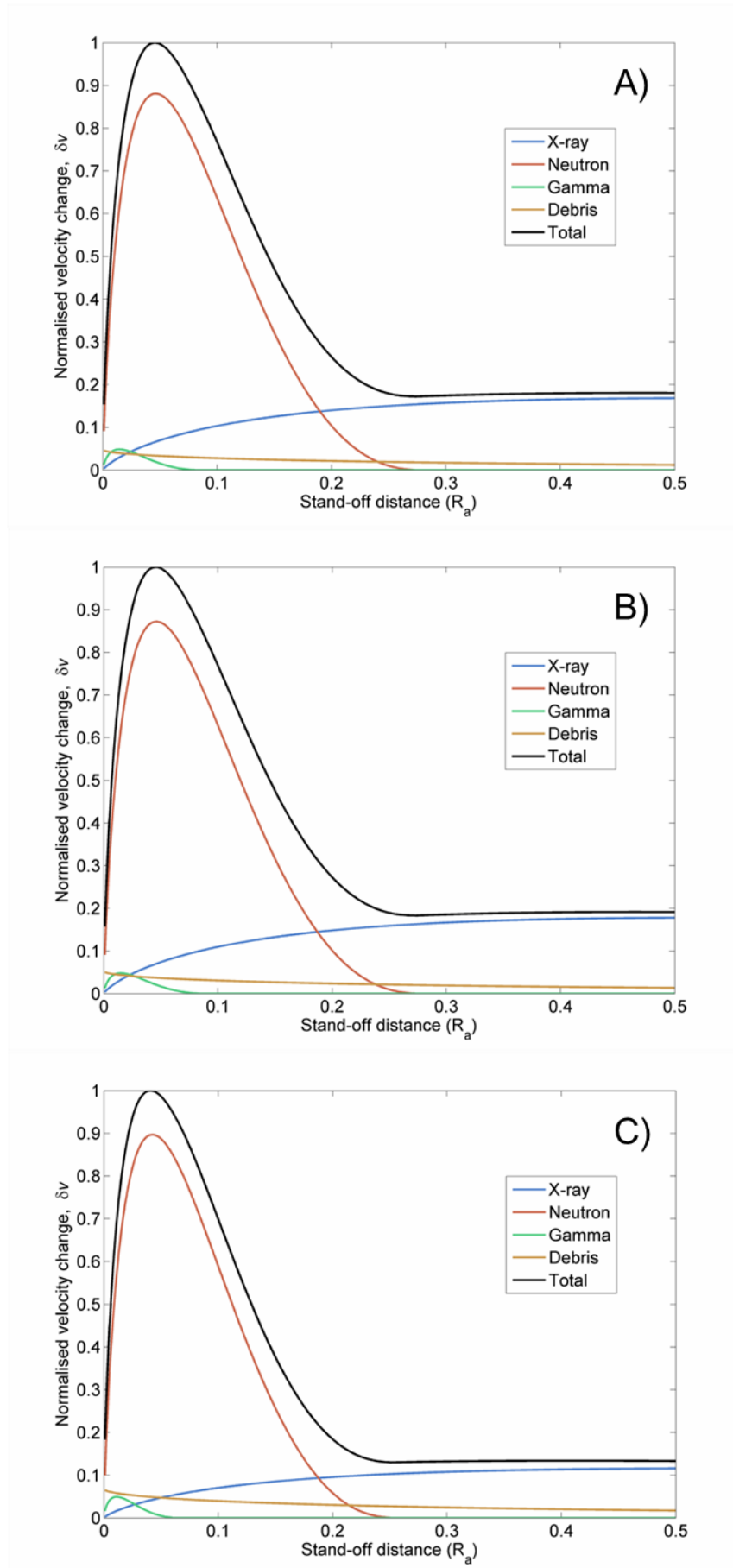
Figure 101 Normalised velocity change of 140-m sized VI₁ as a function of stand-off distance, provided by a 300-kg NI (equivalent to 10-ktons or 100-kg nuclear warhead) at the asteroid arrival. A) S-type. B) C-type. C) M-type. The optimal stand-off distance resides in <0.05 Rₐ.
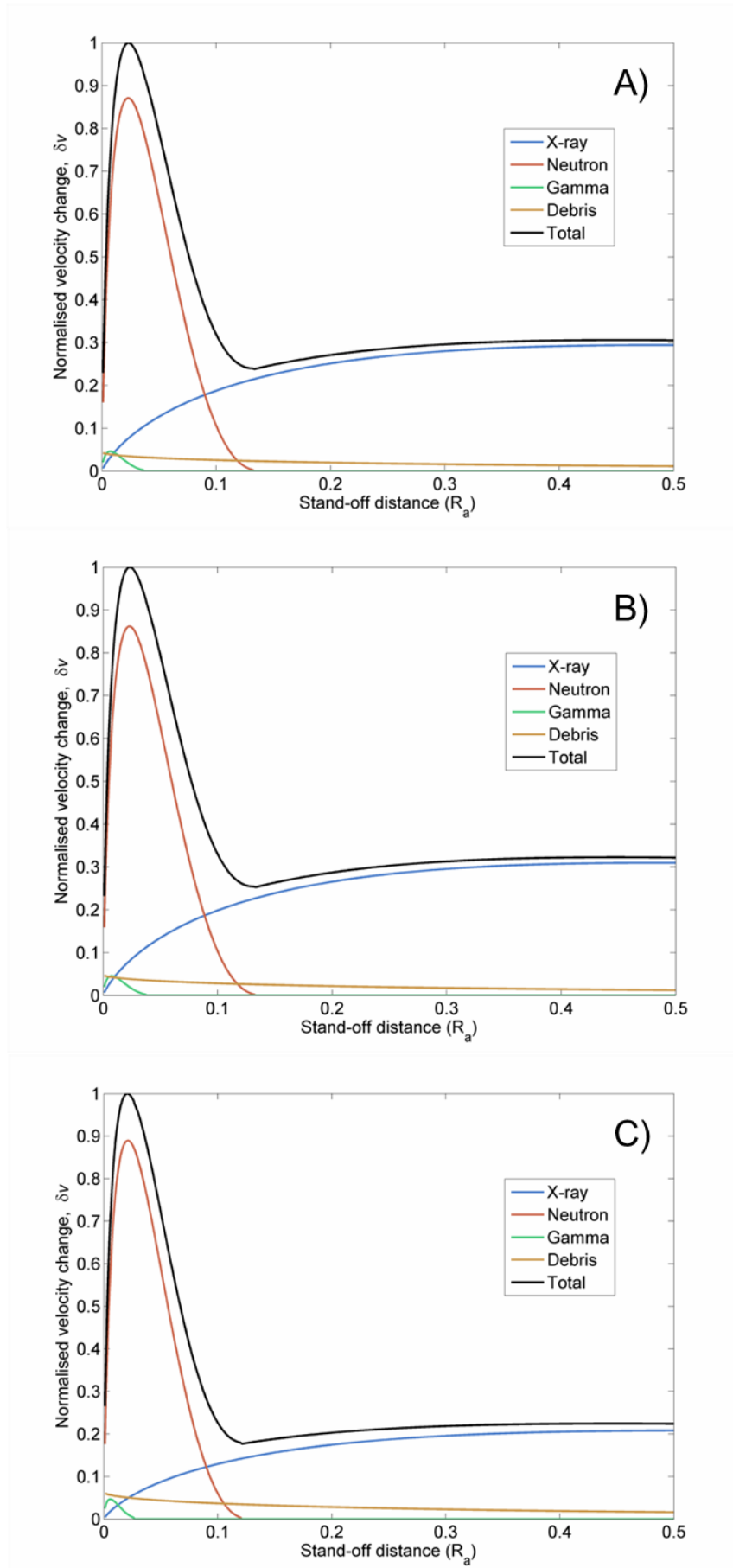
Figure 102 Normalised velocity change of 280-m VI$_1$ as a function of stand-off distance, provided by a 300-kg NI (equivalent to 10-ktons or 100-kg nuclear warhead) at the asteroid arrival. A) S-type. B) C-type. C) M-type. The optimal stand-off distance resides in <0.03 R$_a$.
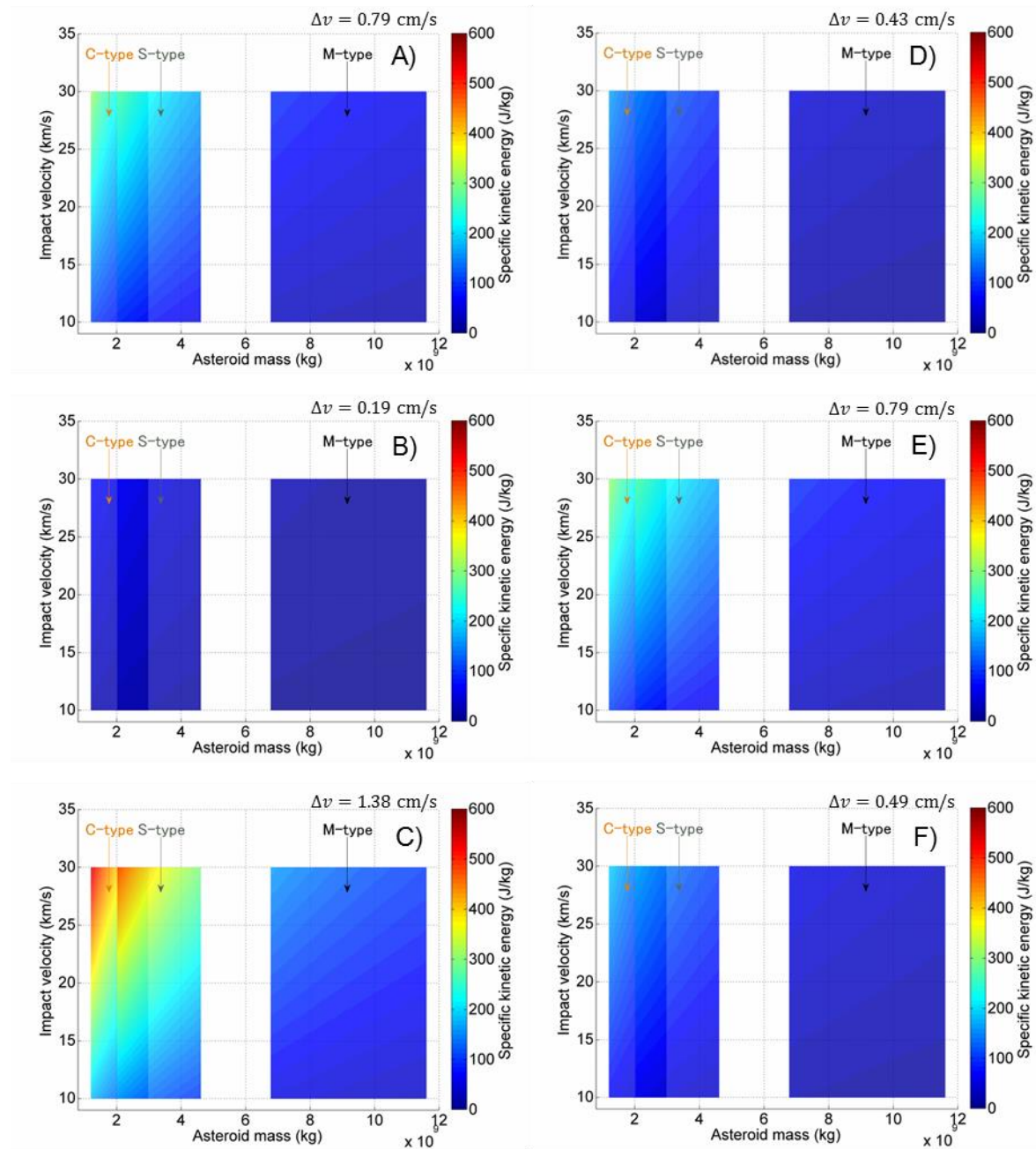
Figure 103 KI's specific kinetic energy ($\mathrm{SKE}|_{\mathrm{KI}}$) vs. impact velocity and asteroid mass for A)-F) VI$_1$-VI$_6$. The KI mass also varies according to the impact velocity such that the safe deflection distance, $2\frac{1}{2}\,\mathbf{b}_{\oplus}$ on the 2036 b-plane is achieved, given the same hazard and mitigation scenario as Figures 36 and 37 in Subsection 3.1.2. These results are valid for both 140-m and 280-m sized asteroids while 280-m sized asteroids may have, to some extent, smaller Q_D^*. The risk of fragmentation and dispersion of the target body fluctuates according to the target asteroid's orbit or required instantaneous velocity change $\Delta\mathbf{v}$ as well as its taxonomic class.

Figure 104 NI's specific kinetic energy ($\mathrm{SKE|_{NI}}$) vs. stand-off distance and asteroid mass for A)-F) 140-m sized VI$_1$-VI$_6$. The NI mass also varies according to the impact velocity such that the safe deflection distance, $2\frac{1}{2}\,\mathrm{b_\oplus}$ on the 2036 b-plane is achieved, given the same hazard and mitigation scenario as Figure 39.
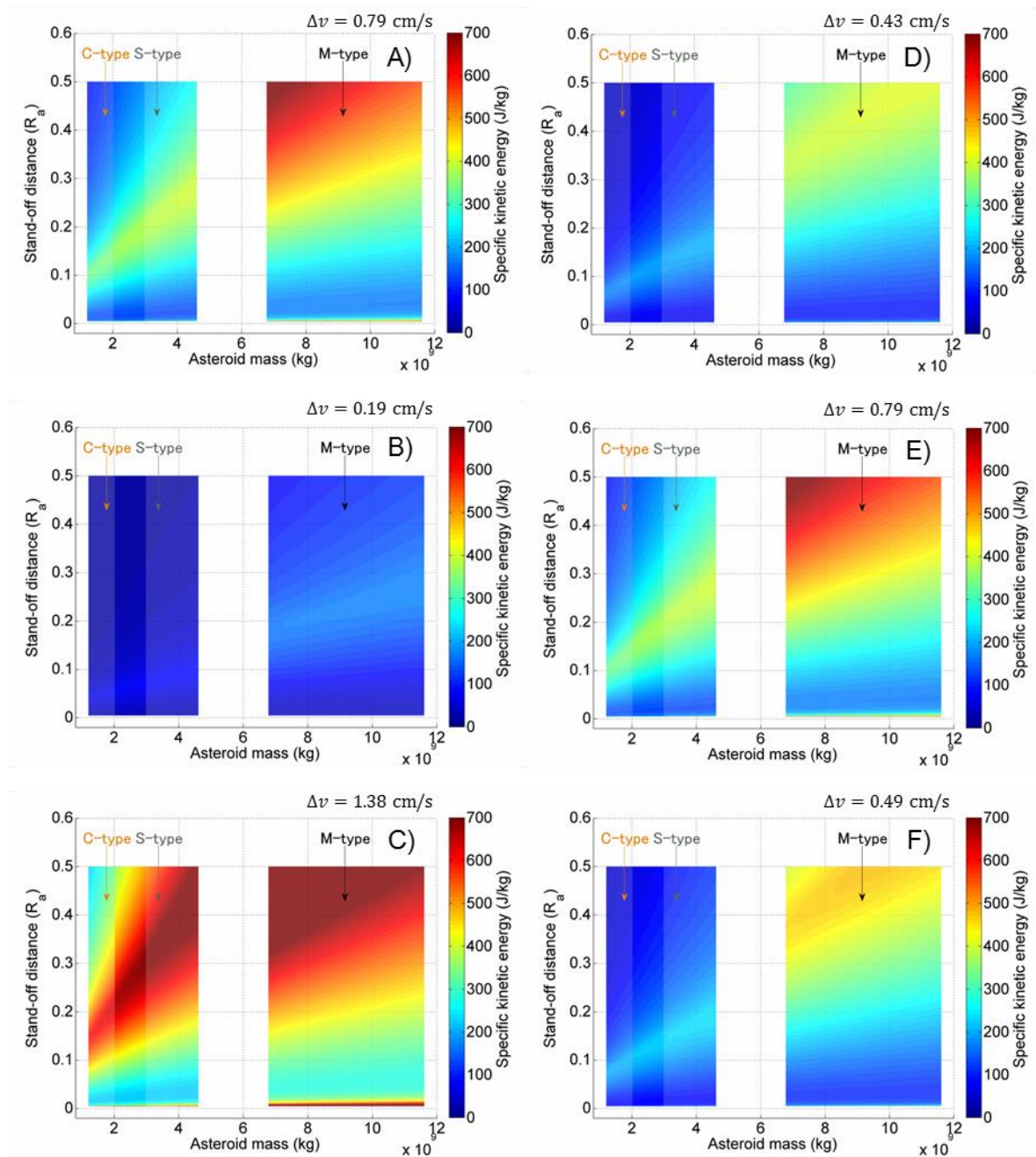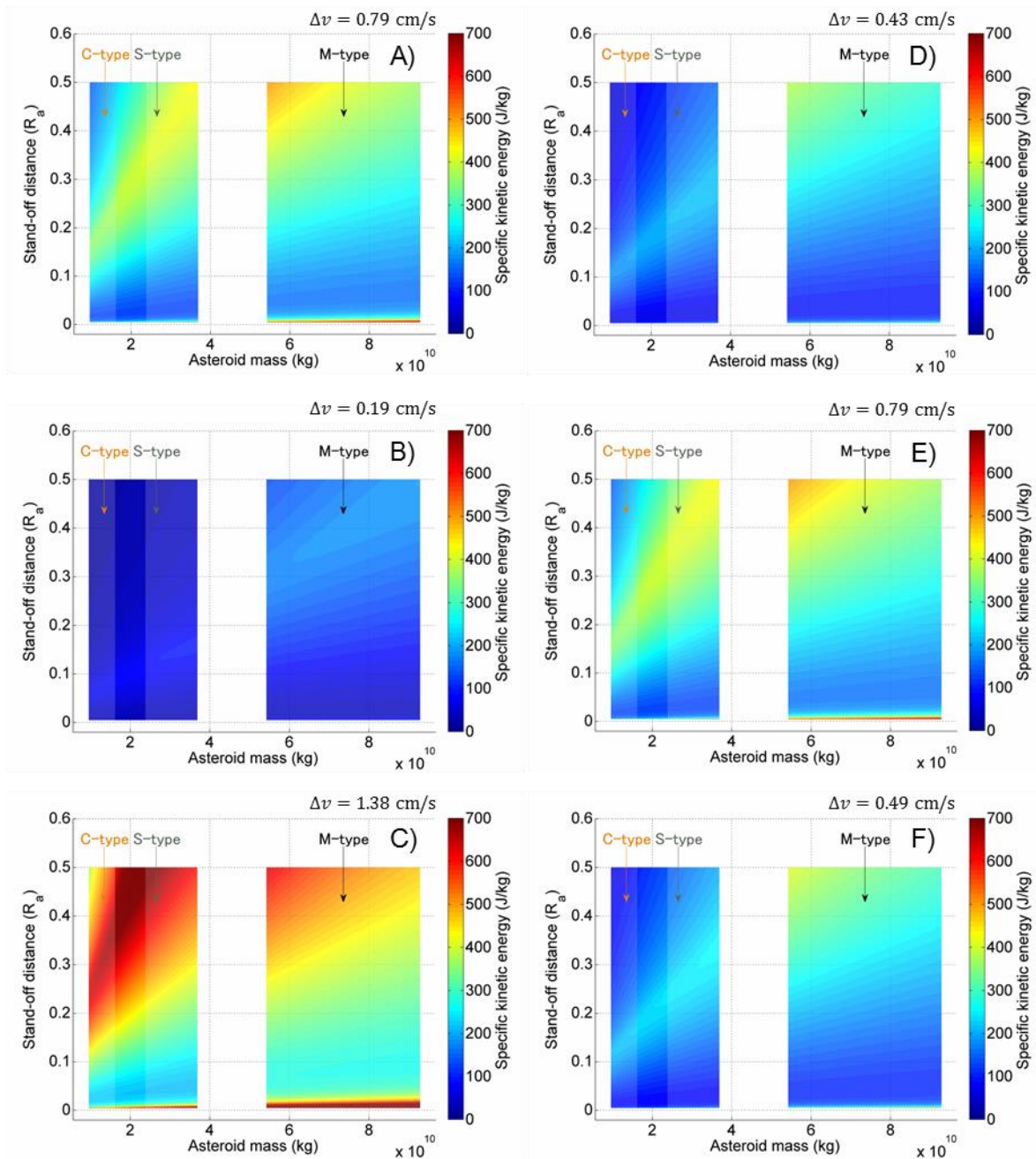
Figure 105 NI's specific kinetic energy ($SKE|_{NI}$) vs. stand-off distance and asteroid mass for A)-F) 280-m sized VI_1-VI_6. The NI mass also varies according to the impact velocity such that the safe deflection distance, $2\frac{1}{2}\,b_{\oplus}$ on the 2036 b-plane is achieved, given the same hazard and mitigation scenario as Figure 40. Overall, the results are almost identical to Figure 45 while a slight shift of the colour map towards larger stand-off distance can be seen in each plot due to the difference in optimality of the NI's deflection efficiency.

A.2.   Deflection missions to VI₁-VI₆

All the results of the required mitigation system mass of KI/NI/SC mission to 140/280-m sized VI₁-VI₆ at the asteroid arrival and the achievable deflection by GT mission to 140/280-m sized VI₁-VI₆ have been summarised here in Figures 106-113. The nominal deflection distance for which a KI/NI/SC mission is designed is equal to the safe b-plane deflection distance of $2\frac{1}{2}\,b_{\oplus}$ on the 2036 b-plane. The initial GT spacecraft mass at the asteroid arrival is given as 1000 kg. The six plots in each figure with subtitles A)-F) correspond to VI₁-VI₆, respectively.

Firstly, it can be seen that the required mitigation system mass of each mission varies according to the target asteroid's orbit, in other words, the required velocity change for the nominal b-plane deflection which differs depending on the target virtual impactor. For example, a KI/NI/SC mission to VI₂ or VI₃ requires the smallest or largest mitigation system mass among the mitigation missions to VI₁-VI₆, which agrees with the required Δv_{safe} for each virtual impactor shown Table 6 in Chapter 1.

In general, asteroid deflection efficiency is greatly subject to the target object's orbit and the GT mission is not an exception. The problem of every GT mission is that its mission lasts years to decade in which the asteroid may orbit multiple revolutions while the deflection leverage is weaker when the asteroid is further away from the Sun (i.e. its perihelion). This in turn means that the GT mission concept of constant stand-off distance may not be preferable as the mission duration becomes longer and as the asteroid semimajor axis becomes larger. It is therefore recommended to study if a variable stand-off distance GT mission can outperform the constant stand-off distance GT mission under certain NEO hazard scenarios.

The SC missions to VI₁ and VI₅ show a noteworthy aspect of the SC. Δv_{safe} for the two scenarios are 0.79 cm/s while Figure 110-A) and E) clearly shows that their required SC mass for the safe b-plane deflection are different unlike the KI and NI missions to VI₁ and VI₅ shown in Figure 106-A), E), Figure 107-A), and E). The reason for this is differences between their orbits; however, this time, it is not due to their different planetary encounter geometries but their different minimum heliocentric distances (i.e. perihelia). VI₁ travels much closer to the Sun than VI₅ travels: the closer to the Sun the asteroid travels, the more efficient the SC mission becomes since the solar flux is inversely proportional to the square of a heliocentric distance (see the two orbits of VI₁ and VI₅ are presented in Figure 14).
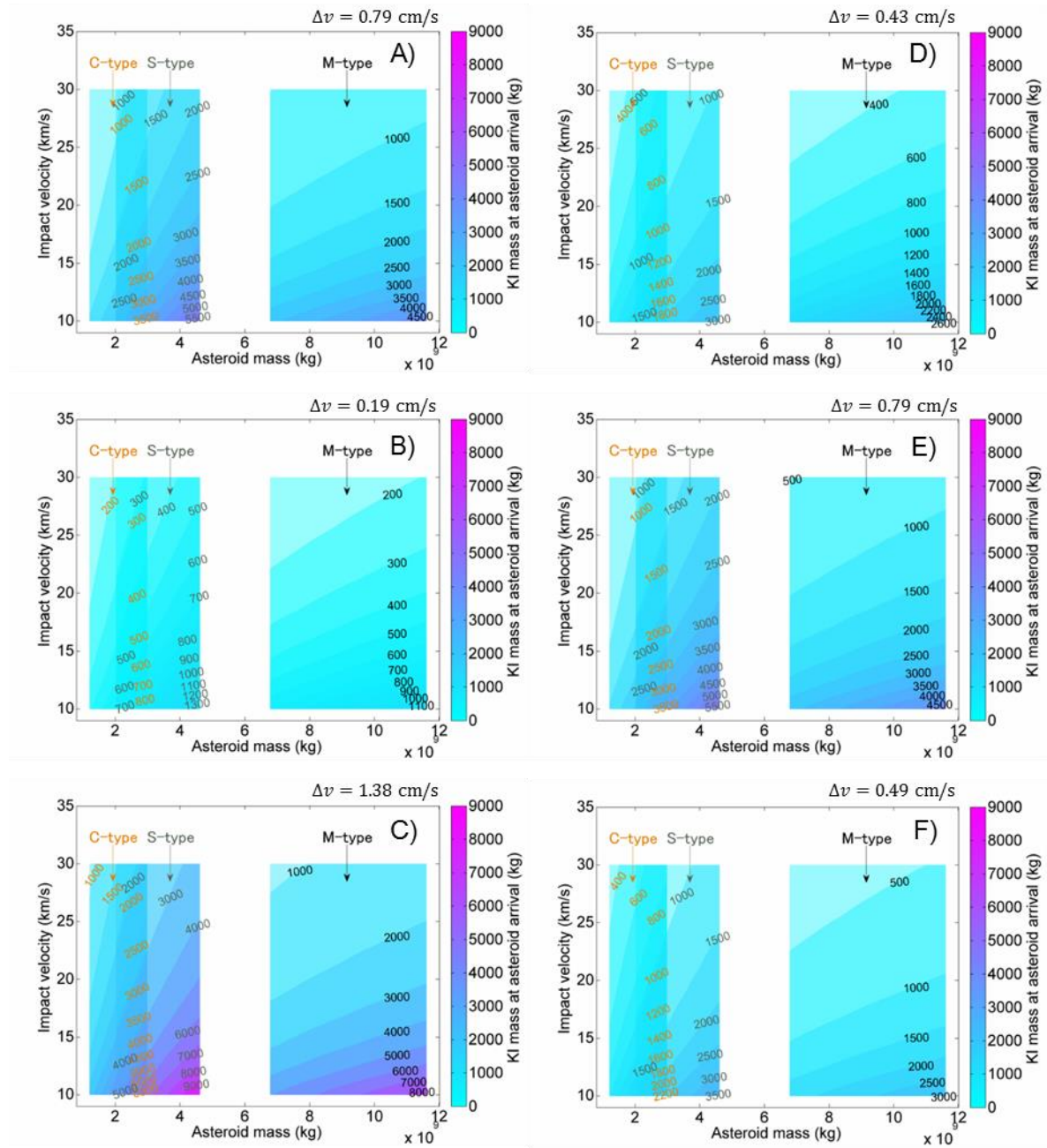
Figure 106 Comparison of required KI mass for the 2036 b-plane deflection of $2\frac{1}{2}$ $b_\oplus$ as a function of asteroid mass and kinetic impact velocity. VI$_1$-VI$_6$ are all 140-m in diameter and they have 10 years of warning time till 13 April 2036 – Earth impact epoch.
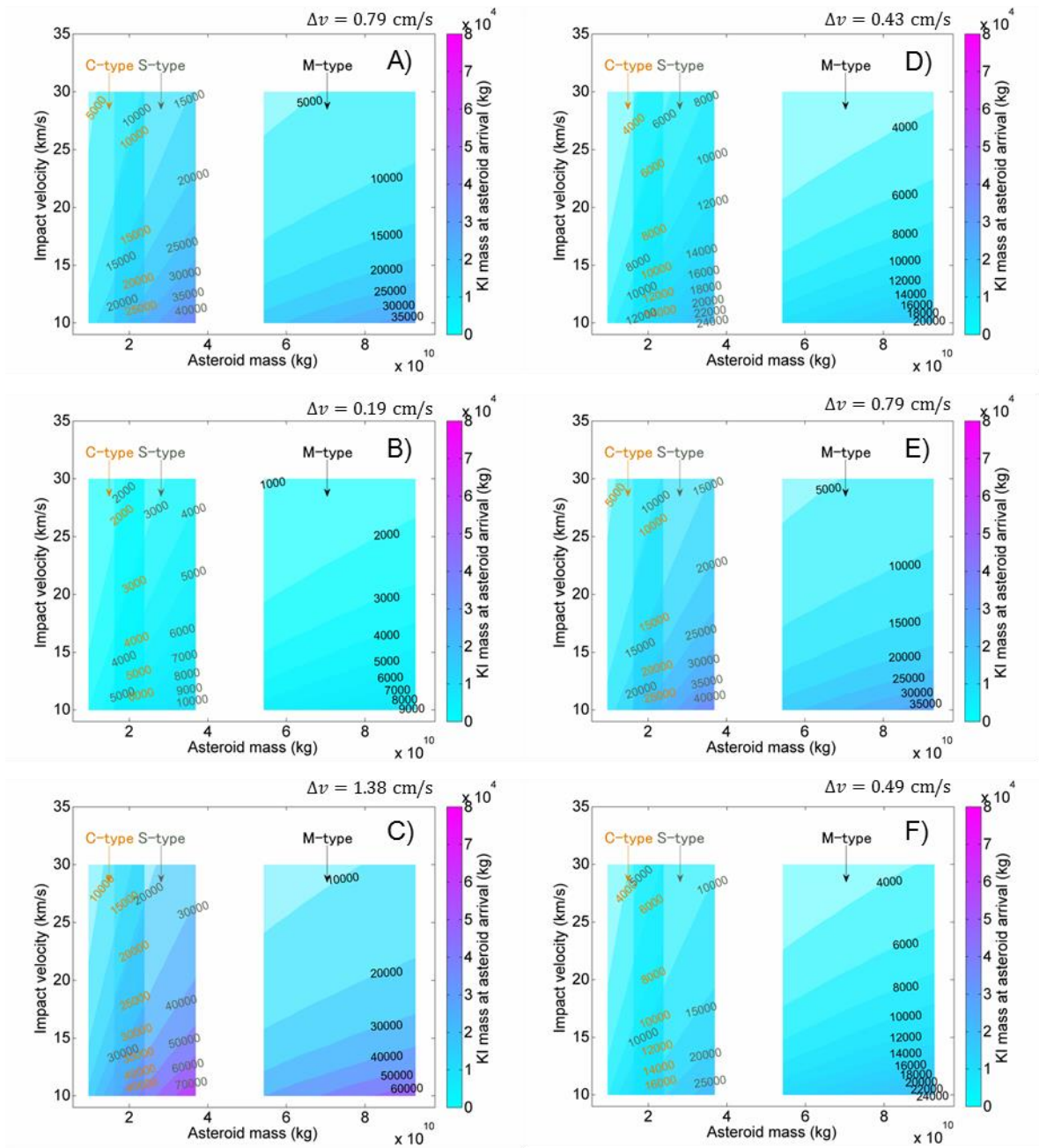
Figure 107 Comparison of required KI mass for the 2036 b-plane deflection of $2\frac{1}{2}$ $b_\oplus$ as a function of asteroid mass and kinetic impact velocity. VI_1-VI_6 are all 280-m in diameter and they have 10 years of warning time till 13 April 2036 – Earth impact epoch.

Figure 108 Comparison of required NI mass for the 2036 b-plane deflection of $2\frac{1}{2}\,b_\oplus$ as a function of asteroid mass and stand-off distance. VI$_1$-VI$_6$ are all 140-m in diameter and they have 10 years of warning time till 13 April 2036 – Earth impact epoch.
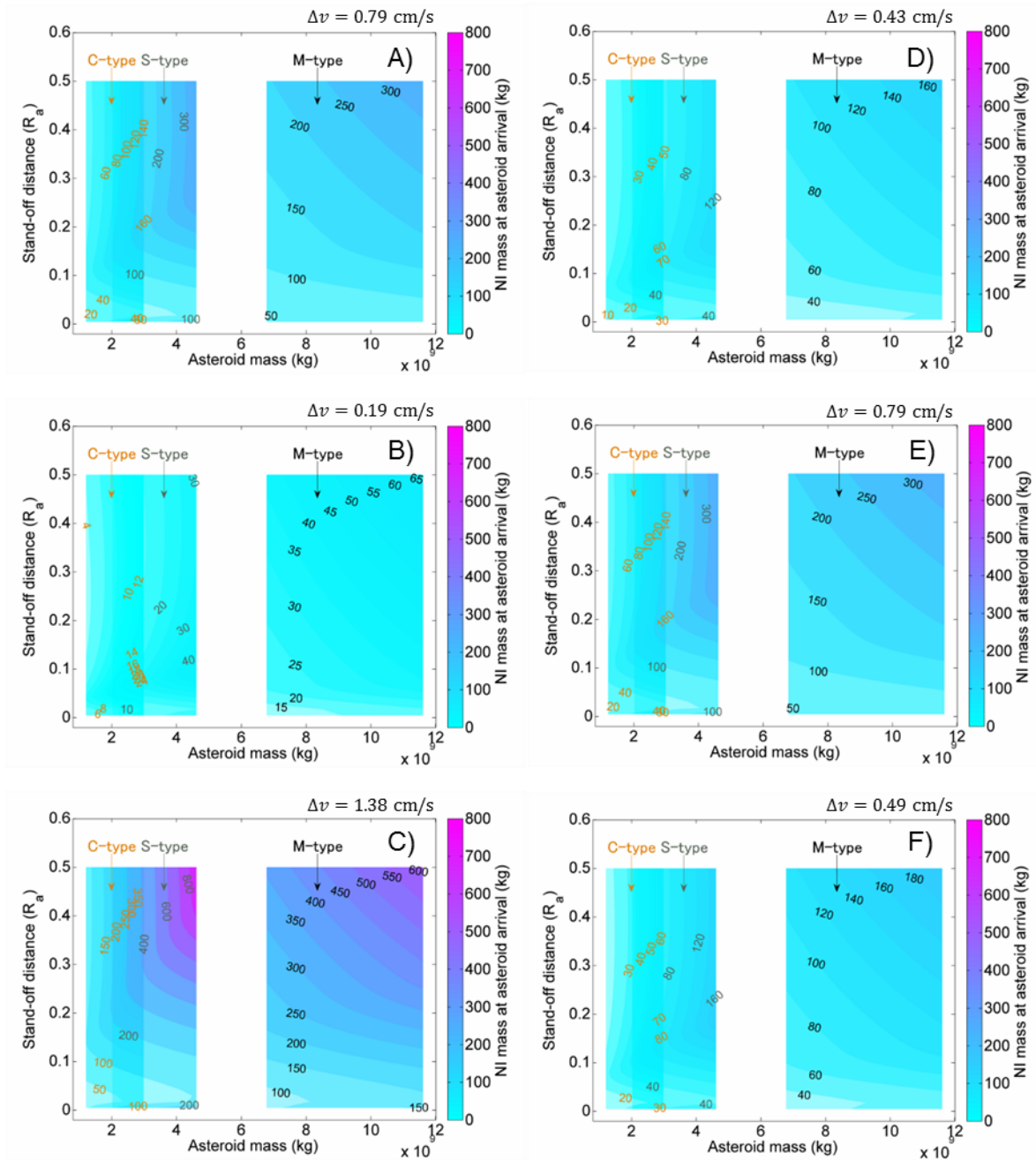
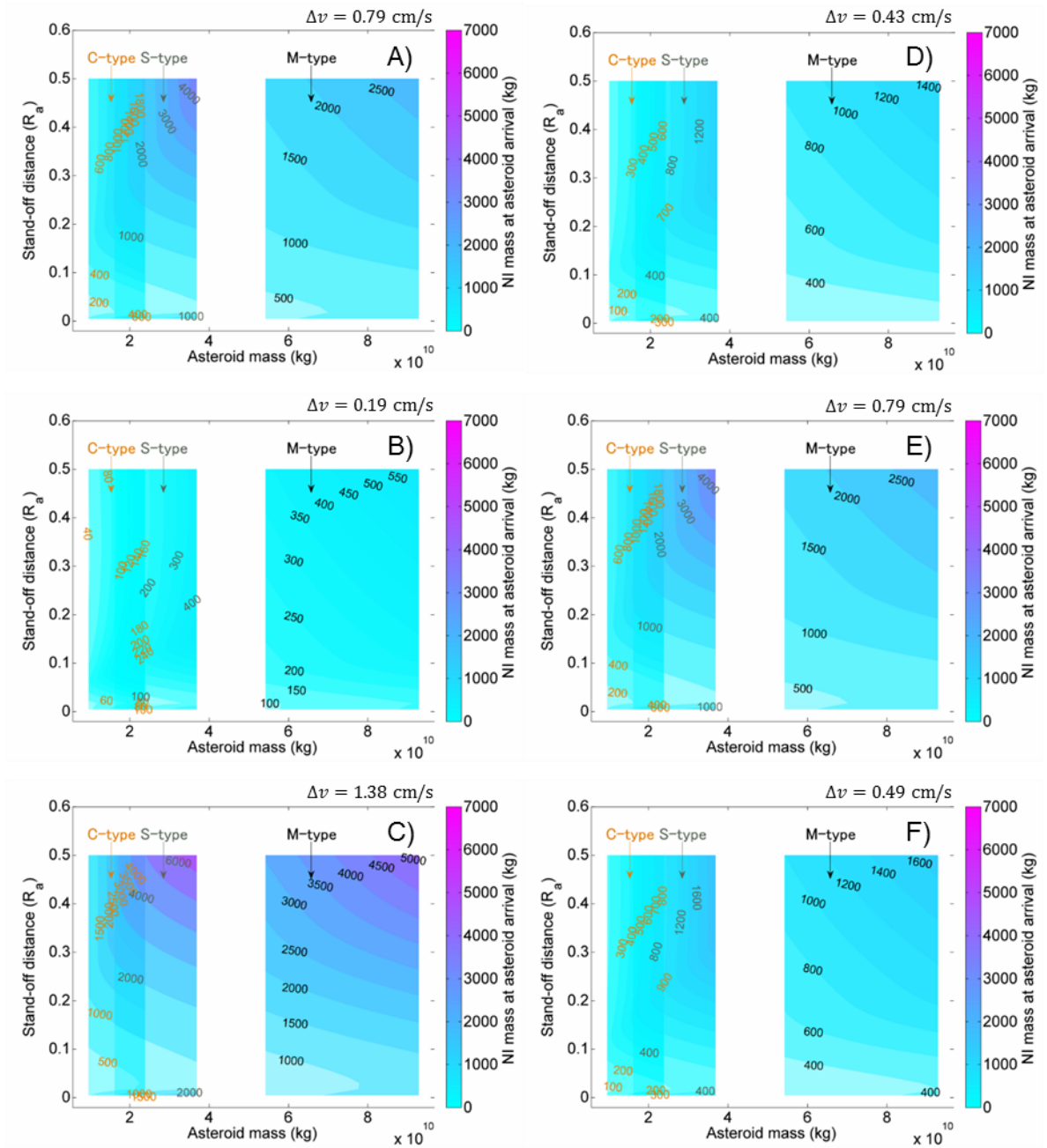**Figure 109 Comparison of required NI mass for the 2036 b-plane deflection of $2\frac{1}{2}\,b_\oplus$ as a function of asteroid mass and stand-off distance. VI$_1$-VI$_6$ are all 280-m in diameter and they have 10 years of warning time till 13 April 2036 – Earth impact epoch.**

Figure 110 Comparison of required SC mass for the 2036 b-plane deflection of $2\frac{1}{2}\,b_{\oplus}$ as a function of asteroid mass and asteroid rotational period. VI$_1$-VI$_6$ are all 140-m in diameter and they have 10 years of warning time till 13 April 2036 – Earth impact epoch.
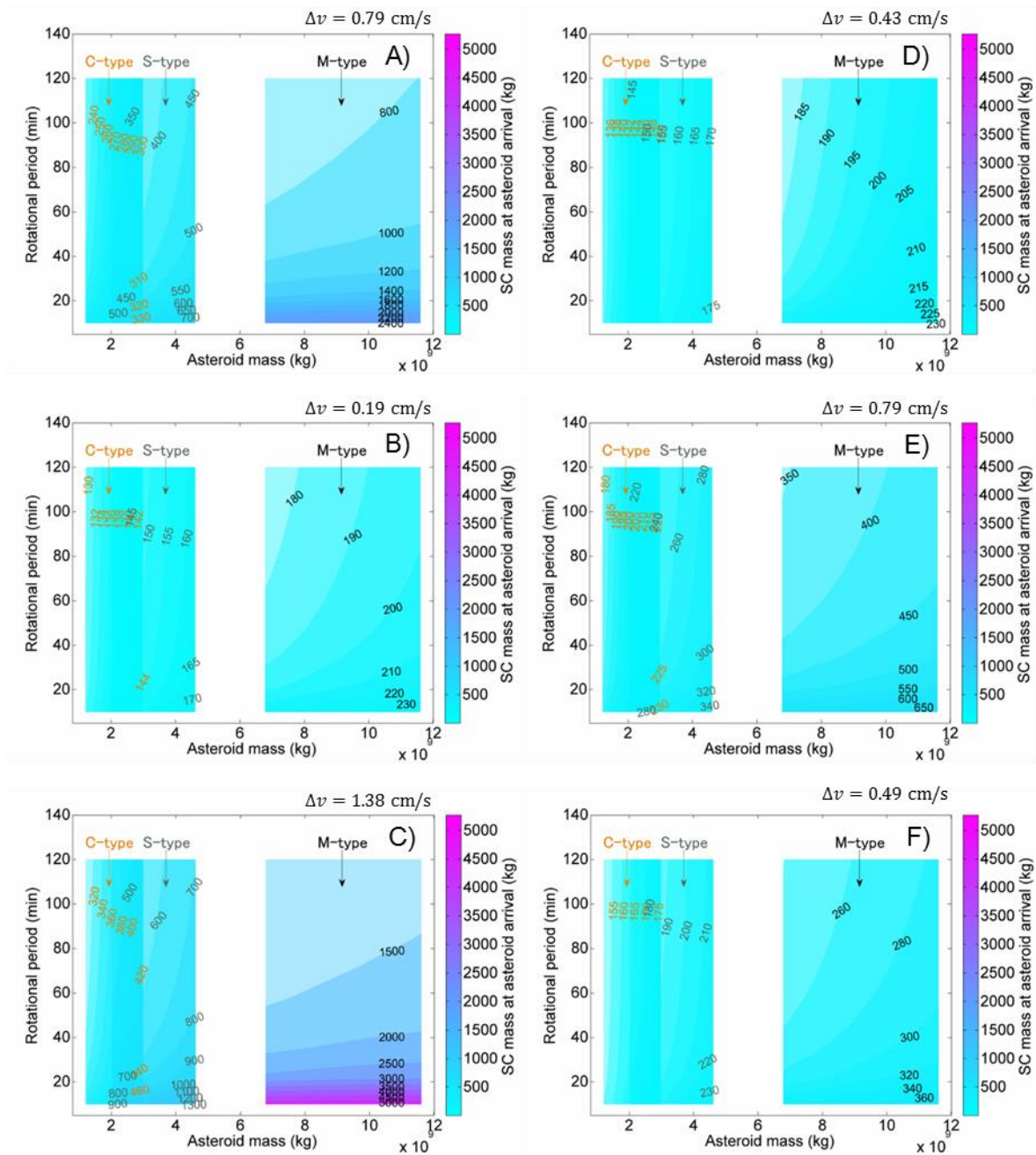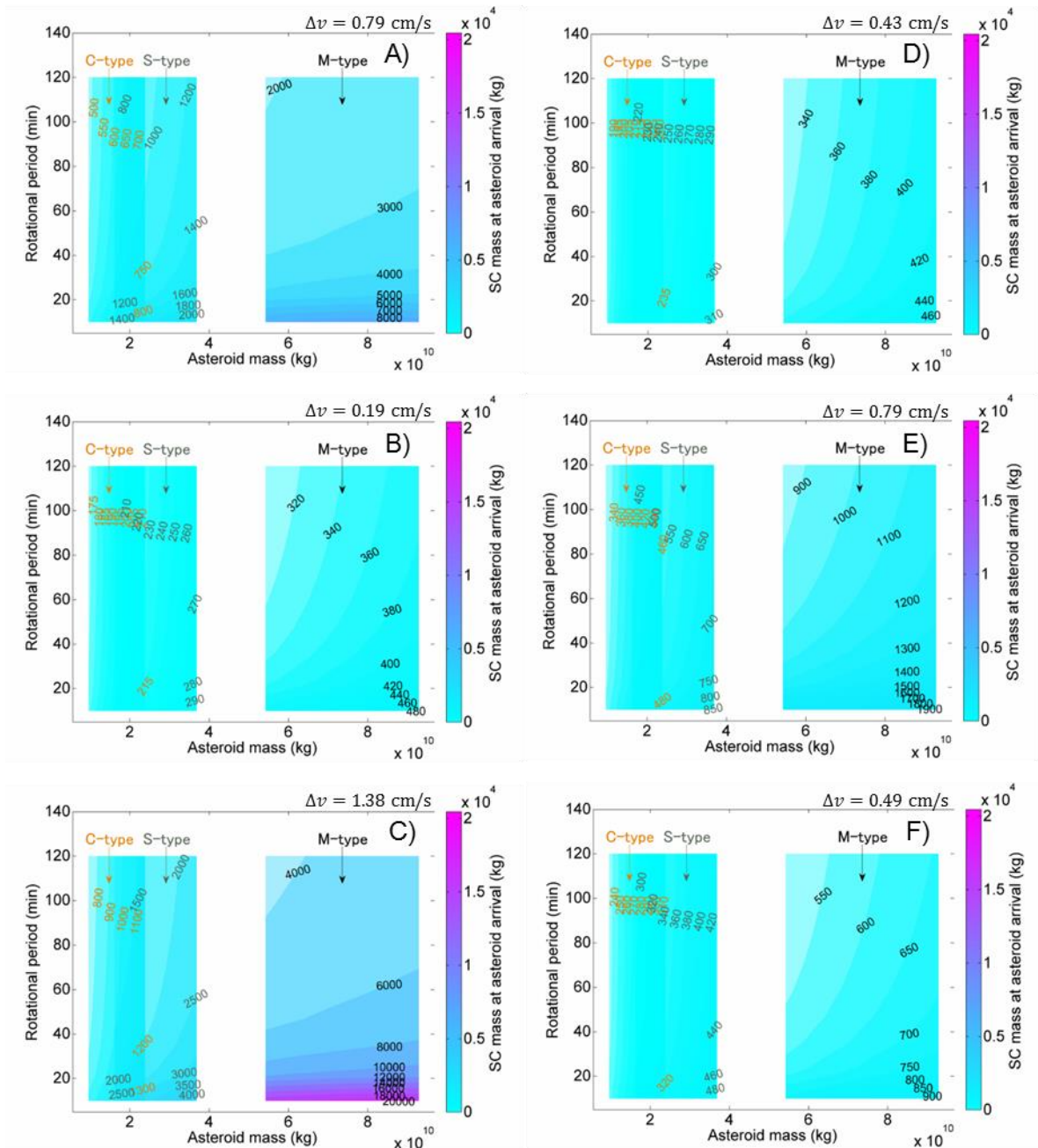
Figure 111 Comparison of required SC mass for the 2036 b-plane deflection of 2½ b⊕ as a function of asteroid mass and asteroid rotational period. VI₁-VI₆ are all 280-m in diameter and they have 10 years of warning time till 13 April 2036 – Earth impact epoch.
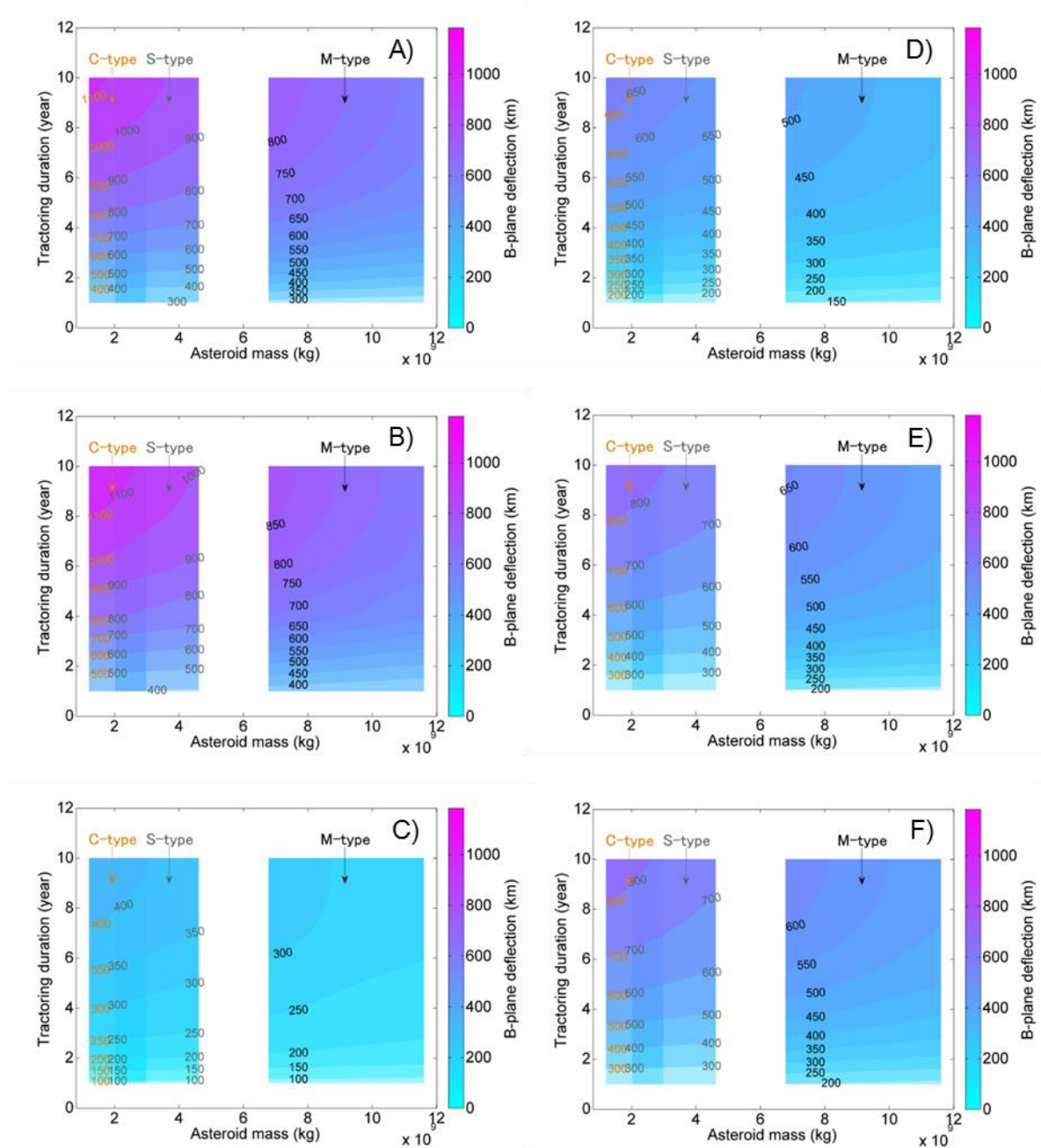
Figure 112 Comparison of b-plane deflection achieved through GT mission to 140-m sized VI₁-VI₆ as a function of asteroid mass and tractoring duration. The initial GT spacecraft mass is 1000 kg. The GT mission begins on 13 April 2026 and lasts for 1-10 years.

Figure 113 Comparison of b-plane deflection achieved through GT mission to 280-m sized VI₁-VI₆ as a function of asteroid mass and tractoring duration. The initial GT spacecraft mass is 1000 kg. The GT mission begins on 13 April 2026 and lasts for 1-10 years.

A.3. Normalised spherical harmonic coefficients of Eros
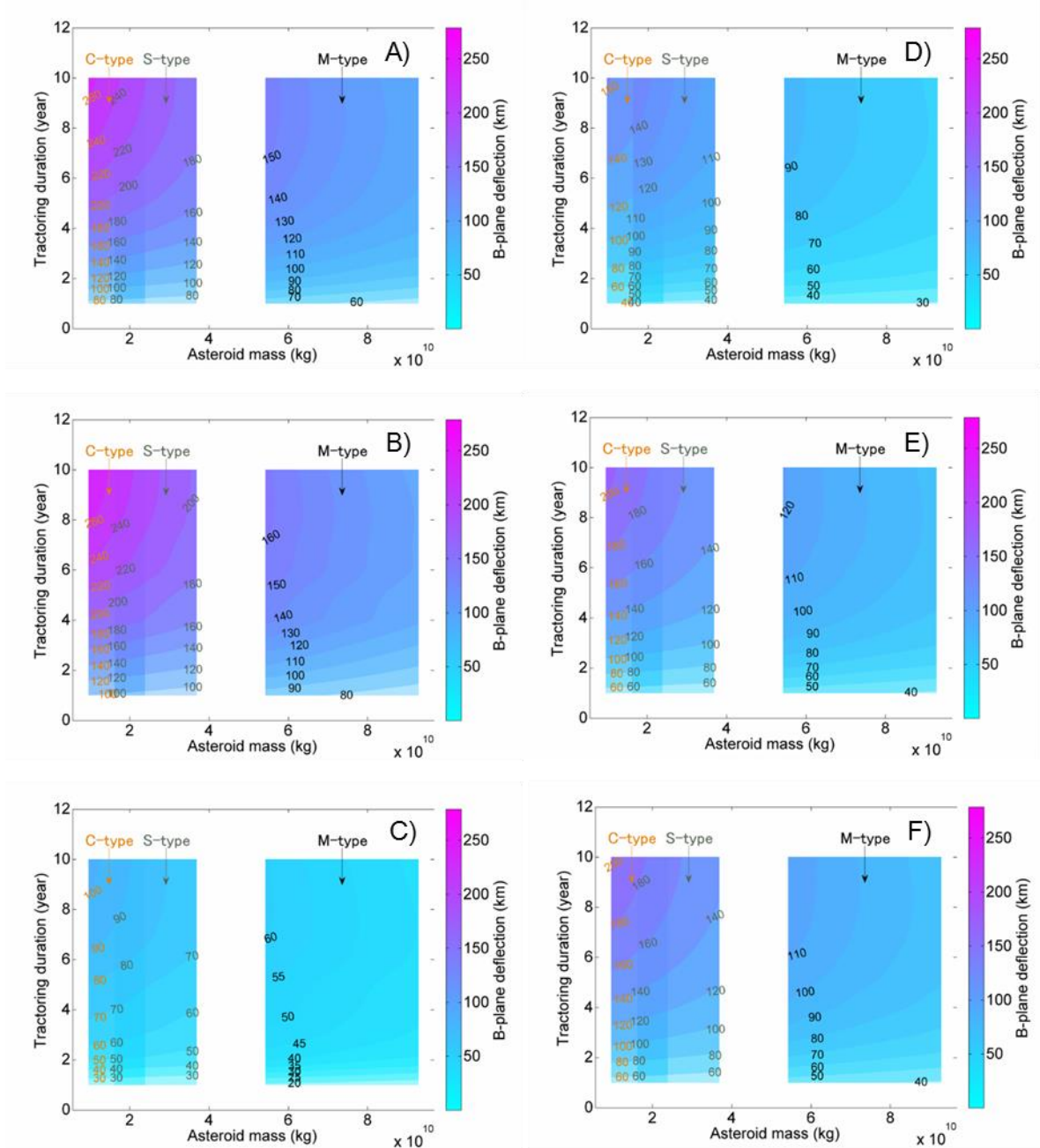
NEAR15A spherical harmonic coefficients of asteroid (433) Eros [137] are referred to in this doctoral thesis in order to represent the inhomogeneous gravitational field about an irregularly-shaped/elongated asteroid. The NEAR15A gravity model is a 15th degree and order model obtained from radiometric tracking (Doppler and range data) and landmark tracking of the NEAR spacecraft in orbit about Eros. The gravity model includes data from the entire mission beginning with orbit insertion on 14 February 2000 and ending with the first descent manoeuvre for landing on 12 February 2001. Table 19 shows all the normalised spherical harmonic coefficients of Eros. The reference radius of the model is 16 km and GM of Eros is $4.46275472004 \times 10^{-4}$ km^3/s^2. These parameters are to be scaled according to the equivalent diameter of the target asteroid about which the spacecraft orbits/hovers.

Table 19 NEAR15A spherical harmonic coefficients of asteroid (433) Eros. $\hat{C}_{lm}$ and $\hat{S}_{lm}$ are normalised coefficients. Maximum values of l and m are 15 as the size of the model is 15×15.

l	m	$\bar{C}_{lm}$	$\bar{S}_{lm}$	l	m	$\bar{C}_{lm}$	$\bar{S}_{lm}$
1	0	0.00E+00	0.00E+00	7	4	-2.43E-04	3.27E-04
1	1	0.00E+00	0.00E+00	7	5	3.77E-03	1.90E-03
2	0	-5.25E-02	0.00E+00	7	6	3.25E-05	-4.96E-04
2	1	-1.64E-06	-1.40E-07	7	7	-6.77E-03	-2.20E-03
2	2	8.24E-02	-2.81E-02	8	0	2.63E-03	0.00E+00
3	0	-1.41E-03	0.00E+00	8	1	-5.00E-05	-1.81E-05
3	1	4.06E-03	3.37E-03	8	2	-3.14E-03	2.80E-05
3	2	1.78E-03	-7.04E-04	8	3	-3.09E-04	-3.19E-05
3	3	-1.04E-02	-1.21E-02	8	4	2.77E-03	-4.81E-04
4	0	1.29E-02	0.00E+00	8	5	4.83E-04	-1.02E-04
4	1	-1.00E-04	1.37E-04	8	6	-2.54E-03	2.39E-05
4	2	-1.75E-02	4.63E-03	8	7	-1.90E-04	-7.00E-05
4	3	-3.00E-04	-1.19E-04	8	8	2.27E-03	1.37E-03
4	4	1.75E-02	-9.11E-03	9	0	1.82E-04	0.00E+00
5	0	6.59E-04	0.00E+00	9	1	-7.66E-04	-1.26E-04
5	1	-2.77E-03	-1.22E-03	9	2	-3.72E-04	-1.89E-04
5	2	-7.83E-04	3.81E-04	9	3	1.42E-03	9.99E-04
5	3	4.58E-03	3.54E-03	9	4	-4.84E-04	-2.75E-04
5	4	4.97E-04	-6.98E-04	9	5	-1.72E-03	-9.80E-04
5	5	-1.02E-02	-5.84E-03	9	6	-2.36E-04	8.49E-05
6	0	-4.98E-03	0.00E+00	9	7	3.06E-03	8.68E-04
6	1	-2.44E-05	-1.24E-04	9	8	4.40E-04	-7.13E-05
6	2	6.54E-03	-1.19E-03	9	9	-3.27E-03	-7.23E-04
6	3	2.88E-04	7.54E-05	10	0	-3.46E-04	0.00E+00
6	4	-5.65E-03	1.77E-03	10	1	-5.92E-04	1.12E-03
6	5	-4.88E-04	4.79E-05	10	2	1.45E-03	-7.68E-04
6	6	5.09E-03	-1.60E-03	10	3	4.20E-04	4.50E-04
7	0	-4.56E-04	0.00E+00	10	4	-3.61E-05	-7.05E-04
7	1	1.72E-03	7.04E-04	10	5	-6.31E-04	-9.25E-04
7	2	3.84E-04	-1.98E-04	10	6	1.53E-03	9.30E-04
7	3	-2.47E-03	-1.44E-03	10	7	7.93E-04	-8.88E-04

l	m	$\bar{C}_{lm}$	$\bar{S}_{lm}$	l	m	$\bar{C}_{lm}$	$\bar{S}_{lm}$
10	8	-9.03E-04	-4.36E-05	13	9	-6.81E-04	-8.48E-05
10	9	-1.58E-03	5.25E-05	13	10	-6.50E-04	-6.43E-05
10	10	1.19E-03	1.35E-03	13	11	1.75E-03	-3.94E-04
11	0	1.54E-03	0.00E+00	13	12	1.38E-04	-5.46E-05
11	1	6.32E-04	-1.39E-03	13	13	-5.98E-04	-1.15E-03
11	2	6.52E-05	-1.34E-03	14	0	-2.01E-03	0.00E+00
11	3	3.91E-04	-2.47E-04	14	1	1.46E-03	1.65E-03
11	4	-1.32E-03	-1.15E-03	14	2	8.13E-03	4.16E-03
11	5	1.90E-03	2.10E-03	14	3	2.09E-03	1.69E-04
11	6	5.57E-04	-2.78E-04	14	4	-3.24E-03	9.78E-04
11	7	1.25E-04	-5.93E-04	14	5	-4.04E-03	-1.34E-04
11	8	7.88E-04	-5.86E-04	14	6	2.35E-03	4.39E-03
11	9	2.83E-03	1.47E-03	14	7	-1.04E-03	-3.22E-03
11	10	-2.92E-04	1.39E-04	14	8	-1.25E-03	-2.33E-03
11	11	-1.28E-03	-9.62E-04	14	9	-1.96E-04	7.97E-04
12	0	2.43E-04	0.00E+00	14	10	1.12E-03	1.76E-04
12	1	6.70E-04	2.66E-03	14	11	1.57E-03	1.46E-04
12	2	3.41E-03	2.11E-03	14	12	-1.72E-03	-7.25E-04
12	3	1.84E-03	7.35E-04	14	13	-3.14E-04	5.10E-05
12	4	9.63E-04	-7.72E-04	14	14	1.32E-03	1.51E-03
12	5	-3.15E-03	-1.16E-03	15	0	2.62E-03	0.00E+00
12	6	1.72E-03	3.87E-03	15	1	-5.22E-03	-1.30E-04
12	7	-7.24E-04	-2.50E-03	15	2	2.87E-04	2.93E-03
12	8	8.40E-04	2.69E-04	15	3	-1.72E-03	4.60E-04
12	9	-1.91E-03	5.08E-05	15	4	2.23E-03	-5.30E-03
12	10	-1.92E-03	-2.43E-03	15	5	-2.95E-03	-3.18E-03
12	11	4.61E-04	3.87E-04	15	6	-2.87E-04	-3.70E-04
12	12	9.05E-04	1.83E-03	15	7	-1.32E-03	-2.38E-04
13	0	3.75E-03	0.00E+00	15	8	-3.08E-03	7.66E-04
13	1	-5.36E-03	-2.29E-03	15	9	-9.75E-04	-8.25E-05
13	2	-4.99E-05	3.81E-04	15	10	2.54E-05	-3.50E-04
13	3	2.24E-03	-2.20E-04	15	11	-8.59E-04	-1.08E-03
13	4	1.38E-03	-5.10E-03	15	12	2.60E-04	2.28E-04
13	5	-1.92E-03	3.39E-04	15	13	1.27E-03	6.00E-04
13	6	1.73E-04	-8.47E-05	15	14	2.12E-04	-1.48E-04
13	7	3.19E-04	-5.95E-06	15	15	-1.14E-03	-1.02E-03
13	8	-1.22E-03	-1.43E-03				

A.4.   Dual-deflection mitigation campaigns against VI_1-VI_6

Here, the Pareto-optimal solutions of the KI-GT/NI-GT/SC-GT mitigation campaigns against the 140-m sized S-type VI_1-VI_6 are summarised in Figures 114-128. The six plots in each figure with subtitles A)-F) correspond to VI_1-VI_6, respectively. The Belief measures of these optimal solutions satisfy either $Bel_{nom} \geq 0.47$ or $Bel_{nom} = 1.0$. The rest of Pareto-optimal solutions of KI-GT/NI-GT/SC-GT mitigation campaigns against C-type and M-type VI_1-VI_6 are omitted in this thesis since the differences between them associated with the differences in taxonomic class have been already covered and discussed in Section 5.2 in Chapter 5.

Figures 114, 119, and 124 show that the optimal Earth departure times of primary mitigation missions with a relatively high nominal b-plane (i.e., optimal solutions with redder dot) deflection is subject to the orbit of the target hazardous asteroid as well as the selected asteroid deflection technique. It appears that the NI/SC Earth departure time of an NI-GT/SC-GT mitigation campaign is generally more limited than that of a KI-GT mitigation campaign regardless of the orbit of the target asteroid. This is due to the difference in transfer orbit of the KI-GT and the NI-GT/SC-GT campaigns.

Interestingly, the minimum Pareto-optimal value of the total mitigation system mass of a KI-GT/NI-GT/SC-GT dual-deflection mitigation campaign against VI_6 results in the largest in comparison with those for VI_1-VI_5 (see Figures 114, 119, and 124). The reason for this high cost of the rendezvous with VI_6 in particular is most likely due to the highest orbital inclination of 22.5 deg among the six virtual impactors considered in this doctoral thesis (see Table 4 in Chapter 1).

More importantly, the rendezvous cost also affects the b-plane deflection achieved through the GT mission, hence the campaign credibility. Figures 118, 123, and 128 clearly show that the achievable post-KI/NI/SC deflection by GT profoundly differs between VI_1-VI_6. According to Figures 122 and 127, the GT mass at the NEA arrival is smaller than 1000 kg in some cases, which is too light for the GT spacecraft to provide any significant b-plane deflection with a 140-m sized object, given the warning time less than 10-20 years. As a consequence, the number of Pareto-optimal solutions that satisfy $Bel_{nom} = 1.0$ changes according to the orbit of the asteroid and, at worst, there is no Pareto-optimal solutions for the dual-deflection campaign with high campaign credibility/high Belief measure as can be seen in Figures 115, 120, and 125.
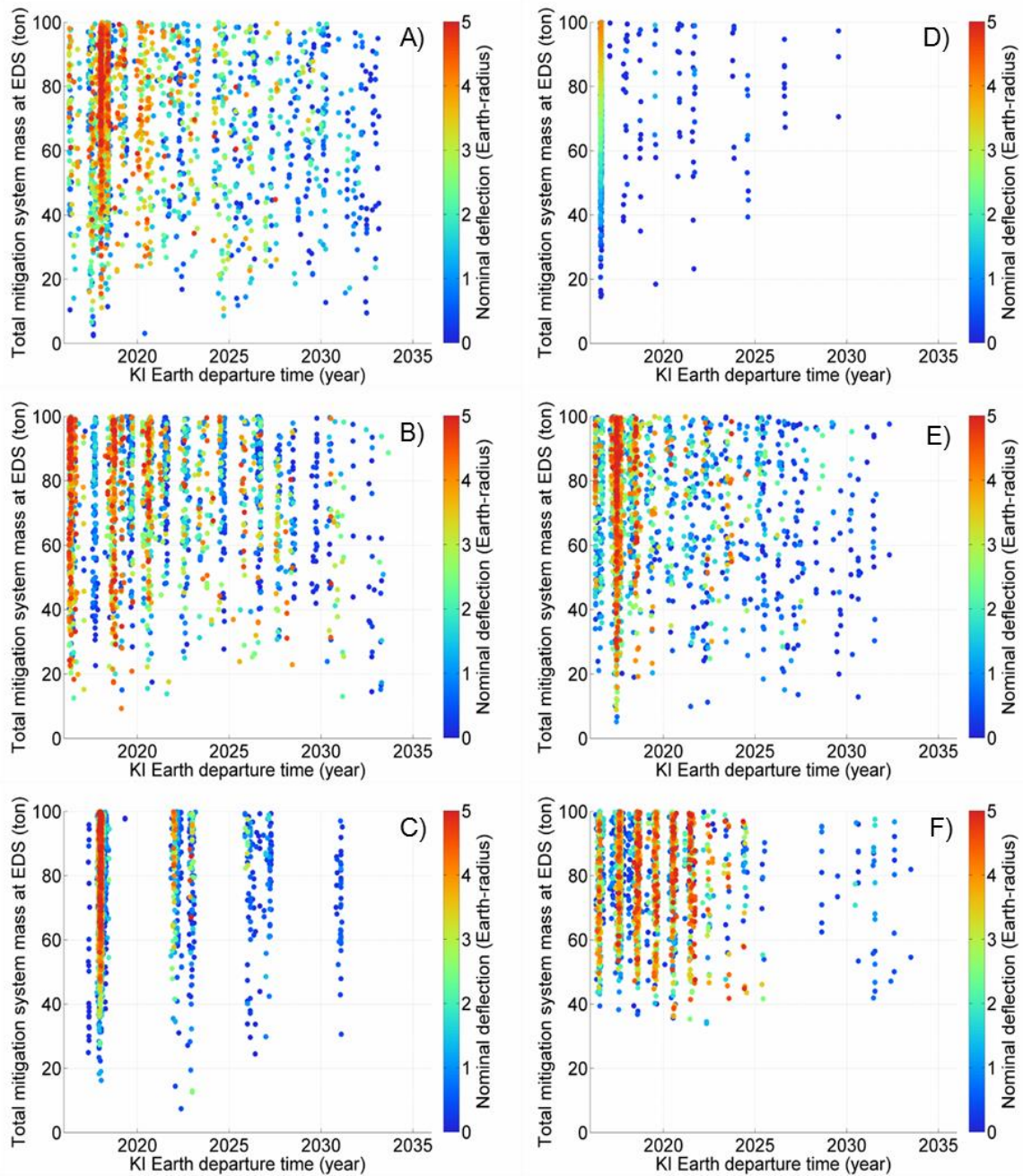
A.4.1. KI-GT mitigation campaign

Figure 114 Pareto-optimal solutions for KI-GT campaigns against S-type VI₁-VI₆ plotted for KI Earth departure time vs. total mitigation system mass at EDS. The colours of the dots represent the degrees of nominal deflection distances between 0.0-5.0 Earth-radii. The Belief of each plot satisfies $Bel_{nom} \geq 0.47$. The subtitles A)-F) correspond to VI₁-VI₆, respectively.
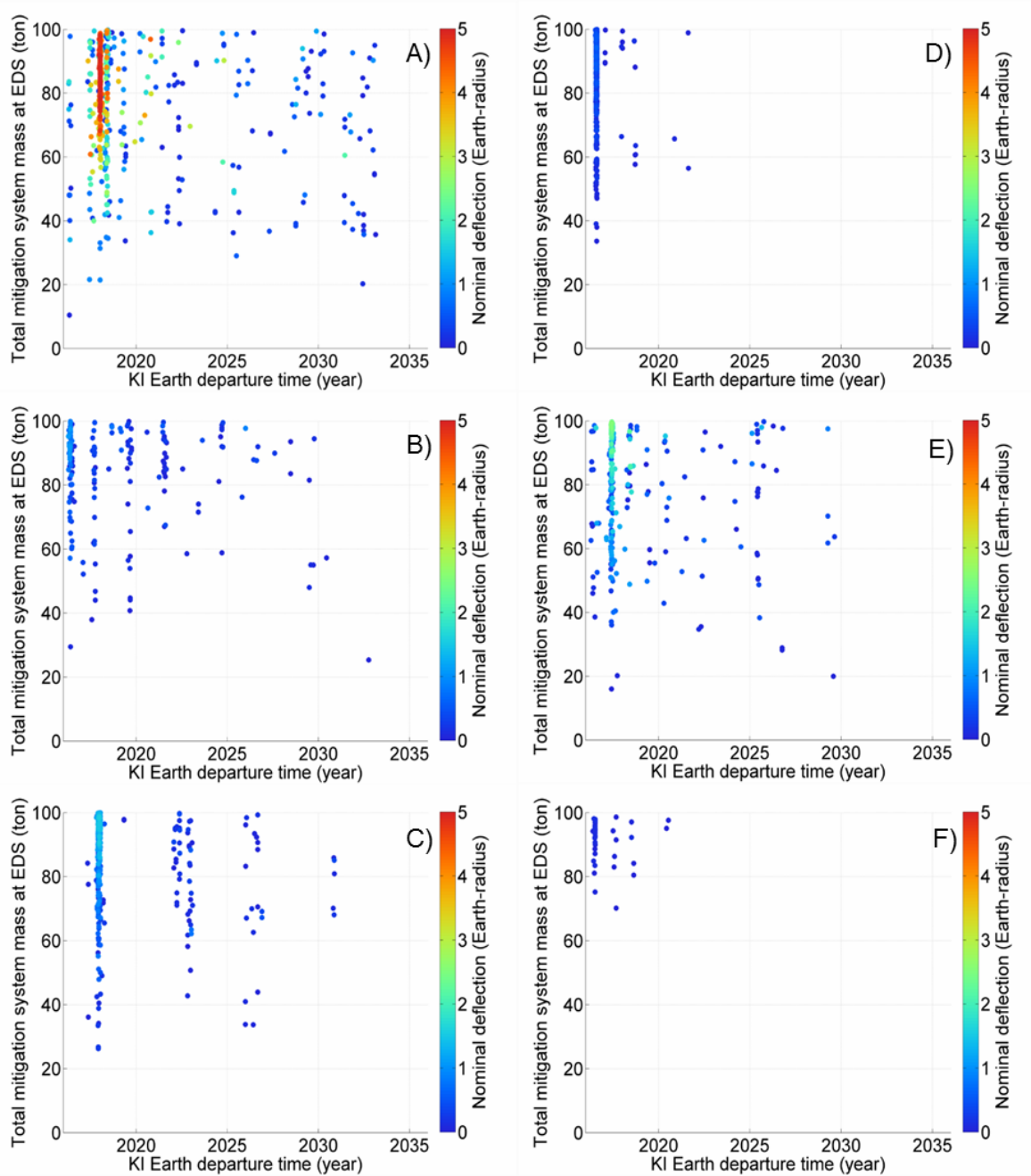
Figure 115 Pareto-optimal solutions for KI-GT campaigns against S-type VI₁-VI₆ plotted for KI Earth departure time vs. total mitigation system mass at EDS. The colours of the dots represent the degrees of nominal deflection distances between 0.0-5.0 Earth-radii. The Belief of each plot satisfies $\mathrm{Bel_{nom}} = 1.0$. The subtitles A)-F) correspond to VI₁-VI₆, respectively.
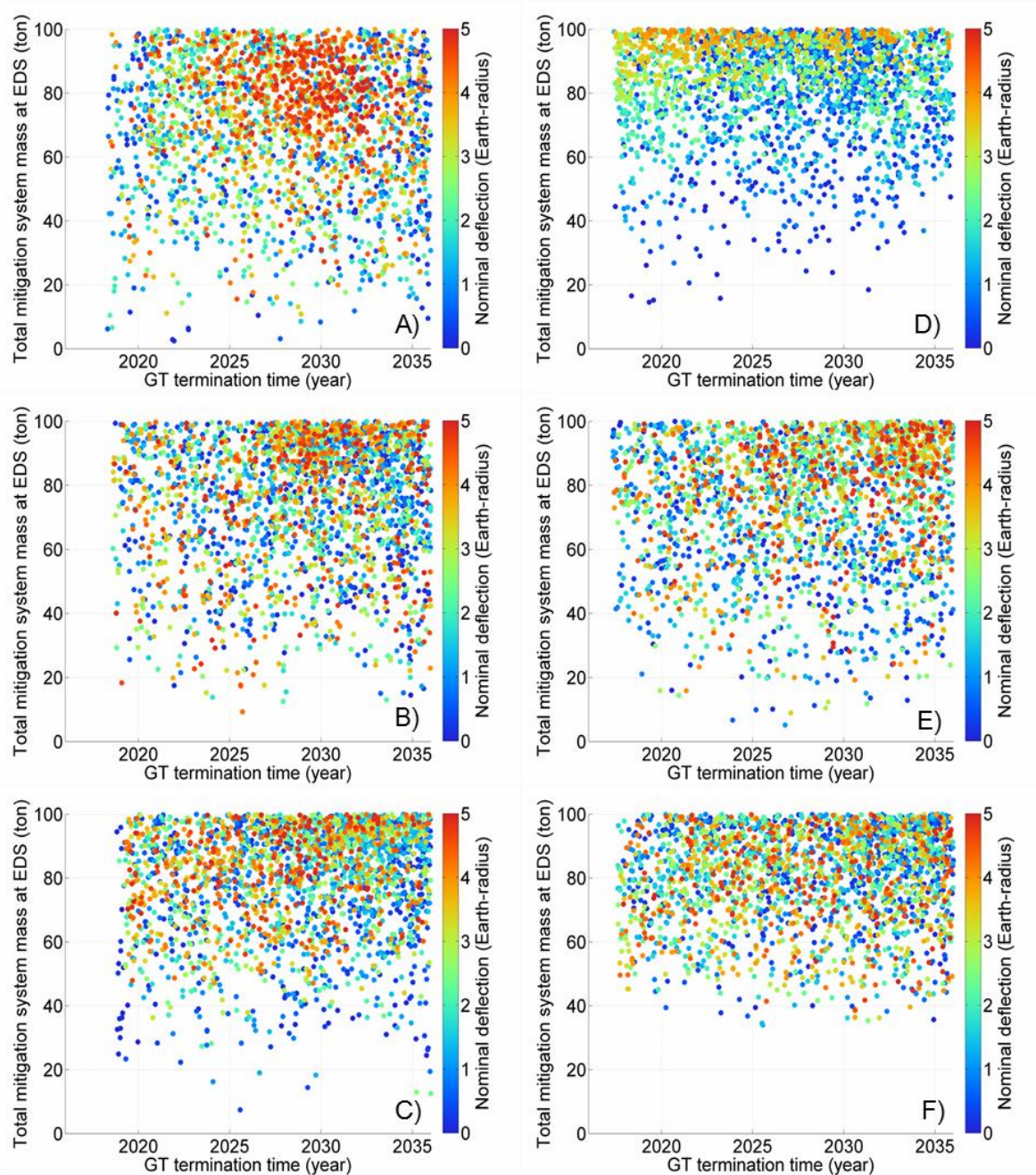
Figure 116 Pareto-optimal solutions for KI-GT campaigns against S-type VI$_1$-VI$_6$ plotted for the GT termination time vs. total mitigation system mass at EDS. The Belief of each plot satisfies $\mathrm{Bel_{nom}} \geq 0.47$. The subtitles A)-F) correspond to VI$_1$-VI$_6$, respectively.
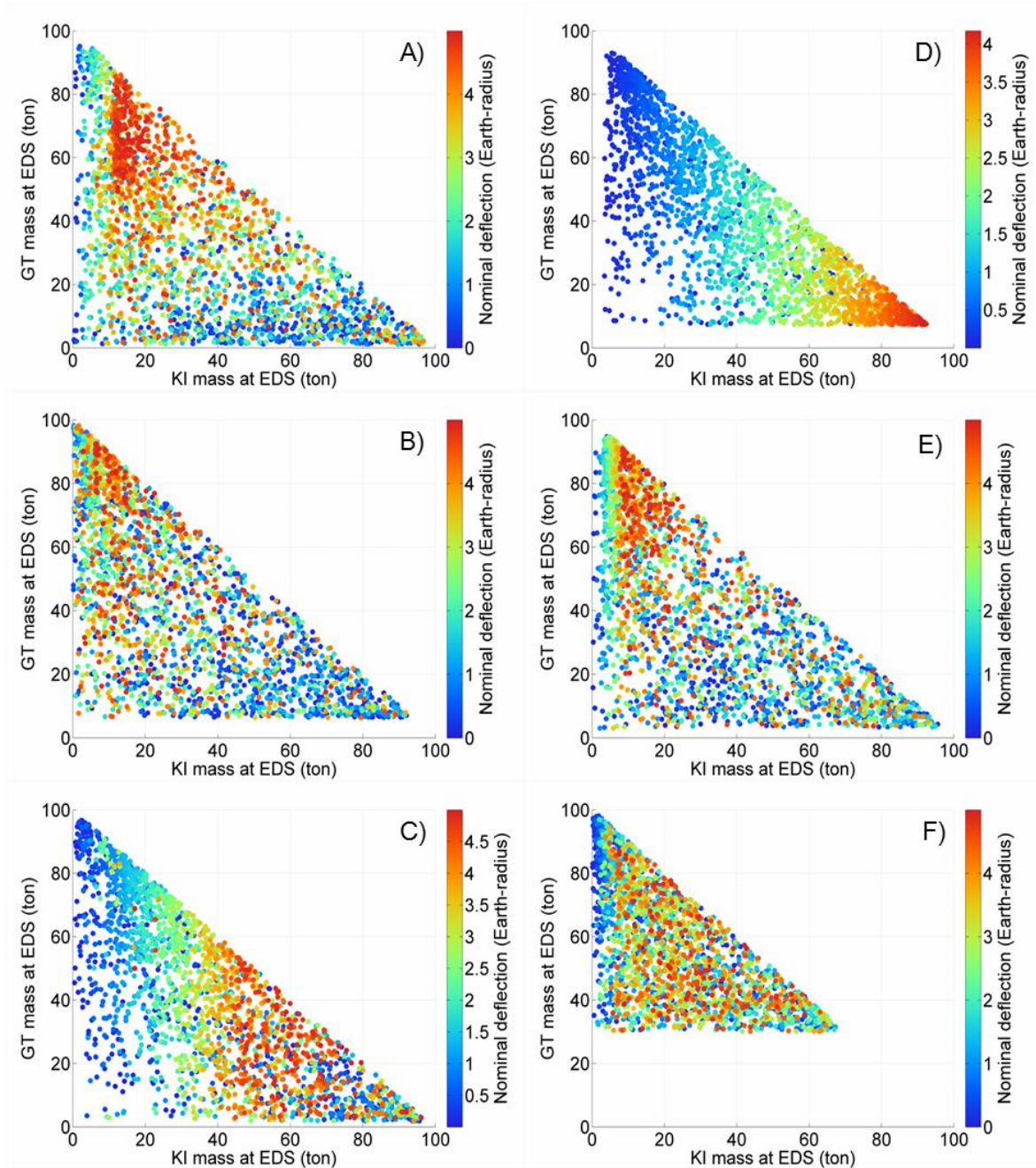
Figure 117 KI mass vs. GT mass at EDS. The Belief of each plot satisfies $Bel_{nom} \geq 0.47$. The subtitles A)-F) correspond to VI_1-VI_6, respectively.
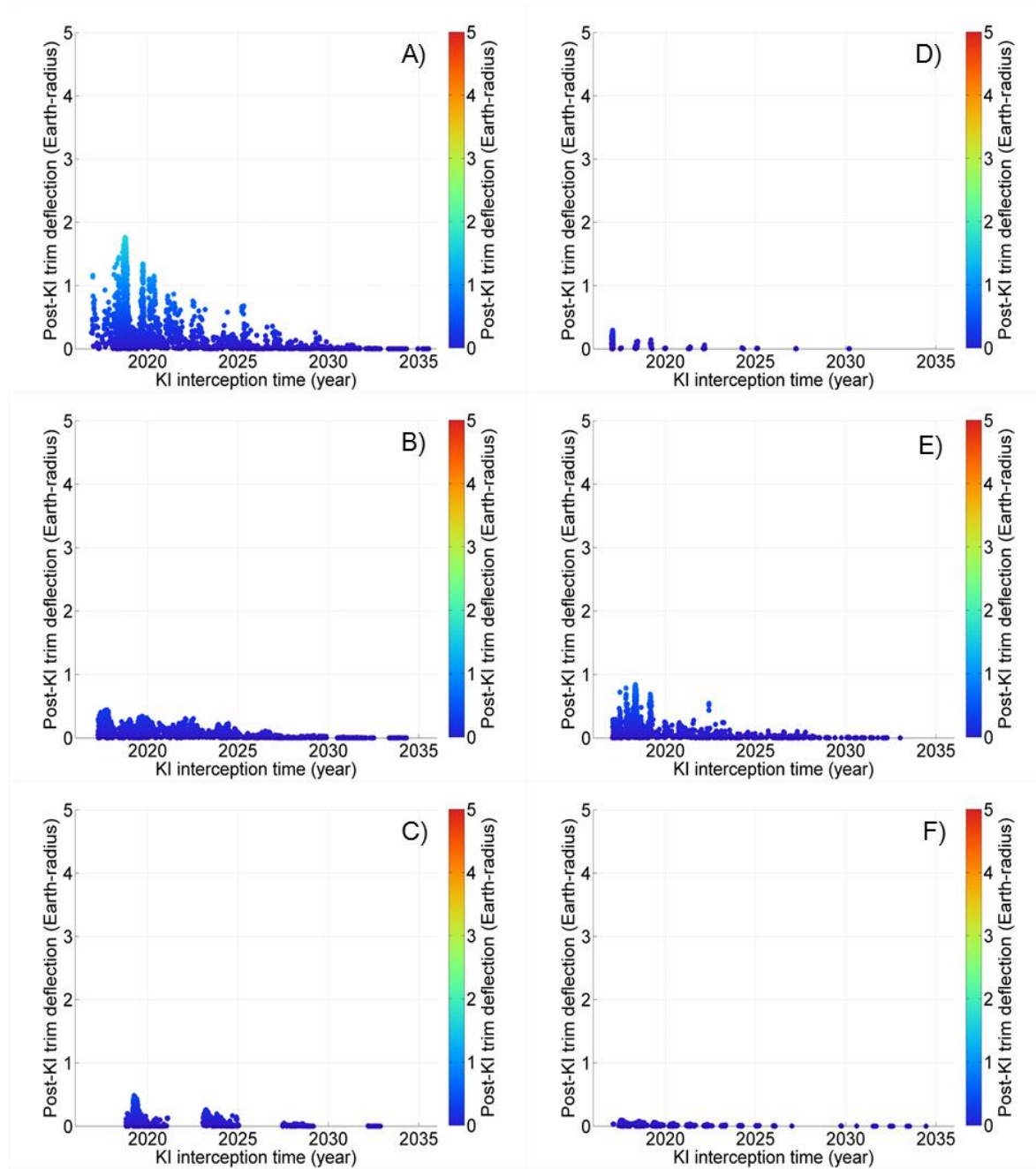
Figure 118 Post-KI deflection by GT. The Belief of each plot satisfies $Bel_{nom} \geq 0.47$. The subtitles A)-F) correspond to VI_1-VI_6, respectively.
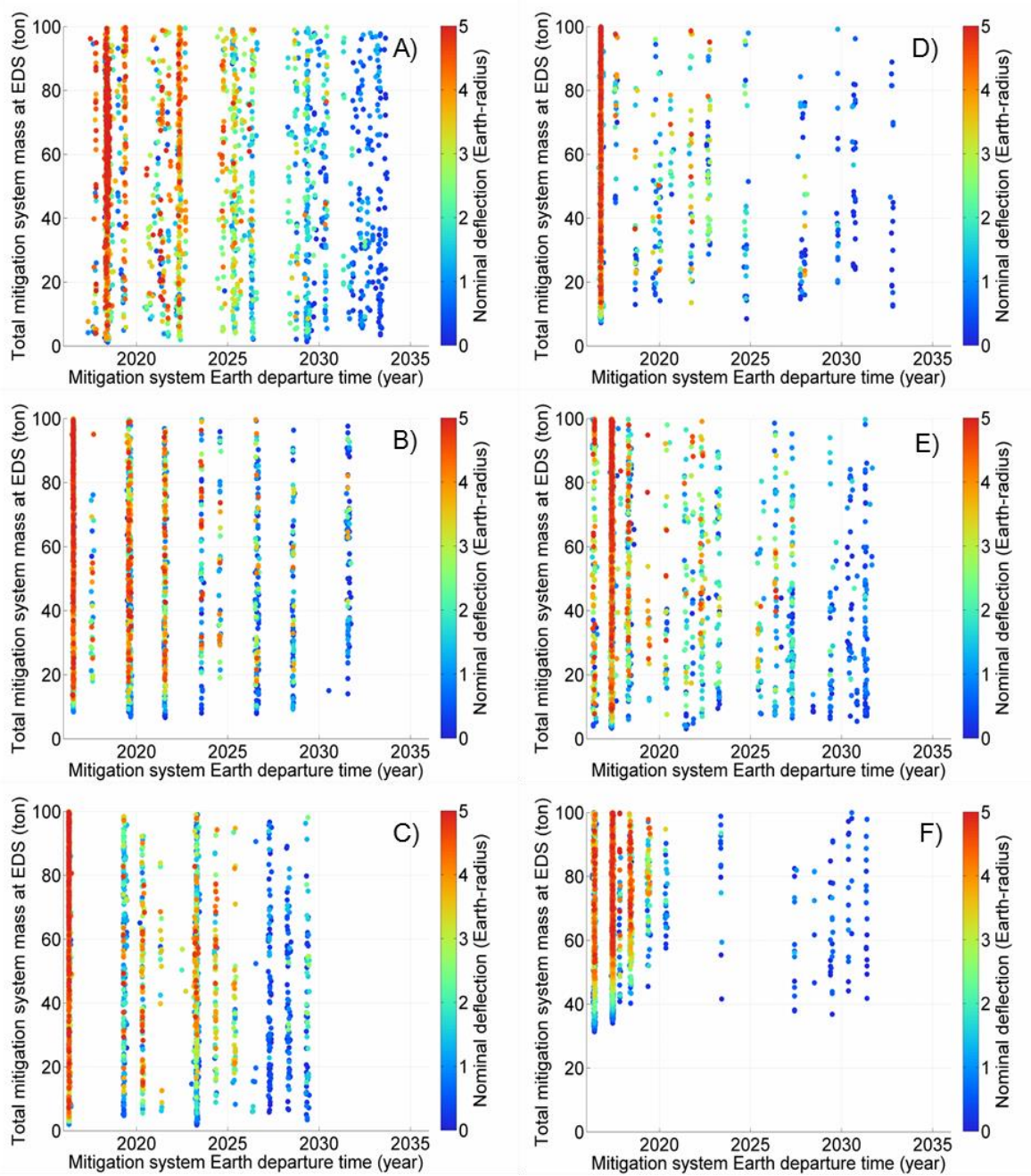
A.4.2. NI-GT mitigation campaign

Figure 119 Pareto-optimal solutions for NI-GT campaigns against S-type VI₁-VI₆ plotted for mitigation system Earth departure time vs. total mitigation system mass at EDS. The colours of the dots represent the degrees of nominal deflection distances between 0.0-5.0 Earth-radii. The Belief of each plot satisfies $\text{Bel}_{nom} \geq 0.47$. The subtitles A)-F) correspond to VI₁-VI₆, respectively.
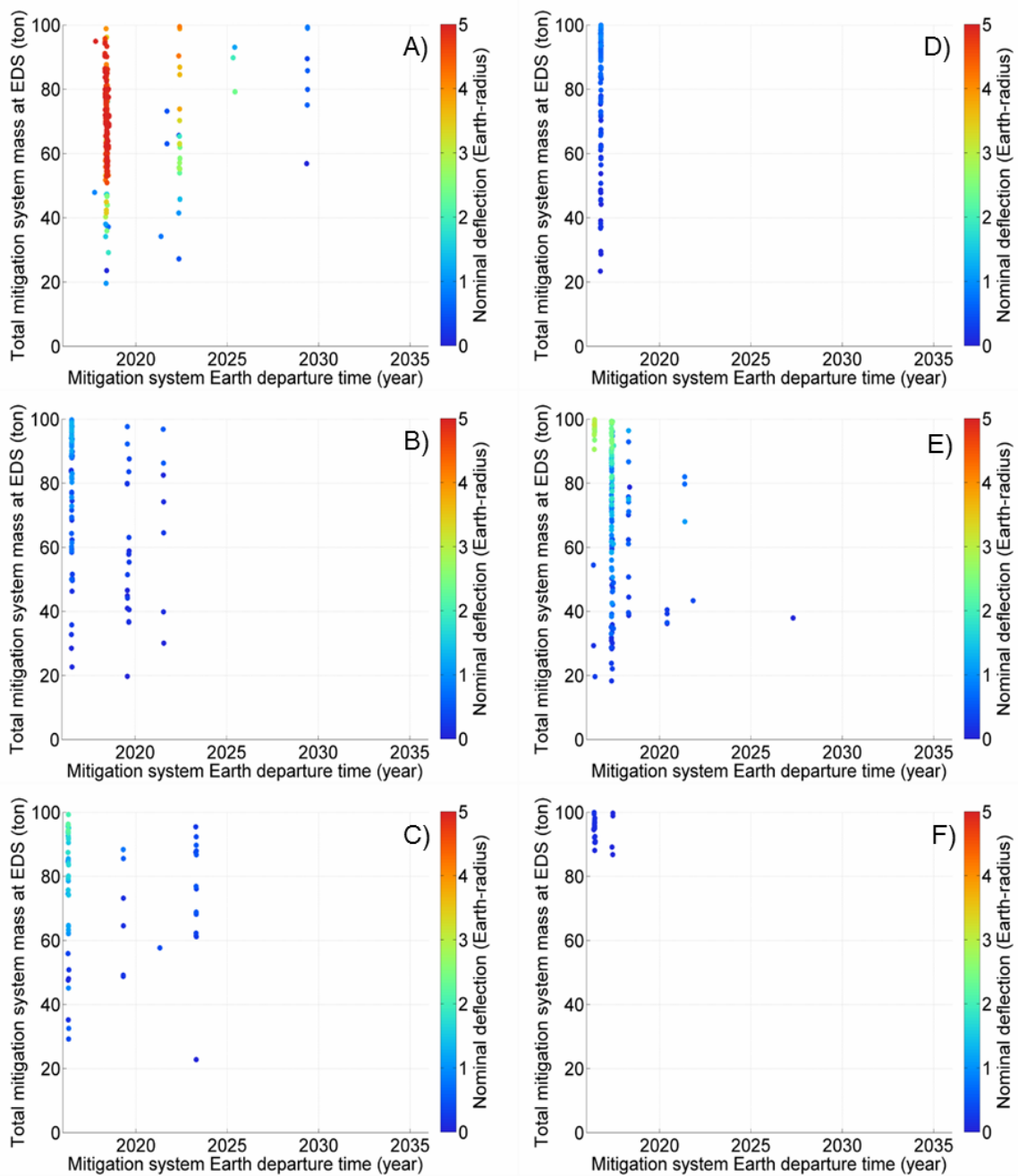
Figure 120 Pareto-optimal solutions for NI-GT campaigns against S-type VI_1-VI_6 plotted for mitigation system Earth departure time vs. total mitigation system mass at EDS. The colours of the dots represent the degrees of nominal deflection distances between 0.0-5.0 Earth-radii. The Belief of each plot satisfies $Bel_{nom} = 1.0$. The subtitles A)-F) correspond to VI_1-VI_6, respectively.

Figure 121 Pareto-optimal solutions for NI-GT campaigns against S-type VI$_1$-VI$_6$ plotted for the GT termination time vs. total mitigation system mass at EDS. The Belief of each plot satisfies Bel$_{nom} \geq 0.47$. The subtitles A)-F) correspond to VI$_1$-VI$_6$, respectively.

Figure 122 NI mass vs. GT mass at NEA arrival. The Belief of each plot satisfies $\mathrm{Bel_{nom}} \geq 0.47$. The subtitles A)-F) correspond to VI_1-VI_6, respectively.

Figure 123 Post-NI deflection by GT. The Belief of each plot satisfies $\mathbf{Bel_{nom}} \geq 0.47$. The subtitles A)-F) correspond to VI$_1$-VI$_6$, respectively.

A.4.3. SC-GT mitigation campaign

Figure 124 Pareto-optimal solutions for SC-GT campaigns against S-type VI$_1$-VI$_6$ plotted for mitigation system Earth departure time vs. total mitigation system mass at EDS. The colours of the dots represent the degrees of nominal deflection distances between 0.0-5.0 Earth-radii. The Belief of each plot satisfies $Bel_{nom} \geq 0.47$. The subtitles A)-F) correspond to VI$_1$-VI$_6$, respectively.
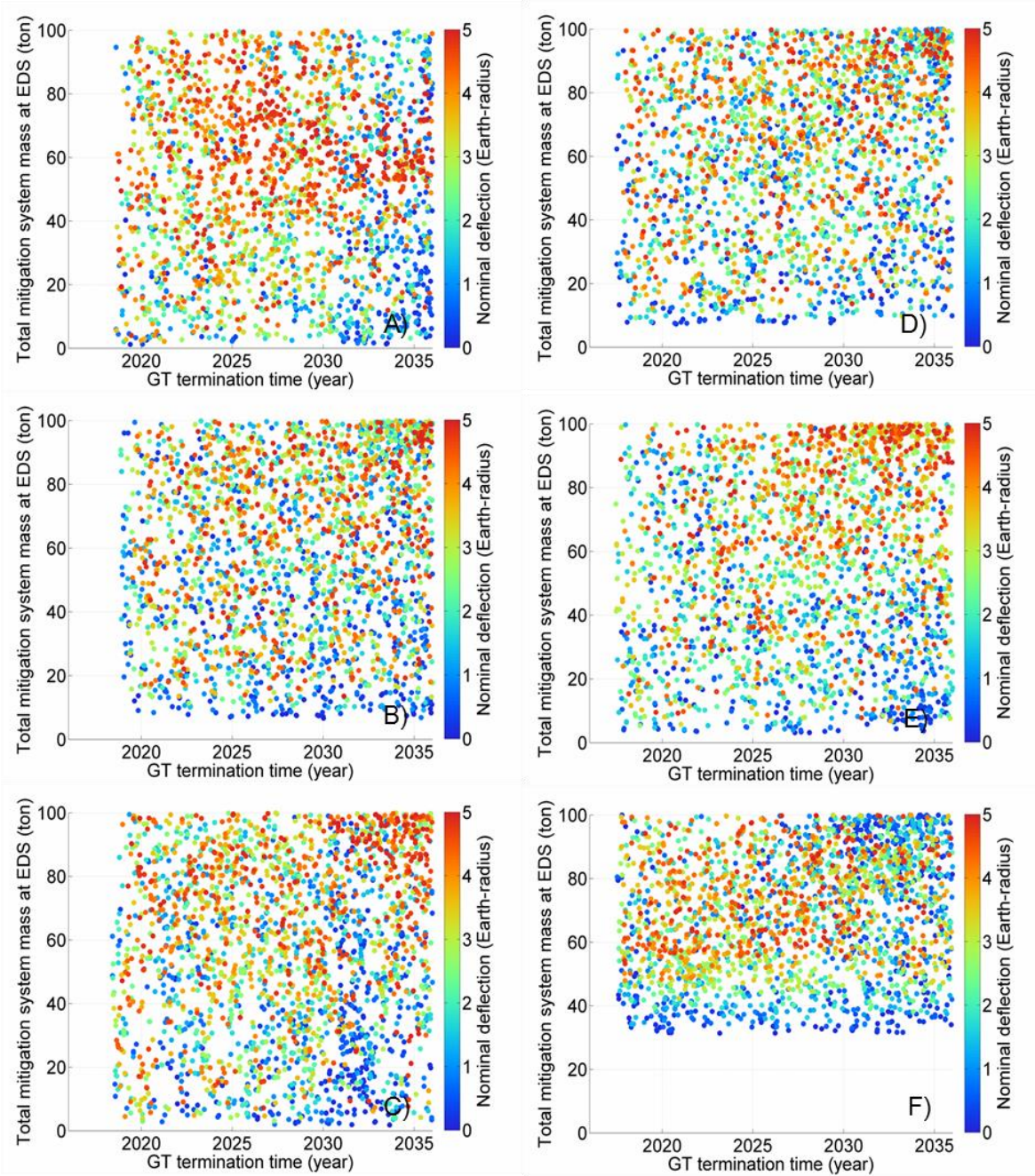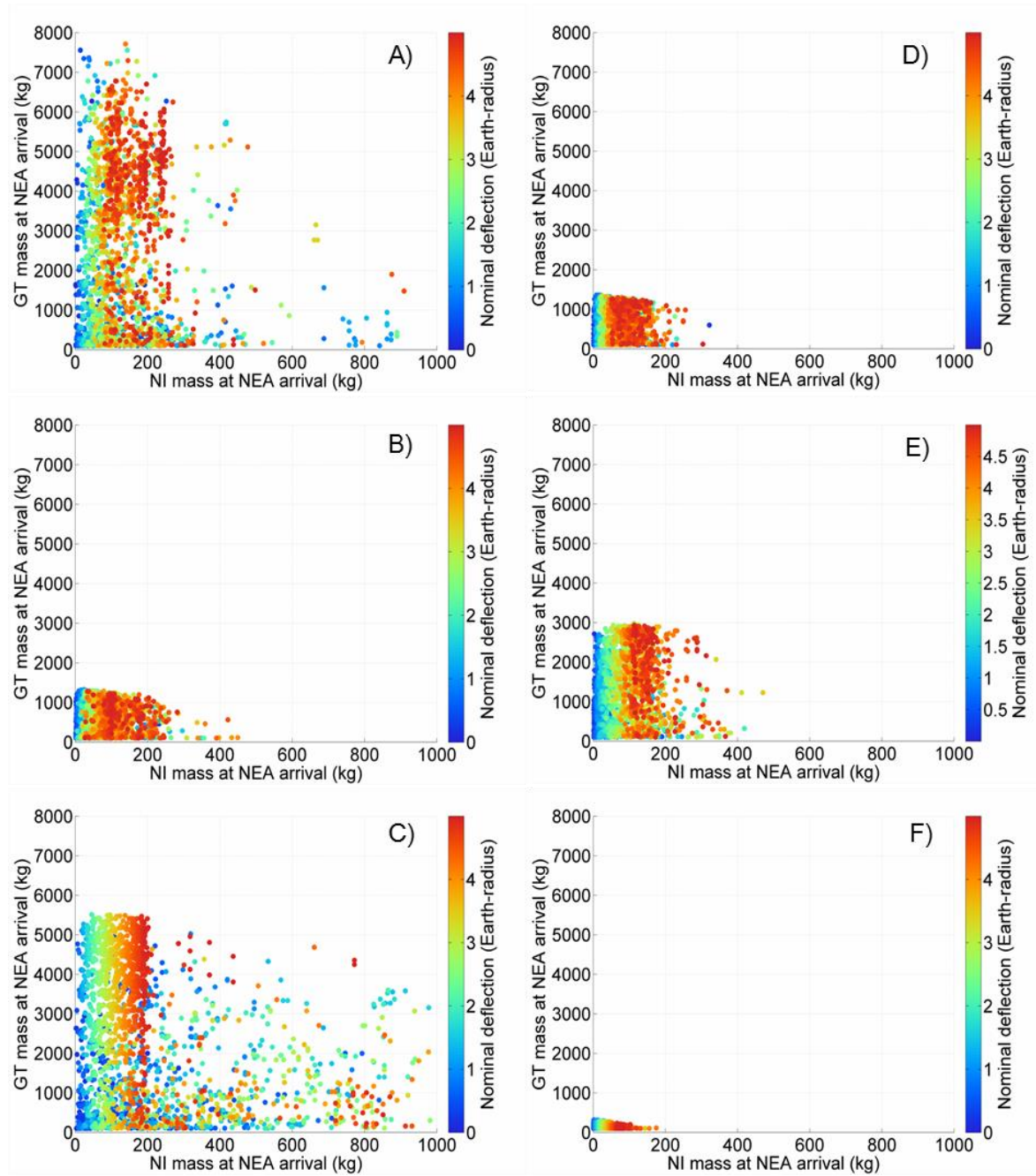
Figure 125 Pareto-optimal solutions for SC-GT campaigns against S-type VI₁-VI₆ plotted for mitigation system Earth departure time vs. total mitigation system mass at EDS. The colours of the dots represent the degrees of nominal deflection distances between 0.0-5.0 Earth-radii. The Belief of each plot satisfies $Bel_{nom} = 1.0$. The subtitles A)-F) correspond to VI₁-VI₆, respectively.
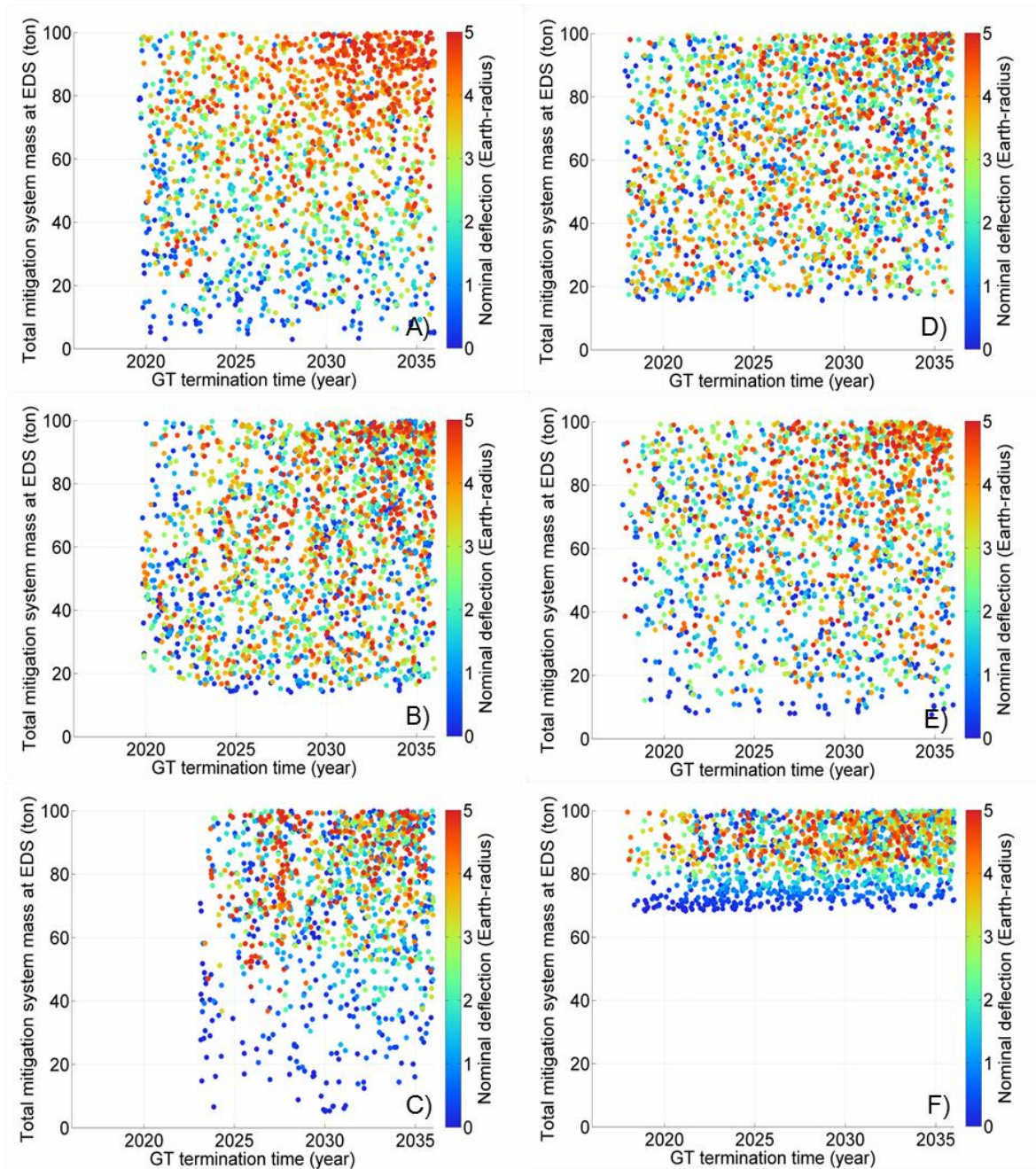
Figure 126 Pareto-optimal solutions for SC-GT campaigns against S-type VI₁-VI₆ plotted for the GT termination time vs. total mitigation system mass at EDS. The Belief of each plot satisfies $\text{Bel}_{\text{nom}} \geq 0.47$. The subtitles A)-F) correspond to VI₁-VI₆, respectively.
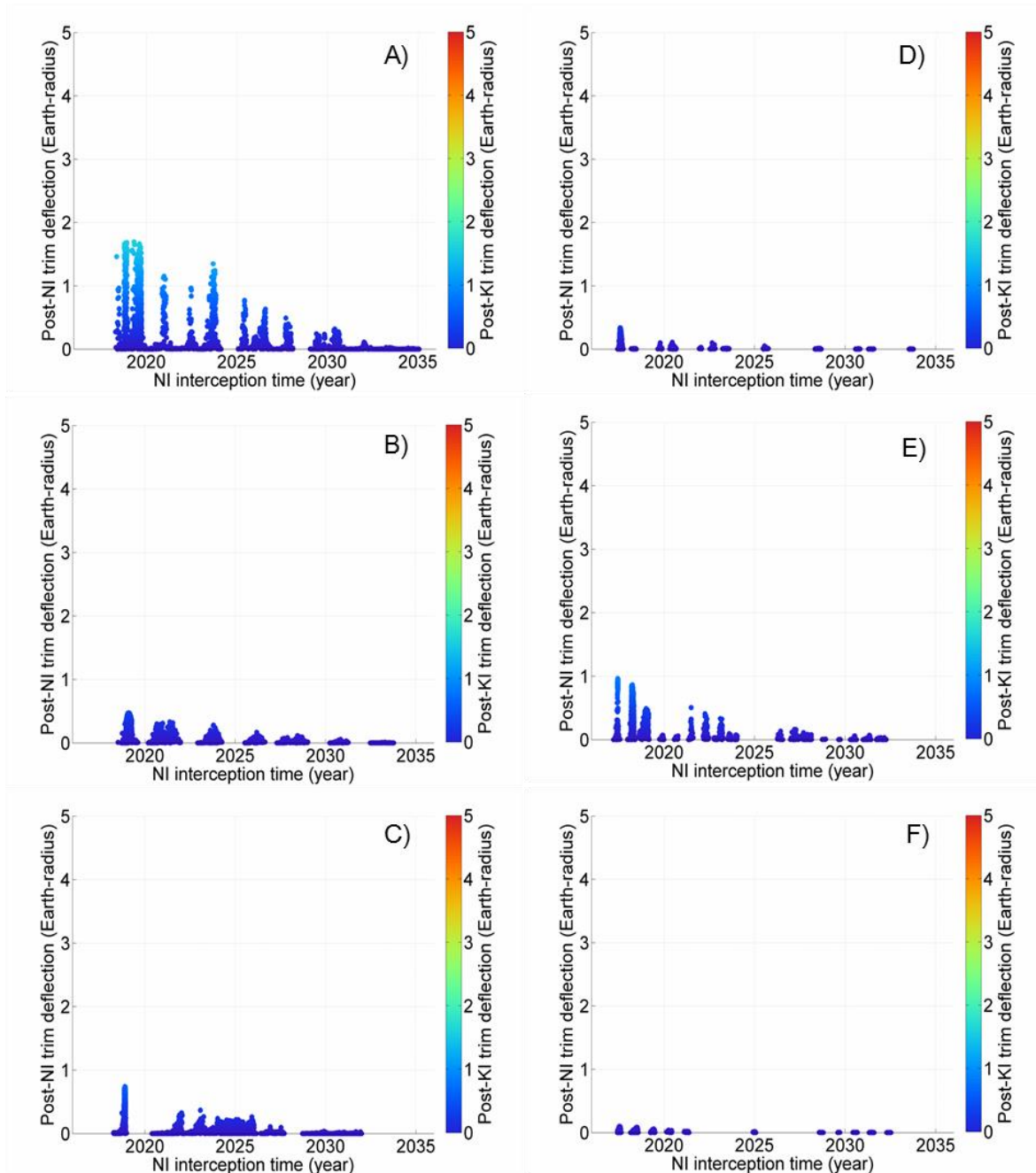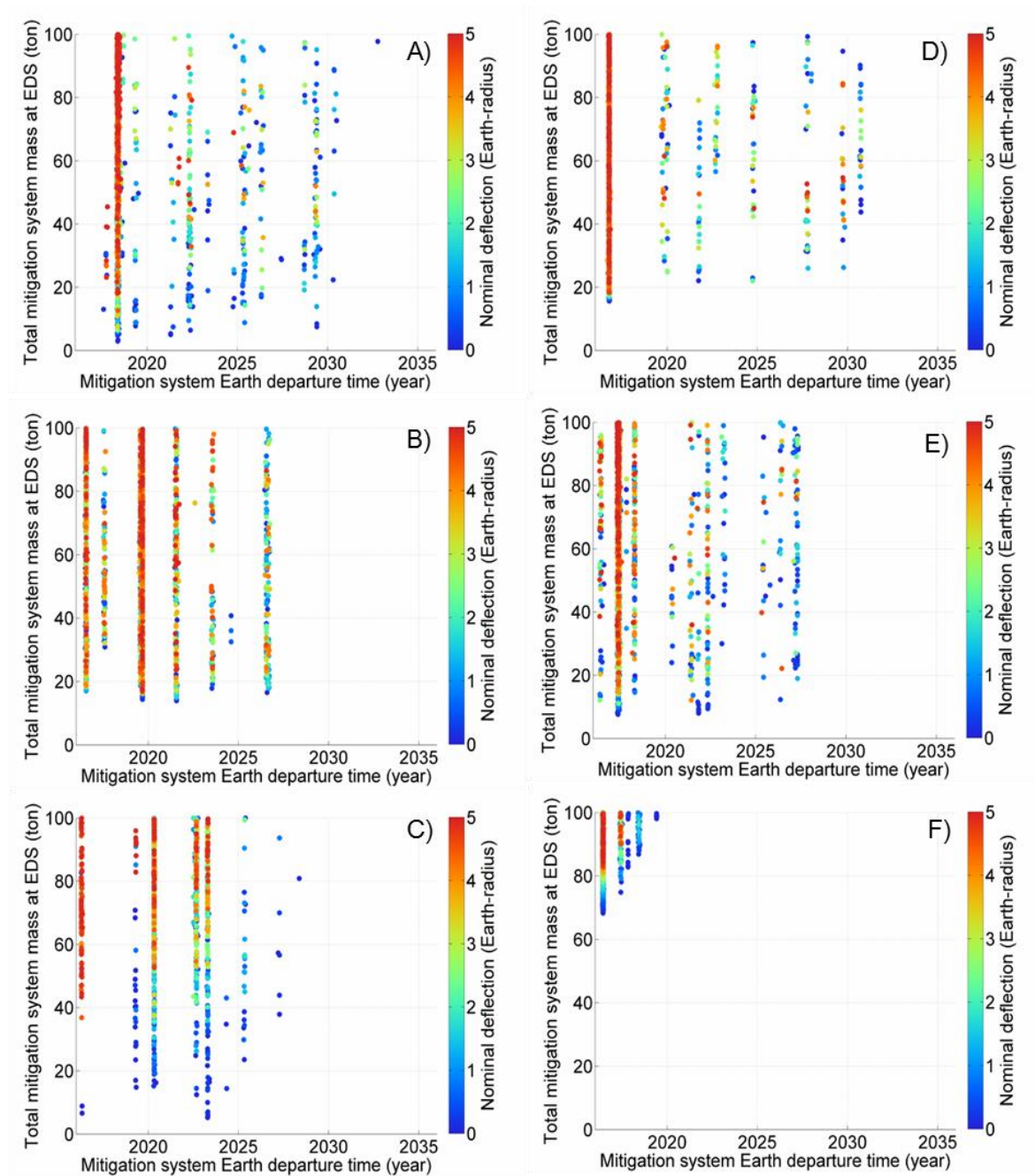
Figure 127 SC mass vs. GT mass at NEA arrival. The Belief of each plot satisfies $Bel_{nom} \geq 0.47$. The subtitles A)-F) correspond to VI_1-VI_6, respectively.
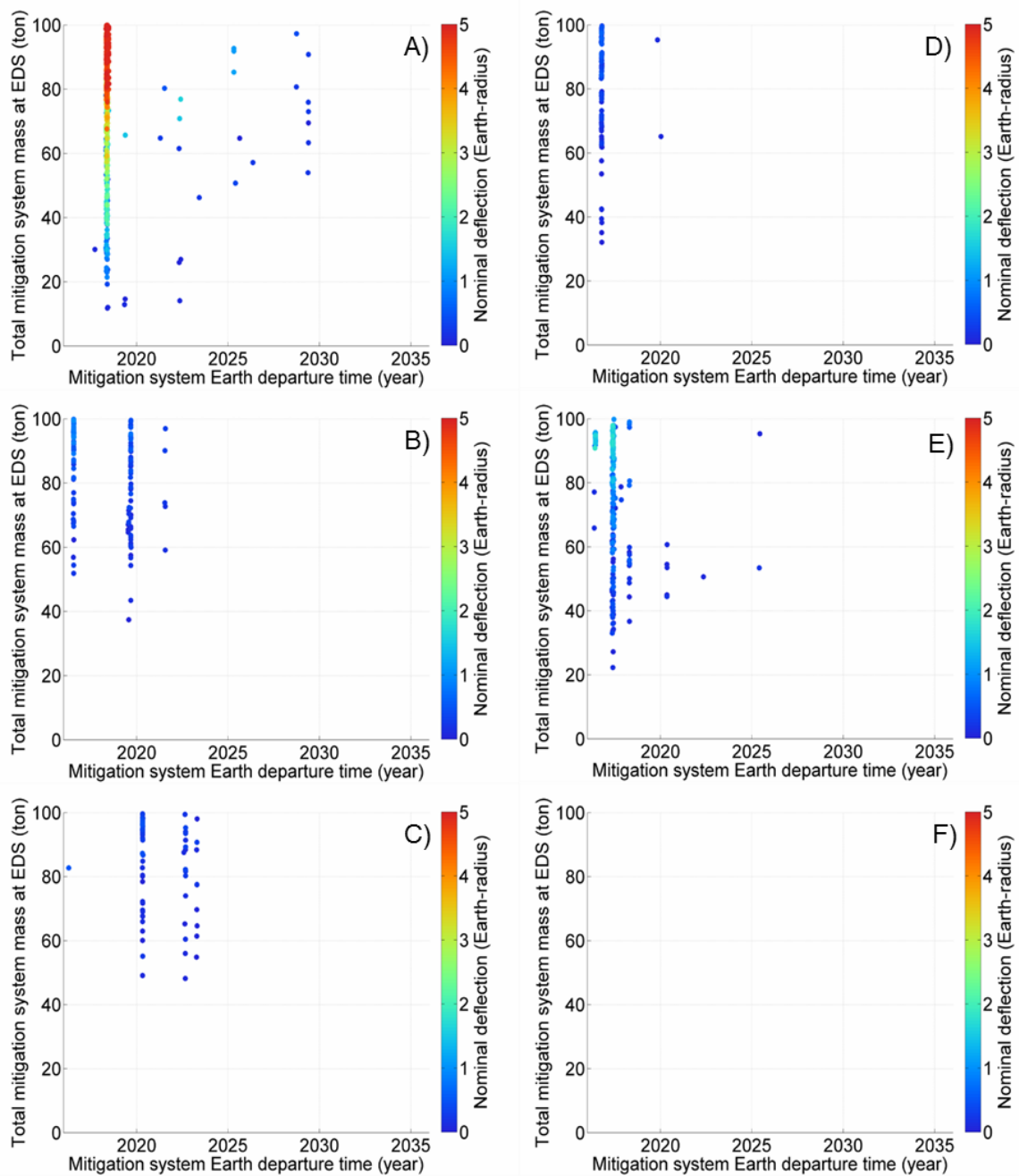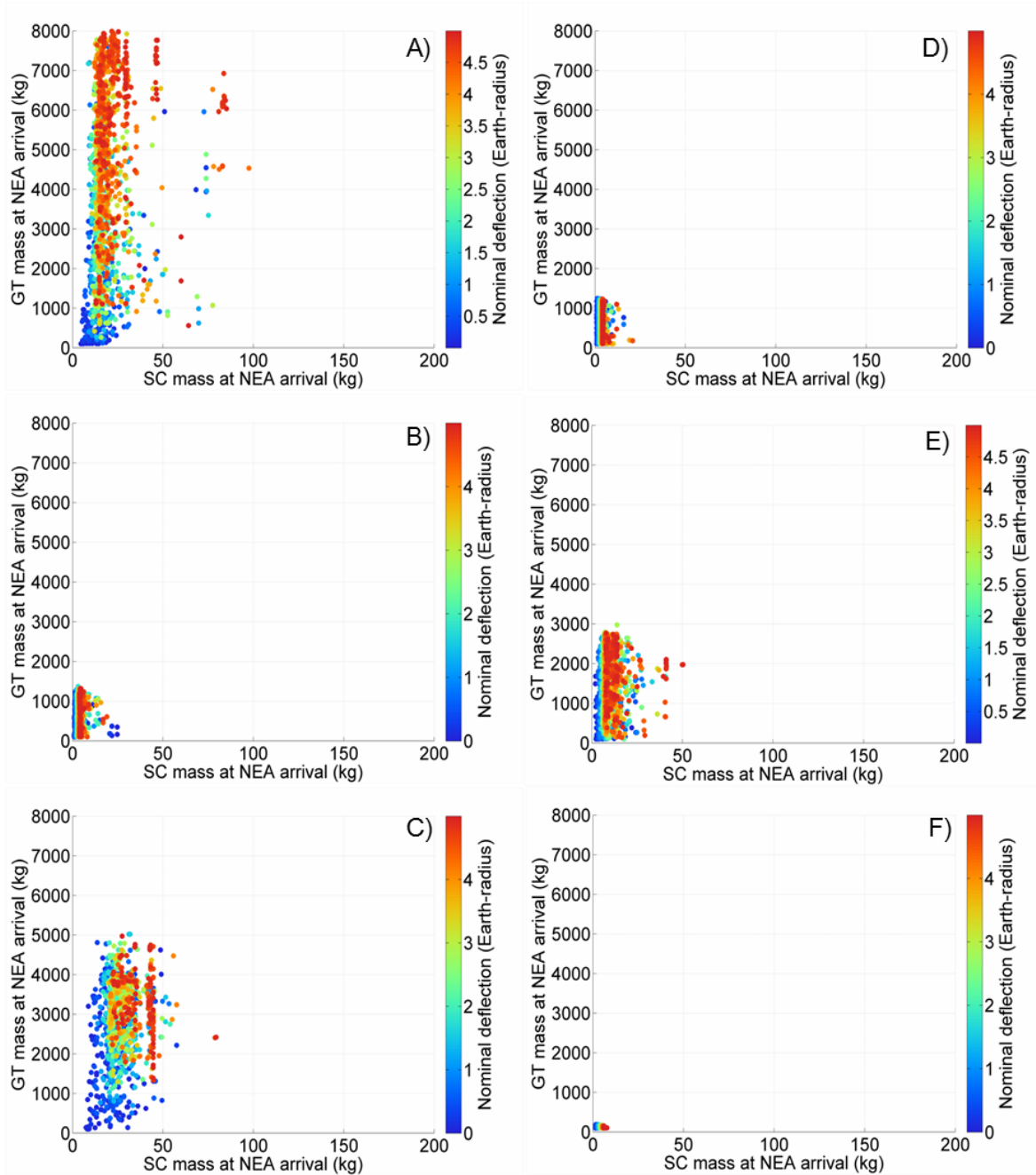
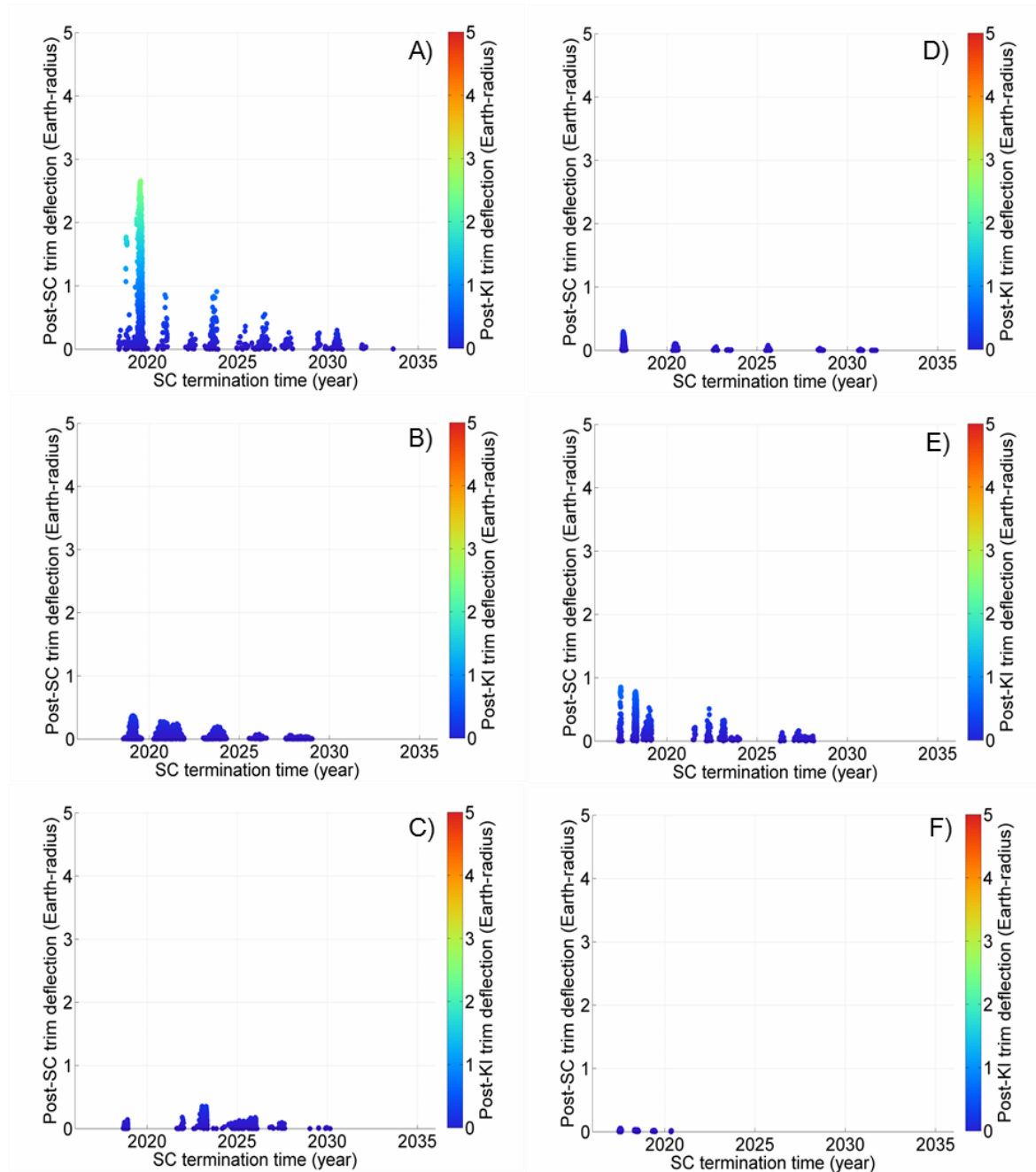**Figure 128 Post-SC deflection by GT. The Belief of each plot satisfies $\text{Bel}_{\text{nom}} \geq 0.47.$ The subtitles A)-F) correspond to $\text{VI}_1\text{-VI}_6$, respectively.**

References

[1]   (2012, 26 November). *Near Earth Object Program*. Available: http://neo.jpl.nasa.gov/stats/

[2]   H. Kuninaka, "Round-Trip Deep Space Maneuver of Microwave Discharge Ion Engines onboard HAYABUSA Explorer," presented at the 32nd International Electric Propulsion Conference, Wiesbaden, 2011.

[3]   "2006 Near-Earth Object Survey and Deflection Study," National Aeronautics and Space Administration, 2006.

[4]   (2010, 15 April). *Near Earth Object Maps*. Available: http://www.arm.ac.uk/neos/

[5]   A. S. Rivkin, *Asteroids, Comets, and Dwarf Planets*. Westport: Greenwood Press, 2009.

[6]   H. Yurimoto, K. Abe, M. Abe, M. Ebihara, A. Fujimura, M. Hashiguchi, K. Hashizume, T. R. Ireland, S. Itoh, J. Katayama, C. Kato, J. Kawaguchi, N. Kawasaki, F. Kitajima, S. Kobayashi, T. Meike, T. Mukai, K. Nagao, T. Nakamura, H. Naraoka, T. Noguchi, R. Okazaki, C. Park, N. Sakamoto, Y. Seto, M. Takei, A. Tsuchiyama, M. Uesugi, S. Wakaki, T. Yada, K. Yamamoto, M. Yoshikawa, and M. E. Zolensky, "Oxygen Isotopic Compositions of Asteroidal Materials Returned from Itokawa by the Hayabusa Mission," *Science,* vol. 333, pp. 1116-1119, 2011.

[7]   J. Brophy, F. Culick, L. Friedman, C. Allen, D. Baughman, J. Bellerose, B. Betts, M. Brown, M. Busch, J. Casani, M. Coradini, J. Dankanich, P. Dimotakis, M. Elvis, I. Garrick-Bethel, B. Gershman, T. Jones, D. Landau, C. Lewicki, J. Lewis, P. Llanos, M. Lupisella, D. Mazanek, P. Mehrotra, J. Nuth, K. Parkin, R. Schweickart, G. Singh, N. Strange, M. Tantardini, B. Wilcox, C. Williams, W. Williams, and D. Yeomans, "Asteroid Retrieval Feasibility Study," Keck Institute for Space Studies, California Institute of Technology, Jet Propulsion Laboratory, Pasadena, CA, 2012.

[8]   (2013, 23 July). *Asteroid Initiative*. Available: http://www.nasa.gov/mission_pages/asteroids/initiative/index.html

[9]   D. J. Tholen, "Asteroid taxonomy from cluster analysis of photometry," Doctor of Philosophy, Planetary Sciences, Graduate College, University of Arizona Press, Arizona, USA, 1984.

[10]   J. Gradie and E. Tedesco, "Compositional Structure of the Asteroid Belt," *Science,* vol. 25, pp. 1405-1407, 1982.

[11]   (2012, 9 December). *Sentinel Mission*. Available: http://b612foundation.org/media/sentinelmission/

[12]   R. P. Binzel, D. F. Lupishko, M. D. Martino, R. J. Whiteley, and G. J. Hahn, "Physical Properties of Near-Earth Objects," in *Asteroids III*, W. F. Bottke Jr., A. Cellino, P. Paolicchi, and R. P. Binzel, Eds., ed Tucson: University of Arizona Press, 2002, pp. 255-271.

[13]   J. A. Wood, *Meteorites and the Origin of Planets*. New York: McGraw-Hill Book Company, 1968.

[14]   M. M. Grady, *Catalogue of Meteorites*. Cambridge: Cambridge University Press, 2002.

[15]   G. W. Wetherill, "Asteroidal sources of ordinary chondrites," *Meteoritics,* vol. 20, pp. 1-22, 1985.

[16]   J. Wisdom, "Chaotic dynamics in the solar system," *Icarus,* vol. 72, pp. 241-275, 1987.

[17]   J. F. Bell, D. R. Davis, W. K. Hartmann, and M. J. Gaffey, "Asteroids: The big picture," in *Asteroids II*, R. P. Binzel, T. Gehrels, and M. S. Matthews, Eds., ed Tucson: University of Arizona Press, 1989, pp. 921-945.

[18]   J. T. Wasson, *Meteorites: Their Record of Early Solar-System History*. New York: W H Freeman & Co, 1985.

[19]   R. Greenberg and M. C. Nolan, "Delivery of asteroids and meteorites to the inner solar system," in *Asteroids II*, R. P. Binzel, T. Gehrels, and M. S. Matthews, Eds., ed Tucson: University of Arizona Press, 1989, pp. 778-804.

[20]   D. Stoffler, A. Bischoff, V. Buchwald, and A. E. Rubin, "Shock effects in meteorites," in *Meteorites and the Early Solar System*, J. F. Kerridge and M. S. Matthews, Eds., ed Tucson: University of Arizona Press, 1988.

[21] G. W. Wetherill and C. R. Chapman, "Asteroids and meteorites," in *Meteorites and the Early Solar System*, J. F. Kerridge and M. S. Matthews, Eds., ed Tucson: University of Arizona Press, 1988, pp. 33-69.

[22] L. Wilson, K. Keil, and S. J. Love, "The internal structures and densities of asteroids," *Meteoritics & Planetary Science,* vol. 34, pp. 479-483, 1999.

[23] D. T. Britt, D. Yeomans, K. Housen, and G. Consolmagno, "Asteroid Density, Porosity, and Structure," in *Asteroids III*, W. F. Bottke Jr., A. Cellino, P. Paolicchi, and R. P. Binzel, Eds., ed Tucson: University of Arizona Press, 2002, pp. 485-500.

[24] C. M. Pieters, J. B. Adams, P. Mouginis-Mark, S. H. Zisk, J. W. Head, T. B. McCord, and M. Smith, "The nature of crater rays: the Copernicus example," *Journal of Geophysics Research,* vol. 90, pp. 12393-12413, 1985.

[25] D. T. Britt and C. M. Pieters, "Darkening in gas-rich ordinary chondrites: Spectral modelling and implications for regoliths of ordinary chondrite parent bodies," presented at the Lunar and Planetary Science Conference XXII, Houston, TX, 1991.

[26] "Defending Planet Earth: Near-Earth Object Surveys and Hazard Mitigation Strategies: Final Report," Committee to Review Near-Earth Object Surveys and Hazard Mitigation Strategies; National Research Council, 2010.

[27] "Near-Earth Object Survey and Deflection Analysis of Alternatives: Report to Congress," National Aeronautics and Space Administration, 2007.

[28] L. W. Alvarez, W. Alvarez, F. Asaro, and H. V. Michel, "Extraterrestrial Cause for the Cretaceous-Tertiary Extinction," *Science,* vol. 6, pp. 1095-1108, 1980.

[29] W. Ailor, "Planetary Defense Conferences: Sharing Information on NEO Threats and Mitigation," The Aerospace Corporation, 2011.

[30] (2013, 25 March). *Herschel intercepts asteroid Apophis*. Available: http://phys.org/news/2013-01-herschel-intercepts-asteroid-apophis.html

[31] A. Milani, S. R. Chesley, P. W. Chodas, and G. B. Valsecchi, "Asteroid Close Approaches: Analysis and Potential Impact Detection," in *Asteroids III*, W. F. Bottke Jr., A. Cellino, P. Paolicchi, and R. P. Binzel, Eds., ed Tucson: University of Arizona Press, 2002, pp. 55-69.

[32] D. Morrison, C. R. Chapman, D. Steel, and R. P. Binzel, "Impacts and the public: communicating the nature of the impact hazard," in *Mitigation of Hazardous Comets and Asteroids*, M. J. S. Belton, T. H. Morgan, N. H. Samarasinha, and D. K. Yeomans, Eds., ed Cambridge: Cambridge University Press, 2004, pp. 353-390.

[33] (2012, 23 November). *Hayabusa 2 Project*. Available: http://b612.jspec.jaxa.jp/hayabusa2/index.html

[34] (2013, 19 June). *OSIRIS-REx Fact Sheet*. Available: http://www.nasa.gov/centers/goddard/pdf/552572main_OSIRIS_REx_Factsheet.pdf

[35] T. J. Ahrens and A. W. Harris, "Deflection and fragmentation of near-Earth asteroids," in *Hazards due to comets and asteroids*. vol. 2, T. Gehrels, M. S. Mathewes, and A. Schumann, Eds., ed Tucson: University of Arizona Press, 1994, p. 897.

[36] P. Hammerling and J. L. Remo, "NEO interaction with nuclear radiation," *Acta Astronautica,* vol. 36, pp. 337-346, 1995.

[37] R. L. Schweickart, E. T. Lu, P. Hut, and C. R. Chapman, "The Asteroid Tugboat," *Scientific American,* pp. 54-61, 2003.

[38] H. J. Melosh, I. V. Nemchinov, and Y. I. Zetzer, "Non-nuclear strategies for deflecting comets and asteroids," in *Hazards due to comets and asteroids*, T. Gehrels, Ed., ed Tucson: University of Arizona Press, 1994.

[39] D. D. Mazanek, C. M. Roithmayr, and J. Antol, "Comet/Asteroid protection system (CAPS): A space-based system concept for revolutionizing Earth protection and utilization of near-Earth objects," *Acta Astronautica,* vol. 53, pp. 405-422, 2003.

[40] J. Olds, A. Charania, M. Graham, and J. Wallace, "The league of extraordinary machines: A rapid and scalable approach to planetary defense against asteroid impactors," NASA Institute for Advanced Concepts, 2004.

[41] E. T. Lu and S. G. Love, "Gravitational tractor for towing asteroids," *Nature,* vol. 438, pp. 177-178, 2005.

[42] C. Bombardelli and J. Peláez, "Ion Beam Shepherd for Asteroid Deflection," *Journal of Guidance, Control, and Dynamics,* vol. 34, pp. 1270-1272, 2011.

[43] G. L. Matloff, "Applying International Space Station (ISS) and solar-sail technology to the exploration and diversion of small, dark, near Earth objects (NEO's)," *Acta Astronautica,* vol. 44, pp. 151-157, 1999.

[44] N. Murdoch, D. Izzo, C. Bombardelli, I. Carnelli, A. Hilgers, and D. Rodgers,

"Electrostatic tractor for near Earth object deflection," presented at the International Astronautical Congress, Glasgow, 2008.

[45]   J. E. Richardson, H. J. Melosh, C. M. Lisse, and B. Carcich, "A ballistics analysis of the Deep Impact ejecta plume: Determining Comet Tempel 1's gravity, mass, and density," *Icarus,* vol. 190, pp. 357-390, 2007.

[46]   M. Yoshikawa, A. Fujiwara, J. Kawaguchi, and Hayabusa Mission & Science Team, "The nature of asteroid Itokawa revealed by Hayabusa," in *Proceedings of the International Astronomical Union Symposium*, 2006, pp. 401-416.

[47]   D. Isbell, F. O'Donnell, and J. G. Watson, "Deep Space 1 Asteroid Flyby," National Aeronautics and Space Administration, 1999.

[48]   J. P. Sanchez, C. Colombo, M. Vasile, and G. Radice, "Multicriteria Comparison Among Several Mitigation Strategies for Dangerous Near-Earth Objects," *Journal of Guidance, Control, and Dynamics,* vol. 32, pp. 121-142, 2009.

[49]   D. K. Yeomans, S. Bhaskaran, S. B. Broschart, S. R. Chesley, P. W. Chodas, M. A. Jones, and T. H. Sweetser, "Near-Earth Object (NEO) analysis of transponder tracking and gravity tractor performance," JPL Task Plan No. 82-120022, 2008.

[50]   H. Schaub and J. L. Junkins, *Analytical mechanics of space systems*. Reston: American Institute of Aeronautics and Astronautics Inc., 2003.

[51]   R. H. Battin, *An Introduction to the Mathematics and Methods of Astrodynamics, Revised Edition*. Reston: American Institute of Aeronautics and Astronautics Inc., 1999.

[52]   W. F. Bottke Jr., A. Morbidelli, R. Jedicke, J.-M. Petit, H. F. Levison, P. Michel, and T. S. Metcalfe, "Debiased Orbital and Absolute Magnitude Distribution of the Near-Earth Objects," *Icarus,* vol. 156, pp. 399-433, 2002.

[53]   J. P. Sanchez and C. R. McInnes, "Accessibility of the resources of near Earth space using multi-impulse transfers," presented at the 2010 AIAA/AAS Astrodynamics Specialist Conference, Toronto, 2010.

[54]   R. B. Adams, J. W. Campbell, R. C. Hopkins, W. S. Smith, W. Arnold, M. Baysinger, T. Crane, P. Capizzo, S. Sutherlin, J. Dankanich, G. Woodcock, G. Edlin, J. Rushing, L. Fabisinski, D. Jones, S. McKamey, S. Thomas, C. Maccone, G. Matloff, and J. Remo, "Near Earth Object (NEO) Mitigation Options Using Exploration Technologies," presented at the 2007 Planetary Defense Conference, Washington, DC, 2007.

[55]   A. Hawkins and J. Bellerose, "Concept of Operations during Proximity Operations at Near Earth Objects," presented at the Planetary Defense Conference: From Threat to Action, Bucharest, 2011.

[56]   Y. Sugimoto, G. Radice, and J. P. Sanchez, "Effects of NEO composition on deflection methodologies," *Acta Astronautica,* vol. 90, pp. 14-21, 2012.

[57]   Y. Sugimoto, G. Radice, M. Ceriotti, and J. P. Sanchez, "Hazardous Near Earth Asteroid Mitigation Campaign Planning based on Uncertain Information on Fundamental Asteroid Characteristics," presented at the 2013 IAA Planetary Defense Conference, Flagstaff, Arizona, 2013.

[58]   D. K. Yeomans, S. Bhaskaran, S. B. Broschart, S. R. Chesley, P. W. Chodas, and T. H. Sweetser, "Deflecting a Hazardous Near-Earth Object," presented at the 1st IAA Planetary Defense Conference: Protecting Earth from Asteroids, Granada, 2009.

[59]   R. R. Yager, M. Federizzi, and J. Kacprzyk, *Advances in the Dempster-Shafer Theory of Evidence*. Hoboken: John Wiley & Sons Inc., 1994.

[60]   T. Nakamura, T. Noguchi, M. Tanaka, M. E. Zolensky, M. Kimura, A. Nakato, T. Ogami, H. Ishida, A. Tsuchiyama, T. Yada, K.Shirai, R. Okazaki, A. Fujimura, Y. Ishibashi, M. Abe, T. Okada, M. Ueno, and T. Mukai, "Mineralogy and major element abundance of the dust particles recovered from Muses-C regio on the asteroid Itokawa," presented at the 42nd Lunar and Planetary Science Conference, Texas, 2011.

[61]   T. Okada, K. Shirai, Y. Yamamoto, T. Arai, and K. Ogawa, "X-ray Fluorescence Spectrometry of Asteroid Itokawa by Hayabusa," presented at the 42nd Lunar and Planetary Science Conference, Texas, 2006.

[62]   M. Abe, Y. Takagi, K. Kitazato, S. Abe, T. Hiroi, F. Vilas, B. E. Clark, P. A. Abell, S. M. Lederer, K. S. Jarvis, T. Nimura, Y. Ueda, and A. Fujiwara, "Near-Infrared Spectral Results of Asteroid Itokawa from the Hayabusa Spacecraft," *Science,* vol. 312, 2006.

[63]   M. K. Shepard, B. E. Clark, M. C. Nolan, E. S. Howell, C. Magri, J. D. Giorgini, L. A. M. Benner, S. J. Ostro, A. W. Harris, B. Warner, D. Pray, P. Pravec, M. Fauerbach, T. Bennett, A. Klotz, R. Behrend, H. Correia, J. Coloma, S. Casulli, and R. A., "A radar survey of M- and X-class asteroids," *Icarus,* vol. 195, pp. 184-205, 2008.

[64]   A. Mainzer, T. Grav, J. Bauer, J. Masiero, R. S. McMillan, R.M.Cutri, R. Walker, E.

Wright, P. Eisenhardt, D. J. Tholen, T. Spahr, R. Jedicke, L. Denneau, E. DeBaun, D. Elsbury, T. Gautier, S. Gomillion, E.Hand, W.Mo, J. Watkins, A. Wilkins, G. L. Bryngelson, A. D. P. Molina, S. Desai, M. G. o. Camus, S. L. Hidalgo, I. Konstantopoulos, J. A. Larsen, C. Maleszewski, M. A. Malkan, J.‑C. Mauduit, B. L. Mullan, E. W. Olszewski, J. Pforr, A. Saro, J. V. Scotti, and L. H. Wasserman, "NEOWISE Observations of Near‑Earth Objects: Preliminary Results," *The Astrophysical Journal,* vol. 743, article id. 156, 17 pp., 2011.

[65] J. R. Masiero, A. K. Mainzer, T. Grav, J. M. Bauer, R. M. Cutri, J. Dailey, P. R. M. Eisenhardt, R. S. McMillan, T. B. Spahr, M. F. Skrutskie, D. Tholen, R. G. Walker, E. L. Wright, E. DeBaun, D. Elsbury, T. Gautier IV, S. Gomillion, and A. Wilkins, "Main Belt Asteroids with WISE/NEOWISE. I. Preliminary Albedos and Diameters," *The Astrophysical Journal,* vol. 741, article id. 68, 20 pp., 2011.

[66] W. H. Ryan and E. V. Ryan, "Rotation Rates of Recently Discovered Small Near‑Earth Asteroids," presented at the Advanced Maui Optical and Space Surveillance Technologies Conference, Maui, 2009.

[67] S. J. Ostro, L. A. M. Benner, M. C. Nolan, C. Magri, J. D. Giorgini, D. J. Scheeres, S. B. Broschart, M. Kaasalainen, D. Vokrouhlický, S. R. Chesley, J.‑L. Margot, R. F. Jurgens, R. Rose, D. K. Yeomans, S. Suzuki, and E. M. D. Jong, "Radar observations of asteroid 25143 Itokawa (1998 SF36)," *Meteoritics & Planetary Science,* vol. 39, pp. 407‑424, 2004.

[68] A. Perret, "Mass determination of a small body in solar system by using a test‑mass during a fly‑by," *Acta Astronautica,* vol. 12, pp. 41‑44, 1985.

[69] S. Abe, T. Mukai, N. Hirata, O. S. Barnouin‑Jha, A. F. Cheng, H. Demura, R. W. Gaskell, T. Hashimoto, K. Hiraoka, T. Honda, T. Kubota, M. Matsuoka, T. Mizuno, R. Nakamura, D. J. Scheeres, and M. Yoshikawa, "Mass and Local Topography Measurements of Itokawa by Hayabusa," *Science,* vol. 312, pp. 1344‑1347, 2006.

[70] R. P. Binzel, A. S. Rivkin, C. A. Thomas, P. Vernazza, T. H. Burbine, F. E. DeMeo, S. J. Bus, A. T. Tokunaga, and M. Birlan, "Spectral properties and composition of potentially hazardous Asteroid (99942) Apophis," *Icarus,* vol. 200, pp. 480‑485, 2009.

[71] D. T. Britt and G. J. Consolmagno S.J., "Modeling the Structure of High Porosity Asteroids," *Icarus,* vol. 152, pp. 134‑139, 2001.

[72] P. Pravec and A. W. Harris, "Fast and Slow Rotation of Asteroids," *Icarus,* vol. 148, pp. 12‑20, 2000.

[73] E. Asphaug, "Interior structures for asteroids and cometary nuclei," in *Mitigation of Hazardous Comets and Asteroids*, M. J. S. Belton, T. H. Morgan, N. H. Samarasinha, and D. K. Yeomans, Eds., ed Cambridge: Cambridge University Press, 2004, pp. 66‑103.

[74] J. Baer, S. R. Chesley, and R. D. Matson, "Astrometric masses of 26 asteroids and observations on asteroid porosity," *The Astronomical Journal,* vol. 141, pp. 143‑155, 2011.

[75] T. G. Müller, T. Sekiguchi, M. Kaasalainen, M. Abe, and S. Hasegawa, "Thermal infrared observations of the Hayabusa spacecraft target asteroid 25143 Itokawa," *Astronomy & Astrophysics,* vol. 443, pp. 347‑355, 2005.

[76] A. W. Harris and P. Pravec, "Rotational properties of asteroids, comets, and TNOs," in *Proceedings of the International Astronomical Union Symposium*, 2005, pp. 439‑447.

[77] C.‑I. Lagerkvist and Å. Claesson, "Spin rates of asteroids," *Earth, Moon, and Planets,* vol. 71, pp. 219‑223, 1996.

[78] S. Hasegawa, T. G. Müller, K. Kawakami, T. Kasuga, T. Wada, Y. Ita, N. Takato, H. Terada, T. Fujiyoshi, and M. Abe, "Albedo, Size, and Surface Characteristics of Hayabusa‑2 Sample‑Return Target 162173 1999 JU3 from AKARI and Subaru Observations," *Publications of the Astronomical Society of Japan,* vol. 60, pp. S399‑S405, 2008.

[79] C. P. Opeil, G. J. Consolmagno, and D. T. Britt, "The thermal conductivity of meteorites: New measurements and analysis," *Icarus,* vol. 208, pp. 449‑454, 2010.

[80] F. Zuiani, M. Vasile, and A. Gibbings, "Evidence‑Based Robust Design of Deflection Actions for Near Earth Objects," *Celestial Mechanics and Dynamical Astronomy,* vol. 114, pp. 107‑136, 2012.

[81] P. Michel, "Physical properties of Near‑Earth Objects that inform mitigation," *Acta Astronautica,* vol. 90, pp. 6‑13, 2012.

[82] T. G. Müller, T. Sekiguchi, M. Kaasalainen, M. Abe, and S. Hasegawa, "Itokawa: The power of ground‑based mid‑infrared observations," in *Proceedings of the International Astronomical Union Symposium*, 2006, pp. 261‑266.

[83] A. W. Harris, "The H‑G asteroid magnitude system: Mean slope parameters," *Abstracts of the Lunar and Planetary Science Conference,* vol. 20, p. 375, 1989.

[84]   C. A. Maddock, "On the dynamics, navigation and control of a spacecraft formation of solar concentrators in the proximity of an asteroid," Doctor of Philosophy, Department of Aerospace Engineering, Faculty of Engineering, University of Glasgow, Glasgow, Scotland, 2010.

[85]   M. Vasile and C. Colombo, "Optimal impact strategies for asteroid deflection," *Journal of Guidance, Control, and Dynamics,* vol. 31, pp. 858-872, 2008.

[86]   H. Agarwal, J. E. Renaud, and E. L. Preston, "Trust region managed reliability based design optimization using Evidence Theory," presented at the 44th AIAA/ASME/ASCE/AHS Structures, Structural Dynamics, and Materials Conference, Norfolk, 2003.

[87]   N. Croisard, M. Vasile, S. Kemble, and G. Radice, "Preliminary space mission design under uncertainty," *Acta Astronautica,* vol. 66, pp. 654-664, 2010.

[88]   D. T. Britt and G. J. Consolmagno S.J., "Stony meteorite porosities and densities: A review of the data through 2001," *Meteoritics & Planetary Science,* vol. 38, pp. 1161-1180, 2003.

[89]   D. T. Britt and G. J. Consolmagno, "Meteorite porosities and densities: A review of trends in the data," presented at the 35th Lunar and Planetary Science Conference, Houston, 2004.

[90]   B. Mason, "The carbonaceous chondrites," *Space Science Reviews,* vol. 1, pp. 621-646, 1962.

[91]   G. J. Flynn, L. B. Moore, and W. Klöck, "Density and Porosity of Stone Meteorites: Implications for the Density, Porosity, Cratering, and Collisional Disruption of Asteroids," *Icarus,* vol. 142, pp. 97-105, 1999.

[92]   E. P. Henderson and S. H. Perry, "A discussion of the densities of iron meteorites," *1954,* vol. 6, pp. 221-240, 1954.

[93]   G. J. Consolmagno S.J. and D. T. Britt, "The density and porosity of meteorites from the Vatican collection," *Meteoritics & Planetary Science,* vol. 33, pp. 1231-1241, 1998.

[94]   R. T. Dodd Jr., W. R. Van Schmus, and D. M. Koffman, "A survey of the unequilibrated ordinary chondrites," *Geochimica et Cosmochimica Acta,* vol. 31, pp. 921-934, 1967.

[95]   M. H. Briggs and G. Mamikunian, "Organic constituents of the carbonaceous chondrites," *Space Science Reviews,* vol. 1, pp. 647-682, 1963.

[96]   J. H. Hubbell and S. M. Seltzer. (1996, 5 April). *Tables of X-Ray mass attenuation coefficients and mass energy-absorption coefficients from 1 keV to 20 MeV for elements Z = 1 to 92 and 48 additional substances of dosimetric interest.* Available: http://www.nist.gov/pml/data/xraycoef/index.cfm

[97]   W. Martienssen and H. Warlimont, *Springer Handbook of Condensed Matter and Materials Data.* Heidelberger: Springer-Verlag, 2005.

[98]   H. Nagahara, I. Kushiro, and B. O. Mysen, "Evaporation of olivine: Low pressure phase relations of the olivine system and its implication for the origin of chondritic components in the solar nebula," *Geochimica et Cosmochimica Acta,* vol. 58, pp. 1951-1963, 1994.

[99]   T. J. Zega and P. R. Buseck, "Fine-grained-rim mineralogy of the Cold Bokkeveld CM chondrite," *Geochimica et Cosmochimica Acta,* vol. 67, pp. 1711-1721, 2003.

[100]   A. Cattaneo, A. F. Gualtieri, and G. Artioli, "Kinetic study of the dehydroxylation of chrysotile asbestos with temperature by in situ XRPD," *Physics and Chemistry of Minerals,* vol. 30, pp. 177-183, 2003.

[101]   H. Palme, J. W. Larimer, and M. E. Lipschutz, "Moderately volatile elements," in *Meteorites and the Early Solar System,* J. F. Kerridge and M. S. Matthews, Eds., ed Tucson: University of Arizona Press, 1988.

[102]   W. J. Tedeschi, J. L. Remo, J. F. Schulze, and R. P. Young, "Experimental Hypervelocity Impact Effects on Simulated Planetesimal Materials," *International Journal of Impact Engineering,* vol. 17, pp. 837-848, 1995.

[103]   K. R. Housen and R. M. Schmidt, "Crater Ejecta Scaling Laws: Fundamental Forms Based on Dimensional Analysis," *Journal of Geophysical Research,* vol. 88, pp. 2485-2499, 1983.

[104]   J. D. Walker and S. Chocron, "Momentum enhancement in hypervelocity impact," *International Journal of Impact Engineering,* vol. 38, pp. A1-A7, 2011.

[105]   K. A. Holsapple, "On the "strength" of the small bodies of the solar system: A review of strength theories and their implementation for analyses of impact disruptions," *Planetary and Space Science,* vol. 57, pp. 127-141, 2009.

[106]   K. A. Holsapple and K. R. Housen, "Momentum transfer in asteroid impacts. I. Theory and scaling," *Icarus,* vol. 221, pp. 875-887, 2012.

[107] C. R. McInnes, "Deflection of near-Earth asteroids by kinetic energy impacts from retrograde orbits," *Planetary and Space Science*, vol. 52, pp. 587-590, 2004.

[108] S. Glasstone, "The Effects of Nuclear Weapons," Atomic Energy Commission, Washington D.C., 1962.

[109] T. B. Cochran, W. M. Arkin, and M. M. Hoenig, *Nuclear Weapons Stockpile: U.S. Nuclear Forces and Capabilities* vol. 1. Cambridge, Massachusetts: Ballinger Publishing Company, 1984.

[110] J. R. Wertz and W. J. Larson, *Space Mission Analysis and Design*, third edition ed.: Microcosm Press, 2003.

[111] D. R. Davis, D. D. Durda, F. Marzari, A. C. Bagatin, and R. Gil-Hutton, "Collisional Evolution of Small-Body Populations," in *Asteroids*, T. Gehrels, Ed., ed Tucson: University of Arizona Press, 1979, pp. 528-557.

[112] V. A. Simonenko, V. N. Norgin, D. V. Petrov, O. N. Shubin, and J. C. Solem, "Defending the Earth against impacts from large comets and asteroids," in *Hazards due to Comets and Asteroids*, T. Gehrels, Ed., ed Tucson, AZ: University of Arizona Press, 1994, pp. 929-953.

[113] E. Asphaug, E. V. Ryan, and M. T. Zuber, "Asteroid Interiors," in *Asteroids III*, W. F. Bottke Jr., A. Cellino, P. Paolicchi, and R. P. Binzel, Eds., ed Tucson: University of Arizona Press, 2002, pp. 463-480.

[114] W. Benz and E. Asphaug, "Catastrophic disruptions revisited," *Icarus*, vol. 142, pp. 5-20, 1999.

[115] J. P. Sanchez, M. Vasile, and G. Radice, "On the consequences of a fragmentation due to a NEO mitigation strategy," presented at the 59th International Astronautical Congress, Glasgow, UK, 2008.

[116] C. A. Maddock, J. P. Sanchez, M. Vasile, and G. Radice, "Comparison of Single and MultiSpacecraft Configurations of NEA deflection by Solar Sublimation," *AIP conference Proceedings*, vol. 886, pp. 303-316, 2007.

[117] C. Gritzner and R. Kahle, "Mitigation technologies and their requirements," in *Mitigation of Hazardous Comets and Asteroids*, M. J. S. Belton, T. H. Morgan, N. H. Samarasinha, and D. K. Yeomans, Eds., ed Cambridge: Cambridge University Press, 2004, pp. 167-200.

[118] R. Kahle, E. Kührt, G. Hahn, and J. Knollenberg, "Physical limits of solar collectors in deflecting Earth-threatening asteroids," *Aerospace Science and Technology*, vol. 10, pp. 256-263, 2006.

[119] (2013, 25 July). *JPL Small-Body Database Browser*. Available: http://ssd.jpl.nasa.gov/sbdb.cgi?sstr=2008HJ

[120] H. Takegahara, Y. Kasai, Y. Gotoh, K. Miyazaki, Y. Hayakawa, S. Kitamura, H. Nagano, and K. Nakamura, "Beam Characteristics Evaluation of ETS-VI Xenon Ion Thruster," in *the 23rd International Electric Propulsion Conference*, Seattle, WA., 1993, pp. 2166-2174.

[121] F. R. Chang-Díaz, "The Vasimr Rocket," *Scientific American*, vol. 285, pp. 90-97, 2000.

[122] M. F. Piszczor, M. J. O'Neill, M. I. Eskenazi, and J. Henry W. Brandhorst, "Stretched Lens Array (SLA) Photovoltaic Concentrator Hardware Development & Testing," in *3rd World Conference on Photovoltaic Energy Conversion*, Osaka, Tokyo, 2003.

[123] B. B. Stephen and D. J. Scheeres, "Control of Hovering Spacecraft Near Small Bodies: Application to Asteroid 25143 Itokawa," *Journal of Guidance, Control, and Dynamics*, vol. 28, pp. 343-354, 2005.

[124] J. Kawaguchi, A. Fujiwara, and T. Uesugi, "Hayabusa—Its technology and science accomplishment summary and Hayabusa-2," *Acta Astronautica*, vol. 62, pp. 639-647, 2008.

[125] (2012, 12 September). *PIA15776: Asteroid 1999 RQ36*. Available: http://photojournal.jpl.nasa.gov/catalog/PIA15776

[126] A. Milani, S. R. Chesley, M. E. Sansaturio, F. Bernardi, G. B. Valsecchi, and O. Arratia, "Long-term impact risk for (101955) 1999 RQ36," *Icarus*, vol. 203, pp. 460-471, 2009.

[127] R. E. Ball, *The Fundamentals of Aircraft Combat Survivability Analysis and Design*. New york: American Institute of Aeronautics and Astronautics Inc., 1985.

[128] Q. Fang and D. Boas, "Tetrahedral mesh generation from volumetric binary and gray-scale images," in *Proceedings of IEEE International Symposium on Biomedical Imaging 2009*, Boston, Massachusetts, 2009, pp. 1142-1145.

[129] D. J. Scheeres and R. W. Gaskell, "Effect of Density Inhomogeneity on YORP: The case of Itokawa," *American Astronomical Society*, vol. 41, p. 559, 2009.

[130] S. C. Lowry, P. R. Weissman, S. R. Duddy, B. Rozitis, A. Fitzsimmons, S. F. Green, M. D. Hicks, C. Snodgrass, S. D. Wolters, S. R. Chesley, J. Pittichová, and P. v. Oers, "The internal structure of asteroid (25143) Itokawa as revealed by detection of YORP spin-up," *Astronomy & Astrophysics,* vol. 562, 2013.

[131] M. T. Zuber, D. E. Smith, A. F. Cheng, J. B. Garvin, O. Aharonson, T. D. Cole, P. J. Dunn, Y. Guo, F. G. Lemoine, G. A. Neumann, D. D. Rowlands, and M. H. Torrence, "The Shape of 433 Eros from the NEAR-Shoemaker Laser Rangefinder," *Science,* vol. 289, pp. 2097-2100, 2000.

[132] H. Ikeda, T. Kominato, M. Matsuoka, T. Ohnishi, and M. Yoshikawa, "Orbit Analysis of Hayabusa around Asteroid Itokawa," presented at the International Astronautical Congress, Valencia, 2006.

[133] C. Foster, J. Bellerose, D. Mauro, and B. Jaroux, "Mission concepts and operations for asteroid mitigation involving multiple gravity tractors," *Acta Astronautica,* vol. 90, pp. 112-118, 2012.

[134] A. W. Harris, M. A. Barucci, J. L. Cano, L. Drube, A. Fitzsimmons, M. Fulchignoni, S. F. Green, D. Hestroffer, V. Lappas, P. Michel, D. Morrison, S. A. Meshcheryakov, N. Saks, and F. Schäfer, "NEOShield: Working towards an international near-Earth object mitigation demonstration mission," presented at the European Planetary Science Congress, Madrid, Spain, 2012.

[135] "Atlas V and Delta IV Technical Summary," United Launch Alliance, LLC, 2013.

[136] K. Deb, A. Pratap, S. Agarwal, and T. Meyarivan, "A Fast and Elitist Multiobjective Genetic Algorithm: NSGA-II," *IEEE Transactions on Evolutionary Computation,* vol. 6, pp. 182-197, 2, April 2002.

[137] (2001, 18 October). *NEAR Collected Shape and Gravity Models.* Available: http://sbn.psi.edu/pds/resource/nearbrowse.html